NTNU

Norwegian University of
Science and Technology

Ice Loading On Ship Hull

Ice Specimen Testing and Stress Analysis of
Local Plate Fields in the Bow Region.

Bendik Johnsen Stephan

Marine Technology
Submission date: June 2017
Supervisor: Bernt Johan Leira, IMT

Norwegian University of Science and Technology
Department of Marine Technology

NTNU
Norwegian University of
Science and Technology

Master's Thesis, Spring 2017

for

Stud. Techn. Bendik Stephan

Ice Loading on Ship Hull: Ice Specimen Testing and Stress Analysis of Local Plate Fields in the Bow Region.

Isbelastning på Skipsskrog: Testing av Is og Spenningsanalyse av Lokale Platemodeller i Baugregionen.

Transport and exploitation of resources in the Northern areas are increasingly focused upon. The corresponding climatic conditions represent a challenge both to the operation and design of ships in these waters.

The presence of sea ice is the main factor hindering operations in Arctic. Sea ice is a complex material and induces high pressures when being in contact with ships or structures. To understand the nature of the associated forces, the ice physics and ice mechanics have to be studied.

For ice-breaking vessels significant forces will be acting on the hull during the interaction process. Determination of both loads and sea ice strength is a difficult process. This is to be considered in more detail in the present thesis.

The following subjects are to be examined:

1. Describe different types of sea ice, and their mechanical and physical properties.
2. Present and discuss models for calculation of contact pressure acting on a floating structure due to presence of ice.
3. Present measurements from uni-axial compression tests of sea ice, performed at UNIS. Also, establish an empirical pressure model based on these measurements.
4. Perform a review of ice classes of polar going ships with focus on regulations provided by DNV GL and IACS.
5. Compare different ice classes of polar going ships by assessing a local ship hull component in Abaqus, with loads obtained from measurements of sea ice and loads obtained by the regulations.
6. Establish a finite element model in Abaqus and analyse this with respect to extreme loads provided by ice ridges. Additionally, assess the effect of varying boundary conditions due to varying support of the local ship hull component. The loads should be established by measurements conducted at UNIS.

The work scope may prove to be larger than initially anticipated. Subject to approval from the supervisor, topics may be deleted from the list above or reduced in extent.

In the thesis the candidate shall present his personal contribution to the resolution of problems within the scope of the thesis work.

Theories and conclusions should be based on mathematical derivations and/or logic reasoning identifying the various steps in the deduction.

The candidate should utilise the existing possibilities for obtaining relevant literature.

The thesis should be organised in a rational manner to give a clear exposition of results, assessments, and conclusions. The text should be brief and to the point, with a clear language. Telegraphic language should be avoided.

The thesis shall contain the following elements: A text defining the scope, preface, list of contents, summary, main body of thesis, conclusions with recommendations for further work, list of symbols and acronyms, references and (optional) appendices. All figures, tables and equations shall be numbered.

The supervisor may require that the candidate, in an early stage of the work, presents a written plan for the completion of the work. The plan should include a budget for the use of computer and laboratory resources which will be charged to the department. Overruns shall be reported to the supervisor.

The original contribution of the candidate and material taken from other sources shall be clearly defined. Work from other sources shall be properly referenced using an acknowledged referencing system.

The thesis shall be submitted in 3 copies:

- Signed by the candidate
- The text defining the scope included
- In bound volume(s)
- Drawings and/or computer prints which cannot be bound should be organised in a separate folder.

Supervisor: Professor Bernt J. Leira

Deadline: June 11th, 2017

Trondheim, January 15th, 2017

Bernt J. Leira

Preface

This report is conducted as an individual master thesis during the spring semester of 2017. The thesis is written with focus on the structural part of the marine engineering field, at the Department of Marine Technology under the Norwegian University of Science and Technology.

The process of conducting analysis by use of Abaqus was time consuming. Additionally, the set-up and modelling of the various boundary conditions were difficult. Thus, the results indicated that the modelling was conducted correctly. Further, the post-processing and plotting of results were a time consuming task, as it was done manually. It have been interesting to investigate the topic of this thesis, applying theory from several subjects, applying the theory to actual cases, and solving problems using advanced software. Parts of the analysis required several hours of research to establish the required set-up and obtain correct results.

Through the subject at Svalbard, I came in contact with Professor Knut Vilhelm Høyland. Apart from the fact that the course at Svalbard was helpful, providing sufficient and useful theory, Høyland invited me to join a course with focus on sea ice mechanics. I would like to thank Knut V. Høyland and Sveinung Løset for a good course with lots of relevant theory for this thesis.

I would like to extend my gratitude to my supervisor Bernt Johan Leira for sufficient guidance and excellent feedback throughout the semester. Both meetings and conversations have been helpful in the process toward the final result. Further, I would like to thank fellow students for guidance in Abaqus and my grandmother for proofreading. Also, a huge thanks to Sigurd Kalvik for lending me a spare computer, letting me run the final analysis as my own computer failed to do so.

Bendik Stephan
Trondheim, June 8, 2017

Summary

Arctic operations are mostly carried out in seas covered in ice. For these operations, both DNV GL and IACS provide regulations for classification of ships. Interaction with ice is difficult to determine, as it could occur in many different ways. The ice vary both spatial and temporal, hence each individual interaction are distinct. The strength of sea ice depends on; ice temperature, porosity, salinity, and load direction.

The main scope of this Master's thesis is to study the behaviour of two plate fields located in the bow region of ice-going vessels, applying measurements of sea ice for load prediction. Uni-axial compression tests and parametric measures have been conducted by UNIS and prediction of ice loads are discussed in papers by Leira et al. (2009), Løset et al. (2006) and Riska (2011).

This Master's thesis presents sea ice theory down to a molecular level. Applying both theory and measurements, the flexural strength of both level ice and ridged ice were predicted. Further, the flexural strengths were applied in estimation of empirical contact pressures. These pressures were compared to pressures obtained from regulations provided by DNV GL and IACS, by conducting an assessment of a local plate field in the bow region. The assessment of the local plate field proved the dimensioning based on regulations to be a minimum requirement. The findings stated that regulations from DNV GL in general provide less contact pressure than similar regulations from IACS. Additionally, it was found that the empirical contact pressure model was able to give a simplified estimate of one interaction with ice, as ice have large temporal and spatial variations.

For the plate model located in the stem area, an empirical ridge ice pressure was applied and the boundary conditions were assessed. The model applied one fixed and three spring modelled boundaries. Findings from the assessment indicated the spring-modelled boundary to approach the behaviour of a fixed condition, as the spring stiffness was increased. Further, the modelling of the boundaries was only able to account for warping of the supportive frames.

Both models suffered from large permanent deformations and entered the non-linear behaviour region, as the applied pressures had a high magnitude. Additionally, the stiffeners providing support for the plates suffered from both plastic hinges and warping.

Sammendrag

Arktiske operasjoner foregår som oftest i hav dekket av is. For slike operasjoner har både DNV GL og IACS reguleringer for klassifisering av skip. Interaksjon mellom båt og is er vanskelig å beregne, ettersom interaksjonen kan foregå på mange forskjellige måter. Isen varierer både i tid og rom. Som et resultat er hver interaksjon særegen. Isstyrken avhenger av isens temperatur, porøsitet, saltinnhold og lastretning.

Hovedfokuset i denne masteroppgaven er responsen til to platemodeller lokalisert i baugområdet på båter som ferdes i arktiske farvann, der lastene er beregnet ut ifra målinger av sjøis. Enakset kompresjonstester og parametriske målinger av sjøis har blitt utført av UNIS og estimater på is-laster er diskutert av Leira et al. (2009), Løset et al. (2006) og Riska (2011).

Denne masteroppgaven presenterer teori på sjøis ned til et molekylært nivå. Gjennom bruk av teori og målinger, er bøyestivheten til både is og isrygger estimert. Videre ble disse målingene brukt i estimering av kontakttrykk, hvorpå kontakttrykkene ble sammenlignet med tilsvarende trykk beregnet gjennom regelverk fra DNV GL og IACS. Sammenligningen ble utført gjennom en analyse av en lokal platemodell lokalisert i baugområdet. Analysene tydet på at dimensjoneringen av platemodellen var et minimumskrav fra DNV GL. Resultatene tydet også på at DNV GL generelt gir et lavere kontakttrykk enn IACS. I tillegg fant en ut at det empiriske kontakttrykket var i stand til å gi et forenklet estimat for en interaksjon med is, ettersom is har store variasjoner i tid og rom.

For platemodellen lokalisert i fremre baugområde ble randbetingelsene analysert med et kontakttrykk beregnet ved hjelp av målinger på en isrygg. Modellen ble testet med en fast innspent og tre fjærmodellerte grensebetingelser. Analysene tydet på at de fjærmodellerte grensebetingelsene tilnærmet seg oppførselen til den fast innspente platen når fjærstivheten ble økt. Rotasjonsfjærene var kun i stand til å modellere sideveis svikt av de omkringliggende stiverne.

Begge modeller led av store permanente deformasjoner og entret ikkelineær oppførsel, ettersom de påførte trykkene var store. I tillegg, led stiverne som støttet platene av både plastisk og sideveis svikt under påføringen av trykk.

Contents

List of Tables

List of Figures

List of Symbols

A	Contact area, applied in contact pressure p_c
A_{ice}	Total area of ice floes
α	= 86400 [seconds/day]
$\hat{\alpha}$	Uniformly distributed random variable in the range [0,1]
A_{nom}	Nominal surface area
A_{ocean}	Total area of a certain ocean area
β	Hull slope, applied in contact pressure p_c
$\hat{\beta}$	Portion of diaemeter D that varies with $\hat{\alpha}$
°C	Degree centigrades, temperature measurement
C	Value relating mass of solid salts and mass of brine
c	Cohesion, in Coulomb-Mohr criterion
CAD	Computer Aided Design
C_{geo}	Constant, depending on ice boundary geometry
C_i	Ice concentration factor
d	Grain size
δ	Load fraction of the total load
$\hat{D}$	Portion of diameter that remains constant
dh_i	Additional ice layer due to growth
DNV GL	Det Norske Veritas Germanischer Lloyd
E	Elastic modulus
$\dot{\varepsilon}$	Strain rate
ε	Strain
ϵ_p	Plastic strain

η_a Volume of air in the unit volume of sea ice

η_b Volume of brine in the unit volume of sea ice

η_m Macro porosity of a ridge

η_T Total porosity of sea ice

F_0 Force required to break the ice sheet

F_B Bending capacity of ice

FDD Freezing degree days

FISCR Finnish-Swedish Ice Class Rules

F_n Normal force between ice and structure

F_R Driving force during rafting of ice

$F_{R,crit}$ Critical resultant force

F_V Vertical component of contact force

g Gravitational acceleration

γ_{ij} Shear deformation in the ij-plane

h_c Thickness of consolidated layer in an ice ridge

h_i Height of ice

h_{ic} Ice contact height, applied in contact pressure p_c

h_k Keel height of ridged ice

h_s Snow height

h_{sail} Sail height of ridged ice

IACS International Association of Classification Societies

$\boldsymbol{K}$ Stiffness vector for a linear system

k Relative amount of salt in brine

κ Spring stiffness for rotational spring [N/rad]

k_i Thermal conductivity of ice

$\boldsymbol{K}_I(\boldsymbol{r})$ Incremental stiffness vector for a non-linear system

$\boldsymbol{K}(\boldsymbol{r})$ Stiffness vector for a non-linear system

k_s Thermal conductivity of snow

k_w Influence factor for narrow loads

L Ice contact length, applied in contact pressure p_c

l_i Latent heat of ice

L_R	Length of raft
MPC	Multi Point Constraint
μ_{ii}	Friction coefficient between ice and ice
ν	Poisson's Ratio
p_c	Contact pressure between ice and structure
$p_{c,crit}$	Critical contact pressure
φ	Angle of internal friction in ice model
ppt	Parts per thousand, weight fraction
q_{ice}	Heat flux, ice
q_{latent}	Heat flux, new ice layer
q_{ocean}	Heat flux, ocean
$q_{surface}$	Heat flux, surface
$\boldsymbol{R}$	Load vector for a linear system
$\boldsymbol{r}$	Displacement vector for a linear system
R	Ratio between h_c and h_i
ρ_b	Brine density
ρ_i	Density of ice
ρ_{pi}	Density of pure ice
ρ_{ss}	Solid salt density
ρ_w	Density of water
R_s	Shear limit
S_b	Brine salinity
σ	Stress
σ_f	Flexural strength of ice
S	Salinity, measured in ppt
T_a	Air temperature
τ_{ii}	Friction force between two ice sheets
τ	Shear force
T_f	Freezing temperature of sea water
T_m	Melting temperature of ice
T_s	Surface temperature

u_{max} Maximum plate displacement

UNIS University Centre of Svalbard

$V_{seawater}$ Volume of seawater in an ice ridge

V_{total} Total volume of an ice ridge

w_k Keel width of ridged ice

w_s Sail width of ridged ice

Å Ångstrøm, 10^{-10} [m]

DNV GL Nomenclature

A_C Contact area equal $h \cdot w$

α Factor depending on A_C

β Angle of web with shell plating

F_A Correction factor for ice reinforced area

F_B Correction factor for design contact area A_C

h Effective contact height

h_0 Equal h or s in general

h_{ice} Ice thickness

k_a Aspect ratio factor for plate field

l Stiffener length

m_p Bending moment factor

p Design pressure

p_0 Basic ice pressure

s Stiffener spacing

σ $0.9\sigma_{ice}$

σ_{ice} Nominal ice strength

t Plate thickness exposed to ice

t_k Thickness corrosion addition

w Critical contact width

w_k Section modulus corrosion factor

IACS Nomenclature

AF	Area factor
A_{fn}	Net cross section area, flange
α_{bow}	Upper ice waterline angle, bow
A_{pn}	Net cross section area
AR_{bow}	Load patch aspect ratio
b_{bow}	Contact area height, bow
β'_{bow}	Normal frame angle, bow
b_f	Flange width
b_w	Distance from flange centre to mid thickness of web
CF_C	Crushing failure class factor
CF_D	Load patch dimension class factor
CF_F	Flexural failure class factor
D	Ship displacement [kt]
fa_{bow}	Shape coefficient, bow
F_{bow}	Total impact force, bow
γ_{bow}	Buttock angle at upper ice waterline, bow
h	Stiffener web height including flange thickness
h_{fc}	Stiffener web height to flange centre
h_w	Stiffener web height
l	Stiffener length
L_{wl}	Water line length
$P_{avg,bow}$	Average pressure in bow region
P_{bow}	Pressure, bow
φ_w	Angle between shell plate and web
PPF_p	Peak pressure factor
Q_{bow}	Line load, bow
s	Stiffener spacing
σ_y	Upper yield stress
t	Plate thickness
t_s	Plate corrosion addition

t_f	Flange thickness
t_{net}	Plate thickness to withstand ice loads
t_{pn}	Net plate thickness equal t_{net}
t_w	Stiffener web thickness
t_{wn}	Net web thickness equal t_w
w_{bow}	Contact area width, bow
x	Distance from forward perpendicular to impact area

Chapter 1

Introduction

The Arctic area covers about $14 \cdot 10^6$ [km^2]. This is mostly covered by ice during wintertime. In September, the ice extent is at its minimum, and the ice covers roughly $8 \cdot 10^6$ [km^2] of the total area (Løset, nd). Arctic operations will therefore be carried out in seas mostly covered in ice.

Operations in Arctic environment have become more relevant over the past years. The search for oil and gas, thus also survey of ice and environment have lead to an increase in Arctic activity. These operations require structures to have sufficient residual strength due to ice-induced stresses. Ice occurs in different size, shape, age, feature type, location and origin. Regarding these parameters, ice will have varying strength and load-inducing properties. In addition, the mechanical behaviour of ice is described by four main parameters; temperature, porosity, grain size and direction, and loading rate (Høyland, 2015).

For Arctic operations, both Det Norske Veritas Germanischer Lloyd (DNV GL) and International Association of Classification Societies (IACS) provide regulations considering ice-hull interactions. These regulations classify ships into classes depending on ice feature type, location and age of the ice they will operate in. Also, the number of repeated rams and vessel speed are considerable when classifying ships. These codes assume that an area subjected to a pressure, represent the ice load. Ice will have different size and shape, and there will occur difficulties regarding an actual load pattern and the resulting contact pressure induced to the hull.

1.1 Background

Uni-axial compression tests and parametric measurements have been conducted by the University Centre of Svalbard (UNIS). To calculate ice loads on ship hulls, highly advanced numerical algorithms and associated computer software such as Abacus are required. Prediction of ice loads have been discussed in papers by Leira

et al. (2009), Løset et al. (2006), Riska (2011) and Thorsen (2012). Interaction with ice could occur in many different ways, and the models of interaction are difficult to determine. There are many difficulties related to the ice-ship interaction. The ice strength has spatial and temporal variations, and is difficult to predict as it depends on several physical parameters. Further, the contact area is difficult to determine due to different crushing and breaking patterns. Regarding these difficulties, there exist simplified methods for calculation of both local and global ice induced loads (Riska, 2011). Prediction of ice induced loads could be established by application of measurements conducted by ice-going vessels (Leira et al., 2009). Hence, these predictions require sufficient numbers of measurements over a long period of time in the area where vessel will operate.

1.2 Objective

Considering difficulties and uncertainties connected to ice-structure interaction, the following topics have been examined:

- Describe different types of sea ice, and their mechanical and physical properties.
- Present and discuss models for calculation of contact pressure acting on a floating structure due to presence of ice.
- Present measurements from uni-axial compression tests of sea ice, performed at UNIS. Also, establish an empirical pressure model based on these measurements.
- Perform a review of ice classes of polar going ships with focus on regulations provided by DNV GL and IACS.
- Compare different ice classes of polar going ships by assessing a local ship hull component in Abaqus, with loads obtained from measurements of sea ice and loads obtained by the regulations.
- Establish a finite element model in Abaqus and analyse this with respect to extreme loads provided by ice ridges. Additionally, assess the effect of varying boundary conditions due to varying support of the local ship hull component. The loads should be established by measurements conducted at UNIS.

1.3 Scope and Limitations

The main scope of this Master's thesis focuses on local ice loads on ship hulls established by application of data from UNIS, and an empirical contact pressure formula. Additionally, a comparison of regulations and the empirical contact pressure will be provided. The boundary conditions of the a local bow model will be assessed to investigate differences in behaviour regarding failure in the supportive frames.

The coast guard vessel KV Svalbard has conducted measurements of sea ice and ice induced stresses. KV Svalbard was therefore chosen as an inspirational ice-going vessel for the comparison of regulations provided by DNV GL and IACS. The plate model applied in the comparison was limited to only apply scantlings from DNV GL. Thus, the design pressure from both DNV GL and IACS, as well as the empirical pressure are applied to the model. Further, the plate assessment applying contact pressure obtained from regulations by IACS, is given in the appendix as the main focus was given the empirical model and the regulations from DNV GL. Considering the regulations, scantlings of the plate model are limited to only consider plate thickness, sectional area of the stiffeners, and design pressure. The dimensioning are based on several general assumptions regarding main dimensions and stiffener spacing.

The sea ice theory will provide details of sea ice down to a molecular level. This will give the reader a better understanding of the measurements provided by UNIS and the results of these measurements. The contact pressure model derived from empirical equations describing the flexural strength of sea ice, bending capacity and vertical force component, is limited to describe short impacts only. Further, the normal force component is limited to only account for vertical forces and a friction component, prior to collapse of the ice sheet.

For the bow model, applying an empirical pressure obtained from ridged ice measurements, the boundary condition assessment was limited to one fixed boundary and three boundaries applying rotational springs. The main focus was given to assessment of the plate and stiffener flanges. These limitations were set to reduce the extent of the thesis and give priority to the most critical sampling locations.

This Master's thesis is limited to include only necessary theory, hence the basic theory on the finite element method is not included. The reader should have sufficient understanding of the basic theory to understand presented theory and results.

The reader should note that this Master's thesis is only describing the first stage of interaction with ice, as the ship continue to navigate in ice, the ice floes will continue to induce stresses to the hull until the ice floes have passed the ship. This Master's thesis will only consider the first interaction in the analysis.

1.4 Structure of the Thesis

This section presents the content of the thesis. The chapters present the different parts, and are arranged in the most chronological order, as listed below:

- Chapter 2 - Presents theory on sea ice, with focus on classification of ice, ice physics and ice mechanics.
- Chapter 3 - Presents measurements from compression tests of ice specimens. Further the experimental set-up, methodology and results are presented.
- Chapter 4 - Presents Ice-structure interaction, with focus on local ice pressure models, relevant input parameters, pressure areas and contact pressure.
- Chapter 5 - Presents a review of ship classification for ice going vessels, with focus on classification presented by DNV GL and IACS.
- Chapter 6 - Presents finite element theory, with focus on non-linear theory.
- Chapter 7 - Presents results from assessment of a local plate model, with focus on a comparison of actual ice loads and loads suggested by regulations.
- Chapter 8 - Presents results from assessment of an advanced local bow model exposed to extreme ice ridge loads. Additionally, an assessment of different boundary conditions is presented here.
- Chapter 9 - Presents an overall discussion of the findings from the thesis.
- Chapter 10 - Presents an overall conclusion of the findings from the thesis.
- Chapter 11 - Presents suggestions for further work and recommendations.

Additional results, data from measurements and MATLAB-scripts will be given in an appendix. The appendix will be arranged in the same chronological order as the main part.

Chapter 2

Sea Ice Theory

As the surveys in Arctic areas are developing, knowledge about ice environment become more relevant. Knowledge about physical and mechanical behaviour of ice is necessary to understand how ice impacts a vessel located in an Arctic environment. There are many parameters and properties describing ice, that will determine what kind of impacts the vessel will be exposed to during interaction with ice. These parameters and properties could be divided into three main topics: *classification of ice*, *ice physics* and *ice mechanics*. In this chapter, the topics will be further described to give the reader a better understanding of topics discussed later.

2.1 Classification of Ice

Ice is generally classified into four categories. For offshore structures and ships, the main concern regarding origin is sea and land ice. The size and shape of these two types of ice, along with different strength, are the main differences. The Feature type describes the degree of deformation of ice, and will hence impact the loading pattern and load amplitude on a ship hull. Over time the ice grows and melts, these are also important factors that impact the ice-ship interaction. The ice position in relation to land will give ice different properties as well. All these different classification topics will be further discussed in this section. This section refers to Høyland (nd) unless other is specified.

2.1.1 Classification by Origin

Ice is divided into four groups regarding the origin. The following four origins are given by World Meteorological Organization (WMO, 1970):

- **Sea ice** is formed at sea due to freezing of sea water.

- **Ice of land origin** is ice formed on land, i.e. glacier ice, found floating in water due to calving.
- **Lake ice** is formed on a lake.
- **River ice** is formed on a river.

The origin will give the ice different properties regarding strength, size and shape. Sea ice will typically have less strength than glacier ice, due to higher salinity and porosity. The size of sea ice compared to glacier ice is also small. The largest observed iceberg originating from a glacier was estimated to have a surface area of 11.000 [km^2].

Further in this master thesis, only sea ice will be discussed. Sea ice originate from saline water, thus further growth could occur from snow on top that mixes with saline water. This impacts the salinity, and also impacts the strength. This is further described under section 2.2.3.

2.1.2 Classification by Feature Type

Sea ice can be divided into groups regarding degree of deformation. Different feature types of ice have different mechanical and thermo-mechanical properties. Also, the size differs between the feature types. WMO (1970) differ between two main categories of feature types, when describing sea ice:

- **Undeformed ice** is ice with little to no mechanical deformation.
- **Deformed ice** is ice with mechanical deformation, typically deformed by the surrounding environment.

The undeformed ice, is often called level ice. This means it consists of only one layer of ice. The deformed ice is often divided into three sub-groups: *rafted ice*, *ice ridges* and *broken ice*. The broken ice is often found in the marginal ice zone where waves break the ice into smaller pieces. Only rafted ice and ice ridges are further described in detail.

Rafted Ice

Rafted ice is defined as an ice sheet overriding another (Tuhkuri, 2014). For this to occur, a driving force F_R must exceed the load capacity F_0 of an ice sheet. Thereafter, the driving force must be able to compress the sheets sufficiently for overriding to occur. This process continues until the friction forces between the ice sheets τ_{ii} are greater than the driving forces. This process could occur several times, hence the ice could obtain more than double thickness as several layers override each other. The process is illustrated in figure 2.1.

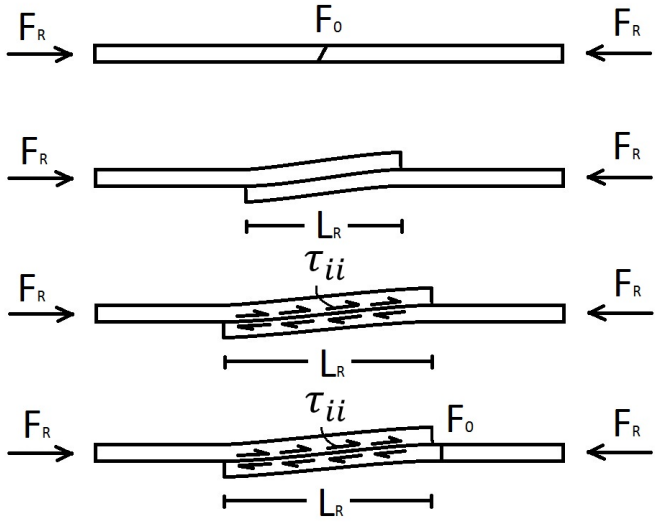

Figure 2.1: Process of rafting of ice. From initial cracking to final state and also initiation of a second layer. Inspired by Tuhkuri (2014).

Initially one requires $F_R > F_0$ to break the ice, as shown in top of figure 2.1. The shear force between the ice sheets depends on the buoyancy and weight of the ice sheets, as well as the friction coefficient μ_{ii} between ice and ice. As the raft length L_R increases, the friction force per unit width between the ice sheets increase described by equation 2.1.

$$\tau_{ii} = \mu_{ii}(\rho_w - \rho_i)gh_iL_R \tag{2.1}$$

Where μ_{ii} is the friction coefficient between two ice sheets, ρ_w is the density of water, ρ_i is the density of ice, g is the gravitational acceleration and h_i is the ice thickness which is assumed constant for both sheets. As the driving force is larger than the friction between the ice sheets, $F_R > \tau_{ii}$, the overriding of one sheet continues until $\tau_{ii} > F_0$, and the ice sheet breaks in another location (as shown at the bottom of figure 2.1).

From 2.1 one observes that the rafting length could be long if μ_{ii} is small and F_R is small enough to keep the ice sheets intact. If the ice sheets are covered in snow the friction increases significantly, hence the rafting length reduces. The rafting length do depend on available forces driving the ice sheets. Additionally, field observations show that thick ice most likely ends up ridging rather than rafting, and thin ice will most likely raft (Tuhkuri, 2014).

Ridged Ice

Ridged ice is defined as compaction of ice where the ice breaks up into blocks that pile up, both over and under the ice sheet. Ridging could occur after the final state of rafting. This is due to breaking of ice into smaller blocks, rather than ice sheets overriding each other. The process is illustrated in figure 2.2.

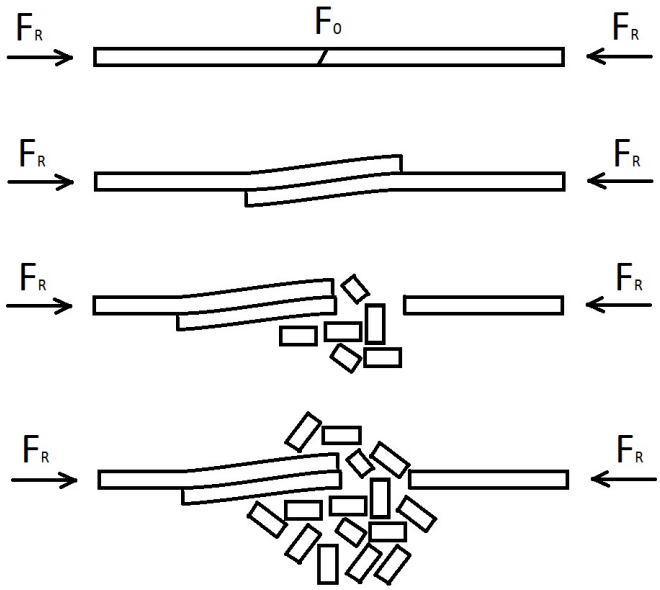

Figure 2.2: Process of ridging of ice, from initial stages of rafting to final stage of ridging. Inspired by Tuhkuri (2014).

From figure 2.2 one can observe that ridging may be initiated by rafting, hence it may as well be directly ridged . The process requires a driving force F_R larger than the capacity of loading F_0 to break the ice into smaller blocks. This process continues until $F_R < F_0$ as the capacity is then greater than the winds and current forcing the ice together.

A simplification of the final state is illustrated in figure 2.3 below. The keel consists of rubble, a mix of ice and water, until consolidation occur. The ratio between the sail and keel height is often in the range 4-5, respectively for first-year ridges. While the ratio is only in the range of 3-4 for old ridges (Timco and Burden, 1997).

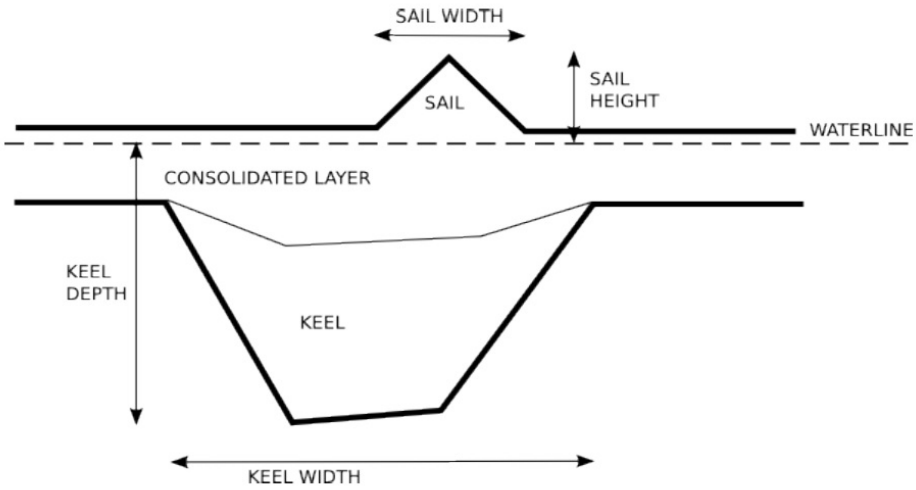

Figure 2.3: The final state of an ice ridge (Tuhkuri, 2014).

Table 2.1 gives a description of the parameters from figure 2.3.

Table 2.1: Parameters for description of ice ridges.

Description		Parameter
Sail width	-	w_s
Sail height	-	h_{sail}
Keel depth	-	h_k
Keel width	-	w_k
Consolidated layer thickness	-	h_c

The reader should be aware of the simplified ridge shape, illustrated in figure 2.3. Ridges may occur in shapes different from this figure.

2.1.3 Classification by Age

Age of ice is by WMO (1970) divided into two subgroups: *First-year ice* and *old ice*. The definition of age is given by the number of summers the ice has survived. This means that first-year ice is not older than one winter. Old ice has survived at least one summer of melt, and is further divided into second-year ice and multi-year ice. Second-year ice has only survived one summers melt, while multi-year ice have survived several summers. The old ice thickness is approximated to be within a range of 1.2-5 [m].

First-year ice is often divided into subgroups regarding thickness. By WMO (1970) the following thickness apply, as listed in table 2.2.

Table 2.2: First-year ice thickness.

Ice notation		Thickness [m]
Thin	-	0.3-0.7
Thin first stage	-	0.3-0.5
Thin second stage	-	0.5-0.7
Medium	-	0.7-1.2
Thick	-	1.2-2

From table 2.2 it is observed that the thin ice is divided into two sub-groups.

2.1.4 Classification by Location

Ice will have different behaviour regarding position in relation to land and open ocean. The position of the ice will determine what kind of boundary conditions the ice is exposed to, hence determine ice behaviour. Høyland (nd) define the following classes of ice locations:

- **Shore ice** is fixed to the shore line and forms the transition to the landfast ice. The shore ice is impacted by the shore.
- **Landfast ice** is only able to move vertically with tide water, as it is horizontally fixed to the shore line.
- **Shear zone ice** defines the transition from landfast ice to the drift ice and is characterized by large deformations.
- **Drift ice** is free to move and will be defined regarding the ice concentration factor C_i, and will have different motion due to the level of ice concentration.
- **Marginal ice zone (MIZ)** is defined as the transition from drift ice to open water.

The ice concentration factor is defined as:

$$C_i = \frac{A_{ice}}{A_{ocean}} \tag{2.2}$$

where A_{ice} is defined as the total area of the ice floes in a certain area A_{ocean}. Figure 2.4 defines the different areas applied by equation 2.2.

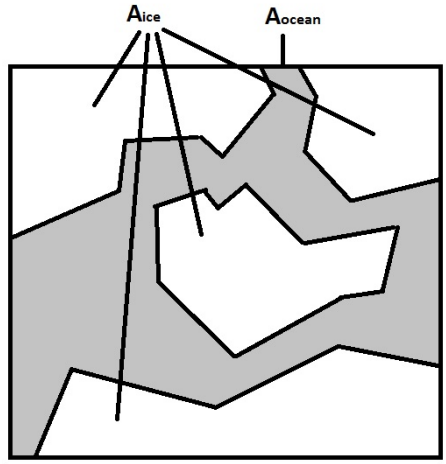

Figure 2.4: Illustration of the areas defining the ice concentration factor C_i.

The shore ice define a transition between land and landfast ice. This ice are often denoted the hinge zone as some ice are fixed to the shore and some ice move together with the tide. This may cause rotation and eventually cracks in the ice cover. Further, the landfast ice can move vertically, hence it is fixed horizontally. The horizontal boundary and extension of the landfast ice zone are determined by the number of islands, sea bed topography and ice thickness. Outside the landfast ice, the ice can move and create a shear zone characterized by large deformations. This zone define the boundary between landfast and drift ice. Regarding the drift ice, one define several ice concentrations. Table 2.3 provides the different concentrations(WMO, 1970). The MIZ defines the transition to open water, where the ice cover is free to move and is affected by waves from open water.

Table 2.3: Ice concentration factors.

Ice concentration		C_i [-]
Very open ice	-	0.1-0.3
open ice	-	0.4-0.6
pack ice	-	0.7-0.8
Very close ice	-	0.9-1
Compact ice	-	1

Figure 2.5 illustrate the different locations ice could obtain during classification by location, from land to open water.

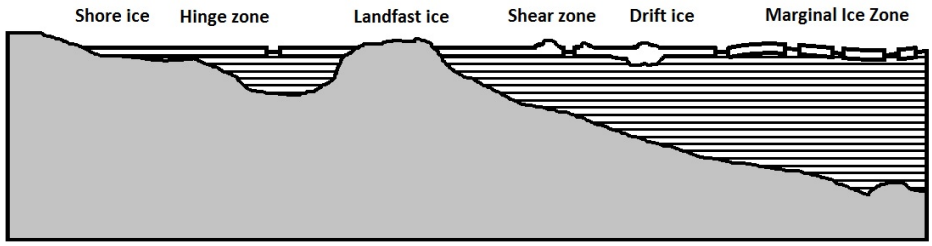

Figure 2.5: Illustration of the different locations defining the classification by location, inspired by Høyland (nd).

2.2 Ice Physics

To understand the mechanical properties of ice, one needs to investigate the physical properties. Ice consist of frozen water where each water molecule consists of two hydrogen atoms and one oxygen atom. The process of ice growth will be further discussed in this section, from the composition of a water molecule to the final stage of fully developed ice. The mechanical properties of ice will depend on several parameters described at an atomic level. This section will provide theory presented by Løset et al. (2006).

2.2.1 Structure of Ice

At a microscopic level, water consist of oxygen atoms (O) covalent bonded with two hydrogen atoms (H). Oxygen consist of eight electrons, where six of them are located in the outer shell. Hydrogen has one electron in the outer shell, so that two hydrogen atoms can create chemical bonds with one oxygen atom. Thus, the hydrogen atom simply consists of their nuclei with a distance 0.96 [Å] from the oxygen nucleus. This form a water molecule, and is bonded trough a hydrogen bond to other water molecules.

As water in liquid form freeze, it undergoes a structural rearrangement on a molecular level. Water molecules are transformed into a crystalline structure. The result is a solid, with crystallographic arrangement of water molecules. Ice frozen under normal conditions is often referred to as ice Ih, or hexagonal ice, due to hexagonal crystalline symmetry. Each hydrogen nuclei with its partial charge is attracted to one of the lone pairs of a neighbouring oxygen molecule. The bond is called hydrogen bond and is weakly ionic. There are six possible arrangements of these types of bonds, as illustrated in figure 2.6

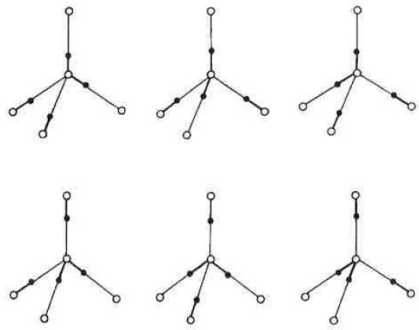

Figure 2.6: Six possible arrangements of how hydrogen and oxygen are bonded. ∘ represents oxygen while • represents hydrogen(Løset et al., 2006).

Each oxygen can bond with three hydrogen atoms in plane, while only one out of

plane, this give a total of four bonds per oxygen atom. In ice Ih the distance between a covalent bonded hydrogen and oxygen atom, is approximately 1 [Å]. While the distance from a hydrogen bonded oxygen and hydrogen atom is approximately 1.76 [Å]. This gives a total distance of 2.76 [Å] between each oxygen atom(Løset et al., 2006).

By applying the Bernal-Fowler rules, it is possible to establish a statistical model for the structure of ice based on the following assumptions (Løset et al., 2006):

- The two hydrogen atoms are attached to each oxygen atom at distances of approximate 1 [Å], hence forming a water molecule.
- The orientation of the water molecule is so that the two hydrogen atoms approximately is directed towards two out of the four surrounding oxygen atoms in a tetrahedrally pattern.
- Between each pair of oxygen atoms there exists only one hydrogen atom.
- Ice Ih will under ordinary conditions exist in one of the configurations corresponding to a certain distribution of the hydrogen atoms relative to the oxygen atoms (Figure 2.6).

Regarding the arrangement of atoms, ice will obtain the oxygen atoms located in series of paralell planes called basal planes. Perpendicular to these planes, one finds the c-axis. The oxygen atoms are ordered in a hexagonal manner, in the basal planes as shown in figure 2.7.

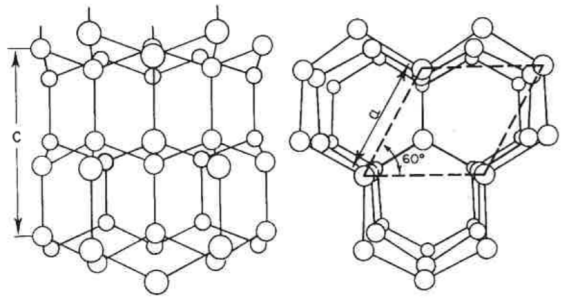

Figure 2.7: Molecular structure of ice, showing the hexagonal structure. The circles represent oxygen atoms, while the lines represent hydrogen bonds. The hydrogen atoms are not shown here. *Left:* The basal planes are shown horizontally, while the c-axis points vertically. *Right:* The hexagonal pattern is illustrated with the c-axis out of plane(Løset et al., 2006).

Figure 2.7 shows that a fracture along any plane normal to the basal plane requires breaking of a minimum of four bonds. While a fracture parallel to the basal plane only requires breaking of two bonds. Regarding the atomic planes, ice will have different properties in different directions. This will be further discussed in section 2.3.3.

2.2.2 Formation of Ice

The freezing temperature T_f of saline water is -1.9 [°C] due to the presence of salt. Generally the salinity S of sea water is 35 [ppt](Høyland, nd). When sea water start to freeze, the basal planes are randomly oriented as a result of heat transportation. Some heat is transported into air, and some is transported into water regarding the basal plane orientation. Wind and waves also initiate random orientation of the basal planes. Due to thermodynamics 2^{nd} law, the generated heat needs to be transported away. In an anisotropic material, the required energy to transport heat away is greater than in an isotropic material. It will require less energy to transport heat away parallel to the basal planes. The initial ice layer is called the primary layer and has a thickness of 0.1-0.15 [m]. As ice continue to grow from below, the heat generated need to be transported to the surface. The favoured orientation of the basal planes is vertical, and a wedge out effect of the horizontal basal planes occurs. This layer is named the wedge out zone and is within the range of 0.05-0.3 [m]. Further growth will be dominated by vertical oriented basal planes only, and is denoted secondary layer. Figure 2.8 shows the process of initial ice development, to a fully developed secondary layer.

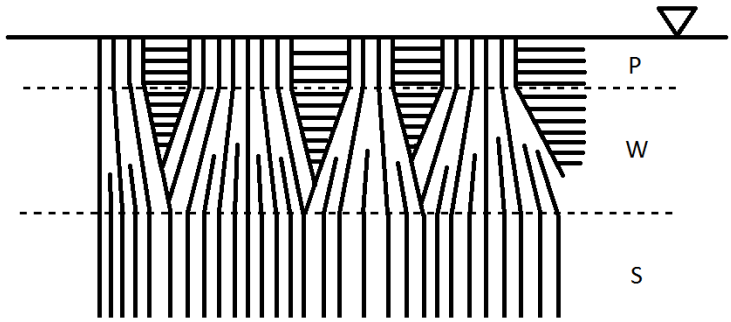

Figure 2.8: Initial formation of ice layers. The basal planes are illustrated with black lines. The C-axis is perpendicular to the basal planes. The primary layer is denoted P, the wedge out zone is denoted W, and the secondary layer is denoted S. The figure only shows the principle, no scale or distances are accurate.

The primary layer will consist of granular ice. While the secondary layer consists of columnar ice. In a horizontal plane cut, the columnar grains will increase in cross section area as the distance from the surface increases. In the bottom most part of the ice sheet, the skeleton layer is located, as illustrated by figure 2.9. From figure 2.9 one could observe the orientation of basal planes in both horizontal and vertical planes trough a layer of first year sea ice. Initially, the primary layer is granular. The wedge out zone, or transition zone, is quite narrow compared to the full thickness of the ice sheet and the wedge out effect is shown by the cross section cut outs to the left in figure 2.9. Further, the grains does increase in size through the columnar zone(secondary layer). Additionally, the basal planes are almost vertically aligned at the bottom most part of the ice layer.

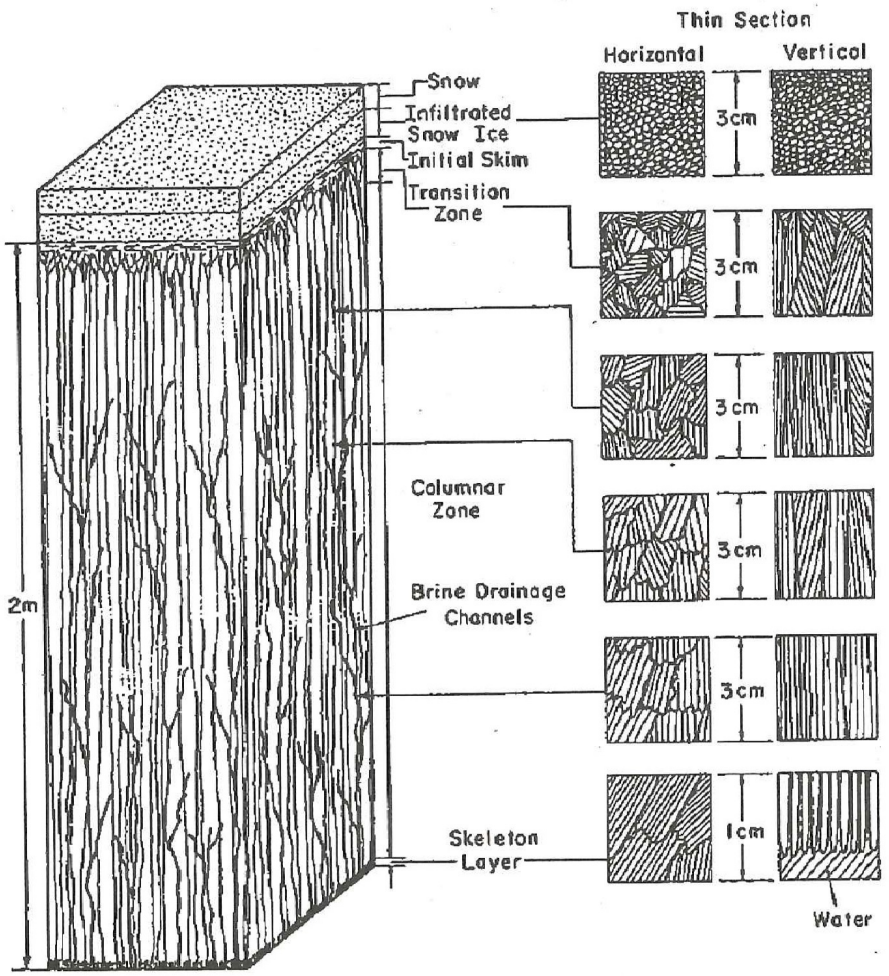

Figure 2.9: Illustrative figure of first year sea ice and how the basal planes and grains vary trough the cross section of the ice cover. To the right, cut outs of the cross section, both horizontal and vertical are shown. The basal planes are drawn as black lines. The figure is taken from Løset et al. (2006).

The skeleton layer consists of ice layers extending into the water below the ice. These platelets are typically less than 0.25 [mm] thin. As the root of these platelets grows thicker, the extensions can entrap brine and gas in pockets. The skeleton layer and brine entrapment are illustrated in figure 2.10.

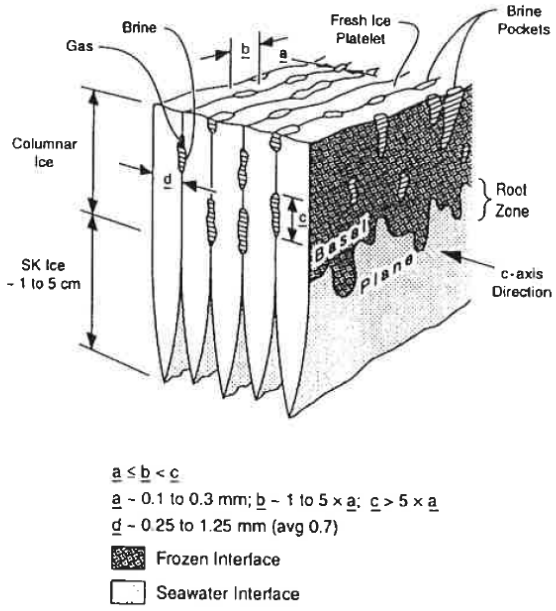

Figure 2.10: Skeleton layer and brine entrapment. SK ice is similar to skeleton layer(Løset et al., 2006).

When brine are entrapped, the brine pockets can migrate as the topmost part of each pocket will freeze and increase the salinity of the remaining brine. Due to this increase, the bottommost part will melt and cause downward motion. This is easily understood regarding heat transport to the surface and the fact that the temperature gradient is positive downwards.

Due to a volume difference between a water molecule and a salt molecule, freezing water do expel salts. The volume of a water molecule is approximately 130 [$Å^3$], while a salt molecule has the volume of approximately 179 [$Å^3$]. Another factor that substantiates the expel of salt, is the distances in the lattice. The distance between two oxygen atoms is 2.76 [Å]. For salt, the distance between two chlorine atoms is 5.64 [Å]. Salinity of the ice will depend on the growth rate. The faster the ice freezes, the more salt is locked in. Temperature is therefore an important parameter for ice properties. This is further discussed in section 2.2.3.

2.2.3 Ice Growth

Ice thickness is one of the most important parameters regarding ice load actions on offshore structures. The thickness of ice is determined by ice growth, and could occur in many forms. The theory provided in this section is mostly referring to Høyland (nd).

Ice growth from above occur when sea ice get flooded and new ice develop on top. This ice is often denoted superimposed ice. Snow could accelerate this process as the ice could become submerged due to added weight. The water may flow trough brine channels or cracks which connect the submerged part to the surface. Additionally, the superimposed ice could be created due to radiation, high air temperatures or rain. The topmost part of the snow layer melts and drizzles down trough the snow. As it reaches the cold zone, it freezes. This causes porous fresh ice. Ice could also grow from inside as brine pockets reach freezing temperature. This growth do not provide much additional volume to the ice. Hence, the process decrease the salinity of the ice. Ice growth from below is the most common form of growth. The access to cold water is continuous and the latent heat released from the freezing process is transported trough the ice and released to the surroundings on top of the ice. This lead to ice growth underneath the ice cover. The ice thickness could be predicted applying Stefan's law when investigating ice growth from below.

Stefan's Law

Stefan's law could be used for prediction of ice growth considering level ice, in an one-dimensional model. To apply Stefan's law, several assumptions are introduced, as described by figure 2.11. It is assumed that there is no layer of snow on top of the ice and that there exists no radiation. Also it is assumed that there is no heat transfer from the ocean to the ice, such that the heat fulx from the ocean is zero($q_{ocean} = 0$). The temperature profile trough the ice is assumed linear and the energy generated by development of an additional ice layer is carried trough the ice to the surface. This imply the following: $q_{latent} = q_{ice} = q_{surface}$. Also, Fourier's law apply to the heat transported trough the ice as described in equation 2.3.

$$q_{ice} = -k_i \frac{\Delta T}{\Delta z} \tag{2.3}$$

Where k_i is the thermal conductivity of ice, z describe thickness and T describe temperature.

From figure 2.11, one obtains the following equation:

$$-k_i \frac{\Delta T}{h_i} = \rho_i l_i \frac{dh_i}{dt} \tag{2.4}$$

Solved with respect to the time dependent ice height, one obtain the following equation:

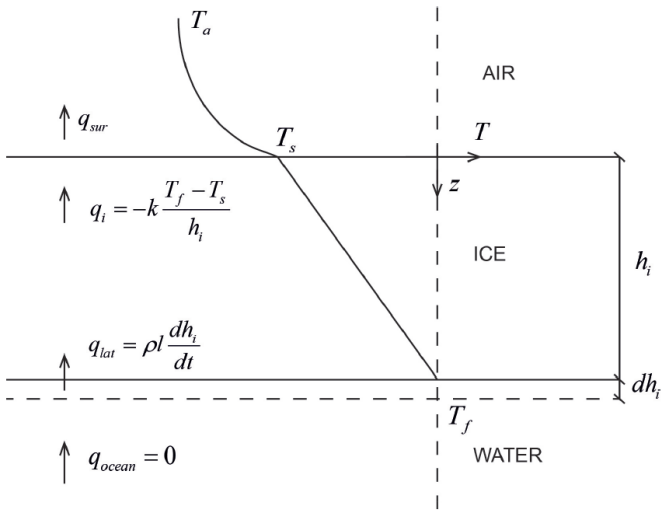

Figure 2.11: Illustration of the assumptions behind Stefan's law(Høyland, nd). The additional ice layer is denoted dh_i, the thickness of ice is denoted h_i, the surface temperature is denoted T_s, the freezing temperature of sea water is defined as T_f and the air temperature is denoted T_a. The heat fluxes are defined in the figure.

$$h_i^2(t) - h_{i,0}^2 = \frac{2k_i}{\rho_i l_i} \int_0^t (T_s - T_f)dt \tag{2.5}$$

Introducing the assumption that the surface temperature T_s is equal the air temperature T_a. Freezing Degree Days (FDD) quantifies the energy amount released at the surface by summing up the difference between the freezing temperature T_f and the air temperature T_a. FDD is given as:

$$FDD = \sum_{days} (T_a - T_f) \approx \frac{1}{\alpha} \int_0^t (T_a - T_f)dt \tag{2.6}$$

Where alpha α is given as the seconds per day, resulting in $\alpha = 86400$ [second/day]. This give Stefan's law in rewritten form:

$$h_i^2(t) - h_{i,0}^2 = \frac{2k_i}{\rho_i l_i} FDD\alpha \tag{2.7}$$

Introducing a layer of snow that provide insulation, Stefan's law is rewritten at the following form:

$$h_i^2(t) - h_{i,0}^2 + \frac{2h_s k_i}{k_s} h_i - \frac{2h_s k_i}{k_s} h_{i,0} = \frac{2k_i}{\rho_i l_i} FDD\alpha \tag{2.8}$$

The assumptions are the same as previous, thus no snow is assumed.

Consolidation of Ridges

Consolidation of ridges is of consideration in design load characterization. First-year ridges are assumed to consist of partially a consolidated layer and rubble, and have not survived a summers melt. Old ridges have survived one or more summers and are assumed to be fully consolidated. This results in larger impact forces. In first-year ridges, the consolidated layer is assumed to be within a range of 2-2.5 times the thickness of the level ice(Høyland, nd). The keel depth is one of the most important parameters. By observation of the sail, one can predict the keel depth as the keel-sail fraction has a ratio of 4-5 for first-year ridges and 3-4 for old ridges, as given by Timco and Burden (1997).

During the lifespan of a ridge, physical, mechanical and geometrical properties will change. Initially the keel consists of rubble that is not yet consolidated. Due to temperature difference between ice and sea water, freeze bonds develop. There exist three important heat fluxes, the surface flux $q_{surface}$, the oceanic flux q_{ocean} and the internal flux q_{re} as illustrated by figure 2.12. The surface flux freezes the water pockets between the ice blocks, from above. A consolidated layer is then formed. The internal flux is partially used in freezing of the water pockets, namely freeze bonds, and partially consumed by the flux from the ocean.

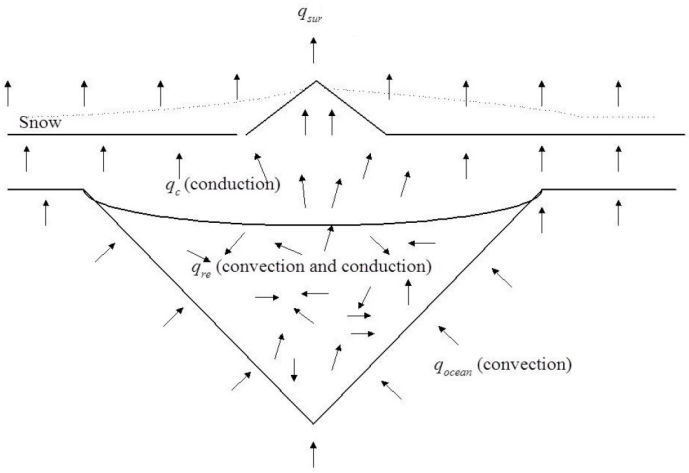

Figure 2.12: Illustration of the heat fluxes in a first-year ridge. The figure is taken from Høyland (nd).

Further growth of the consolidated layer, defines the main phase in the life of a ridge. During this phase, the heat fluxes into the air $q_{surface}$ dominate. The thickness of the consolidated layer is important. By a numerical model, the consolidated layer thickness h_c could be found by equation 2.9.

$$h_c(t)^2 = h_{c,0}(t_0)^2 + \frac{h_i(t)^2 - h_{i,0}(t_0)^2}{\eta_m} \tag{2.9}$$

Where $h_{c,0}$ denotes the initial consolidated thickness, $h_{i,0}$ denotes initial ice thickness, h_i denotes the ice thickness and η_m denotes the macro porosity of the ice ridge. The macro porosity is a volume fraction given as:

$$\eta_m = \frac{V_{seawater}}{V_{total}} \tag{2.10}$$

Where V_{total} is the volume of both ice and sea water in the rubble layer. To estimate the ratio between the ice thickness h_i and the consolidated layer thickness h_c, a ratio R is introduced. Equation 2.11 defines this ratio, which normally is between 1.5 and 2.

$$R = \frac{h_c}{h_i} \tag{2.11}$$

The rubble beneath the consolidated layer only feel the water below. Hence, it is thermally insulated by the freezing front defined by the consolidated layer. This result in continuously decay of the rubble.

In the decay phase, the ridge is exposed to melting from both top and bottom. If the ridge survives one summers melt, it turns into a second-year ridge. At the surface of the ridge, the sun radiation and warm air create fresh melt water, as snow and surface ice melt. As the fresh water has a freezing point above the temperature in the rubble, and it drizzle downwards, it will freeze as it reaches the keel. Heat is released as freezing occurs, resulting in an increased temperature. Hence, both freezing and melting occur during the decay phase. This is only possible if the temperature in the keel is below the freezing point of the melt water. As the ridge survives several summers melt, it turns into a multi-year ridge. The multi-year ridges are recognized by even smother sail surface and a somewhat lower salinity as they have had more summers to drain salt due to melting.

2.2.4 Temperature, Density, Salinity and Porosity in Ice

Temperature is an essential property for ice, as well as other materials. The temperature determine the material phase, and quantifies the vibration energy stored by a mass. For sea ice with a salinity of 35 [ppt], the freezing temperature

is -1.9 [°C]. Density describes the compactness of the material and is defined as a mass per volume. For sea ice, the strength is interrelated with its density, as the density depends on porosity. This is because the ice consists of pure ice, trapped gases, salts, and brine pockets. The total porosity η_T is a sum of gas and brine fractions, respectively η_a and η_b. Both theory and experiments have shown that the relative volume of brine existing in sea ice will determine mechanical, thermal and electrical properties of the ice. Further does the volume of air and gas in ice pose a major portion of the total porosity. Knowledge about the total porosity is therefore important(Cox and Weeks, 1983). The density of ice could be described by equation 2.12.

$$\rho_i = (1 - \eta_a)\left(1 + \frac{S}{\alpha T \rho_w}(\rho_w - \rho_{pi})\right)\rho_{pi} \tag{2.12}$$

Table 2.4: Parameters of ice density.

ρ_i	-	density of sea ice
ρ_{pi}	-	density of pure ice
ρ_w	-	density of water
η_a	-	volume of air in the unit volume of sea ice
α	-	constant equal -0.0182 $[1/°C]$
S_i	-	salinity of ice
T_i	-	temperature of ice

Formulas are empirically derived by Cox and Weeks (1983), Cox and Weeks (1975), Leppäranta and Manninen (1988) and Pounder (1965) to approximate porosity of ice. By measuring temperature, salinity and density it is possible to determine the porosity of ice. The porosity describes the strength of ice. The total porosity is given as:

$$\eta_T = \eta_a + \eta_b \tag{2.13}$$

Where η_a is defined as:

$$\eta_a = 1 - \frac{\rho_i}{\rho_{pi}} + \rho_i S_i \frac{F_2(T_i)}{F_1(T_i)} \tag{2.14}$$

and η_b is defined as:

$$\eta_b = \frac{V_b}{V} = \frac{\rho_i S_i}{F_1(T_i)} \tag{2.15}$$

The two functions $F_1(T_i)$ and $F_2(T_i)$ are given as(Cox and Weeks, 1983):

$$F_1(T_i) = \rho_b(T_i) \cdot S_b(T_i) \cdot (1 + k(T_i)) \tag{2.16}$$

$$F_2(T_i) = [(1 + C(T_i))\frac{\rho_b(T_i)}{\rho_i} - \frac{C(T_i)\rho_b(T_i)}{\rho_{ss}} - 1] \tag{2.17}$$

Parameters in 2.16 and 2.17 are given in table 2.5 and are approximated to apply for the compression test of ice provided in chapter 3. Subscript i denotes ice.

Table 2.5: Parameters of porosity approximation.

ρ_b	-	Brine density
S_b	-	Brine salinity
k	-	Relative amount of salt in brine, typical between 0 and 2.68 [-]
C	-	Value relating mass of solid salts and mass of brine, typical between 0 and 1.09 [-]
ρ_{ss}	-	Solid salt density

Values from table 2.5 are obtained from Cox and Weeks (1983).

2.3 Ice Mechanics

Considering ice mechanics, the strength of ice is impacted by several factors. It is difficult to describe the exact impact from each of the parameters, hence an interaction between them will impact the strength(Moslet, 2007). Studies by Sinha (1989), Weeks and Assur (1967), Timco and Weeks (2010), Løset et al. (2006) and Gans and Woodmansee (1992) have shown that the temperature, porosity, grain size and load rate are the dominating parameters regarding ice strength. Ice is a crystalline material equal to metals, and has both ductile and brittle behaviour. Thus, there are two factors which make ice somewhat different from metals. The grains are relatively large and ice exists close to its freezing point. These two factors increase the material behaviour complexity.

Sea ice is a multi-phase material consisting of air and brine pockets, solid salts and pure ice. As a result, sea ice is a complicated material to study, and a description of the material behaviour consists of two parts: solid and fluid material behaviour. Therefore, one needs to include both linear and non-linear material behaviour to describe the solid part of the material behaviour, and visco-elastic and visco-plastic behaviour to describe the fluid part. The fluid material behaviour is time dependent and will hence be assumed negligible regarding the short impact time during ship-ice interaction. The term visco relate to time dependent behaviour.

Further in this section, mechanics of ice will be presented. The material is mostly referring to Løset et al. (2006).

2.3.1 Elastic Modulus of Ice

Regarding a time-independent one-dimensional case, the stress-strain relation is expressed with Hooke's law. The stress-strain relation describes the stress as a function of strain.

$$\sigma = E \cdot \varepsilon \tag{2.18}$$

Where σ is the applied stress and ε is the total strain. The elastic modulus can then be expressed by

$$E = \frac{\sigma}{\varepsilon} \tag{2.19}$$

Where σ is given by the applied force F over the nominal area A_{nom}. As only the short-term loading is considered due to short impact duration, the most important behaviour is considered elastic-plastic. The ice will hence undergo three different phases, elastic deformation prior to first yield, plastic strain hardening prior to the peak stress and finally softening after reaching the peak stress. The behaviour is illustrated in figure 2.13.

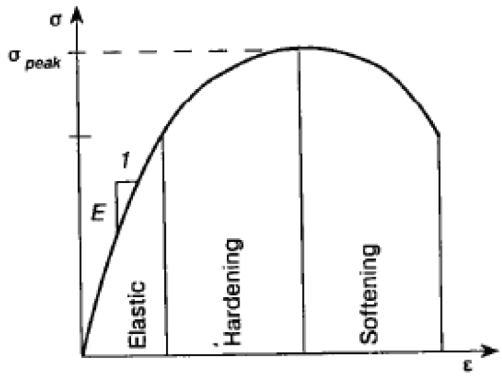

Figure 2.13: Stress-strain diagram for a non-linear material model(Løset et al., 2006).

The elastic strain of ice is a result of deformation of the atomic bonds and is a reversible process (Moslet, 2007). Several papers provide different relations between Young's modulus and key parameters such as porosity and temperature. Gans and Woodmansee (1992) present a relation between Young's modulus and total porosity trough FEM modelling. They observed the degradation of Youngs modulus due to porosity. The following relation was found:

$$E = E_0 e^{-\alpha \cdot \eta_T} \tag{2.20}$$

where E_0 is the Young's modulus excluding porosity, and α is an empirically found constant. Sinha (1989) presents the elastic modulus given as:

$$E = 9.61 + 1.1 \cdot 10^{-2}(T_m - T_k) \tag{2.21}$$

where T_m is the melting temperature of the material in Kelvin, and T_k is the temperature of the ice in Kelvin. Another relationship was suggested by Weeks and Assur (1967) between the Young's modulus for sea ice and fresh water ice, using η_b as the brine volume.

$$E = E_0 \cdot (1 - \eta_b)^4 \tag{2.22}$$

From previous field testing by Moslet (2007), it is reasonable to expect a Young's modulus in level ice to be around 9.6 [GPa] for temperatures between $-10°$C and $0°$C.

2.3.2 Failure Modes of Ice

Von-Mises and Tresca failure criteria could usually be applied to describe material failure. These models only require one material property to determine failure. The Tresca criterion assumes the material to behave elastically until a certain shear limit R_s. This model assumes failure in the plane where the largest shear stress occurs (see figure 2.14). The criterion is described by equation 2.23, where τ is the shear stress and R_s the material capacity or shear limit.

$$\tau \leq R_s \tag{2.23}$$

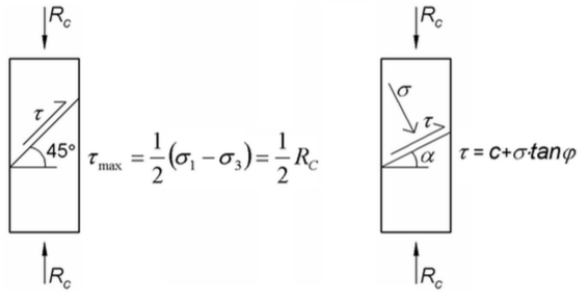

Figure 2.14: To the left, the failure is shown at a critical combination of shear and normal stresses according to von-Mises failure criteria. To the right, the Coulomb-Mohr failure criteria has been taken into account(Løset et al., 2006).

The Tresca model fits to materials such as metals with equal behaviour in tension and compression. Materials such as ice, rocks and soil, are weak in tension

and pressure dependent behaviour must be taken into account. Since the Tresca criterion requires similar behaviour in compression and tension, which is not the case for ice, other models sould be applied. The model that accounts for this phenomenon is the Coulomb-Mohr model. Where the most critical combination of normal and shear stress results in failure as given by equation 2.24.

$$\tau \leq c + \sigma \cdot \tan\varphi \tag{2.24}$$

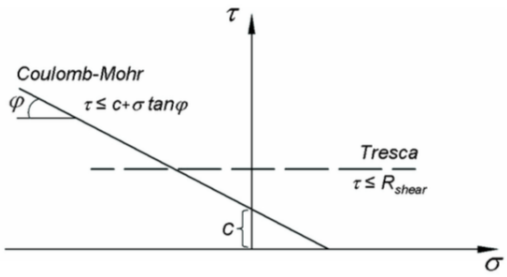

Figure 2.15: The Tresca and Coulomb-Mohr models in a $\tau - \sigma$ plane(Løset et al., 2006).

In figure 2.15, σ and τ are respectively normal stress and shear stress in a given plane, c is the cohesion and φ is the angle of internal friction. If φ equals $\pm 45°$, then Tresca criterion could be applied.

2.3.3 Material Properties and Parameters of Ice

The mechanical behaviour of sea ice depends on several parameters. To properly describe the mechanical behaviour, one should distinguish between state variables and material type. The two most important state variables are the loading or strain rate $\dot{\varepsilon}$, and the temperature T. The material type is governed by the grain size d and orientation of the grains, and the porosity η_T. Regarding material properties, they should be independent of sample size and a function of both state variables and type of material (Løset et al., 2006).

The parameters that govern the mechanical behaviour of ice are temperature T, total porosity η_T, grain size d and the loading rate $\dot{\varepsilon}$. Also the direction of load regarding basal plane direction is an important parameter.

Temperature has several impacts on the mechanical behaviour. Firstly, it impacts the mechanical behaviour itself as it for most materials determines whether the material is brittle or ductile. Secondly, it determines the porosity, as the porosity of sea ice depends on the temperature of the ice. The temperature does impact the growth rate which in terms affect the ability to capture brine and gas pockets. Also, the temperature determines further development of the gas and brine

pockets. Generally, the ice becomes less resistant to stresses and suffers a lowered Young's modulus due to increased temperature.

Porosity has shown to impact the capacity of ice. Timco and Weeks (2010) and Moslet (2007) have shown that porosity impacts Young's modulus, Poisson's ratio and ice strength. Also, the size of the pores impacts the strength.

Grain size impacts the mechanical behaviour of ice since the boundaries of each grain increase due to increased grain size. Sliding occurs along the grain boundaries due to shear stress and will result in stress concentrations and decohesion along the boundaries.

Strain rate has shown great impact on the mechanical properties of ice. The strength of ice increases with increasing strain-rate before it reaches a ductile to brittle transition, and the strength decreases. The transition and relation between strength and strain rate are shown in 2.16

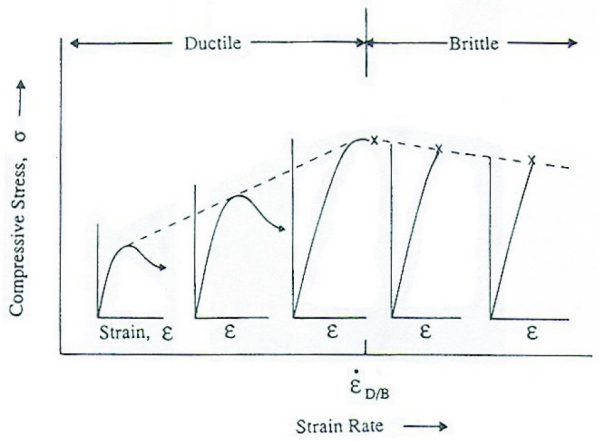

Figure 2.16: Behaviour of stress-strain curve depending on strain rate (Høyland, 2015).

From figure 2.16, the ductile behaviour is defined when the peak is reached and the stress decay with increasing compression. Brittle behaviour is defined as a sudden end in the load curve. Also, there exists a transition region, where the ice will have its maximum capacity.

Load direction regarding the grain direction is especially important. As ice grows in a vertical direction one obtain columns of grains vertically. Ice will have

sufficiently more strength in vertical compression, compared to horizontal compression as slipping along the grains occur more easily than breakage between the basal planes. The different grain directions relatively to compression and tension are given in figure 2.17.

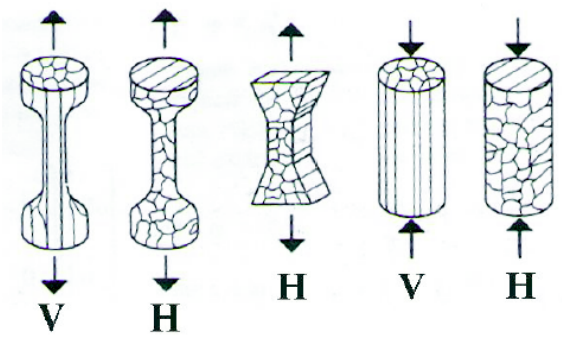

Figure 2.17: Uniaxial tension and compression of ice with different columnar direction. V denotes vertical columnar direction, while H denotes horizontal direction. The arrows denote compression or tension (Høyland, 2015).

Due to the atomic structure of ice (presented in section 2.2.1) the ice will have less strength along the basal planes compared with the strength along the c-axis. Thus, slipping along grain boundaries occurs most often. Regarding this, empirical formulas have been derived for compressive strength of ice relatively to the grain boundaries(Moslet, 2007). The strength is dependent on strain rate $\dot{\varepsilon}$ and porosity η_T which in term are temperature dependent. v and h denote columnar direction, c denotes compression, as illustrated by figure 2.17.

$$\sigma_{c,v} = 160 \cdot (\dot{\varepsilon})^{0.22} \left[1 - \left(\frac{\eta_T}{0.20}\right)^{0.5}\right] \tag{2.25}$$

$$\sigma_{c,h} = 37 \cdot (\dot{\varepsilon})^{0.22} \left[1 - \left(\frac{\eta_T}{0.27}\right)^{0.5}\right] \tag{2.26}$$

Equation 2.25 and 2.26 are valid for porosities up to about 0.2 [-]. Also, these equations are best fit, such that they do not necessarily present the upper most limit of capacity. Timco and Frederking (1990) found that $\sigma_{c,v} \approx$ 5-15 [MPa] and $\sigma_{c,h} \approx$ 2-5 [MPa] for porosities around 0.1-0.15 [-].

Timco et al. (1994) investigated a database of about 2500 reported measurements on flexural strength of sea ice from around the world. It was found that sample size, test type and load rate had little influence on the results. Further, it was found that flexural strength of ice correlated well with the brine porosity η_b of the sea ice. The brine porosity could be estimated knowing the temperature, density

and salinity of each test sample. The flexural strength was plotted towards the brine porosity as shown in figure 2.18.

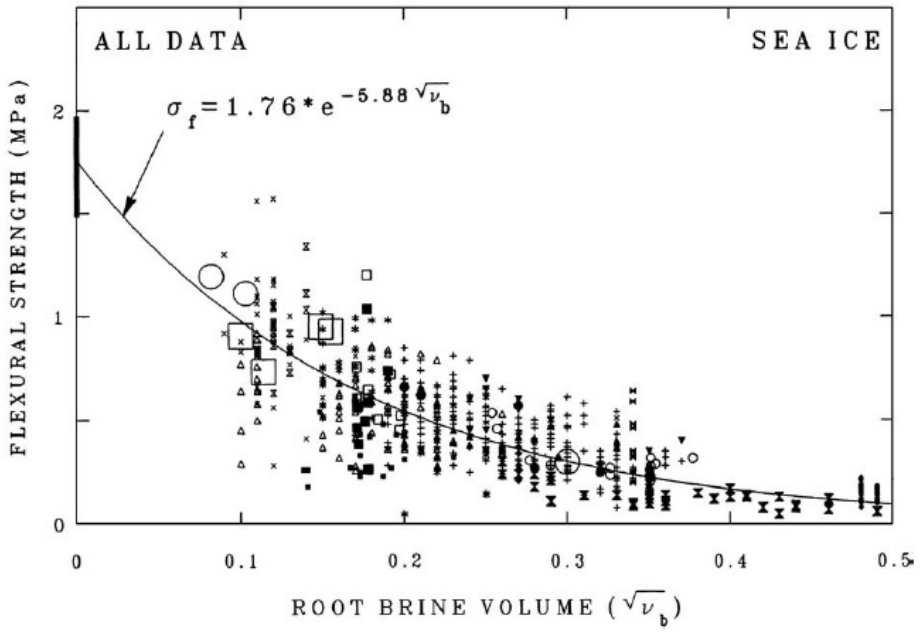

Figure 2.18: Flexural strength of sea ice σ_f plotted towards the root of the brine porosity η_b(Timco et al. (1994) denote the brine porosity ν_b). The curve is a best fit exponential trough the data. The figure is courtesy of Timco et al. (1994).

The flexural strength of ice has been found to fit the following equation, after investigation by Timco et al. (1994).

$$\sigma_f(\eta_b) = 1.76 \cdot e^{-5.88 \cdot \sqrt{\eta_b}} \tag{2.27}$$

where η_b is the brine volume fraction. This formula was based on several assumptions and restrictions. The load direction of each test was parallel to the original ice growth direction in order to simulate an ice breaking vessel. The grain structure and size were not accounted for due to lack of information from the source that produced the test results. The loading rate had no influence on the results. For each beam, the average salinity was applied to represent each sample. The brine volume, or fraction, η_b was applied as a variable describing the flexural strength. Reasonably because η_b describe the part of the ice that is not solid, and as the non-solid part increases, there exist less solid ice, hence the strength is reduced. Also, the brine fraction is related to the temperature T and the salinity S as described under section 2.2.4.

Chapter 3

Measurement of Sea Ice Strength

Assessment of sea ice strength is a complex procedure, where the sea ice strength depend on several parameters. The ice strength is an important parameter in the design process of ships. To assess sea ice strength, compression tests and parametric measurements could be performed. Cylindrical ice samples are drilled out from the ice cover, at certain locations and either tested in situ or brought back to a cold laboratory for testing later.

This chapter presents compression tests performed both in situ and at a cold laboratory at UNIS. Approximately 1300 samples were tested during the year 2004 and 2005 in areas close to Svalbard. Knut V. Høyland has given permission to apply the data in this master thesis, for further studies of behaviour of sea ice in interaction with ships.

3.1 Ice Compression Test

This thesis will give priority to two groups of samples. The first group of samples were gathered at Frysjaodden between May 31^{st} and June 6^{th} 2004. These samples consist of vertical specimens of level ice. The second group of samples were gathered in the Barents Sea October 21^{st} 2004. These samples consist of both vertical and horizontal specimens from a ice ridge. These two groups of samples were chosen as representatives for level ice and ice ridges, due to a large amount of obtained data within each group. The data of level ice consist of 91 samples, while the ice ridge data consist of 108 different samples.

Further in this section, the experimental set-up, measurements, results and discussion of the compression test are presented. The results are considering variations and equalities in ice strength towards descriptive parameters such as porosity and temperature. Also, the results apply to establish approximations of the flexural

strength for both level ice and ice ridges. Further, these results will be applied in a structural analysis presented in chapter 7 and 8.

3.1.1 Experimental Set-up

In order to prepare each sample for a compression test, the ice samples were cut into cylinders with parallel end surfaces as shown in figure 3.1a.

(a) Ice sample cutting rig.

(b) Compression-rig KOMPIS.

Figure 3.1: In figure 3.1a the two blades are mounted in parallel with a distance 175 [mm] and are manually driven. In figure 3.1b is the ice sample set-up for compression using KOMPIS shown.

Several measurements were conducted prior to compression, these are further discussed under section 3.1.2. For the compression tests, one used KOMPIS which is a uni-axial compression test machine designed especially for this purpose. KOMPIS compress ice between one fixed and one mechanically driven plate. The compression setup, is illustrated in figure 3.1b. From figure 3.1b the fixed plate is observed under the ice specimen. Above the specimen, a spacer is placed between the specimen and the moving plate. The vertical pipes shown in the figure guide the moving plate to ensure that the two surfaces remain parallel during compression. KOMPIS log the applied force, and the displacement of the moving plate in the time domain. The compression velocity is also measured, such that the strain rate could be found.

3.1.2 Measurement of Sea Ice Specimens

Some measurements were made prior to compression, such as the main dimensions of each sample. As the ice samples had some irregularities, both length and diameter of the ice sample were averaged. These values were necessary to measure regarding stress and strain rate calculations. Additionally, also for calculations of density. The core temperature was measured by drilling holes into the remaining ice pieces post compression and the salinity was measured after the ice had melted(See figure 3.2). Each sample was stored over night for melting, in clean, sealed boxes. From these measurements, the porosity could be found. Results from these measurements are found under section 3.1.3

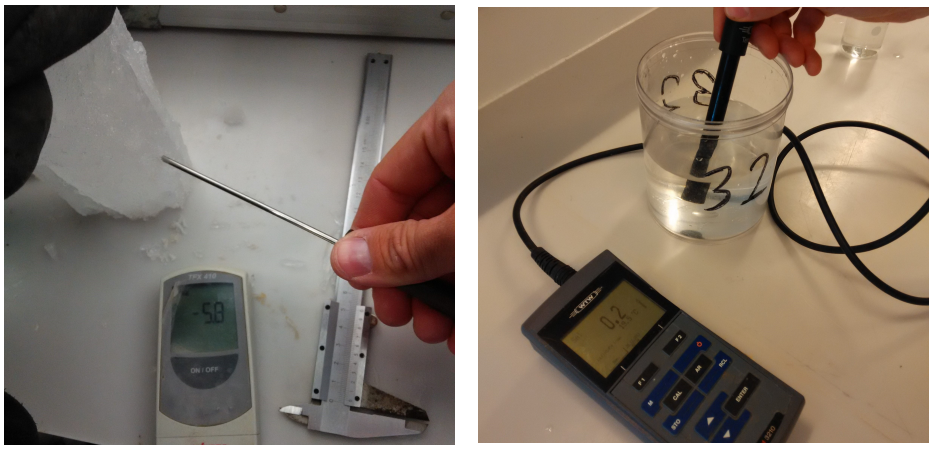

(a) Temperature measurement of the remaining of the ice specimens.

(b) Salinity measurement of the melted ice samples.

Figure 3.2: The two measurements performed post compression of each ice sample. The figures are only illustrative and not a part of actual results.

The results provided by Knut V. Høyland consisted of measurements of maximum stress σ_{max}, salinity S, core temperature T_i, ice feature and drilling direction. Further it was given whether the sample suffered from brittle, ductile or a combination of the two failure modes. From previous measurements conducted at UNIS during the course AT-334 *Arctic Marine Measurements Techniques, Operations and Transport* the average length and diameter of each specimen were set to 175 [mm] and 70 [mm], respectively. This simplification was necessary to introduce, to establish density data for the specimens, and will be further used in this master thesis. This will in some cases either over- or underestimate the density. Hence, a sensitivity study should be performed to investigate the effect of changing diameter. The distance between the blades in figure 3.1a was measured to 175 [mm], hence the most variable measure will be the diameter of each specimen.

3.1.3 Results of Sea Ice Specimen Testing

This section will provide results based on the measurements conducted in 2004 and 2005. The results will be divided into two groups regarding ice feature, respectively level ice and ridged ice. The measurements consist of many measurements, hence only plots of compressive strength versus salinity and temperature will be included to describe each data set. The total data set of porosities could be found in appendix A.1 and A.2, for level ice and ridged ice respectively. For these results, a diameter 70 [mm] and a length 175 [mm] were applied. The compressive strength $\sigma_{c,v}$ denotes compression parallel to the growth direction (see figure 2.17).

Level Ice Measurements

The level ice measurements have been sorted and plotted applying MATLAB scripts given in appendix B.

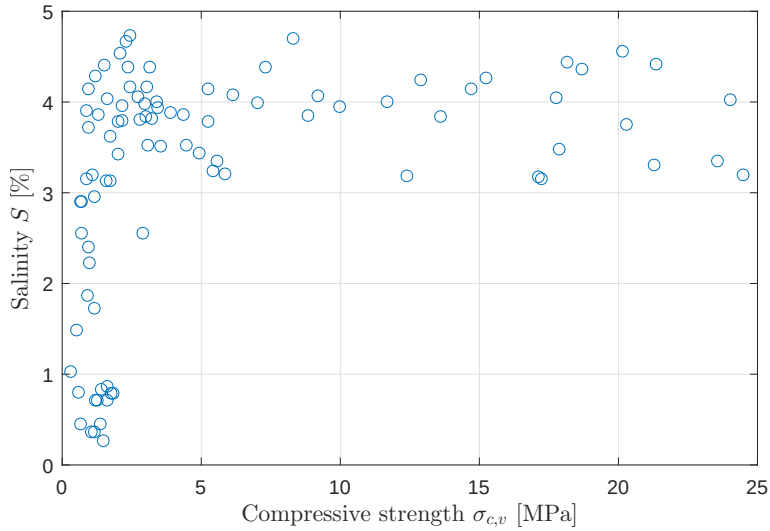

Figure 3.3: Compressive ice strength $\sigma_{c,v}$ plotted towards salinity S.

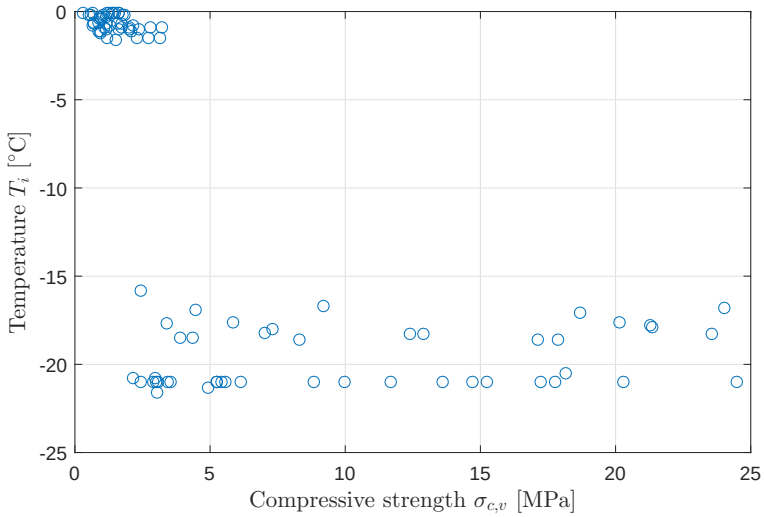

Figure 3.4: Compressive ice strength $\sigma_{c,v}$ plotted towards core temperature T.

Figure 3.3 and 3.4 presents the data for level ice. The method of estimating the porosity is described under section 2.2.4 and the MATLAB scripts that estimates the porosity are provided by K. V. Høyland and based on Cox and Weeks (1983). In figure 3.3 one can observe that the low salinity samples only reach a max value of to 2.5 [MPa] in compression. This is not corresponding with Timco and Weeks (2010), as low saline ice should be stronger than high saline ice. From the data set, it was found that the low saline ice had high temperatures as shown in the top left corner of figure 3.4. Hence, they became ductile and suffered from collapse before the cold ones with high salinity.

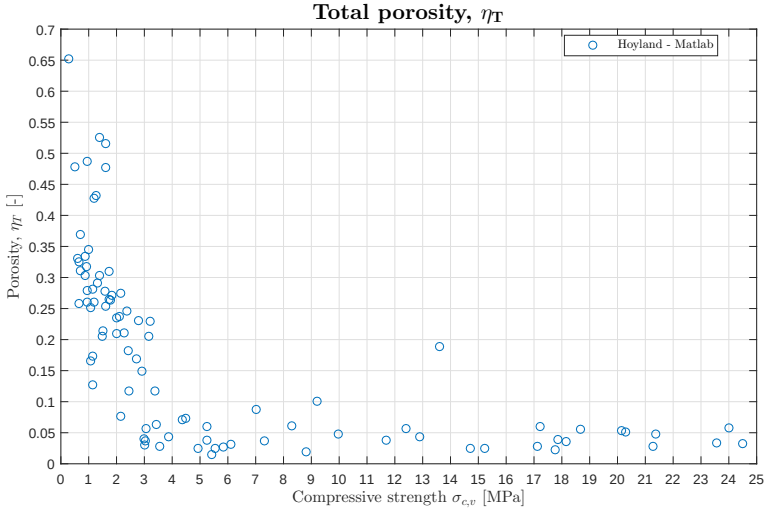

Figure 3.5: The compressive ice strength $\sigma_{c,v}$ plotted towards total porosity η_T.

Figure 3.5 present a scatter plot of how the compressive strength vary with the total porosity. The figure substantiates the theory (Moslet, 2007), as high compressive strength only exists for the samples with low porosity.

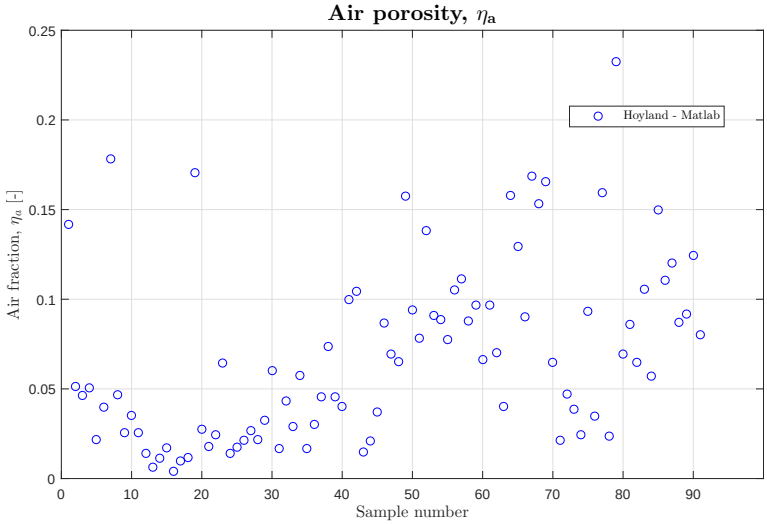

Figure 3.6: The sample number plotted towards an approximated air porosity η_a.

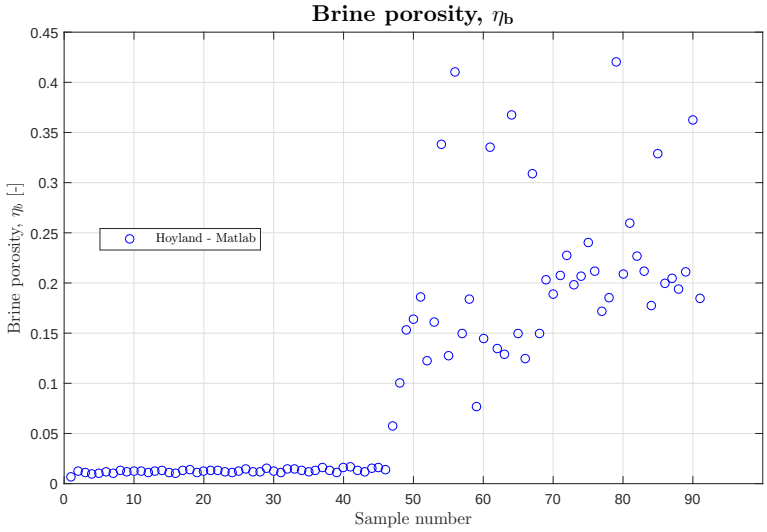

Figure 3.7: The sample number plotted towards an approximated brine porosity η_b.

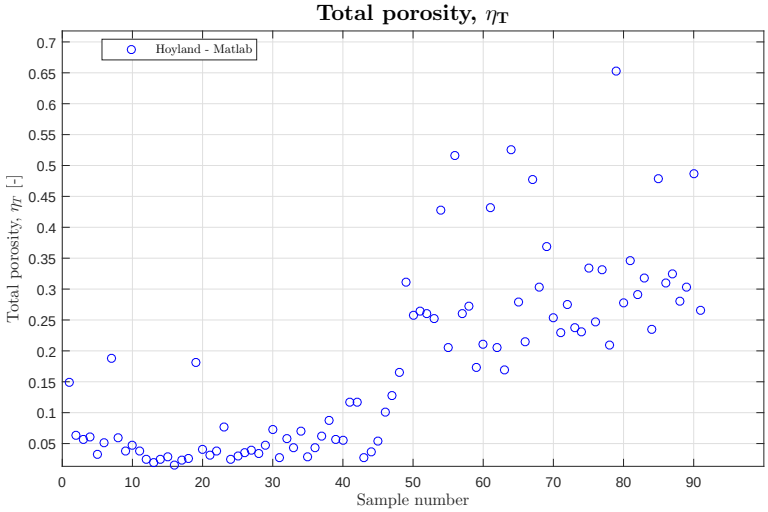

Figure 3.8: The sample number plotted towards an approximated total porosity η_T.

Figure 3.6 shows that air porosity exists for all samples regardless of core temperature. Figure 3.7 show that brine porosity is stronger connected to the core temperature. Sample 1 to 46 had a core temperature between -21 to -15.8 [°C]. While sample 47 to 91 had core temperatures between -0.1 to -1.5 [°C]. Figure 3.8 presents the sum of both air and brine porosity as total porosity.

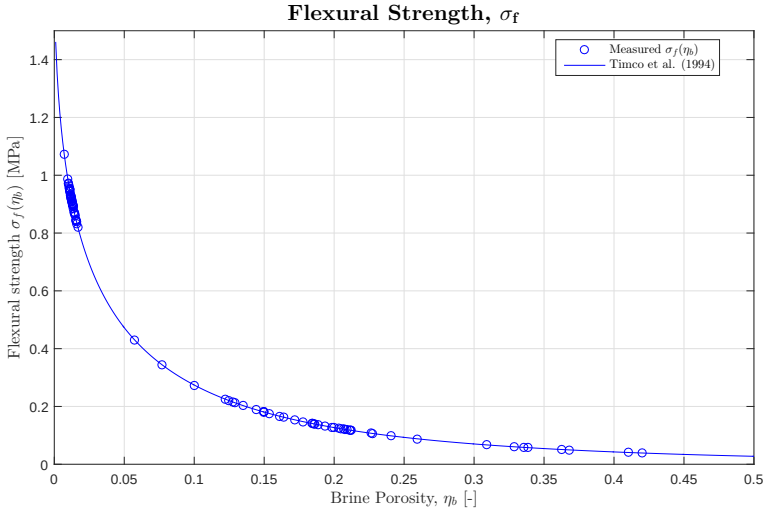

Figure 3.9: The flexural strength $\sigma_f(\eta_b)$ plotted towards an approximated brine porosity η_b. Timco et al. (1994) provided equation 3.1 for approximation of the flexural strength $\sigma_f(\eta_b)$ which is plotted here. Reasonably do the measurements follow the curve.

Figure 3.9 is estimated applying equation 3.1

$$\sigma_f(\eta_b) = 1.76 \cdot \exp^{-5.88 \cdot \sqrt{\eta_b}} \tag{3.1}$$

which approximates the flexural strength, based on work by Timco et al. (1994). The plot of the flexural strength shows that low porosities, hence low temperatures, result in the highest flexural strength. This coincide with Moslet (2007). Initially, the volume was assumed constant with a value of 0.06735 $[m^3]$. This assumption is not necessarily valid due to irregularities from brine channels and cracks. In order to assess the validity of the initial assumption, a sensitivity study of varying volume was performed. All samples were cut with the rig shown in figure 3.1a, and the length of 175 [mm] has been kept constant through the assessment. Table 3.1 presents the different diameters applied to account for irregularities. Also, the table presents the mean air, brine and total porosity, as well as mean flexural strength for each diameter.

Table 3.1: Presentation of the mean values: diameter $\overline{D}$, air porosity $\overline{\eta_a}$, brine Porosity $\overline{\eta_b}$, total porosity $\overline{\eta_T}$ and flexural strength $\overline{\sigma_f}$ from level ice testing.

Test #	$\overline{D}$ [mm]	$\overline{\eta_a}$ [-]	$\overline{\eta_b}$ [-]	$\overline{\eta_T}$ [-]	$\overline{\sigma_f}$ [MPa]
1	70	0.06906331	0.10865094	0.17771425	0.53290562
2	69	0.04473790	0.11182306	0.15656096	0.52611649
3	68	0.02782597	0.11513616	0.14296213	0.51926007
4	67	0.01566240	0.11859871	0.13426111	0.51233537
5	66	0.00843636	0.12221984	0.13065620	0.50534138
6	65	0.00408550	0.12600938	0.13009488	0.49827706
7	64	0.00124890	0.12997793	0.13122683	0.49114132
8	63	0.00057424	0.13413696	0.13471121	0.48393306
9	62	0.00023557	0.13849886	0.13873443	0.47665115
10	61	0.00000000	0.14307703	0.14307703	0.46929441

Table 3.1 shows that an increase in density, due to reduced diameter, reduce the average air porosity $\overline{\eta_a}$ hence increases the average brine porosity $\overline{\eta_b}$. This increase reduces the average flexural strength $\overline{\sigma_f}$. Table 3.2 shows the deviation between the initial assumed diameter of 70 [mm] and the reduced diameters.

Table 3.2: Presentation of the deviation of the average flexural strength between the initially assumed diameter D = 70 [mm] and the reduced diameters.

Test #	$\overline{D}$ [mm]	$\overline{\sigma_f}$ [MPa]	Deviation [%]
1	70	0.53290562	0.000
2	69	0.52611649	1.274
3	68	0.51926007	2.561
4	67	0.51233537	3.860
5	66	0.50534138	5.172
6	65	0.49827706	6.498
7	64	0.49114132	7.837
8	63	0.48393306	9.189
9	62	0.47665115	10.556
10	61	0.46929441	11.937

From table 3.2 it is observed that a reduction in volume, presented by a reduction in diameter, would give a reduction in the average flexural strength up to 12 [%].

In order to investigate the fact that the degree of irregularities will vary between each specimen, another method was applied. A diameter of 61 [mm](as for test number 10) will assume that all samples have large defects or irregularities regarding shape. While a diameter of 69 [mm](as for test number 2) will assume small to almost no defects or irregularities. Therefore, three different tests were performed. The tests were conducted by letting a part of all diameters be uniformly distributed on a given range, as described by equation 3.2.

$$D = \hat{\beta} \cdot \hat{\alpha} + \hat{D} \text{ [mm]} \tag{3.2}$$

Where D describes the diameter of each specimen, $\hat{\beta}$ describes a portion of the diameter multiplied with a uniformly distributed random number $\hat{\alpha}$ in the range of [0,1] and $\hat{D}$ describes the fixed portion of the diameter i.e. the lower limit of the diameter. Table 3.3 presents the three different tests where all samples had random varying diameters.

Table 3.3: Test results from varying a portion $\hat{\beta}$ of the diameter D with a uniformly distributed random number $\hat{\alpha}$ in the range [0,1]. The deviation is compared with test 1 from table 3.2.

Test #	$\hat{D}$ [mm]	$\hat{\beta}$ [mm]	$\overline{\sigma_f}$ [MPa]	Deviation [%]
1	60	10	0.49903247	6.356
2	65	5	0.51496424	3.367
3	69	1	0.52925880	0.684

The deviation of test 1, presented in table 3.3, tend to be marginally lower than the deviation from test 6 (table 3.2). Equally for test 2, the result tend to be somewhat lower than test 4 (table 3.5). Finally test 3 tends to be between the deviation of test 1 and 2 (table 3.2). From table 3.3 test 1 would present a data set containing everything from small to large defects and irregularities. Test 2 would present a data set of small to medium defects, while test 3 would present a data set with only small irregularities or defects.

Ridged Ice Measurements

The ridged ice measurements have been sorted and plotted applying the same MATLAB scripts as the level ice data, given in appendix B.

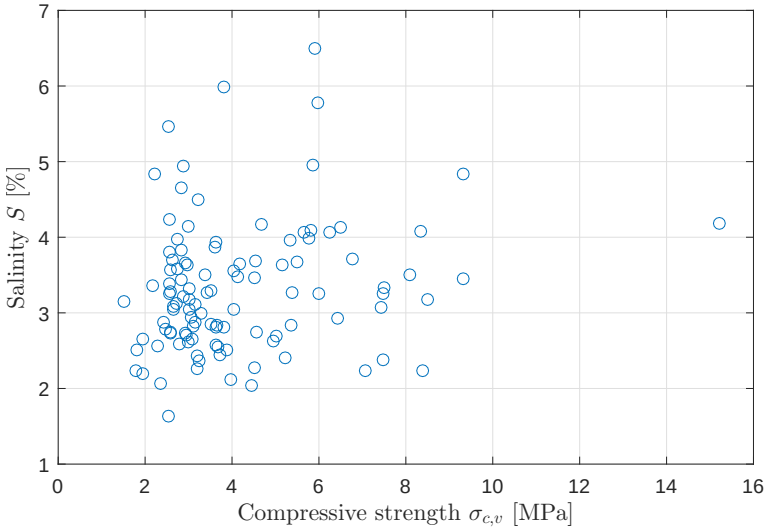

Figure 3.10: Compressive ice strength $\sigma_{c,v}$ plotted towards salinity S.

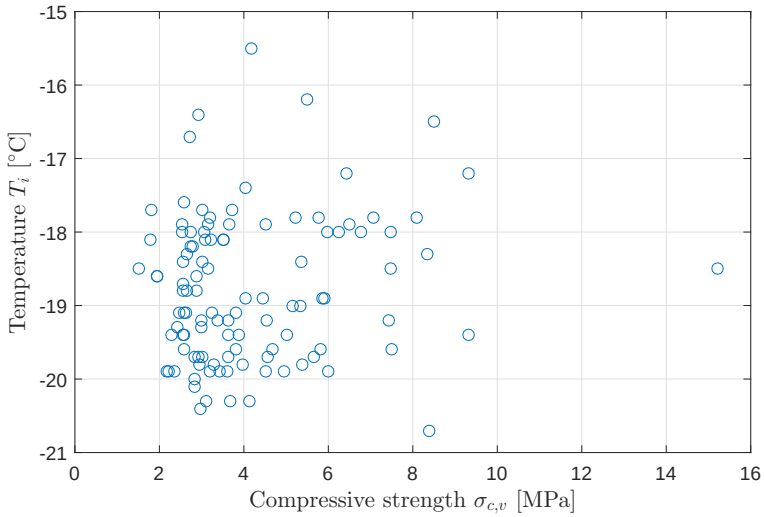

Figure 3.11: Compressive ice strength $\sigma_{c,v}$ plotted towards core temperature T.

Figure 3.10 and 3.11 present the data for ridged ice. As for the level ice, the same method of estimating the porosity is applied here. Compared to level ice, the ridged ice have a larger spread in salinity while it do only reach a maximum compressive strength of 15.5 [MPa]. Also, the temperatures are located between -15 and -21 [°C].

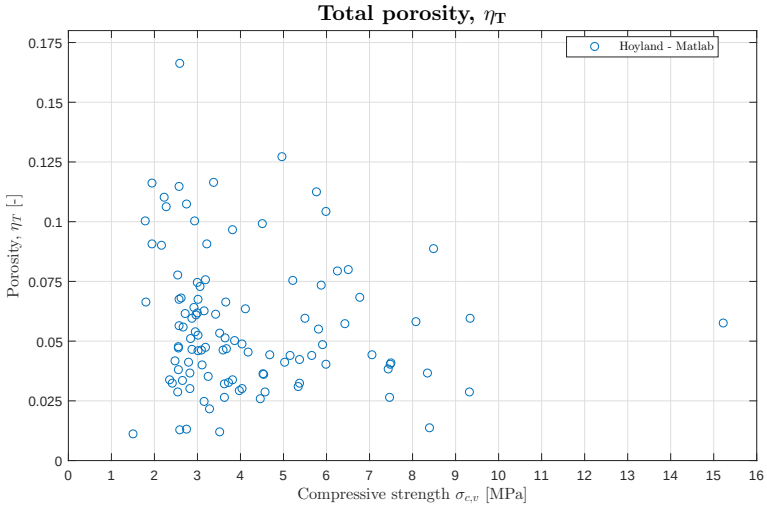

Figure 3.12: The compressive ice strength $\sigma_{c,v}$ plotted towards total porosity η_T.

Figure 3.12 presents the total porosity η_T for the ridged ice plotted towards the compressive strength $\sigma_{c,v}$. Compared to the level ice results presented in figure

3.5, these total porosities are low and concentrated between 0 and 0.12 [-]. The low porosities and the measurement date of 21^{st} of October indicate that this is a second-year ridge, according to Ekeberg (2015).

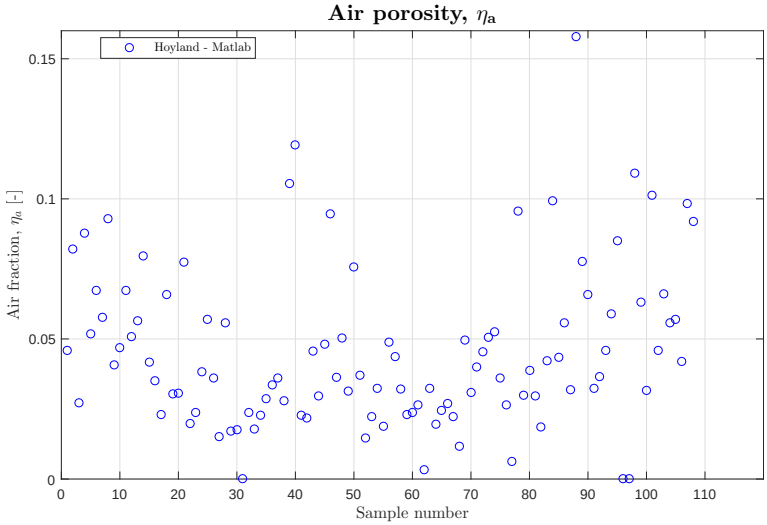

Figure 3.13: The sample number plotted towards an approximated air porosity η_a.

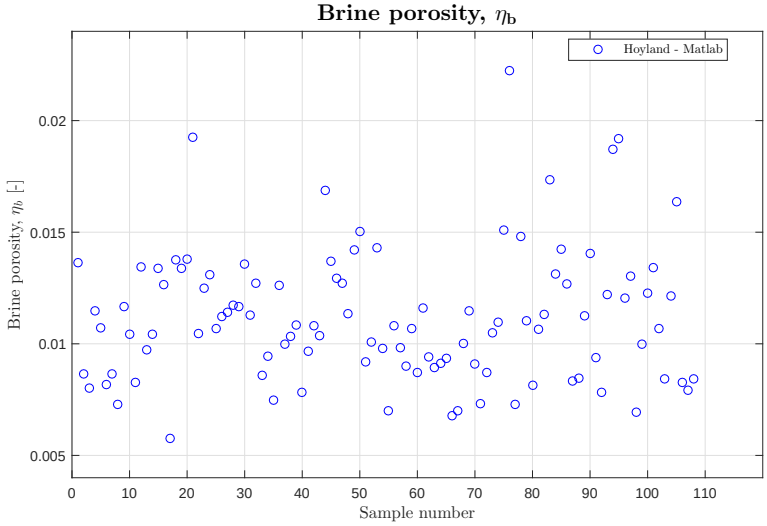

Figure 3.14: The sample number plotted towards an approximated brine porosity η_b.

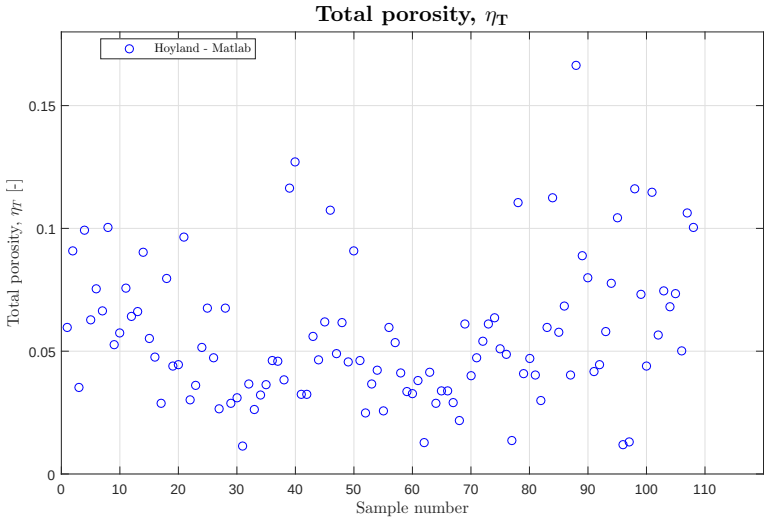

Figure 3.15: The sample number plotted towards an approximated total porosity η_T.

From figure 3.13 and 3.14 one observes that the air porosity η_a dominates the total porosity η_T. This indicates that brine pockets have had time to consolidate, which according to theory of a second-year ridge substantiates the assumption. Figure 3.15 presents the total porosity η_T as a sum of both brine and air porosity.

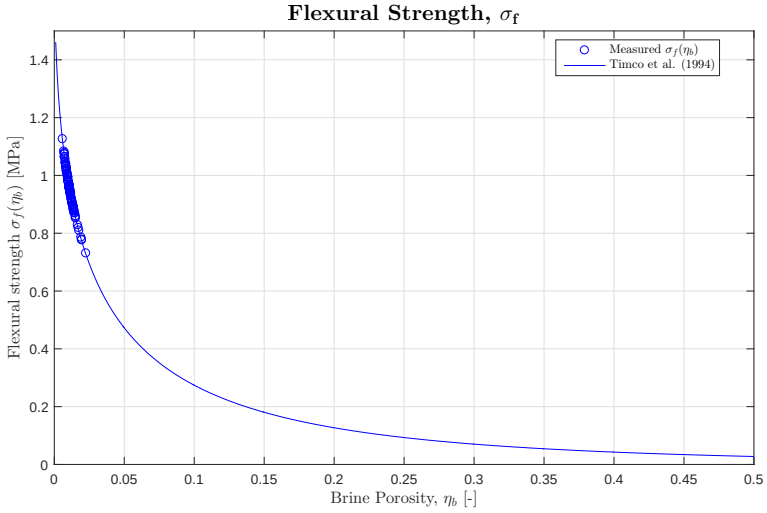

Figure 3.16: The flexural strength $\sigma_f(\eta_b)$ plotted towards an approximated brine porosity η_b. Timco et al. (1994) provided equation 3.1 for approximation of the flexural strength $\sigma_f(\eta_b)$ which is plotted here. Reasonably do the measurements follow the curve.

Figure 3.16 applies equation 3.1 to approximate the flexural strength. All the brine porosities are close to zero, as shown by figure 3.14, hence the flexural strengths became high. As this ridge is more consolidated, higher flexural strength is expected. Equally the level ice calculations, the initial assumed volume was set to 0.06735 [m^3]. The same sensitivity study was conducted to check the variety due to varying volume. Table 3.4 presents the results where the average diameter varies from 70 to 61 [mm].

Table 3.4: Presentation of the mean values: diameter $\overline{D}$, air porosity $\overline{\eta_a}$, brine Porosity $\overline{\eta_b}$, total porosity $\overline{\eta_T}$ and flexural strength $\overline{\sigma_f}$ from ridged ice testing.

Test #	$\overline{D}$ [mm]	$\overline{\eta_a}$ [-]	$\overline{\eta_b}$ [-]	$\overline{\eta_T}$ [-]	$\overline{\sigma_f}$ [MPa]
1	70	0.04555749	0.01115385	0.05671134	0.95350702
2	69	0.02064662	0.01147949	0.03212611	0.94511641
3	68	0.00765671	0.01181961	0.01947631	0.93655736
4	67	0.00250895	0.01217506	0.01468402	0.92782510
5	66	0.00057358	0.01254680	0.01312038	0.91891472
6	65	0.00021532	0.01293582	0.01315114	0.90982113
7	64	0.00000000	0.01334323	0.01334323	0.90053910
8	63	0.00000000	0.01377018	0.01377018	0.89106320
9	62	0.00000000	0.01421797	0.01421797	0.88138785
10	61	0.00000000	0.01468795	0.01468795	0.87150727

Table 3.4 shows that increased density reduces the average air porosity and increases the average brine porosity. Regarding the increased density, the average flexural strength is reduced as it only depends on the brine porosity. An assessment of the deviation in average flexural strength between the initially assumed diameter of 70 [mm] and the reduced diameters is presented in table 3.5.

Table 3.5: Presentation of the deviation of the average flexural strength between the initially assumed diameter D = 70 [mm] and the reduced diameters.

Test #	$\overline{D}$ [mm]	$\overline{\sigma_f}$ [MPa]	Deviation [%]
1	70	0.95350702	0.000
2	69	0.94511641	1.042
3	68	0.93655736	1.938
4	67	0.92782510	2.853
5	66	0.91891472	3.786
6	65	0.90982113	4.738
7	64	0.90053910	5.710
8	63	0.89106320	6.702
9	62	0.88138785	7.715
10	61	0.87150727	8.750

Table 3.5 indicates that a data set with large imperfections and brine channels could obtain a reduction in the average flexural strength up to 8.75 [%].

Similar to the results from the level ice specimen test, a uniformly distributed random number $\hat{\alpha}$ was added to a part of the diameter as described by equation 3.2. Which in term gave the ability to investigate difference between large and small defects and imperfections in the data set. Table 3.6 presents the three different test where all samples had random varying diameters within certain limits.

Table 3.6: Test results from varying a portion $\hat{\beta}$ of the diameter D with a uniformly distributed random number $\hat{\alpha}$ in the range [0,1]. The deviation is compared with test 1 from table 3.2.

Test #	$\hat{D}$ [mm]	$\hat{\beta}$ [mm]	$\overline{\sigma_f}$ [MPa]	Deviation [%]
1	60	10	0.90366712	5.230
2	65	5	0.92983790	2.482
3	69	1	0.94950352	0.420

The results in the rightmost column presents deviations between the flexural strength of the data set with varying diameter and the data set with assumed 70 [mm] diameter for the total set. Test 1 in table 3.6 is slightly lower than test 7 from table 3.5. For test 2 (from table 3.6), the results are lower than test 4 (from table 3.5). Finally, for test 3, the result is between result 1 and 2 (from table 3.5). Equal table 3.3, table 3.6 presents different degrees of defects and deformations. Test 1 present large deformations, test 2 present small to medium deformations while test 3 presents a data set with small to no irregularities or defects.

3.1.4 Discussion of Measurments

The level ice data presented in figure 3.3 indicates that only ice with salinity above 3 [%] reach higher compressive strength. The less saline ice only reach compressive strengths up to 2.5 [MPa]. From the data set, the low saline samples are gathered from the top of the level ice. Regarding the fact that the ice were gathered in May, radiation and melt water may have mixed up with snow on top, and frozen as it interacts with the cold front of the ice layer. This will cause a less saline ice with granular structure, and give ice less resistant to compressive forces as the ice is granular. Figure 3.4 indicates that temperatures also impact the strength of the ice. From the data set, most of the high temperature samples was denoted ductile failure and low salinity. This coincide with Timco and Weeks (2010) and figure 3.3, as high temperatures give a ductile and weak ice. Further, the salinity was low and should give a stronger ice. Thus, the temperature had a larger effect on the strength.

Figure 3.5 presents the total porosity plotted toward compressive strength, the plot indicates that only low porosity samples are allowed to reach high compressive strengths. This coincide well with Moslet (2007), as low porosity give stronger ice

due to more ice per volume. From figure 3.8 one can observe that the first 46 samples have low total porosity. From the data set, it is noted that these samples also had low core temperatures. Hence, both temperature, salinity and porosity determine the compressive strength of the ice specimen. Figure 3.9 shows that the flexural strength approximation is divided into two main groups. Considering figure 3.7 one could see why, as the first 46 samples have low brine porosity, and low brine porosity give higher flexural strength.

The sensitivity study of varying diameter describes defects or irregularities of each sample (table 3.3). By varying the diameter, the density of each sample changes, which in terms change the porosity and flexural strength. Letting the diameter vary within 10 [mm], the deviation in flexural strength became 6.356 [%] from the initially assumed case where the diameter was fixed to 70 [mm]. By letting the diameter only vary within 5 [mm] the deviation became 3.367 [%] and for the case where the diameter only varied within 1 [mm] the deviation became 0.684 [%]. Sea ice will never be truly perfect. By applying a diameter of 70 [mm], one will obtain the highest flexural strength of the sea ice based on the previously presented measurements. By accounting for large variety in the degree of imperfection, one could apply the flexural strength of 0.499 [MPa] and only deviate 6.356 [%] from the highest flexural strength of 0.533 [MPa].

The ridged ice data presented in figure 3.10 and 3.11 indicate that regardless of salinity and temperature, the samples cover a range of compressive stresses. The salinity vary from 2 to 6 [%] for a range of compressive strengths from 2 to 10 [MPa]. For the same range of compressive strengths, the temperature varied from -15.5 to -20.5 [°C]. This ridge has had time to consolidate both water pockets between the ice blocks, and the brine pockets within the ice. Reasonably because the total porosities are quite low as shown in figure 3.12 and the measurements that took place 21^{st} of October would indicate that this is a second-year ridge as stated by (Ekeberg, 2015). Also note that the total porosity presented in figure 3.12 is low compared to the same plot for level ice presented in figure 3.5.

Figure 3.13 and 3.14 indicate that the total porosity are dominated by the air porosity. As the brine pockets within the ridge continuously consolidate when exposed to cold temperatures, the brine porosities reduce. While the approximated air porosity do not change with the same rate when exposed to cold temperatures. Because of the low variety in the brine porosity, the flexural strengths presented in figure 3.16 are located in one group with an average strength of 0.954 [MPa]. Compared to the level ice measurements presented in figure 3.9, the ridged ice has almost twice as much flexural strength. Also, a higher flexural strength is expected for the ridged ice, as it has had more time to consolidate.

The sensitivity study presented in table 3.5 indicate that the ridged ice has less deviation than for the level ice, when considering imperfections and defects that may occur in an ice sample. One reason is less variation in the brine porosity compared to the level ice measurements. By letting the diameter be as low as 61 [mm], the deviation between the initial average flexural strength became 8.75 [%] which is lower than 12 [%] obtained from the level ice sensitivity study. When let-

ting the diameter vary within 10 [mm] by a uniformly distributed random number added to the lower limit of the diameter of 60 [mm], the deviation became 5.23 [%]. This is 1.13 [%] lower than the result from the same test performed on level ice. To obtain the highest safety margin when applying the flexural strength to a structural interaction problem, the initial assumption of perfect samples with no defects and a diameter of 70 [mm] should be applied. This would lead to a flexural strength of 0.954 [MPa]. If the variety of defects and imperfections are accounted for, one could apply a strength of 0.904 [MPa] and deviate 5.23 [%] from the initial value.

Chapter 4

Ice-Structure Interaction

In ship design, regarding operations in ice-infested waters, there are many parameters that are necessary to investigate. Considering interaction between ships and ice, both global actions and local pressures should be analysed. For this master thesis, only local pressure and interaction models are further investigated. Local loads are essential when local structural strength is predicted. By data collection and observations from the operational area, the properties of level ice and ice ridges could be established to describe the ice conditions. When the ice conditions in the operation area are established, the required ship strength could be estimated by including the ice conditions in the design loads. These loads could be predicted by establishment of contact mechanics. This chapter will cover a local ice pressure model for prediction of ice loads on a ship hull.

4.1 Local Ice Pressure Model

Contact between a ship hull and ice result in local loads as the ice break up during interaction. These loads are commonly assumed to act as local load patches on the ship. Regarding level ice, these patches will have a small vertical extend, while horizontally they are of greater extend. Within the load patch area, the model assume uniform loading from ice interaction. These assumptions are rough, hence an exact model is difficult to predict without strain measurements from an ice going vessel. For ridged ice, the vertical extend will be greater than for level ice as a fully consolidated first-year ridge is typically is 2-2.5 times the thickness of level ice. The following sections will provide additional information for the local ice pressure model. The material is referring to Riska (2011) and Riska and Kämäräinen (2011).

4.1.1 Ice Interaction

Prior to the failure of the ice sheet, crushing occur in different forms. The two main forms are spalling and crushing as presented in figure 4.1.

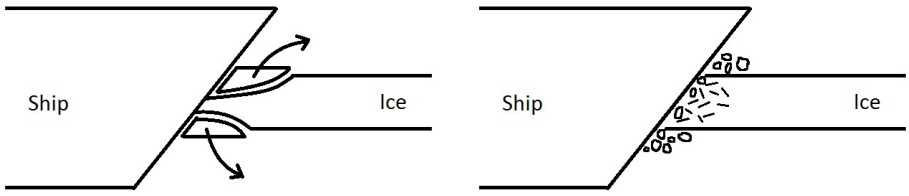

(a) Spalling. (b) Crushing.

Figure 4.1: The two failure modes of ice, prior to flexural failure. The figure is inspired by Høyland (nd). Note that no scale is taken into account, only the principle of failure mode is illustrated.

The contact height will vary between the two modes described by figure 4.1a and 4.1b. Further description of this is given in section 4.1.3.

For level ice, the ice is most often failing in bending. Initially, the hull crushes the ice edge during contact, as described in figure 4.1. This will continue until the contact area A is sufficiently large and able to create a vertical force component F_V, and the ice cover will fail in bending as the moment induced by the vertical force is greater than the flexural strength σ_f of the ice. For ridged ice, the loads induced to the hull will be estimated as if the thickness of the consolidated layer equals level ice thickness. In a 2D perspective, the forces that occur during interaction between sea ice and a ship hull is presented in figure 4.2.

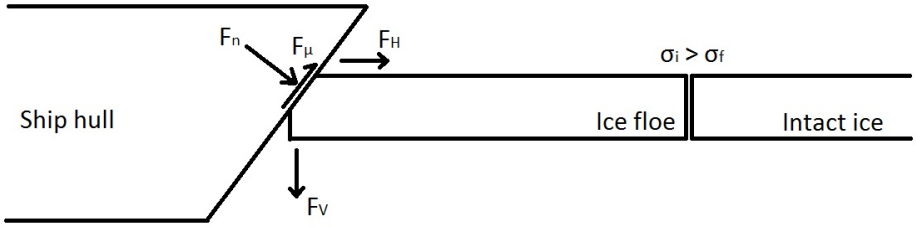

Figure 4.2: The forces acting during interaction between ship and ice, post ice crushing. The figure is inspired by Riska (2011).

From figure 4.2 the normal force F_n is decomposed into a horizontal and a vertical force component, F_H and F_V respectively. Where the horizontal component is assumed to be negligible, as the vertical force will induce a larger moment due to a larger lever arm relatively to the center of rotation. The force induced by friction

between ice and hull F_μ is assumed to relate to the normal force F_n as described by equation 4.1.

$$F_\mu = \mu \cdot F_n \tag{4.1}$$

When F_V is large enough to induce a moment that causes stresses σ_i larger than the flexural strength σ_f, the ice breaks off from the intact ice. The reader should know that this only describes the first stage of interaction with ice, as the ship continue to navigate in ice, the ice floes will continue to induce stresses to the hull until the floes have passed the ship. This master thesis will only consider the first ship-ice interaction in the analysis.

4.1.2 Relevant Input Parameters

The governing parameters for description of ice induced loads are the ice thickness h_i and the flexural strength σ_f. As the ship is beaching upon the ice, a vertical force component F_V will be induced to the hull. When the bearing capacity F_B of the ice is reached, the ice breaks. The bearing capacity is described by equation 4.2:

$$F_B = C_{geo} \cdot \sigma_f \cdot h_i^2 \text{ [N]} \tag{4.2}$$

where C_{geo} is a coefficient depending on the geometry of the horizontal boundary of the ice floe. C_{geo} is normally suggested in the range 0.25 to 1 [-] (Riska, 2011). σ_f is the flexural strength described by equation 2.27 and h_i is ice thickness. Equation 4.2 is based on the assumption of static behaviour.

4.1.3 Load Patch Area

When ice break or crush locally, the surface in contact with the ship hull do not necessarily remain even. As this shape is difficult to predict, an idealization of the load patch is required. The simplification is presented in figure 4.3 and consists of three input parameters, respectively the ice contact height h_{ic}, the load length L and the contact pressure p_c.

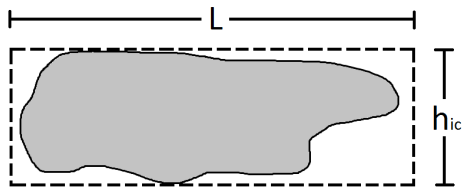

Figure 4.3: Simplification of interaction area between ice and structure.

Vertical extended frames will normally give a load length equal the frame spacing, while horizontal extended stiffeners give a load length equal the span. The load should be applied to give the largest possible response. Usually, the most critical locations are the centre of a plate field, and at the midspan of the stiffeners and frames.

Riska and Kämäräinen (2011) discuss the development of the contact height between hull and ice, presented by the Finnish-Swedish Ice Class Rules(FISCR). The reduction of height is presented in figure 4.4

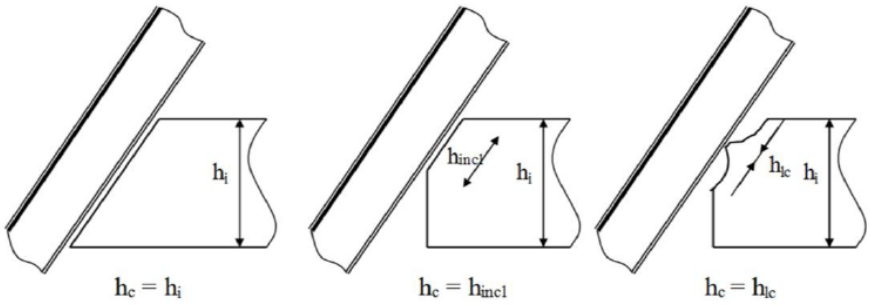

Figure 4.4: Ice height reduction due to development of regulations(Riska and Kämäräinen, 2011).

Figure 4.4 display different models of ice height during interaction with a structure. To the left, the total ice height defines the contact height. In the middle, the contact height is defined as only a part of the total height, hence the contact pressure will increase significantly. To the right, the contact height is defined as a narrow tip, creating an almost line load like interaction. These models are developed based on assumptions of different ice failure patterns during interaction. The left and middle figure, are based on crushing as given in figure 4.1b. The right figure is based on spalling, as illustrated in figure 4.1a.

4.1.4 Contact Pressure

The pressure over the load patch is assumed to be uniformly distributed. For simplicity one could consider static loads in an initial design phase, due to a short impact duration. This is only a simplification, and not necessarily the case during interaction with ice. Assuming a constant pressure p_c over an area A, one obtains the following equation for the normal force:

$$F_n = A \cdot p_c \text{ [N]} \tag{4.3}$$

If the ice is assumed to fail in bending, and the maximum flexural strength is the governing ice strength, one obtain the following set of equations. Where the flexural strength is given as:

$$\sigma_f(\eta_b) = 1.76 \cdot \left(e^{-5.88 \cdot \sqrt{\eta_b}}\right) \text{ [MPa]} \tag{4.4}$$

By introducing equation 4.2, and the fact that the vertical force F_V equals the bearing force F_B one obtains:

$$F_V = C_{geo} \cdot 1.76 \cdot \left(e^{-5.88 \cdot \sqrt{\eta_b}}\right) \cdot h_i^2 \text{ [N]} \tag{4.5}$$

By simple geometry, the vertical force on the hull could be expressed by the normal force as given in equation 4.6.

$$F_V = F_n \left(\sin(\beta) - \mu \cdot \cos(\beta)\right) \text{ [N]} \tag{4.6}$$

Simple calculations give equation 4.7 for the pressure applying over an area when inserting 4.6 into 4.3 and dividing by the area.

$$p_c = \frac{F_n}{A} = \frac{C_{geo} \cdot 1.76 \left(\cdot e^{-5.88 \cdot \sqrt{\eta_b}}\right) \cdot h_i^2}{A \cdot \left(\sin(\beta) - \mu \cdot \cos(\beta)\right)} \text{ [MPa]} \tag{4.7}$$

where the contact area is given as:

$$A = h_{ic} \cdot L \text{ [m}^2\text{]} \tag{4.8}$$

The contact pressure p_c depends on the brine porosity η_n, the ice thickness h_i, the contact area $A(h_{ic}, L)$, the hull slope β, the coefficient depending on the horizontal boundary geometry C_{geo} and the friction μ between ice and hull.

Chapter 5

Review of Ship Classification

In the design phase of a polar ship, several parameters should be considered. The environmental parameters and the operational limits are important for classification of polar operating ships. DNV GL and IACS provide regulations for vessels operating in ice-infested waters and the Arctic area. These regulations are given as a guideline for design of ships. The classes are normally divided into the duration of operation in ice infested waters, and the impact conditions regarding ice interactions, feature type and age. While some classes are limited to assisted operations only.

This chapter will give a review of different ice classes for ships. DNV GL - *Ships for Navigation in Ice* (Veritas, 2016), and IACS - *Unified Requirements for Polar Ships* (IACS, 2016), are presented and also compared in the following sections.

5.1 Classification of Ships Navigating in Ice - DNV GL

This section presents a brief review of the different ice classes provided by DNV GL. The local design loads and contact area will be presented for the class *Icebreaker* POLAR-10, as KV Svalbard is classified with this class. A short review regarding plate and stiffener requirements will also be presented.

5.1.1 Review of Ice Classes

DNV GL provides several classes for ice going ships, regarding the degree of exposure to ice and area of operation. For light ice conditions the classes ICE-C and ICE-E apply. These two classes are the lowest ice classes provided by DNV GL, hence intended to describe basic ice strengthening. Further, DNV GL presents

SEALERS which regard vessels built for catching in cold regions. The WINTERIZATION class applies to ships designed for service in cold climate environment. The DAT(-X°C) class provides regulations for materials in ships where the intention is to operate in cold regions with low air temperatures for a long period in time. Finally, the two main groups of ice classes are divided into Baltic and Arctic area of operation.

Classification for Baltic Areas

Classification for Baltic areas applies to vessels operating in the northern Baltic and areas of similar conditions. The Baltic ice strengthening classes consist of four notations, where the classes are equivalent to FSICR classes. The amount of ice, from light to difficult ice condition, and the assistance from icebreakers determine the notation. The notations are presented in table 5.1.

Table 5.1: Northern Baltic ice classes presented in relation to FSICR classes, and the amount of ice and assistance they depend on.

DNV GL	FSICR	h_{ice}	Assistance
ICE-1A*	1A Super	1 (Difficult)	No
ICE-1A	1A	0.8 (Difficult)	Yes
ICE-1B	1B	0.6 (Moderate)	Yes
ICE-1C	1C	0.4 (Light)	Yes

From table 5.1 one could observe that the difference in the two highest notations are the required assistance and ice thickness.

Classification for Polar Areas

Classification for Polar areas applies to vessels operating unassisted in sub-Arctic, Arctic and Antarctic areas. Each class is designed to encounter a particular condition of ice, regarding thickness and strength of the ice cover. Depending on whether the vessel is intended to encounter pressure ridges or other features of remarkable larger thickness than average, the vessel is either denoted POLAR-XX or ICE-XX, where XX corresponds to the average ice thickness. Regarding ramming, the ICE class is limited to no ramming, while the POLAR class is assumed to endure occasional ramming. The notation *Icebreaker* is assigned to vessels that could take several attempts of ramming to break the ice. The different notations and assigned ice properties are presented in table 5.2.

Table 5.2: Arctic ice classes, ice properties and ramming conditions.

Ice Class	σ_{ice} [MPa][a]	h_{ice} [m][b]	Ramming condition*
ICE-05	4.2	0.5	Not anticipated
ICE-10	5.6	1	Not anticipated
ICE-15	7.0	1.5	Not anticipated
POLAR-10	7.0	1.0	Occasional(2.0)
POLAR-20	8.5	2.0	Occasional(3.0)
POLAR-30	10.0	3.0	Occasional(4.0)
Icebreaker	As POLAR	As POLAR	Repeated

[a] The nominal ice strength. [b] The ice thickness.
* The values in parenthesis denotes the minimum ramming speed, V_{RAM}, in [m/s]. For notation *Icebreaker* the minimum ramming speed is 2.0 [m/s], hence not less than 1.5 times the POLAR-class speed if POLAR-class is specified.

5.1.2 Design Loads

KV Svalbard is assigned the notation *Icebreaker* POLAR-10. The following section will hence give priority to the notation *Icebreaker* POLAR-10 and the associated design loads. To limit the scope, only local loads applied to the bow region will be further discussed. However, it is important to note there exist several other important loads that apply to vessels in ice-infested waters.

Local ice pressures are an important consideration during design. DNV GL states that all classified vessels shall withstand local ice pressure applied in the reinforced areas. The local design ice pressure is defined in equation 5.1:

$$p = F_B \cdot p_0 \text{ [kPa]} \tag{5.1}$$

where F_B is a correction factor for the design contact area, and p_0 is the basic ice pressure given by equation 5.2

$$p_0 = 1000 \cdot F_A \cdot \sigma_{ice} \text{ [kPa]} \tag{5.2}$$

Where σ_{ice} is the nominal ice strength from table 5.2 and the factor of 1000 converts equation 5.2 from [MPa] to [kPa]. A correction factor for the reinforced area is introduced by the coefficient F_A. This factor equals 1 in the stem and bow area. Regarding other locations, this coefficient varies between 0.2 to 0.8. F_B from equation 5.1 is given as:

$$
\begin{aligned}
F_B &= \frac{0.58}{A_c^{0.5}} \text{ for } A_c \leq 1.0m^2 \text{ [-]} \\
&= \frac{0.58}{A_c^{0.15}} \text{ for } A_c > 1.0m^2 \text{ [-]}
\end{aligned}
\tag{5.3}
$$

where $A_c = h \cdot w$ is the contact area, as given by figure 5.1. Where h is the effective height of the contact area, taken as $0.4h_{ice}$, for other regions h varies between 0.4 and 0.8 of h_{ice}. w is the critical width of the contact area. w is taken as the length corresponding to the longitudinal stiffener length.

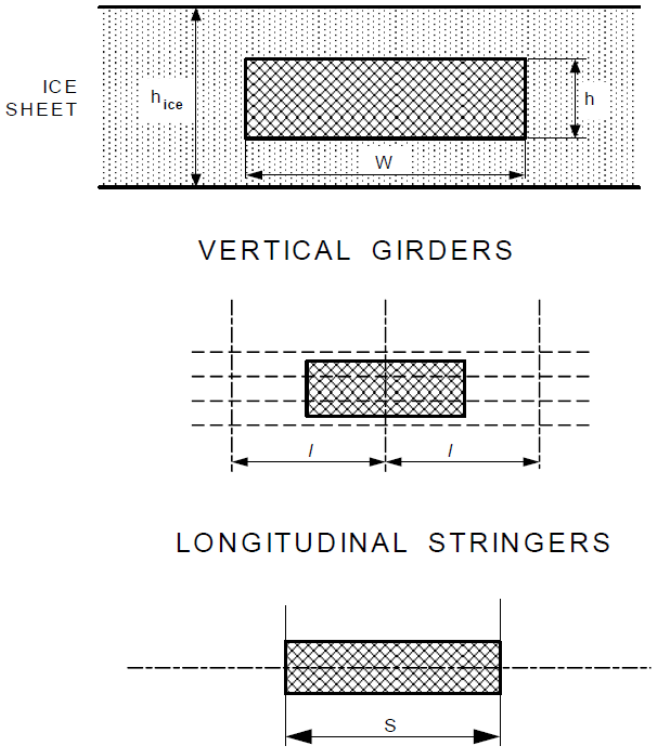

Figure 5.1: Design contact area provided by DNV GL, applied for local ice pressures.

5.1.3 Local Dimensioning

The minimum requirements to local members and plating are essential in a design phase. DNV GL presents requirements for plate thickness, longitudinal stiffeners, other stiffeners and girders. The local model will only consist of plating and longitudinal stiffeners, hence dimensioning of girders and other stiffeners will be not be further assessed. The requirements in this section apply to members and plating directly exposed to ice pressure.

The thickness of the plating t exposed to ice loads should not be less than expressed in equation 5.4:

$$t = 23 \cdot k_a \cdot \frac{s^{0.75}}{h_0^{0.25}} \sqrt{\frac{k_w p_0}{m_p \sigma_{ice}}} + t_k \text{ [mm]} \tag{5.4}$$

k_a describes the aspect ratio for the plate field, and is in the range of 1-0.85 depending on the ratio between the stiffener spacing and length. k_w is the influence factor correcting for narrow loads perpendicular to the stiffener spacing with a maximum value of 1. h_0 is equal the stiffener spacing s, i.e. 0.4 [m]. p_0 and σ_{ice} are respectively the basic ice pressure and ice strength applied in equation 5.1 and 5.2. m_p is the bending moment factor as a function of the ice thickness and stiffener spacing, with a value typically between 27.4 and 2.68. t_k is a corrosion addition.

The longitudinal stiffeners are defined longitudinal if they are aligned parallel to the water line. The web sectional modulus should not be less than given by equation 5.5.

$$Z = \frac{41 \cdot h_o^{1-\alpha} \cdot l^{2-\alpha} \cdot p_0 \cdot w_k}{\sigma \sin(\beta)} \text{ [mm}^3\text{]} \tag{5.5}$$

h_0 equals the stiffener spacing or the contact area height, whichever is the smallest value, and l defines the span of the longitudinal stiffeners. The factor α depends on the contact area A_C, for A_C less than 1 [m^2], α is 0.5 and for A_C larger than 1 [m^2], α is 0.15. w_k is a section modulus corrosion factor, and σ equals $0.9\sigma_{ice}$ of the ice strength previously defined in table 5.2. While β equals the angle of the web with shell plating as defined by equation 5.6.

$$\beta = \arctan\left(\frac{\tan(\gamma)}{\sin(\theta)}\right) \tag{5.6}$$

Both γ and θ are defined in figure 5.2.

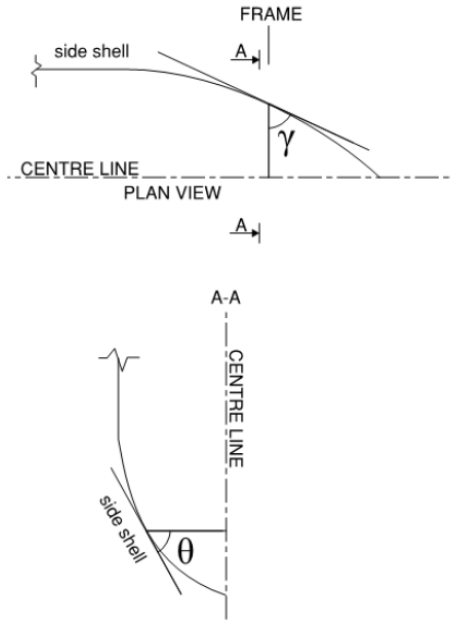

Figure 5.2: Definition of the web angles γ and θ, to obtain β, with shell plating presented by DNV GL.

5.2 Classification of Ships Navigating in Ice - IACS

In this section, a brief review of the ice classes provided by IACS will be presented. The class most similar to *Icebreaker* POLAR-10, PC-1, will be further assessed considering local design loads and contact area. A short review regarding plate and stiffener requirements will also be presented.

5.2.1 Review of Ice Classes

IACS defines the different polar classes into seven classes, where the ice condition is defined by WMO (1970). The classes are intended to divide vessels into different operational capabilities and strengths. Table 5.3 presents the classes and the description regarding operational limits, using WMO ice nomenclature.

Table 5.3: Polar classes as presented by IACS, described by WMO nomenclature.

Class	Ice description
PC 1	Year-round operation in all polar waters
PC 2	Year-round operation in moderate multi-year ice conditions
PC 3	Year-round operations in second-year ice which may include multi-year ice inclusions
PC 4	Year-round operations in thick first-year ice which may include old ice inclusions
PC 5	Year-round operations in medium first-year ice which may include old ice inclusions
PC 6	Summer/autumn operation in medium first-year ice which may include old ice inclusions
PC 7	Summer/autumn operation in thin first-year ice which may include old ice inclusions

5.2.2 Design Loads

The design scenario for determination of the design loads is ice-hull impact in the bow region. In this model, the design load is given as an average pressure $P_{avg,bow}$ uniformly distributed over a rectangular area of height b_{bow} and width w_{bow}. These parameters are denoted the load parameters, hence they are determined by the bow shape. Further assessment requires ice load characteristics for the bow area. The shape coefficient fa_{bow}, the total impact force F_{bow}, line load Q_{bow} and pressure P_{bow} are hence required. Further assessment will consider the bow region only.

For the bow region, the dimensions for the load patch could be obtained by the following equations (5.7 and 5.8) by applying equation 5.12, 5.13 and 5.14:

$$w_{bow} = \frac{F_{bow}}{Q_{bow}} \text{ [m]} \tag{5.7}$$

$$b_{bow} = \frac{Q_{bow}}{P_{bow}} \text{ [m]} \tag{5.8}$$

and the average pressure $P_{avg,bow}$ is obtained by:

$$P_{avg,bow} = \frac{F_{bow}}{w_{bow} \cdot b_{bow}} \text{ [MPa]} \tag{5.9}$$

The shape coefficient fa_{bow} is to be taken as the minimum of equation 5.10:

$$fa_{bow} = \min(fa_{bow,1}, fa_{bow,2}, fa_{bow,3}) \text{ [-]} \tag{5.10}$$

where the three functions are given by equation 5.11:

$$\begin{aligned} fa_{bow,1} &= \left(0.097 - 0.68 \cdot \left(\frac{x}{L_{wl}} - 0.15\right)^2\right) \cdot \frac{\alpha_{bow}}{(\beta'_{bow})^{0.5}} \text{ [-]} \\ fa_{bow,2} &= 1.2 \cdot CF_F \cdot \frac{1}{\left(\sin(\beta'_{bow}) \cdot CF_C \cdot D^{0.64}\right)} \text{ [-]} \\ fa_{bow,3} &= 0.60 \text{ [-]} \end{aligned} \tag{5.11}$$

where L_{wl} is defined as the water line length measured at the upper ice water line and x is the distance from the forward perpendicular to the impact area. D is defined as the ship displacement in [kt] and should not be taken less than 5 [kt]. While CF_C is defined as crushing failure class factor equal 17.69 for PC-1. CF_F is defined as flexural failure class factor equal 68.60 and CF_D is defined as load patch dimension class factor equal 2.01 for PC-1. The total force F_{bow} is given by equation 5.12:

$$F_{bow} = fa_{bow} \cdot CF_C \cdot D^{0.64} \text{ [MN]} \tag{5.12}$$

The line load Q_{bow} is given by equation 5.13:

$$Q_{bow} = F_{bow}^{0.61} \cdot \frac{CF_D}{AR_{bow}^{0.35}} \text{ [MN/m]} \tag{5.13}$$

The pressure P_{bow} is given by equation 5.14:

$$P_{bow} = F_{bow}^{0.22} \cdot CF_D^2 \cdot AR_{bow}^{0.3} \text{ [MPa]} \tag{5.14}$$

In equation 5.13 and 5.14 a load patch aspect ratio AR_{bow} is introduced. This aspect ratio is defined as:

$$AR_{bow} = 7.46 \cdot \sin(\beta'_{bow}) \geq 1.3 \text{ [-]} \tag{5.15}$$

Where β'_{bow} is given as:

$$\beta'_{bow} = \arctan\left(\frac{\sin(\alpha_{bow})}{\tan(\gamma_{bow})}\right) \tag{5.16}$$

Both β'_{bow}, α_{bow} and γ_{bow} are defined by figure 5.3.

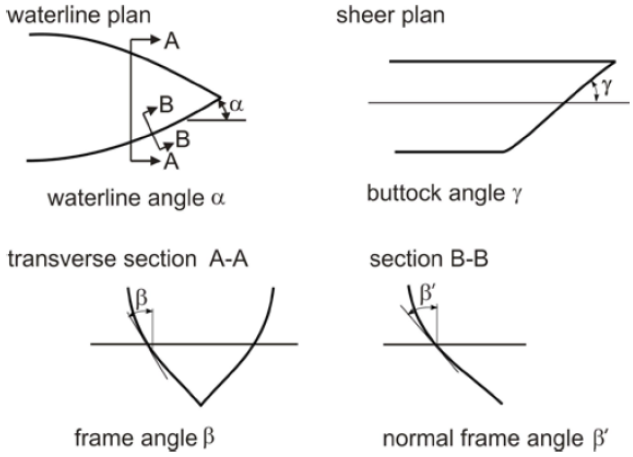

Figure 5.3: Hull angles provided by IACS.

5.2.3 Local Dimensioning

Consideration of local loads requires local dimensioning to withstand applied loads. IACS provides a minimum required plate thickness as a function of frame orientation, transverse and longitudinal local frames, web frames and load-carrying stringers. For continuous members, the boundary conditions are assumed fixed. For other members, the boundaries are assumed simply supported unless the boundaries could be proven to provide significantly rotational restraints. The requirements apply to members and plating directly exposed to ice pressure. Only plating and longitudinal stiffeners will be further assessed.

The thickness t of plating exposed to ice loads should not be taken less than given by equation 5.17:

$$t = t_{net} + t_s \text{ [mm]} \tag{5.17}$$

where t_s is the corrosion addition and t_{net} is the plate thickness required to withstand ice loads. The plate thickness t_{net} depends on the orientation of the supporting stiffeners. For longitudinally supported plating, where the stiffeners are

aligned less than 20 degrees normal to the waterline, the net thickness is given by equation 5.18:

$$t_{net} = 500 \cdot s \cdot \frac{((AF \cdot PPF_p \cdot P_{avg,bow})/\sigma_y)^{0.5}}{(1 + s/(2 \cdot l))} \text{ [mm]} \tag{5.18}$$

where s is the stiffener spacing and l is the length. AF is an area factor equal 1 for the bow area of the PC 1 icebreaker notation. PPF_p is a peak pressure factor depending on the stiffener spacing and not to be taken less than 1.5 for longitudinal stiffened plating. σ_y is the minimum upper yield stress of the applied steel. If the stiffener spacing is larger than the load patch height ($b \leq s$), equation 5.18 will have an additional correction term added, to correct for larger spacing. The additional correction term is added in equation 5.19.

$$t_{net} = 500 \cdot s \cdot \frac{((AF \cdot PPF_p \cdot P_{avg,bow})/\sigma_y)^{0.5} \cdot (2b/s - (b/s)^2)^{0.5}}{(1 + s/(2 \cdot l))} \text{ [mm]} \tag{5.19}$$

The plastic sectional modulus of the longitudinal stiffeners should not be taken less than equation 5.20:

$$Z_p = A_{pn} \cdot \frac{t_{pn}}{20} \cdot \frac{h_w^2 \cdot t_{wn} \cdot \sin(\varphi_w)}{2000} + \frac{A_{fn} \cdot (h_{fc} \cdot \sin(\varphi_w) - b_w \cdot \cos(\varphi_w))}{10} \text{ [mm}^3\text{]} \tag{5.20}$$

where A_{pn} is the net cross section area of the local stiffener, A_{fn} is the net cross section area of the stiffener flange, t_{pn} is the net plate thickness equal to t_{net}. t_{wn} is the net web thickness equal to t_w without corrosion addition. The remaining parameters are illustrated in figure 5.4

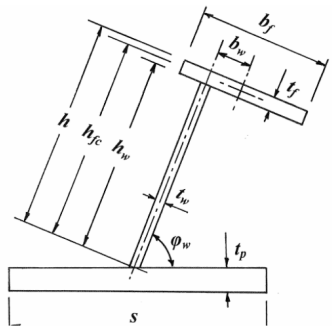

Figure 5.4: Stiffener dimensions provided by IACS, apply to both longitudinal and transverse stiffeners.

5.3 Similarities and Differences in Classification of Ships

The previous sections have presented the main content of the classification rules provided by DNV GL and IACS. The priority was given to the classes *Icebreaker* POLAR-10 and PC-1. DNV GL divides the classes with respect to the area of operation, considering Baltic and Polar areas. The classes are given different notation regarding the ice thickness and ramming condition they are exposed to. While IACS defines their classes with respect to the operational time and expected ice age. Hence, the strength requirements are based on ice condition regardless of area.

Regarding the design loads, DNV GL proposes that the load patch equals 0.4 of the ice thickness multiplied with the stiffener span. Also, correction factors for varying pressure over the load patch are included in the calculations. The calculations depend mostly on the geometry of the local part and the class notation of the vessel. While IACS proposes shape coefficients and class factors that apply to the loads, the loads are thus used to obtain the load patch dimensions and the total load patch pressure is obtained from the force divided by the load patch area. Another difference is the various load scenarios presented in the regulations. DNV GL provides several load scenarios, such as beaching, compression amidships and local pressure. IACS does only present bow impacts as a design scenario.

The local dimensioning does in both cases provide regulations for the plate thickness. The thickness consists of two terms where one is the net thickness, and the second is a corrosion addition. The first term does differ in the two standards, as DNV GL includes aspect ratio and an influence factor, while IACS provides area factors and pressure peak factors. IACS also accounts for the different ratios between stiffener spacing and load height through several formulas for the net thickness. For the sectional modulus, DNV GL provides the regular sectional modulus, while IACS presents the plastic sectional modulus. The plastic sectional modulus does apply to models where plastic deformations are allowed. Holm (2012) provides a numerical comparison of the regulations provided by DNV GL and IACS in his master thesis. He found that IACS classes are dependent on the ship displacement, while DNV GL classes are independent. Additionally, he found the plate thickness and design load to be generally higher for IACS class PC-1, compared to DNV GL class *Icebreaker* POLAR-10.

Chapter 6

Finite Element Theory

During interaction with ice, the local deformations and displacements could be large. The boundaries could also change during interaction, i.e. when two structural parts come in contact during displacement. When large displacement is induced, the geometry would likely change during the process. Hence, the assumption of small displacements and linear elastic behaviour are no longer valid. To account for the large displacement, change of geometry and boundaries, a non-linear model could be applied. This chapter presents the non-linear model.

6.1 Non-linear Finite Element Method

This section presents the difference between linear and non-linear behaviour and the fundamental theory of non-linear finite element method. The linear analysis and the fundamental assumptions are shortly presented prior to presentation of the non-linear behaviour. The theory in section 6.1.1 is referring to Leira (2011) while section 6.1.2 refers to Moan (2003).

6.1.1 Linear Analysis

In the linear model, the assumption of small displacements and linear-elastic material behaviour are valid. The linear model could be described by equilibrium between forces, where the model remain at rest with no acceleration. Hence, the sum of forces equals zero. These forces induce stresses, which in turn are related to the strains trough Hooke's law(equation 6.1).

$$\begin{aligned}
\varepsilon_x &= \frac{1}{E}\left(\sigma_x - \nu\sigma_y - \nu\sigma_z\right) \\
\varepsilon_y &= \frac{1}{E}\left(\sigma_y - \nu\sigma_x - \nu\sigma_z\right) \\
\varepsilon_z &= \frac{1}{E}\left(\sigma_z - \nu\sigma_x - \nu\sigma_y\right)
\end{aligned} \tag{6.1}$$

where ν describes the Poisson ratio. The strains are derivatives of the displacements in x-, y- and z-direction, respectively described by equation 6.2.

$$\begin{aligned}
\varepsilon_x &= \frac{\partial u}{\partial x} \\
\varepsilon_y &= \frac{\partial v}{\partial y} \\
\varepsilon_z &= \frac{\partial w}{\partial z}
\end{aligned} \tag{6.2}$$

where u, v and z describe the displacements in the respective direction. The angular deformations γ_{ij} are related to the following displacements, where the subscripts ij denote the plane where the deformations occur(x, y or z), given in equation 6.3.

$$\begin{aligned}
\gamma_{xy} = \gamma_{yx} &= \frac{\partial u}{\partial y} + \frac{\partial v}{\partial x} \\
\gamma_{xz} = \gamma_{zx} &= \frac{\partial u}{\partial z} + \frac{\partial w}{\partial x} \\
\gamma_{yz} = \gamma_{zy} &= \frac{\partial v}{\partial z} + \frac{\partial w}{\partial y}
\end{aligned} \tag{6.3}$$

which in turn are related to the shear strains ε_{ij} and shear forces τ_{ij} trough equation 6.4.

$$\begin{aligned}
\gamma_{xy} = 2\varepsilon_{xy} &= \frac{2(1+\nu)}{E}\tau_{xy} \\
\gamma_{xz} = 2\varepsilon_{xz} &= \frac{2(1+\nu)}{E}\tau_{xz} \\
\gamma_{yz} = 2\varepsilon_{yz} &= \frac{2(1+\nu)}{E}\tau_{yz}
\end{aligned} \tag{6.4}$$

Further it is assumed that the stresses induced by the forces, are below yield. When stresses above yield occur, the elastic theory should be corrected. The linear elastic

model is described by the following relation between stresses and strains, given by figure 6.1.

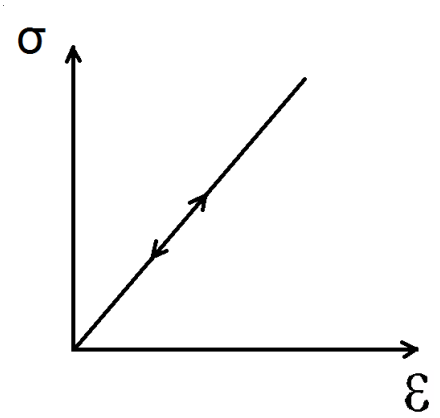

Figure 6.1: The linear elastic material model, described by a linear relation between stress σ and strain ε.

To solve the linear finite element problem, the relation between system stiffness $\boldsymbol{K}$, the displacement vector $\boldsymbol{r}$ and the load vector $\boldsymbol{R}$ are established and solved. The relation is given by equation 6.5.

$$\boldsymbol{K}\boldsymbol{r} = \boldsymbol{R} \tag{6.5}$$

which yields the inverted solution:

$$\boldsymbol{r} = \boldsymbol{K}^{-1}\boldsymbol{R} \tag{6.6}$$

By application of this theory, linear problems could be solved under the assumption of equilibrium in internal forces and stresses, compatibility between displacements and strains, and the relation between stress and strain described by Hooke's law. This is not necessarily always applicable regarding larger deformations and non-linear material behaviour, hence non-linear analysis should be applied.

6.1.2 Non-Linear Analysis

The non-linear model requires adjustment of the theory that apply to the linear model. In non-linear problems, the displacement is usually large and not linear related to the load. Often, the displacements are large, and when the loads are removed, the final state is different from the initial geometry. The material properties are non-linear, and the relation between stress and strain is a function of stress, strain and/or time. Compared to the linear model, these impacts are difficult to compute and require methods applying iterations to obtain a final result.

A model may be loaded so that the relation between stress and strain no longer applies to a linear model. The stresses may reach a level inducing a non-linear condition, thus unloading from such a condition appears to follow the initial stress-strain relationship(Described by Hooke's law). The effect is illustrated in figure 6.2.

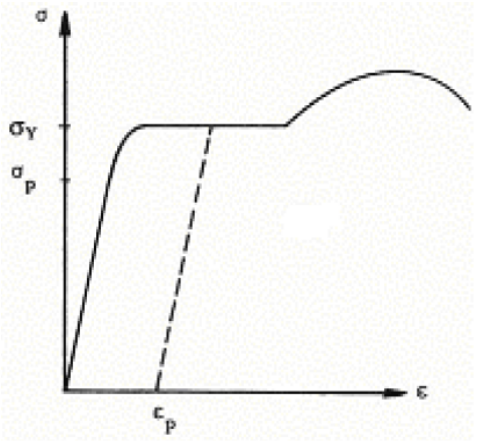

Figure 6.2: The non-linear stress-strain relation. σ_p denotes the limit for linear relationship, σ_Y denotes the yield stress and the dotted line describes the unloading process applying linear theory(Moan, 2003).

The model will not return to its initial state post loading, as yielding occurs. According to this theory, one needs more than linear formulations to describe the stress relation to strains. Yielding may induce larger displacements and deformations to the model. As the assumption of small displacements does not apply, and the fact that geometry may change during deformation, the stiffness relation will depend on the displacement. This leads to the following relation between loads, displacements and model stiffness.

$$\boldsymbol{K}(\boldsymbol{r})\boldsymbol{r} = \boldsymbol{R} \tag{6.7}$$

Equation 6.7 could be solved analytically for a certain load. Thus it is more common to apply iterative methods to solve the problem. By rewriting equation 6.7 to differential form, one obtains:

$$\frac{d}{d\boldsymbol{r}}(\boldsymbol{K}(\boldsymbol{r})\boldsymbol{r})d\boldsymbol{r} = \boldsymbol{K}_I(\boldsymbol{r})d\boldsymbol{r} = d\boldsymbol{R} \tag{6.8}$$

where $\boldsymbol{K}_I(\boldsymbol{r})$ denotes the incremental stiffness, which include both the initial stiffness $\boldsymbol{K}_0$ as well as the geometrical stiffness $\boldsymbol{K}_G$. Resulting in equation 6.9.

$$\boldsymbol{K}_I = \boldsymbol{K}_0 + \boldsymbol{K}_G \tag{6.9}$$

Equation 6.8 could be solved by incremental methods. Abaqus and Moan (2003) present the modified Euler-Cauchy method. This method applies an update of the n^{th} step where the total load $\boldsymbol{R}_n$ and the displacement $\boldsymbol{r}_n$ occur. This introduce a residual force vector $\boldsymbol{R}_r$ which is the difference between the internal force vector $\boldsymbol{R}_{int}(\boldsymbol{r}_n)$ and the total load vector for the n^{th} step. This gives the following equation:

$$\boldsymbol{R}_r = \boldsymbol{R}_{int}(\boldsymbol{r}_n) - \boldsymbol{R}_n \tag{6.10}$$

By adding the residual force vector to the next load increment, the residual forces are accounted for. This reduces the external loads and global equilibrium is obtained. The method is described by the following equations:

$$\boldsymbol{\Delta R}_{n+1} = \boldsymbol{R}_{n+1} - \boldsymbol{R}_n \tag{6.11}$$

$$\boldsymbol{R}_{eq} = \boldsymbol{R}_n - \boldsymbol{R}_{int}(\boldsymbol{r}_n) \tag{6.12}$$

By applying equation 6.10, 6.11 and 6.12 one obtains equation 6.13:

$$\begin{aligned} \boldsymbol{\Delta r}_{n+1} &= \boldsymbol{K}_I(\boldsymbol{r}_n)^{-1}\boldsymbol{\Delta R}_{n+1} - \boldsymbol{K}_I(\boldsymbol{r}_n)^{-1}(\boldsymbol{R}_{int}(\boldsymbol{r}_n) - \boldsymbol{R}_n) \\ &= \boldsymbol{K}_I(\boldsymbol{r}_n)^{-1}\left[\boldsymbol{\Delta R}_{n+1} + \boldsymbol{R}_{eq}\right] \\ &= \boldsymbol{K}_I(\boldsymbol{r}_n)^{-1}\left[\boldsymbol{\Delta R}_{n+1} - \boldsymbol{R}_r\right] \end{aligned} \tag{6.13}$$

$$\boldsymbol{r}_{n+1} = \boldsymbol{r}_n + \boldsymbol{\Delta r}_{n+1} \tag{6.14}$$

The method focus on obtaining $\boldsymbol{R}_{int}(\boldsymbol{r}_n)$. Compared to section 6.1.1, this is a more complex method of solving the problem. Each step in the non-linear analysis requires an update of the system stiffness vector, and hence solution of the system of equations. The computational time of such a step is almost equal the time of conducting a linear analysis.

Chapter 7

Results of Analysis Based on Level Ice Measurements and Regulations

To investigate the local ice loads' impact on local details of a ship hull, a FE model is established and assessed. The results in this chapter are based on theory and measurements presented in previous chapters. The local model will be analysed using Abaqus and dimensioned applying measures from DNV GL presented in chapter 5. DNV GL and IACS classification will be assessed with their respective ice pressures. Also, ice strength found by measurements in chapter 3 and the pressure model presented under section 4.1.4 will be applied.

7.1 Presentation of the Local Plate Model

In this section, the local plate model will be presented. During the calculations, it was necessary to do assumptions. The assumptions are hence made within reasonable limits trying to fit an actual local model of KV Svalbard.

7.1.1 Location of the Local Plate Model

The model is a section of the bow located as described by figure 7.1. It is located at the water line in the bow area. Half of the plate is above water level.

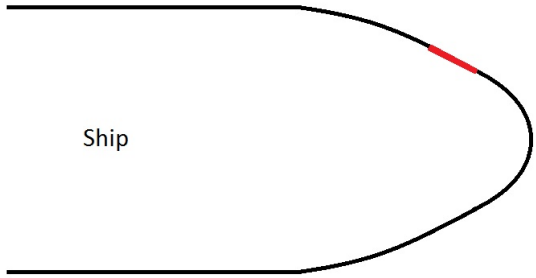

Figure 7.1: The location of the local plate field is marked as a thick red line in the bow region of the hull.

7.1.2 Dimensioning

The main dimensions of the plate field were arbitrarily set to a width of 2 [m] and a length of 2.5 [m]. The following dimensions, presented in table 7.1, were found through computations applying theory from section 5.1. The stiffener span was chosen arbitrarily to fit the width of the plate field, and the hull angles were set to 60° so that the web angle β ended at 63°. The hull angles are defined in figure 5.2 and the web angle is defined in equation 5.6.

Table 7.1: Dimensions of the local plate field found by applying DNV GL regulations.

Description	Parameter	Dimension
Arbitrarily chosen parameters		
Stiffener spacing	s	400 [mm]
Stiffener length	l	2500 [mm]
Calculated parameters		
Plate thickness	t	10.5 [mm]
Section modulus	Z_{min}	140600 [mm^3]

The section modulus Z_{min} do not describe the dimensions of the stiffeners. By application of the section modulus and basic calculations, the following dimensions for the stiffeners were obtained(Table 7.2).

Table 7.2: Dimensions of the local stiffeners.

Description	Parameter	Dimension
Web height	h_{web}	120 [mm]
Web thickness	t_{web}	10 [mm]
Flange height	t_{flange}	10 [mm]
Flange width	w_{flange}	120 [mm]
Section modulus	Z	161680 [mm^3]

From table 7.2, the section modulus was chosen to be slightly larger than the one recommended by DNV GL regulations.

7.1.3 The Model

By application of the dimensions presented in section 7.1.2, a model was established using Abaqus and S4R elements as discussed in appendix C. The model was assumed located close to the bow with boundaries consisting of longitudinal girders parallel to the stiffener span and transverse frames perpendicular oriented to the span. Figure 7.2 presents the actual model, without boundaries.

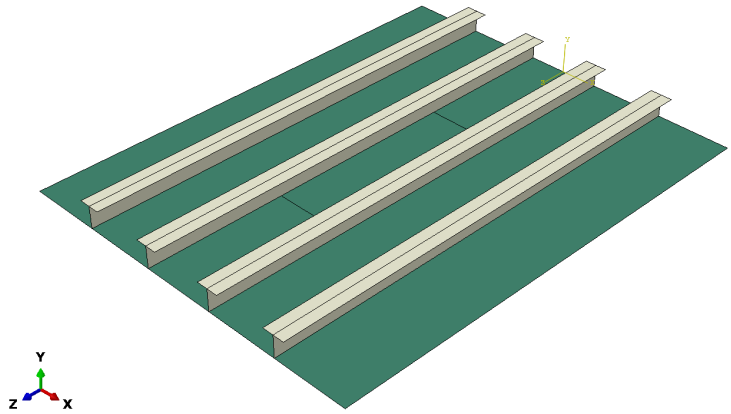

Figure 7.2: Local plate model obtained by DNV GL requirements. The green colour represents the plate, while the white sections represent the stiffeners.

Both plate and stiffeners are assigned the same material properties, given in table 7.3

Table 7.3: Material properties assigned to the model.

	Parameter	Dimension
Youngs Modulus	E	207000 [MPa]
Yield stress	σ_y	488 [MPa]
Poisson's ratio	υ	0.3 [-]
Density	ρ_s	$7.85 \cdot 10^{-6}$ [kg/mm^3]

The material model was assumed to behave non-linear, where the material model is important to ensure correct behaviour. The following table presents the plastic behaviour is applied in the analysis. The first value of table 7.4 defines the initial yield stress σ_y.

Table 7.4: The applied plastic strain model for steel.

Stress σ [MPa]	Plastic strain ε_p
488	0.0000
509	0.0020
520	0.0038
532	0.0065
545	0.0110
556	0.0163
567	0.0219
584	0.0358
597	0.0509
605	0.0682
611	0.0901

The plate was assessed with fixed boundary conditions. As the surrounding girders were assumed to provide sufficient stiffness, the edges of the plate were assumed to neither deflect nor rotate. This is an essential assumption as it impacts the results regarding plate behaviour.

During loading of the model, the pressure was applied directly to the plate in between the stiffeners. Under this type of loading, the assessment of the plate is in focus. As the ice could take many arbitrary shapes during breaking and crushing, the plate is most likely to have large load concentrations. Regarding this, and the small plate thickness, the pressure is applied to the plate to assess the most critical part of this local model. The reader should therefore be aware of the focus on the plate behaviour. Hence, the stiffeners are not put into focus in the same manner. For further stiffener assessment, see appendix E.

7.2 Assessment of Ice Pressure

Previously presented are three possible models for local ice pressure: The measurements presented under chapter 3 with the contact pressure model presented under section 4.1.4, DNV GL and IACS.

The DNV GL regulations provide the contact pressure for an arbitrary contact area A_c. From the regulations, F_A equals 1 [-], and σ_{ice} equals 7 [MPa], so that the contact pressure resulted in the following equation:

$$p_c = F_B \cdot 7000 \text{ [kPa]} \tag{7.1}$$

where F_B depends on the size of the contact area, and for a contact area below 1 [m^2] this factor became the following:

$$F_B = \frac{0.58}{\sqrt{A_c}} = 0.917 \text{ [-]} \tag{7.2}$$

which results in a contact pressure of 6.419 [MPa] as the contact area was set to 0.4 [m^2].

The IACS regulations had a somewhat different approach to obtain the contact pressure. The shape coefficient $f_{a,bow}$ was taken as a minimum of three equations (see equation 5.11) and found equal 0.6 [-]. The total force F_{bow} was found by applying the shape coefficient with the crushing failure class factor CF_C, for PC 1 equal 17.69, and the ship displacement D in [kt] equal 6.375. This gave the following equation:

$$F_{bow} = fa_{bow} \cdot CF_C \cdot D^{0.64} = 0.6 \cdot 17.69 \cdot 6.375^{0.64} = 34.7 \text{ [MN]} \tag{7.3}$$

Applying the flexural failure class factor CF_D equal 2.01 and a load patch aspect ratio AR_{bow} equal 6.65, one obtain both the line load Q_{bow} and the pressure P_{bow} given in the following equations:

$$Q_{bow} = F_{bow}^{0.61} \cdot \frac{CF_D}{AR_{bow}^{0.35}} = 34.7^{0.61} \cdot \frac{2.01}{6.65^{0.35}} = 9.012 \text{ [MN/m]} \tag{7.4}$$

$$P_{bow} = F_{bow}^{0.22} \cdot CF_D^2 \cdot AR_{bow}^{0.3} = 34.7^{0.22} \cdot 2.01^2 \cdot 6.65^{0.3} = 15.56 \text{ [MPa]} \tag{7.5}$$

Applying equation 7.3, 7.4 and 7.5, the average pressure $p_{avg,bow}$ was given by the following equation:

$$P_{avg,bow} = \frac{F_{bow}}{w_{bow} \cdot b_{bow}} = \frac{F_{bow}}{\frac{F_{bow}}{Q_{bow}} \cdot \frac{Q_{bow}}{P_{bow}}} = \frac{34.7}{3.85 \cdot 0.58} = 15.56 \text{ [MPa]} \tag{7.6}$$

under the assumption that the contact area was kept constant regardless of the applied regulation. This means that the average pressure $P_{avg,bow}$ was applied to a contact area of 0.4 [m^2] and resulted in a lower resultant force impacting the plate, as IACS suggested a larger contact area equal 2.233 [m^2].

Applying the following equation (eq. 7.7) for the empirical contact pressure $p_{c,emp}$:

$$p_{c,emp} = \frac{F_n}{A_c} = \frac{C_{geo} \cdot 1.76 \left(\cdot e^{-5.88 \cdot \sqrt{\eta_b}} \right) \cdot h_i^2}{A_c \cdot \left(\sin(\beta) - \mu \cdot \cos(\beta) \right)} \text{ [MPa]} \tag{7.7}$$

and the average flexural strength $\overline{\sigma_f}$ from the level ice measurements presented in section 3.1.3, the empirical contact pressure $p_{c,emp}$ was obtained. This was performed by keeping the hull angle β, and contact area A_c constant, as well as the ice boundary geometry C_{geo}. Respectively, they were kept at 63°, 0.4 [m^2] and 1 [-]. The empirical pressure $p_{c,emp}$ applies to an area of 0.4 [m^2] and an ice thickness of 1 [m] as initially assumed when conducting the modelling presented by DNV GL. The contact pressure model depends on the ice height so that $p_c \propto h_i^2$. The values applied and the resulting empirical ice contact pressure are given in table 7.5.

Table 7.5: Results from sea ice measurements and application of empirical formula given in equation 7.7, applying flexural strength data from table 3.3.

$\overline{\sigma_f}$ [MPa]	-	0.499
h_i [m]	-	1
β [°]	-	63
A_c [m^2]	-	0.4
μ	-	0.1
$p_{c,emp}$ [MPa]	-	1.475

Where the friction coefficient μ is suggested to equal 0.1 by Riska (2011).

7.3 Model Response Analysis

This section presents the results from the analysis of the previously presented model. The three different pressures will be assessed. These tests are conducted to investigate difference in response and also whether the model is sufficiently dimensioned regarding the applied loads. The magnitude of stresses and the displacement will be considered to compare the pressures and also whether the dimensioning is sufficient.

The loading was assumed static, with a uniform pressure applied at the centre of the model, where the contact area was located in between two stiffeners. It is important to note the simplification of actual conditions, as the loading vary

temporally and spatially. Considering large variation in ice thickness and strength, contact area, ramming speed and fracture model, this model is regarded a simplification. The principle of a short interaction with ice is still covered as it is reasonable to believe that such a condition could occur during operations.

Figure 7.3 presents the load patch where the contact pressure is applied.

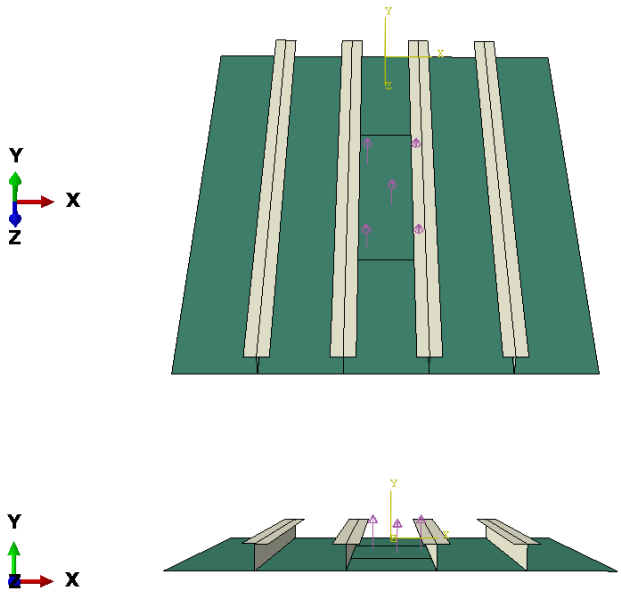

Figure 7.3: The load patch, located at the centre of the model, in between two stiffeners. The coordinate system is presented to the left in both figures, and presents the angle of view.

7.3.1 Assessment of Pressure Models

This section presents the results from assessment of the three different pressures, which were obtained from measurements of sea ice and assessment of ice classification rules. In order to ensure convergence of the results, all models are subjected to a mesh refinement. During these analysis, the boundary conditions are assumed fixed.

The model is assessed with the following three pressures as presented by table 7.6.

Table 7.6: The applied ice pressures obtained from measurements of ice, DNV GL and IACS.

Empirical [MPa]	DNV GL [MPa]	IACS [MPa]
1.475	6.419	15.56

As the model was assessed assuming non-linearities, the system is updated for each load increment. Where the load increment is described by an initial load and a proportionality factor, adding load increments to obtain a stable solution for each step. The first step in the analysis is an unloaded model. Further steps apply load incrementally until the sum of the increments equals 1, and the total load is applied.

The analysis was conducted using mesh refinement, starting at 120 [mm] element size. Further, the element size has been reduced to half of the previous step, and the following element sizes were applied to mesh the model: 120, 60, 30 and 15 [mm]. Throughout the analysis, five sampling locations were applied to the model. Due to the reduction of element size, the sampling locations narrowed down and became more accurate to the sampling location. The figure 7.4 shows the most exact location of sampling.

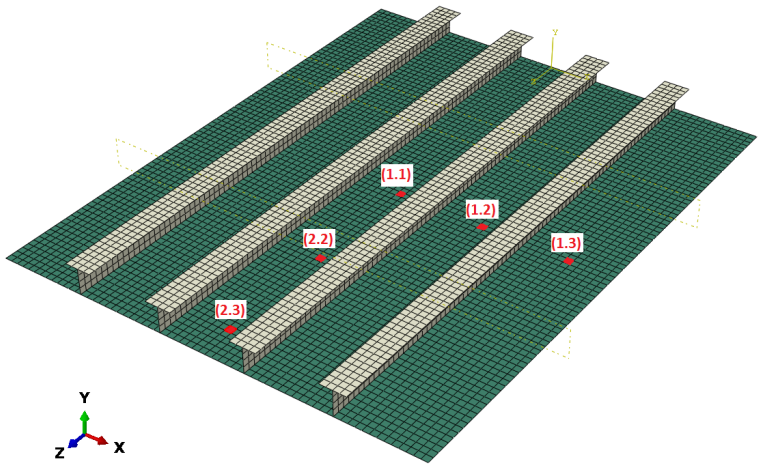

Figure 7.4: The five sampling elements applied to the model where the stress-strain curves are sampled at, expressed by red dots.

As the model is fully symmetric, only one fourth of the model was necessary to assess. The previous figure (7.4) shows the concept of this symmetry.

7.3.2 Assessment of Empirical Ice Pressure Model

In figure 7.5 a comparison of the two stress-strain plots obtained from the meshes of 120 and 15 [mm] are presented for the direction perpendicular to the stiffeners.

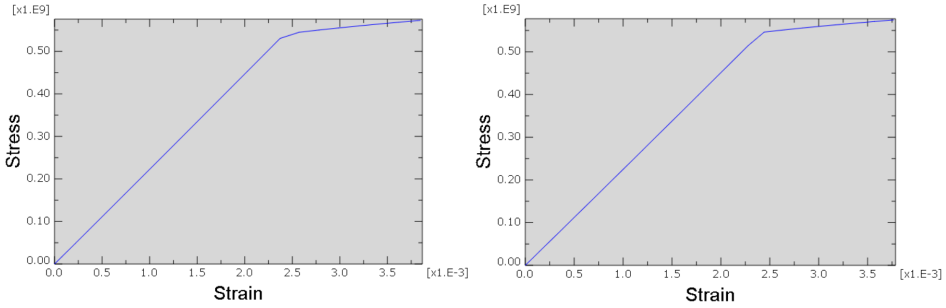

(a) Mesh size: 120 [mm]. (b) Mesh size: 15 [mm].

Figure 7.5: Stress-strain curve from location 1.1, in x-direction.

Figure 7.5 presents two results, from respectively 120 and 15 [mm] mesh size. Figure 7.5 occurs to yield when the strain reaches 0.00225 [-] and the stress is approximate 530 [MPa], while figure 7.5b is closer to initial yield when the strain has a value of 0.0024 [-] and the stress has a value of 550 [MPa]. Both curves present the non-linear material behaviour as presented in table 7.4.

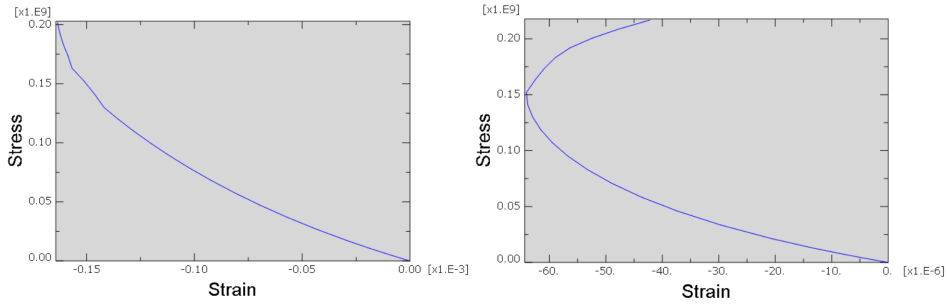

(a) Mesh size: 120 [mm]. (b) Mesh size: 15 [mm].

Figure 7.6: Stress-strain curve from location 1.1, in z-direction.

In figure 7.6 both plots show the effect of how strains in z-direction are impacted by the stresses in x-direction, and how they can develop due to initial yield in x-direction. The curve in figure 7.6b turns and the stresses in z-direction become dominant so that the strains start to increase. The reason for this development of stresses is the stiffener direction. The two curves in figure 7.6b and 7.5b are more correlated than figure 7.6a and 7.5a, due to accuracy of the results.

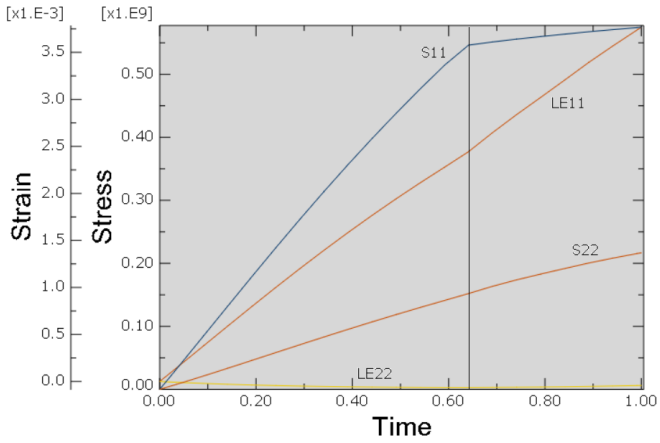

Figure 7.7: Stress and strain in both x- and z-direction plotted over time. The labels are corresponding to the stresses in the following manner: S11 and LE11 define the stress and strains in x-direction respectively, S22 and LE22 define the stress and strains in z-direction respectively.

From figure 7.7 one could observe that the plasticity in x-direction from figure 7.5 occurs when the strains in figure 7.6 are at a minimum. From the line denoted LE22 in the bottom part of the plot, one observes that the plasticity of the line denoted S11 occurs at the minimum value of LE22 which in terms are related to the very same minimum value of figure 7.6. This corresponds well with Moan (2003).

These stress strain curves, resulted in the following contour plots for displacement(Fig. 7.8) and stress(Fig. 7.9 and 7.10). The contour plots are obtained for a mesh of 15 [mm].

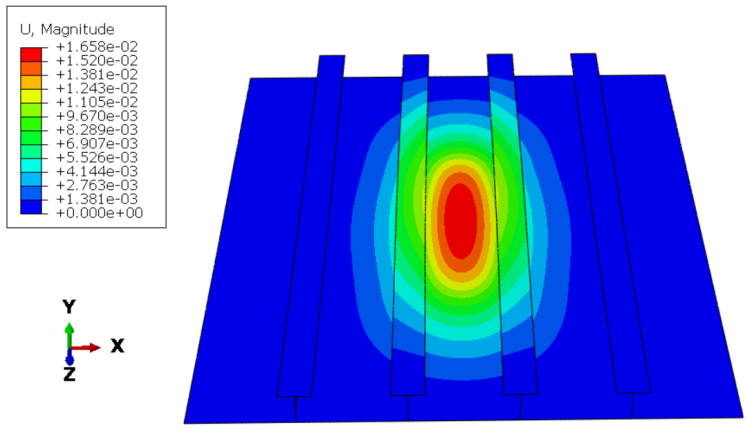

Figure 7.8: Displacement of the plate field, with a 15 [mm] mesh size.

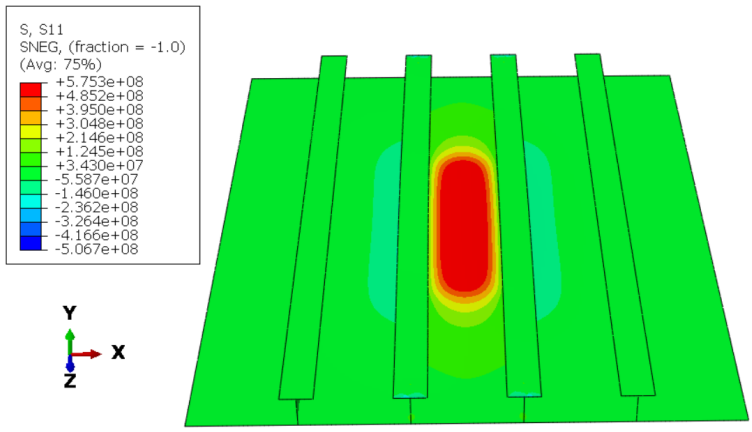

Figure 7.9: Stress in x-direction in the plate field, with a 15 [mm] mesh size.

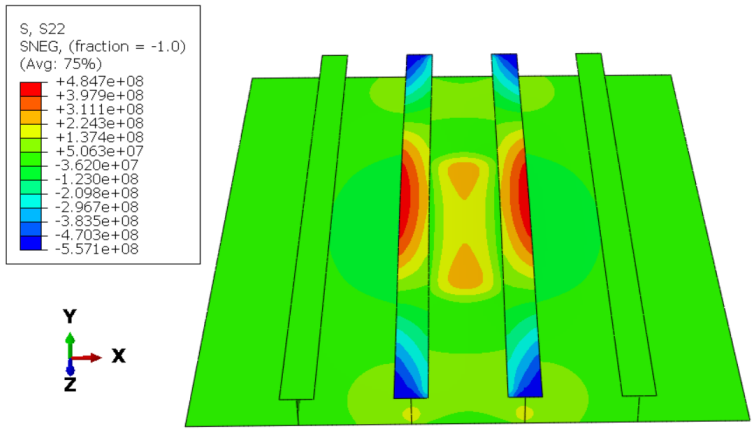

Figure 7.10: Stress in z-direction in the plate field, with a 15 [mm] mesh size.

From figure 7.8 the max displacement was found at the centre with a magnitude of 16.58 [mm]. In figure 7.9 the maximum stress in x-direction occurred at the location of the load, where the magnitude was found to be 575.3 [MPa]. The stiffeners in figure 7.10 had the largest compressive stress at the ends, with a magnitude of -557.1 [MPa] and the largest tension of 484.7 [MPa] occurring at the middle of the stiffeners. The tension is below yield, and the stiffener will behave linear at the middle cross section.

7.3.3 Assessment of DNV GL Ice Pressure Model

By applying a pressure of 6.419 [MPa] as calculated from regulations provided by DNV GL, the following plots were obtained for location (1.1) (see figure 7.4).

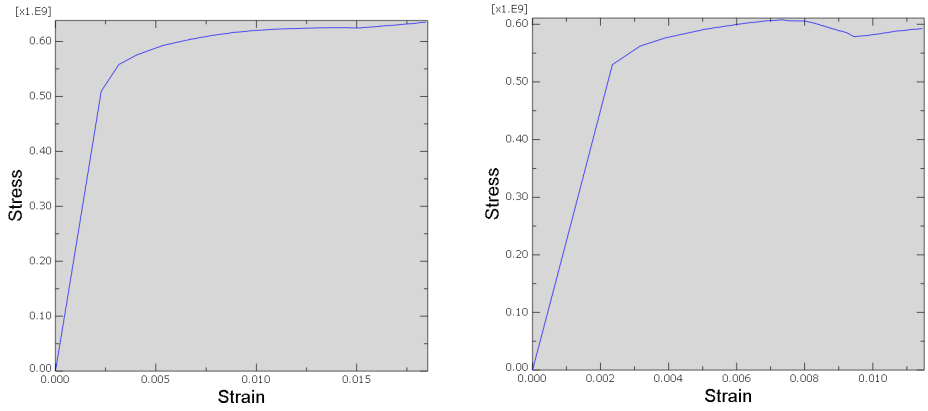

(a) Mesh size: 120 [mm]. (b) Mesh size: 15 [mm].

Figure 7.11: Stress-strain curve from location 1.1, in x-direction.

Figure 7.11 presents results from both 120 and 15 [mm] mesh size. From the figures one could observe that the initial yield stress increases from approximately 510 [MPa] in figure 7.11a to 530 [MPa] in figure 7.11b, while the strains at initial yield are approximately 0.0021 [-] for both mesh sizes. The difference in the two plots occurs due to a small change in the sampling location as the mesh is refined. The non-linear material model is also here obtained.

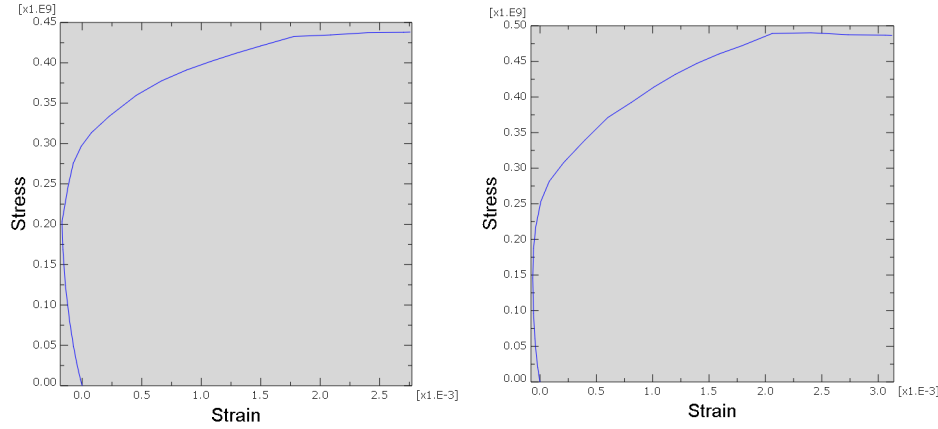

(a) Mesh size: 120 [mm]. (b) Mesh size: 15 [mm].

Figure 7.12: Stress-strain curve from location 1.1, in z-direction.

From figure 7.12 one could observe the effect of the Poisson's ratio. The stresses are able to develop in x-direction before initial yield occurs and the stresses in z-direction are dominant. It is reason to believe that this effect is obtained due to the orientation of the stiffeners.

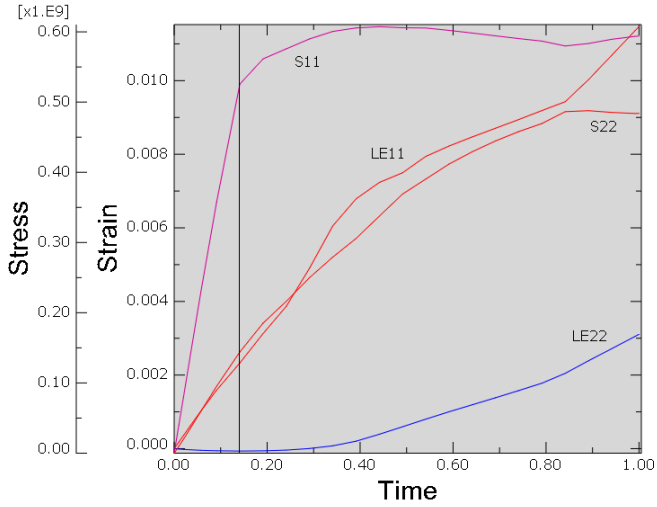

Figure 7.13: Stress and strain in both x- and z-direction plotted over time. The labels are corresponding to the stresses in the following manner: S11 and LE11 define the stress and strains in x-direction respectively, S22 and LE22 define the stress and strains in z-direction respectively.

The vertical black line in figure 7.13 shows the relation between the two figures 7.11 and 7.12. Here, line denoted LE22 which represents the strains in z-direction is at its minimum while stresses in x-direction, represented by S11, is at first yield. This substantiates the assumption of initial yielding in x-direction followed by domination of stresses in z-direction, as presented by figure 7.12b.

The previously presented stress strain curves, resulted in the following contour plots for displacement(Fig. 7.14) and stresses(Fig. 7.15 and 7.16) for a mesh size of 15 [mm].

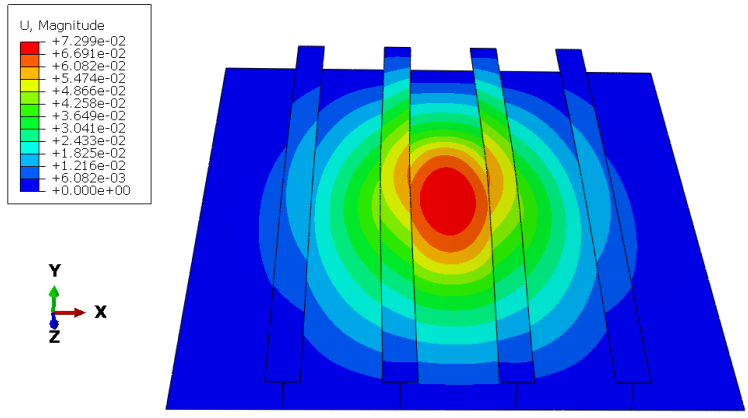

Figure 7.14: Displacement of the plate field, with a 15 [mm] mesh size.

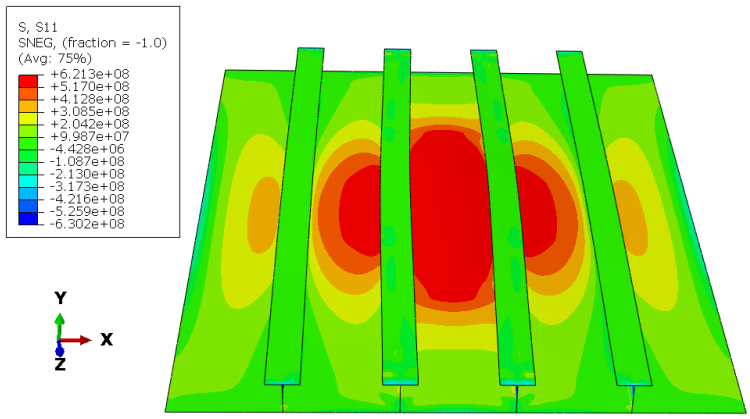

Figure 7.15: Stress in x-direction in the plate field, with a 15 [mm] mesh size.

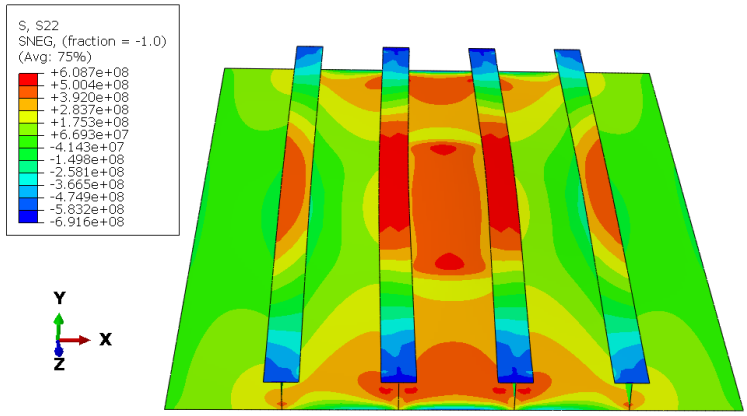

Figure 7.16: Stress in z-direction in the plate field, with a 15 [mm] mesh size.

From figure 7.14 the largest displacement was found to be 72.99 [mm]. The maximum stress in x-direction had a magnitude of 621.3 [MPa](Fig. 7.15) while the maximum stress in z-direction had a magnitude of 608.7 and -691.6 [MPa], respectively in tension and compression(Fig. 7.16). The stresses in z-direction occurred both in the plate and the stiffeners. In addition, one could observe that the outermost stiffeners are affected by the increased pressure, compared to the model where the empirical ice pressure was applied (fig. 7.10).

The Results from the assessment of IACS regulations will be given in appendix D.3 to limit the extent of the main part.

7.4 Discussion of Results

The three pressures obtained by the empirical equation and the two regulations, result in different pressures. The first model was assessed with the empirical pressure, which was low compared to the two pressures obtained by the regulations. The two ice pressures obtained from DNV GL and IACS regulations had a larger magnitude. The three pressures obtained from the empirical calculation, DNV GL and IACS regulations were found to equal 1.475, 6.419 and 15.56 [MPa]. These pressures induced stresses to the plate with a magnitude over initial yield, where the initial yield define the initiation of non-linearity. Further, the resultant forces acting on the plate were found to equal 590, 2567.6 and 6224 [kN] for the empirical, DNV GL and IACS pressure respectively. Comparing the empirical pressure with the one obtained from IACS, the pressure level is almost 11 times larger for IACS.

The plate behaviour due to increased pressure was expected, as an increase in pressure would induce larger stresses to the plate field. The empirical ice pressure resulted in a total plate deflection of 16.58 [mm]. Compared to the pressure model obtained from DNV GL regulations, which resulted in a total deflection of 72.99 [mm], and the IACS pressure model which gave a deflection of 219.9 [mm]. The empirical pressure model had a quite low total displacement compared to the main dimensions of the plate field. Considering the pressure from IACS, the plate suffered from large displacement.

Further, the effect of the Poisson's ratio is an interesting effect. This could be observed by the three plots (figure 7.7, 7.13 and D.11) in the time domain. Initially, all the three models had an increase in the stresses in z-direction, while the strains were negative until yielding in x-direction occurred and the strains became positive in z-direction. Due to initial yielding, the plate lost its capacity in x-direction and the stresses in z-direction became dominant. The connection between strains and stresses are described by Hooke's law, and validated by the three figures previously referred to.

The stresses induced in the plate do reach initial yield in all three models, thus the plate does enter the non-linear behaviour region. For the empirical ice load model, only the field between the middle stiffeners reaches initial yield in x-direction, while the two other models has a larger field of initial yielding. From the figures 7.15 and D.13 one can observe how the stiffeners impact stresses, considering the stress pattern in x-direction at the plate. This indicates the effect of stiffener support, and the reason for the stresses in z-direction as indicated by figure 7.16 and D.14. Compared to figure 7.10, one could see how the two outermost stiffeners are subjected to stresses due to bending as well. Also, one should note that the stress pattern in the middle stiffeners is changed due to increased pressure. The empirical ice pressure do induce small warping of the middle stiffeners. The stresses along the flange edge closest to the applied pressure are smaller than for the outer edge of the same stiffener. As the stiffener warps, the inner side is slightly compressed while the outer edge suffers from tension. This warping effect explains the difference in stresses across the cross section of the stiffeners. This very same effect do not occur at the middle stiffeners, in the two models where pressures

from the regulations were applied. For the two respective models, the effect occurs at the outermost stiffeners. The reason for the warping effect is due to the plate deflection and plate yielding.

Chapter 8

Results of Analysis Based on Ridged Ice Measurements

Operations in Arctic environment require sufficient structural resistance as different ice features may be encountered. The largest obstacles that may be encountered during operations in ice infested waters are ice ridges(Riska, 2011). Impacts from ridged ice are often considered the governing design action for ships and offshore structures(Ekeberg, 2015). The ridged ice is often considered extreme loads in design, hence it is important to study the loads induced by ridged ice on a ship hull, and the response of the hull.

This chapter contains an assessment of a local FE model of a ship bow interacting with an ice ridge. The model is established by Computer Aided Design (CAD) using Autodesk Fusion 360. The data and measurements applied to obtain the contact pressure are described in chapter 3. The interaction model is presented in chapter 4. The main focus in this analysis is aimed at local response and assessment of different boundary conditions.

8.1 Presentation of the Local Bow Model

This section presents the local bow model. The dimensions are based on regulations provided by DNV GL and assumed to fit the actual hull of KV Svalbard. Throughout the calculations of the dimensions, several assumptions were applied within reasonable limits. These assumptions are described further in this section.

8.1.1 Location of the Local Bow Model

The model is a section of the bow located as described by figure 8.1. It is located at the water line in the stem area. Half of the plate is above water level.

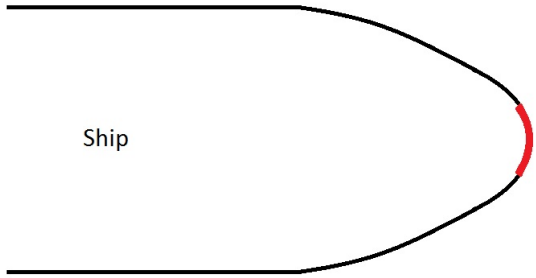

Figure 8.1: The location of the local bow plate field is marked as a thick red line in the stem area of the hull.

8.1.2 Dimensioning

In the stem region, transverse girders are separated with less distance than other other regions. The transverse girder spacing was set to 1 [m], resulting in a plate length with the same dimension. Additionally, the girder span was set to 2 [m] resulting in a plate width of 2 [m]. Compared to the flat plate model presented in chapter 7, the stiffener spacing was reduced from 400 to 200 [mm] for this model. Additionally, the plate thickness was increased regarding the results from chapter 7 and the increased contact pressure $p_{c,emp}$ presented in table 8.5.

Table 8.1: Dimensions of the local bow model found by applying DNV GL regulations.

Description	Parameter	Dimension
Arbitrarily chosen parameters		
Stiffener spacing	s	200 [mm]
Stiffener length	l	1000 [mm]
Plate thickness	t	35 [mm]
Calculated parameters		
Section modulus	Z_{min}	104680 [mm^3]

The recommended minimum section modulus Z_{min} do not provide any dimensions for the stiffeners. By iteration, the dimensions presented in table 8.2 were found.

Table 8.2: Dimensions of the local stiffeners.

Description	Parameter	Dimension
Web height	h_{web}	170 [mm]
Web thickness	t_{web}	15 [mm]
Flange height	t_{flange}	15 [mm]
Flange width	w_{flange}	60 [mm]
Section modulus	Z	108584 [mm^3]

This resulted in a slightly larger section modulus Z compared to recommendations by DNV GL.

8.1.3 The Bow Model

The bow model is curved in two directions to approximate the bow of an ice going vessel. The model is inspired by KV Svalbard. For KV Svalbard Thorsen (2012) suggests a stem angle at the water line γ equal 33°. While the average waterline entrance angle α in the bow region was suggested 59°. Figure 5.3 presents the different angles. For this model, the average stem angle γ equal 33°. While the average waterline entrance angle α was found equal 75° due to the curvature of the model. Hence, the results presented here will not represent the exact behaviour of the hull of KV Svalbard.

Applying the dimensions presented under section 8.1.2, the model was established using CAD. This resulted in the following model, presented in figure 8.2.

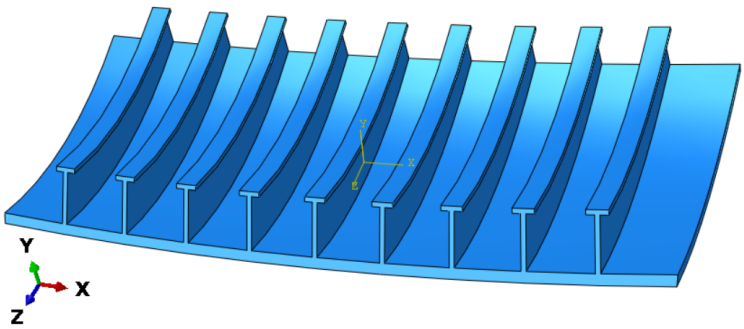

Figure 8.2: Local bow model obtained by DNV GL regulations. The support are assumed to consist of transverse girders perpendicular to the stiffeners(long edges), while longitudinal frames are located at each end(short edges).

The model is created applying two different curvatures, where the following data apply, as presented by table 8.3. Further, the plate width is considered the edges

perpendicular to the stiffeners, while the plate length is the edges parallel to the stiffeners.

Table 8.3: Curvatures that apply to the local bow model.

Description	Parameter	Dimension
Along the plate width		
Arch radius	r_w	10 [m]
Arch length	b_w	2 [m]
Along the plate length		
Arch radius	r_l	1.5 [m]
Arch length	b_l	1 [m]

The model is assigned the material properties given in table 8.4.

Table 8.4: Material properties assigned to the model.

	Parameter	Dimension
Youngs Modulus	E	207000 [MPa]
Yield stress	σ_y	488 [MPa]
Poisson's ratio	υ	0.3 [-]
Density	ρ_s	$7.85 \cdot 10^{-6}$ [kg/mm^3]

The ridged ice will induce loads large in magnitude resulting in non-linear material behaviour. Hence, a plastic behaviour model is applied in the analysis. The material model was presented under section 7.1.3 in table 7.4. A contact area was assumed to apply at the centre of the plate over an width of 0.4 [m] and the total plate length. This results in direct loading of the three middle stiffeners and a contact area of 0.4 [m^2].

8.2 Assessment of Ridged Ice Pressure

The empirical pressure model presented under chapter 4 in section 4.1.4 will be applied to conduct analysis on the bow model subjected to loads from ridged ice. The data for ridged ice provided under chapter 3 in section 3.1.3, are applied to define the flexural strength of the ice.

Assuming that the ice specimens tested had a varying degree of defects and letting the average varying diameter describe these defects, the average flexural strength $\overline{\sigma_f}$ was approximated to 0.904 [MPa]. The diameter varied from 60 to 70 [mm] by applying a uniformly distributed random number between 0 and 10 [mm] to

a lower limit diameter of 60 [mm]. The empirical contact pressure presented in section 4.1.4 given by equation 8.1 define the contact pressure applied to the model.

$$p_{c,emp} = \frac{C_{geo} \cdot \sigma_f(\eta_b) \cdot h_i^2}{A \cdot \left(\sin(\beta) - \mu \cdot \cos(\beta)\right)} \text{ [MPa]} \tag{8.1}$$

The horizontal geometry coefficient C_{geo} was assumed to equal 0.75 accounting for irregularities along the horizontal boundary of the ice. The contact area A was set to 0.4 [m^2]. The friction coefficient μ was set to 0.1 as suggested by Riska (2011). From the drilling of the ridge, the deepest location of measurement was at a depth of 3.63 [m] giving h_i equal 3.36 [m]. Applying the hull angles discussed under section 8.1.3, where α was set to approximately 75° and γ was set to 33°, the contact pressure was found to equal:

$$p_{c,emp} = \frac{0.75 \cdot 0.904 \cdot 3.63^2}{0.4 \cdot \left(\sin(34°) - 0.1 \cdot \cos(34°)\right)} = 47 \text{ [MPa]} \tag{8.2}$$

By assuming a normal frame angle β described by the following equation, under geometrical considerations:

$$\beta = \arctan\left(\frac{\tan(\gamma)}{\sin(\alpha)}\right) = \arctan\left(\frac{\tan(33°)}{\sin(75°)}\right) = 34 \text{ [°]} \tag{8.3}$$

The data input applied to obtain the pressure are listed in table 8.5

Table 8.5: Results from sea ice measurements and application of empirical formula given in section 4.1.4.

$\overline{\sigma_f}$ [MPa]	-	0.904
h_i [m]	-	3.63
β [°]	-	34
A_c [m^2]	-	0.4
μ	-	0.1
$p_{c,emp}$ [MPa]	-	47

8.3 Bow Model Response Analysis

Results of the analysis performed on the model, will be presented in this section. The ridged ice contact pressure will be applied to the model to assess the behaviour of the plate field. An assessment of the boundary conditions will be conducted as well. Further, the dimensioning will be checked regarding if it is sufficient enough to resist the applied loads. The main focus is given the plate and the stiffener flanges.

The model is loaded with a static uniform pressure applied at the middle of the plate, as presented in figure 8.3.

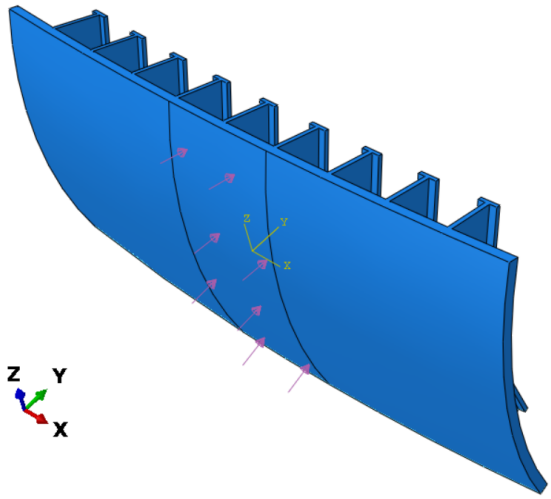

Figure 8.3: The bow model with applied pressure, marked by purple arrows. The applied pressure was 47 [MPa] over an area of 0.4 [m^2].

The reader should know that this is a simplified analysis when considering actual conditions. Loads will normally have a large spatial and temporal variation, regarding parameters as fracture model, vessel speed, area of contact, ice thickness and ice strength.

8.3.1 Assessment of Response

This section provides the results obtained from assessment of the local bow model subjected to the empirical ice contact pressure. During this assessment, the boundaries are assumed fixed against translation and rotation.

The pressure applied to the model was an uniform pressure with a magnitude of 47 [MPa] over an area of 0.4 [m^2].

The model in this analysis is modelled as a continuum shell, providing the ability to refine meshes over the model thickness. As one could refine the mesh over the thickness, and thereby obtain accurate results over the thickness, it is not necessary to conduct a mesh refinement to the whole model. Hence, a fixed mesh is sufficient as it is refined close to loaded areas. As this model applies continuum shell, the applied elements are C3D8R.

Plate Response - Stiffener Side

The plate was assessed at 20 locations, 10 of them at located at the stiffener side and 10 located at the load side. All locations provide stress and strain for both x- and z-direction. The stiffener side locations are presented in figure 8.4. Due to symmetry only one fourth of the plate was assessed.

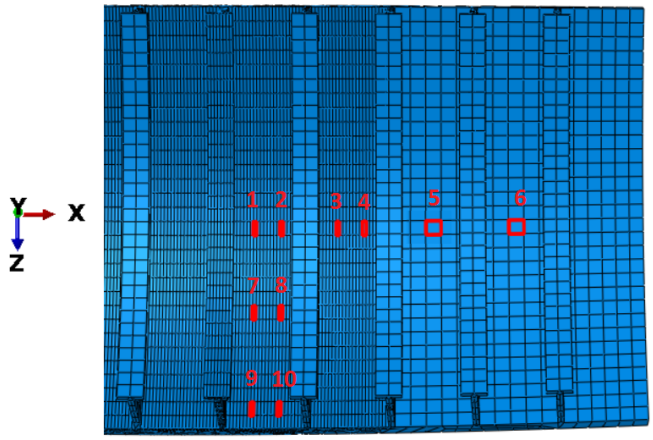

Figure 8.4: The sampling elements (1-10) on the stiffener side that provide stress and strain data in-plane, are marked in red. Note that the presented part is only a part of the model.

Further will the stress versus true strain curves for each sampling element be presented. The reader should note the different scales of the axes applied in the plots. The following plots will present data for the stiffener side of the plate.

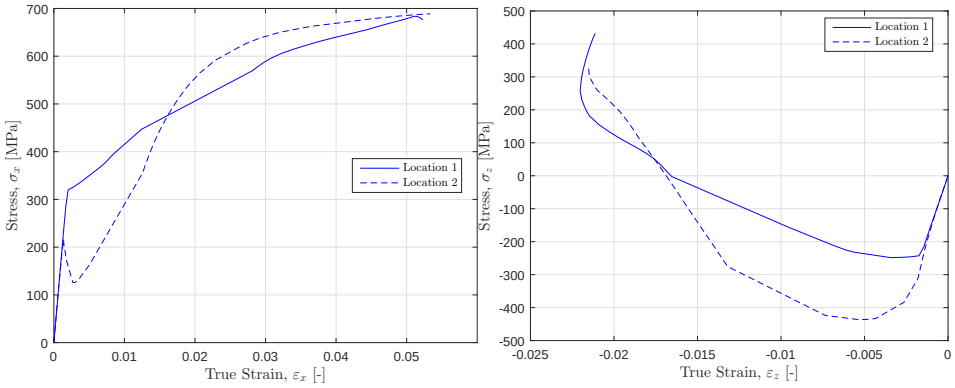

(a) Stress σ_x versus true strain ε_x.

(b) Stress σ_z versus true strain ε_z.

Figure 8.5: Stress σ versus true strain ε at location 1 and 2.

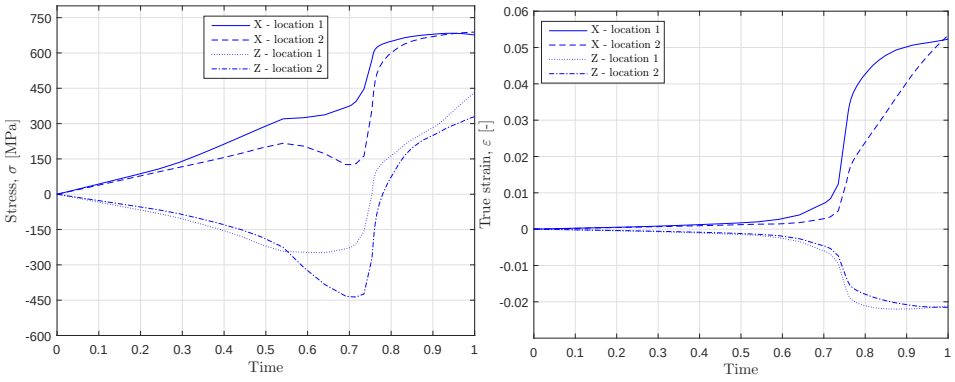

(a) Stress σ plotted versus time.

(b) True strain ε plotted versus time.

Figure 8.6: Stress σ and true strain ε at location 1 and 2 plotted over time. The time axis describes the load fraction δ, where 0 equals unloaded condition and 1 equals fully loaded.

Figure 8.5a and 8.5b present the stress versus true strain for location 1 and 2. The correlation between location 1 and 2 is not obvious regarding both figure 8.5a and 8.5b. While figure 8.6a and 8.6b present a more obvious correlation between the two locations. These two figures present stresses and true strains plotted versus the amount of applied load. From figure 8.6a one can observe that the stresses in x-direction for both locations increases almost linear until a load fraction δ equals 0.55 is applied. The same is observed for the stresses in z-direction. The correlation between figure 8.5a and 8.5b is found in figure 8.6a and 8.6b when the applied load fraction δ is between 0.7 and 0.8. The sudden increase in both stresses and strains occur due to collapse of the middle stiffener and warping of the two stiffeners located next to the middle one, as illustrated in figure 8.7, 8.8 and 8.9.

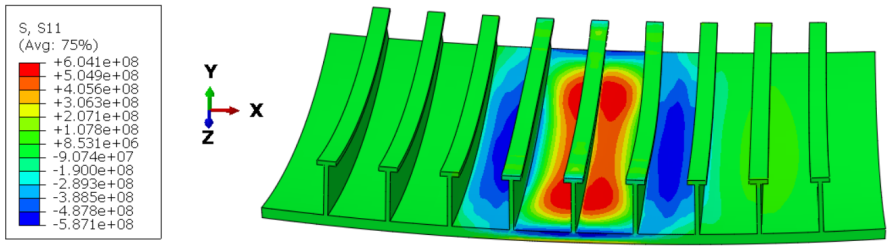

(a) Load fraction equals 0.735.

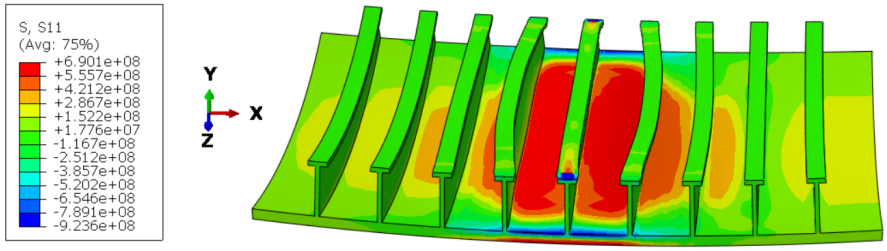

(b) Load fraction equals 1.

Figure 8.7: Contour plot of the stress in x-direction of the bow model, for two different load fractions.

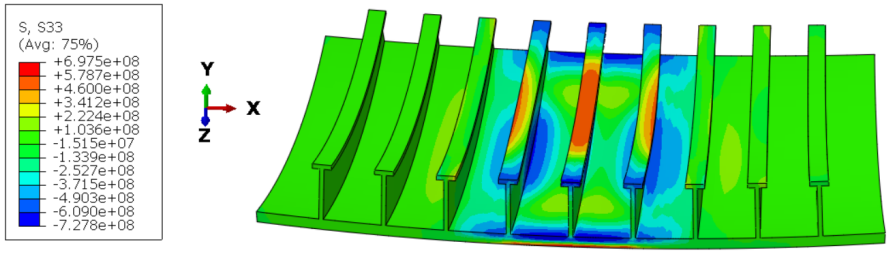

(a) Load fraction equals 0.735.

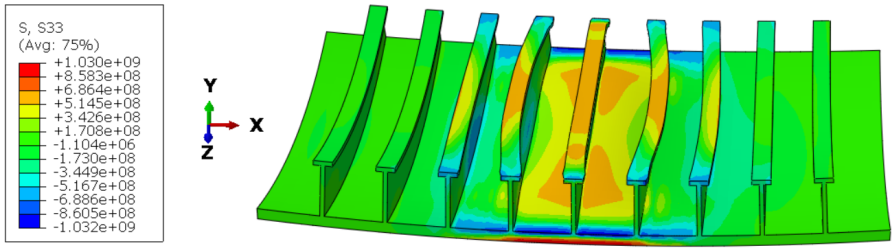

(b) Load fraction equals 1.

Figure 8.8: Contour plot of the stress in z-direction of the bow model, for two different load fractions.

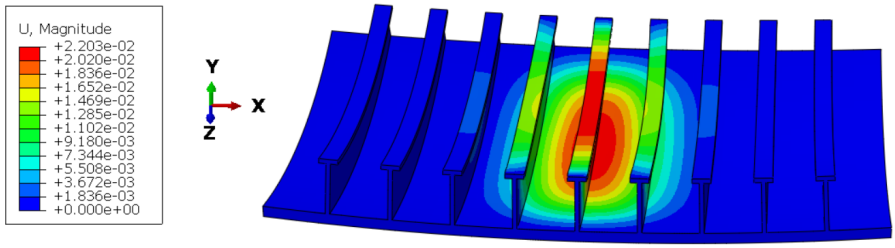

(a) Load fraction equals 0.735.

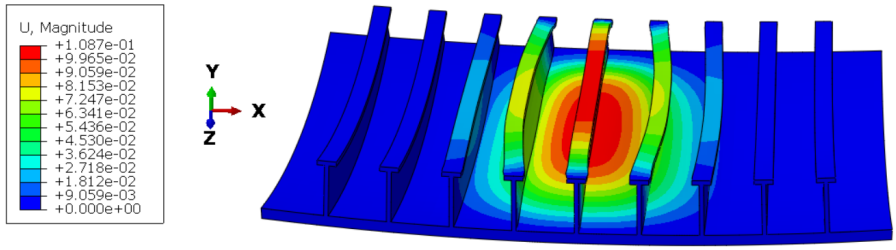

(b) Load fraction equals 1.

Figure 8.9: Contour plot of the displacement in y-direction of the bow model, for two different load fractions.

Figure 8.7, 8.8 and 8.9 present the plate model before and after collapse for stress in x-direction, stress in z-direction and displacement in y-direction respectively. The load fraction δ describes the amount of load applied. A load fraction δ of 0.735 implies that only 34.55 [MPa] is applied, while a load fraction of 1 results in an applied pressure of 47 [MPa]. In figure 8.7 the maximum plate stress changes from 604 to 690 [MPa] in tension after the collapse. In compression, the maximum stress changes from -587 to -924 [MPa] after collapse. Also, the change in stress pattern from figure 8.7a to 8.7b should be noted. In figure 8.8 the maximum stress changes from 222.4 to 686.4 [MPa] in compression, while for tension the maximum stress changes from -727.8 to 1032 [MPa]. In figure 8.9 the maximum displacement of the plate changes from 0.0022 [m] in figure 8.9a to 0.1087 [m] in figure 8.9b. The reader should note how the pattern change and how the induced stresses impact the stiffener behaviour.

Plate Response - Load Side

Both sides of the plate were assessed, and the following section provides results for the load side of the plate. Due to symmetry, only one fourth of the plate was assessed. The load side locations are presented in figure 8.10.

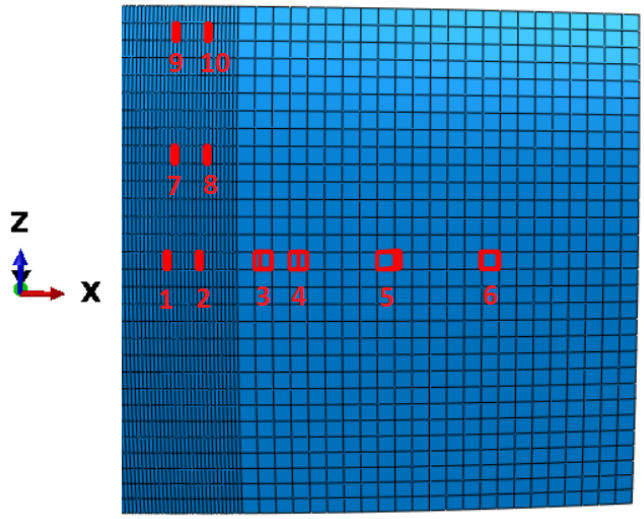

Figure 8.10: The sampling elements (1-10) on the load side that provide stress and strain data in-plane are marked in red. Note that the presented part is only a part of the model.

The analysis gave rise to the following plots, for location 1 and 2. The figures below present the results.

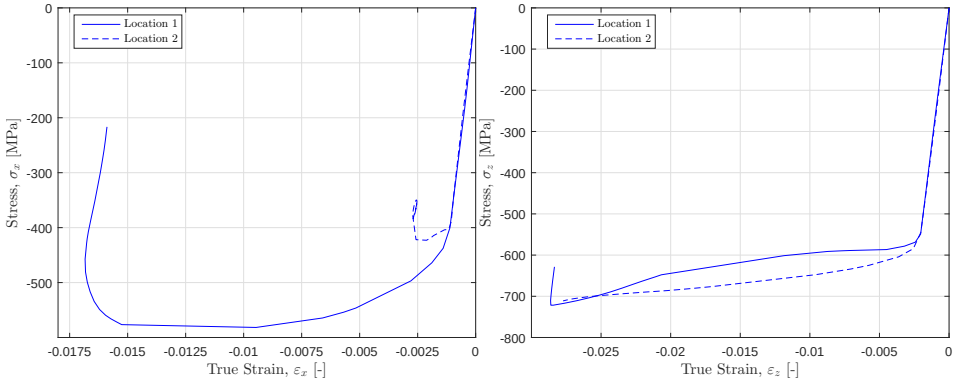

(a) Stress σ_x versus true strain ε_x.

(b) Stress σ_z versus true strain ε_z.

Figure 8.11: Stress σ versus true strain ε at location 1 and 2.

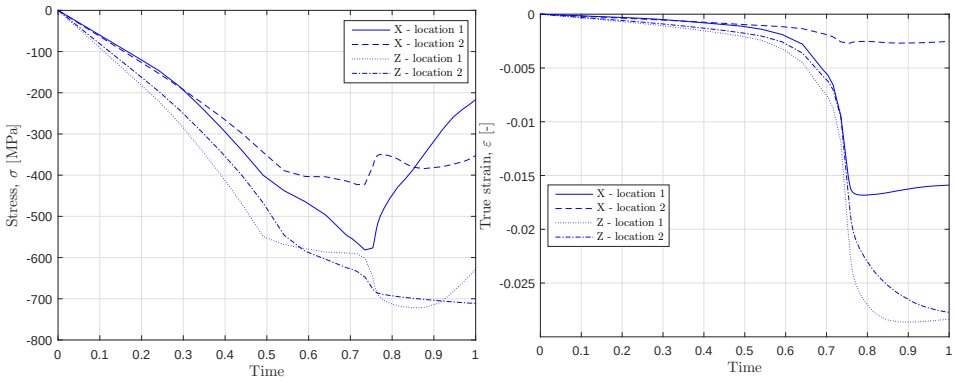

(a) Stress σ plotted versus time.

(b) True strain ε plotted versus time.

Figure 8.12: Stress σ and true strain ε at location 1 and 2 plotted over time. The time axis describes the load fraction δ, where 0 equals unloaded condition and 1 equals fully loaded.

Figure 8.11a and 8.11b present stress versus true strain for the loaded side of the plate. In figure 8.11a one can observe equal initial behaviour for compressive stresses below -400 [MPa]. For compressive stresses below -400 [MPa] the behaviour differ. Reasonably due to warping of the stiffener closest to location 2. In figure 8.11b one can observe almost equal behaviour for both locations. This is well understood by looking at the figures 8.12b and 8.12a, and the curves plotted for the z-direction. In the same figures, for x-direction, one can observe a large difference in the strains between a load fraction of 0.7 and 1. This explains the difference for the behaviour below -400 [MPa] as illustrated by figure 8.11a. As for figure 8.6a and 8.6b, figure 8.12a and 8.12b also have a sudden change in the curves between the load fraction of 0.7 to 0.8. This is related to the warping and collapse of the stiffeners. The assessment gave the following contour plots, presented in figure 8.13, 8.14 and 8.15.

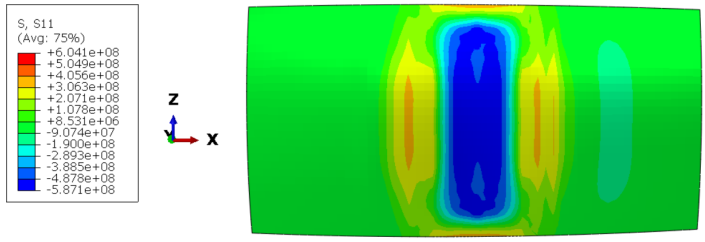

(a) Load fraction equals 0.735.

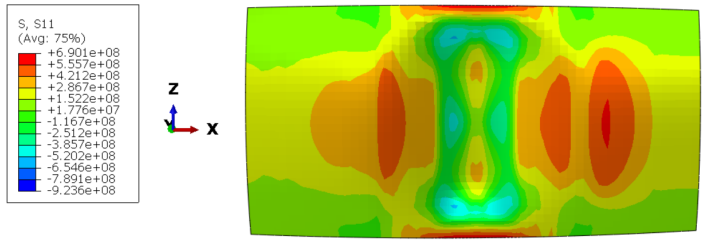

(b) Load fraction equals 1.

Figure 8.13: Contour plot of the stress in x-direction of the bow model, for two different load fractions.

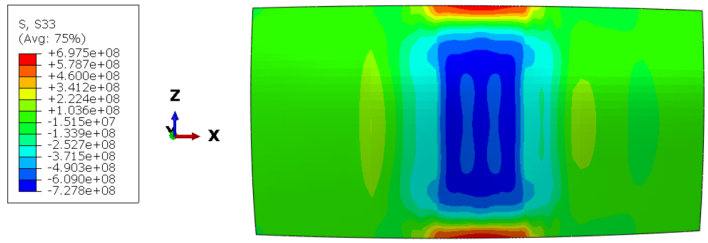

(a) Load fraction equals 0.735.

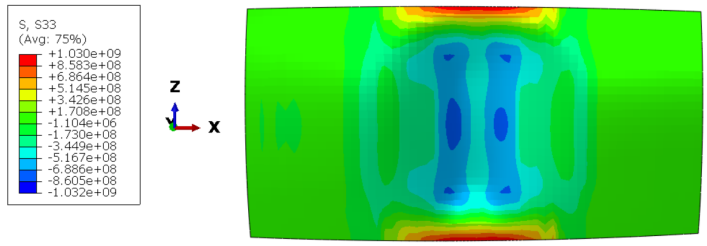

(b) Load fraction equals 1.

Figure 8.14: Contour plot of the stress in z-direction of the bow model, for two different load fractions.

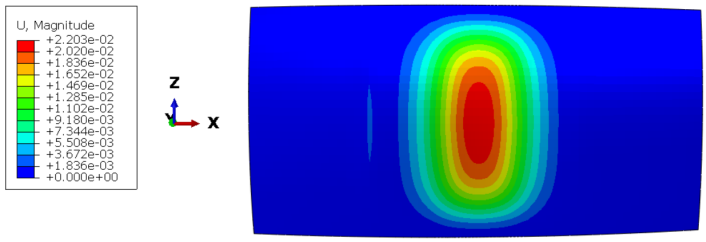

(a) Load fraction equals 0.735.

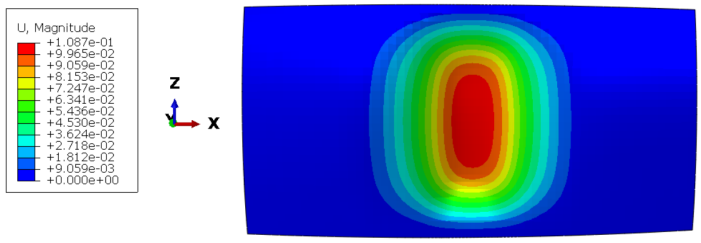

(b) Load fraction equals 1.

Figure 8.15: Contour plot of the displacement in y-direction of the bow model, for two different load fractions.

In figure 8.13 the stresses in x-direction are presented. Indicated by figure 8.13a, the plate suffers from compressive stresses of -581 [MPa] and tensile stresses of 405.6 [MPa] prior to stiffener collapse. While figure 8.13b indicates a dominance of tensile stresses with a magnitude of 691 [MPa] and compressive stresses with a magnitude of -520 [MPa] post collapse. In figure 8.14 the stresses in z-direction is presented. Here the compressive stresses increase from -727.8 to -1032 [MPa], and the tensile stresses increase from 697.5 to 1030 [MPa], after the collapse. The displacement in y-direction, described by figure 8.15, increases from 0.0022 [m] to 0.1087 [m] due to collapse of the stiffeners. The reader should notice the changes in contour pattern due to changes in load fraction.

For the rest of the sampling locations, the results are found in appendix F.1. The stiffeners indicated both collapse and buckling behaviour. Hence, an assessment of the stiffeners were necessary, and is found in appendix F.2.

8.4 Assessment of Boundary Conditions

In the previous analysis, presented under section 8.3.1, fixed boundaries were applied. Fixed boundaries are in most cases not an actual model of the boundaries, as the supporting girders will not be infinitely stiff. To obtain the most realistic result of the model response, and study the effect of varying support, the boundaries were changed. This section will provide further information on the set-up and results of the boundary condition assessment. The applied load is set to a pressure of 47 [MPa], equally the previous assessment.

8.4.1 Modelling of the Boundary Conditions

Due to the curvature of the model, each stiffener cross section had an individual plane applied with origin located at the point where the stiffener webbing and plate interacts, as shown in figure 8.16a. To simulate the support of the surrounding girders, a rotational spring with spring stiffness κ was applied to the origin of the local coordinate system at each stiffener end (figure 8.16a). The location of this rotational spring is an important factor, as it defines the assumed behaviour of the supporting girder. For this analysis, an assumption of warping only applied. The boundary of each spring were set to grounded, i.e. fixed to the ground. Each spring were assigned with a rotational degree of freedom around the local x-axis. To assign this rotational stiffness to the entire cross section, a multi point constraint (MPC) was applied to the outline of each stiffener and jointed to the point where the spring was located. The MPC is a rigid connection, where all forces and moments are transferred to a given location. The MPC connection is illustrated in figure 8.16b.

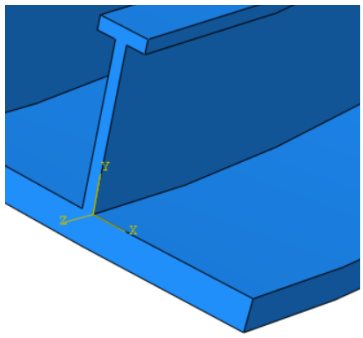

(a) The local coordinate system for each stiffener end.

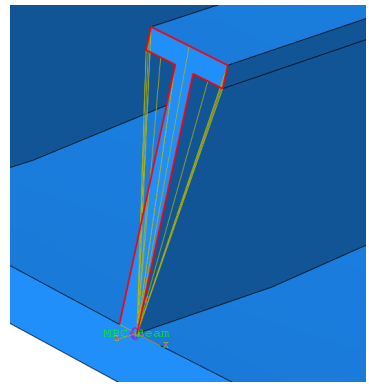

(b) The edges of each stiffener jointed to the local spring with a MPC, are marked in red.

Figure 8.16: Modelling of rotational boundaries. The y-axis is parallel to the web and the z-axis is perpendicular to the stiffener cross section. Each stiffener end are assigned an individual spring located in the origin of the coordinate system in figure (a). The yellow lines illustrate the MPC.

From figure 8.2, the short edge defines the length and the long edge defines the width of the plate. Along the length, the boundaries are restrained with no deflection or rotation. Hence, the supporting frames are assumed infinitely stiff. This is applied to reduce the extent of the assessment of the boundaries, and keep the main focus on the supporting girders. The plate edge over the width is restrained against translation and rotation in all directions globally, while each stiffener are allowed to rotate around the local x-axis and move along the local z-axis. Further, the stiffener cross sections are fixed against translation in x- and y-direction and rotation about the y- and z-axis locally. This, together with the applied springs, will simulate warping of the supportive girder. The local boundaries for the stiffeners will conduct the same behaviour of interaction between girder and stiffener as if welded together.

8.4.2 Spring Stiffness

To simulate different girder dimensions, various spring stiffness κ were assigned to the different analysis. The following table presents the different stiffness applied in the analysis.

Table 8.6: Different stiffness κ assigned to the springs.

Analysis #	-	Stiffness, κ [N/rad]
1	-	$1 \cdot 10^3$
2	-	$1 \cdot 10^6$
3	-	$1 \cdot 10^9$

The different values of spring stiffness were chosen arbitrarily, hence no dimensional calculations of the supportive girders were performed to predict these values.

8.4.3 Results of Boundary Condition Assessment

For this assessment, the sampling locations remain the same as for the assessment of the model with fixed boundaries. For the plate, both stresses and true strain were measured in x- and z-direction. Equal measures as previous were conducted for the stiffener flanges. This assessment will focus on the varying behaviour due to changes in the spring stiffness as given in table 8.6.

Plate Assessment - Stiffener Side

For the stiffener side of the plate, the following stress versus true strain plots apply for the three different variations of spring stiffness.

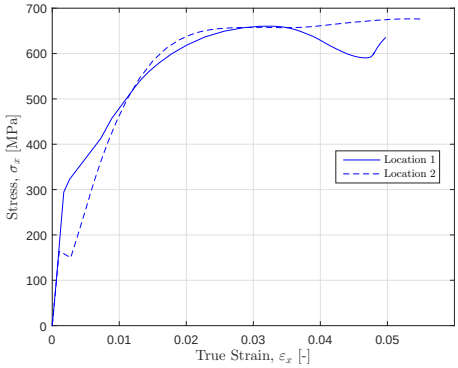

(a) Spring stiffness $\kappa = 1 \cdot 10^3$ [N/rad].

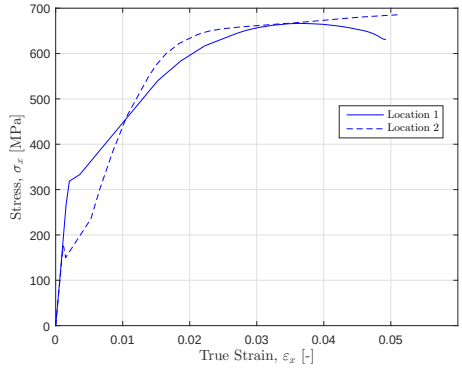

(b) Spring stiffness $\kappa = 1 \cdot 10^6$ [N/rad].

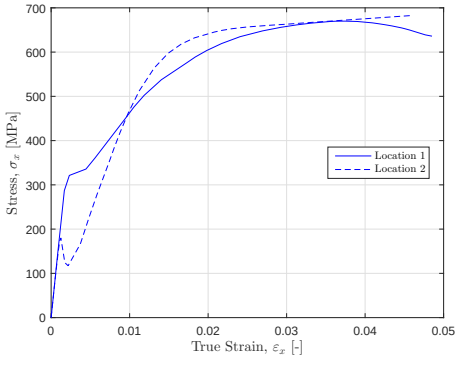

(c) Spring stiffness $\kappa = 1 \cdot 10^9$ [N/rad].

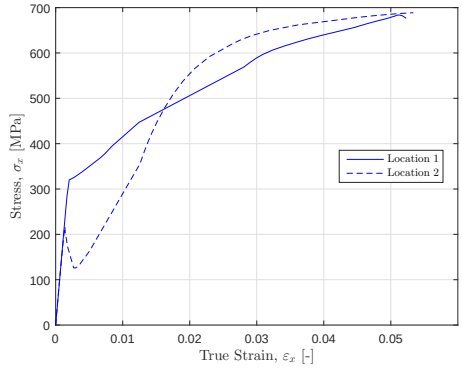

(d) Fixed boundary condition.

Figure 8.17: Stress σ_x versus true strain ε_x in x-direction at location 1 and 2 on the stiffener side.

From figure 8.17 one can observe similar behaviour for the stress versus true strain curves. In figure 8.17a the initial yield in location 1 is located at 300 [MPa], while for figure 8.17b and 8.17c the initial yield is located at approximately 325 and 330 [MPa] respectively. For location 2, the initial yield is located at 160 [MPa] for a spring stiffness of κ equal $1 \cdot 10^3$ in figure 8.17a. This change as the spring stiffness is increased. In figure 8.17b, the initial yield for location 2 is 170 [MPa]. While in figure 8.17c, the initial yield is 175 [MPa]. The curves for both locations tend to approach the behaviour of the stress versus true strain for a fixed boundary condition, as the spring stiffness is increased. This is well understood by the following figure.

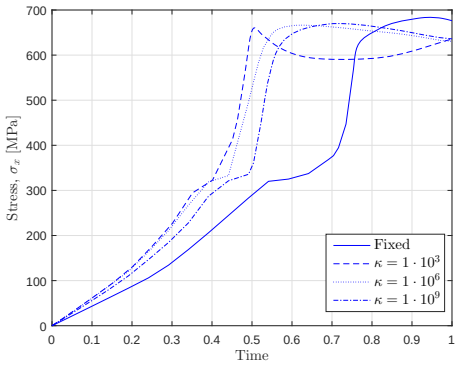

(a) Stress, σ_x, location 1.

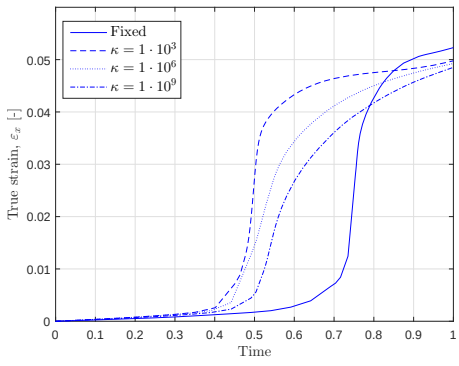

(b) True strain, ε_x, location 1.

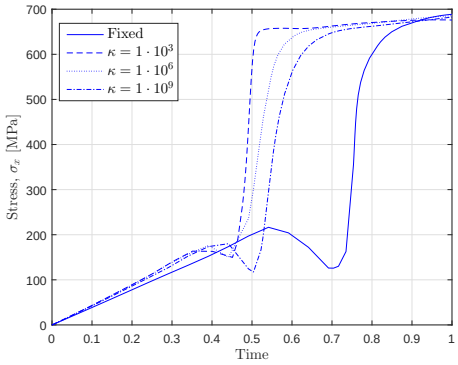

(c) Stress, σ_x, location 2.

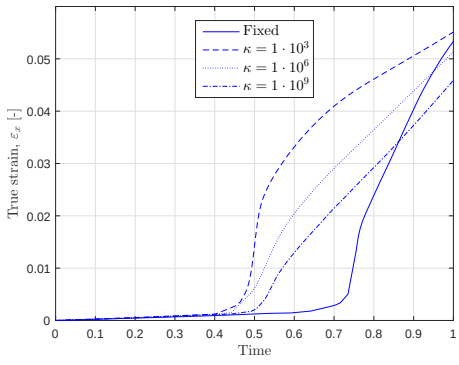

(d) True strain, ε_x, location 2.

Figure 8.18: Stress σ_x and true strain ε_x in x-direction at location 1 and 2 plotted over time. The scale on the x-axis present the load fraction.

Figure 8.18 does prove that the plate behaviour in location 1 and 2 tends to approach the behaviour of a plate with fixed boundaries. Additionally, one can observe that the capacity of the model now is reduced as the sudden increase in both stress and true strain has been reduced from a load fraction between 0.7 and 0.8, down to a load fraction between 0.4 and 0.6. It is observed that an increase in stiffness from κ equals 10^3 to 10^9 [N/rad] does not improve the capacity significantly.

The same assessment is applied in the z-direction for location 1 and 2. The following figures present the results of this assessment.

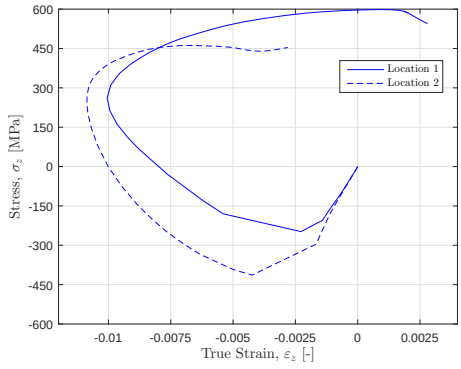

(a) Spring stiffness $\kappa = 1 \cdot 10^3$ [N/rad].

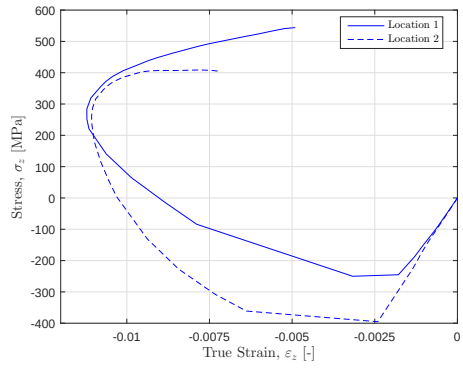

(b) Spring stiffness $\kappa = 1 \cdot 10^6$ [N/rad].

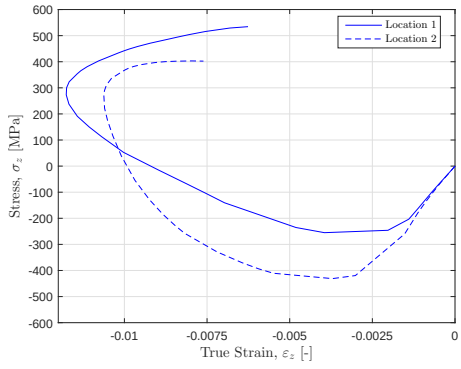

(c) Spring stiffness $\kappa = 1 \cdot 10^9$ [N/rad].

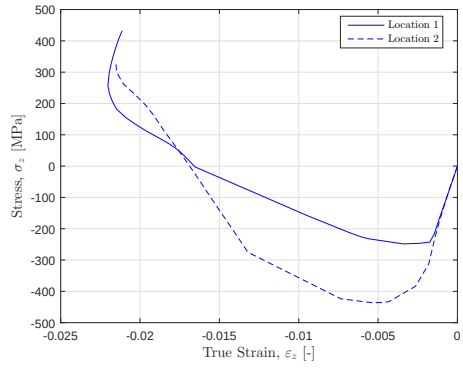

(d) Fixed boundary condition.

Figure 8.19: Stress σ_z versus true strain ε_z in z-direction at location 1 and 2 on the stiffener side. Note the different scales between each figure.

In figure 8.19, the curves for the spring supported stiffeners tend to develop positive stresses in the final state. For the spring stiffness κ equals 10^3, presented in figure 8.19a, the strains and stresses in location 1 become positive when δ equals 1. This indicates the effect of the Poisson's ratio and the impact of plate capacity. In figure 8.19b and 8.19c the strains are reduced, due to more support from the increased spring stiffness κ, while the stresses still became positive. The same effect is observed for location 2, thus less stress and strain are observed. For location 2, the compressive stresses are larger prior to collapse compared to location 1, and indicate less stress in x-direction at location 2 prior to collapse. This could be observed by looking at figure 8.18a and 8.18c, and the difference in stress magnitude at a load fraction between 0.4 and 0.5. The curves in figure 8.19a, 8.19b and 8.19c tend to turn toward positive strains at approximate 300 [MPa] of tensile stresses. This is explained by figure 8.20 below.

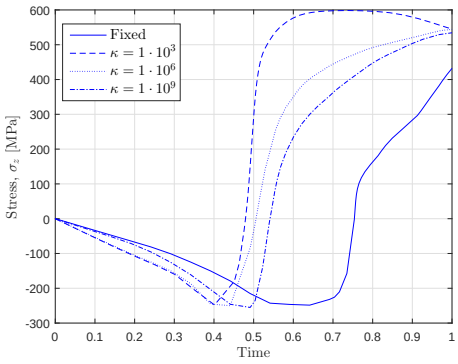

(a) Stress, σ_z, location 1.

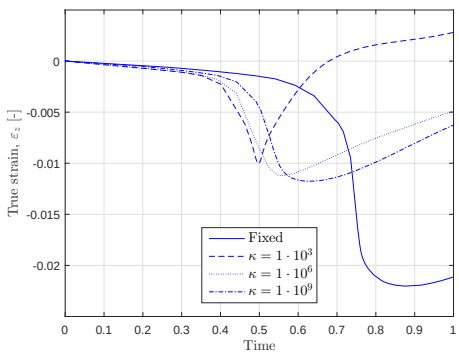

(b) True strain, ε_z, location 1.

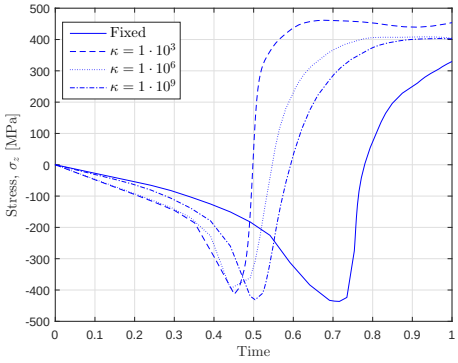

(c) Stress, σ_z, location 2.

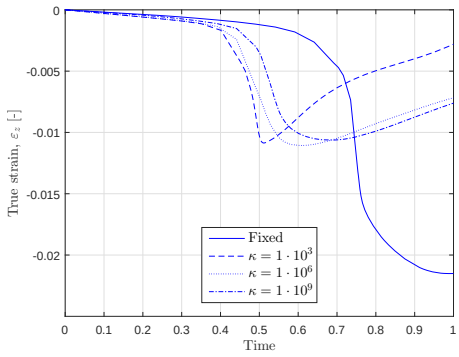

(d) True strain, ε_z, location 2.

Figure 8.20: Stress σ_z and true strain ε_z in z-direction at location 1 and 2 plotted over time. The scale on the x-axis presents the load fraction.

In figure 8.20 it is shown how the increased spring stiffness approaches the behaviour of the fixed boundary condition. Equal the stresses and strains in figure 8.18, the same capacities are observed here, for a load fraction δ between 0.4 and 0.6. From figure 8.20b and 8.20d one can observe that the curve for spring stiffness κ equals 10^3 has steeper curve after the turning point (located at a load fraction of 0.5) compared to the stiffer springs. From the stress curves presented in figure 8.18 and 8.20 one can observe capacities of approximately 0.4, 0.45 and 0.5 for spring stiffness κ equals 10^3, 10^6 and 10^9 respectively. The strains from the same figures indicate the same capacities. To avoid buckling of the plate model, the load capacity equals 18.8 [MPa] for a spring stiffness κ equals 10^3, while the load capacity equals 21.15 [MPa] for κ equals 10^6, and 23.5 [MPa] for κ equals 10^6. This is a reduction compared to the load capacity of 34.55 [MPa] for the plate model with fixed boundaries.

The assessment gave the following contour plots of displacement in y-direction and stresses in x- and z-direction. Note that the load fraction for these plots equals 1, hence the total load of 47 [MPa] is applied.

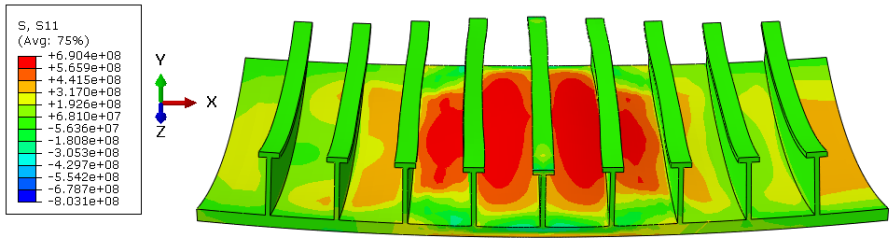

(a) Spring stiffness $\kappa = 1 \cdot 10^3$ [N/rad].

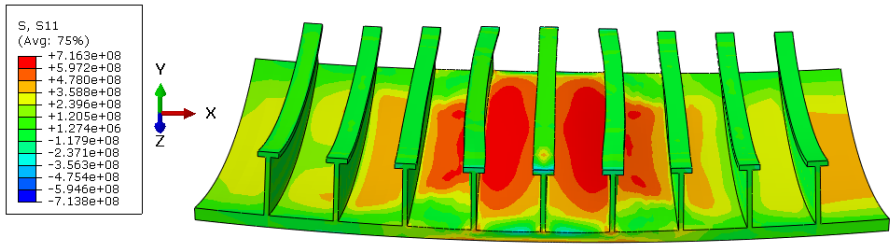

(b) Spring stiffness $\kappa = 1 \cdot 10^6$ [N/rad].

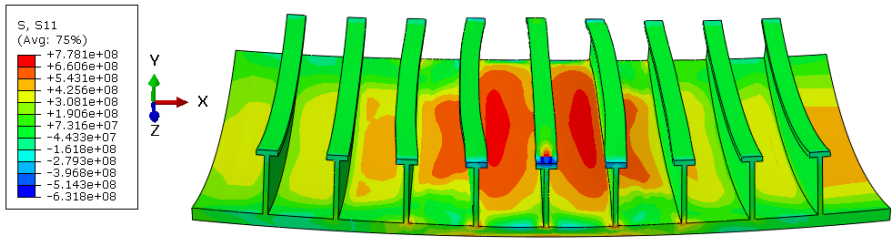

(c) Spring stiffness $\kappa = 1 \cdot 10^9$ [N/rad].

Figure 8.21: Contour plot of stresses in x-direction σ_x for fully loaded model for the different spring stiffness. The load fraction equals 1.

From figure 8.21a one can observe a large extent of tensile stresses with a magnitude of 690 [MPa] located at the centre of the plate. In figure 8.21b one can observe a smaller concentration of tensile stresses located at the centre of the plate with a higher magnitude. The maximum tensile stress reaches a magnitude of 716.3 [MPa]. While figure 8.21c has a further reduced field of tensile stresses with a magnitude of 778.1 [MPa]. This indicates that the increased boundary support raise the capability of tackling stresses, and also a better support provided to the plate by the stiffeners, regarding Hooke's law.

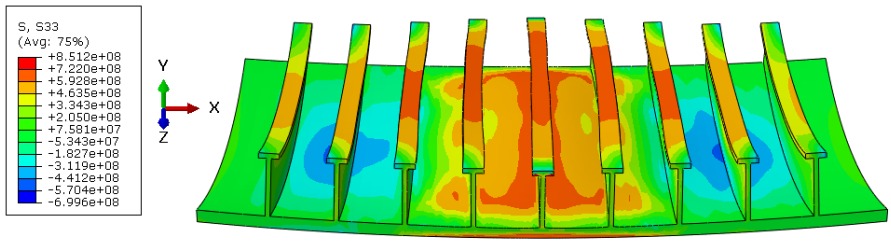

(a) Spring stiffness $\kappa = 1 \cdot 10^3$ [N/rad].

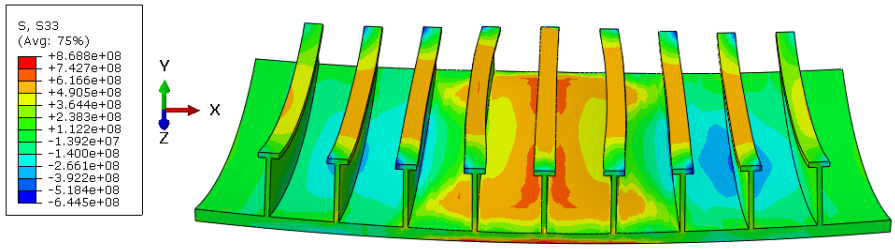

(b) Spring stiffness $\kappa = 1 \cdot 10^6$ [N/rad].

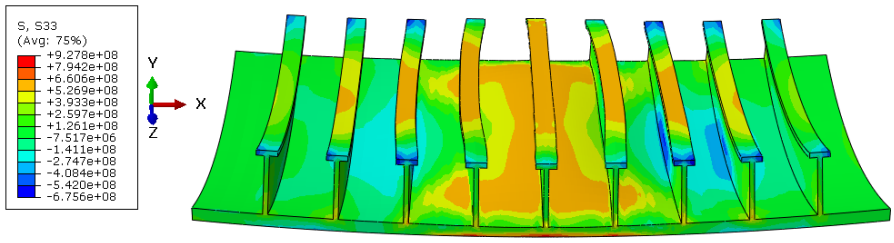

(c) Spring stiffness $\kappa = 1 \cdot 10^9$ [N/rad].

Figure 8.22: Contour plot of stresses in z-direction σ_z for fully loaded model for the different spring stiffness. The load fraction equals 1.

In figure 8.22a the tensile stress reaches a value of 722 [MPa] closest to the middle stiffener. The area of large stress is reduced further in figure 8.22b and reaches a magnitude of 742.7 [MPa]. In figure 8.22c the magnitude of the stress at the centre of the plate is 660.6 [MPa]. This indicate more support from the stiffeners as the spring stiffness is increased.

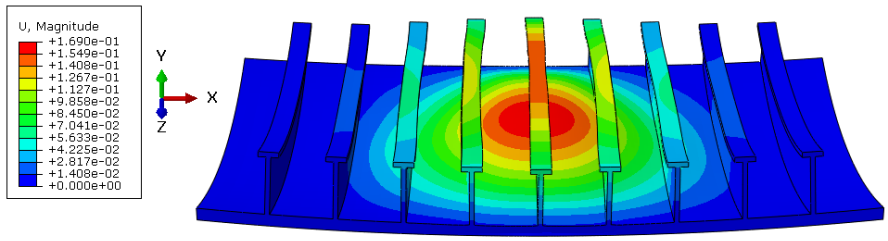

(a) Spring stiffness $\kappa = 1 \cdot 10^3$ [N/rad].

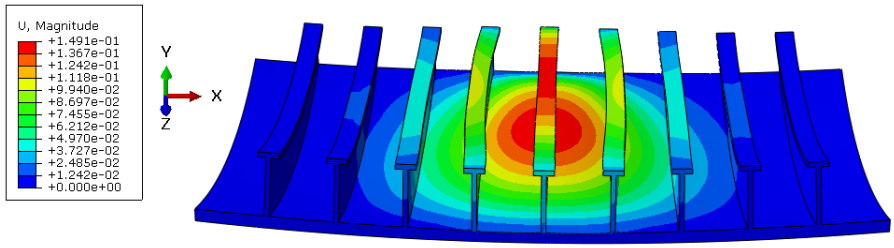

(b) Spring stiffness $\kappa = 1 \cdot 10^6$ [N/rad].

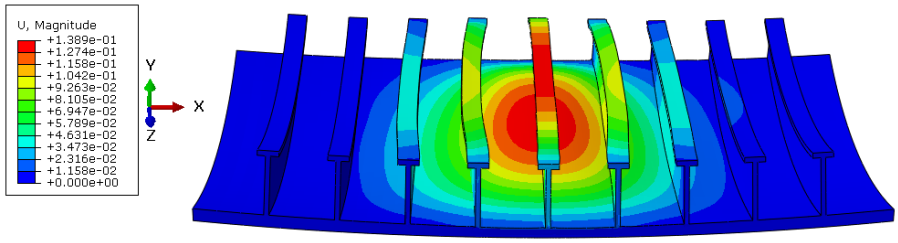

(c) Spring stiffness $\kappa = 1 \cdot 10^9$ [N/rad].

Figure 8.23: Contour plot of displacement in y-direction for fully loaded model for the different spring stiffness. The load fraction equals 1.

From figure 8.23a the maximum displacement is found equal 0.169 [m] for the centre of the plate. This is further reduced as the spring stiffness κ is increased. From figure 8.23b the maximum displacement is found equal 0.1491 [m], while in figure 8.23c the magnitude of the displacement is further reduced to a value of 0.1389 [m], for the centre of the plate. Hence, a fixed boundary would provide more support and less deflection. For the fixed boundary, the maximum displacement was found to equal 0.1087 [m].

Plate Assessment - Load Side

For the loaded side of the plate, the following stress versus true strain plots apply for the three different variations of the spring stiffness κ.

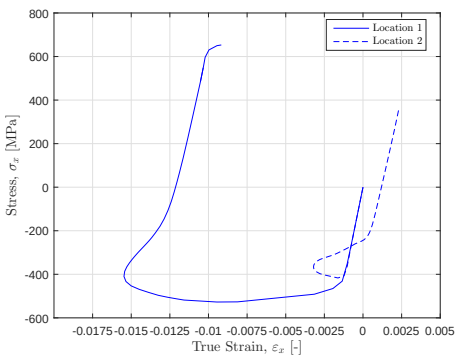

(a) Spring stiffness $\kappa = 1 \cdot 10^3$ [N/rad].

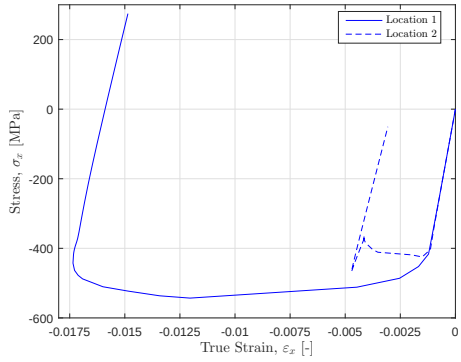

(b) Spring stiffness $\kappa = 1 \cdot 10^6$ [N/rad].

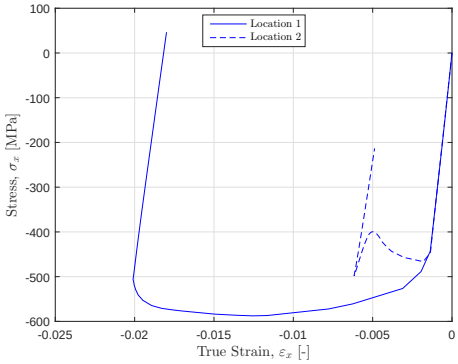

(c) Spring stiffness $\kappa = 1 \cdot 10^9$ [N/rad].

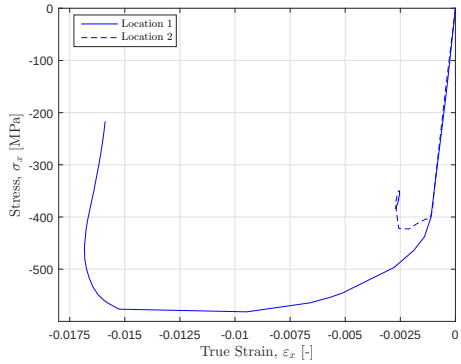

(d) Fixed boundary condition.

Figure 8.24: Stress σ_x versus true strain ε_x in x-direction at location 1 and 2 on the load side.

In figure 8.24 the curves for location 1 tend to approach the behaviour of the fixed boundary model, as the spring stiffness κ is increased, while location 2 show a different behaviour. Figure 8.24a indicate a minimum compressive stress of -525 [MPa] for location 1, and -410 [MPa] for location 2. While figure 8.24b presents a minimum compressive stress of -440 [MPa] for location 1, and -460 [MPa] for location 2. Figure 8.24c indicates a minimum compressive stress of -575 [MPa] for location 1, and -500 [MPa] for location 2. For location 1 in all figures, it is obvious that Hooke's law applies to the stress versus true strain curves. Until first yield, both locations tend to have equal behaviour as the fixed boundary model. Further study of the behaviour is given by the following figure.

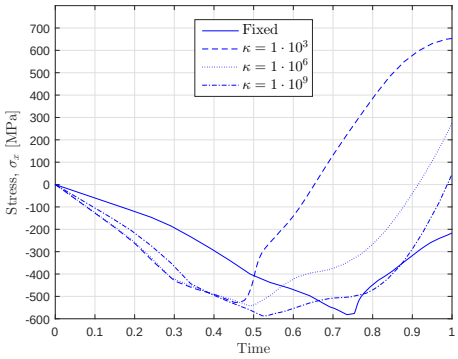

(a) Stress, σ_x, location 1.

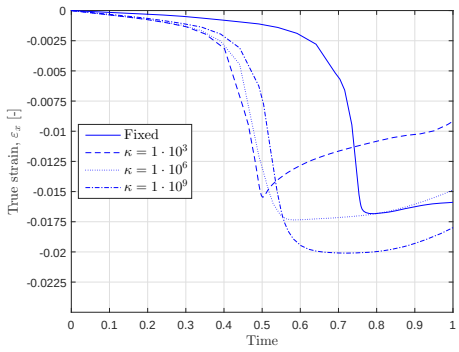

(b) True strain, ε_x, location 1.

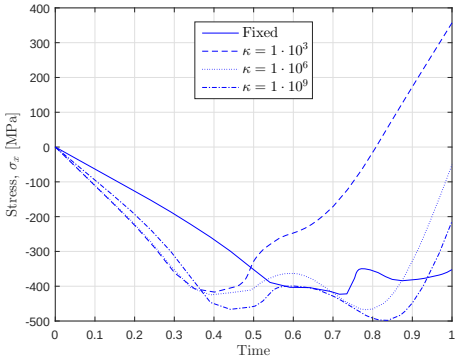

(c) Stress, σ_x, location 2.

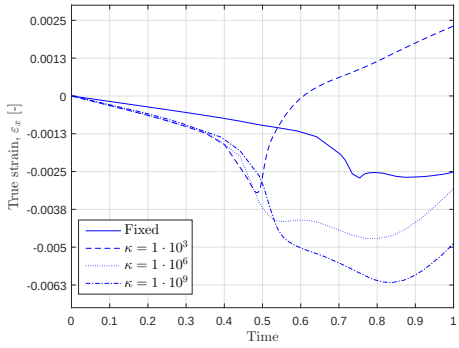

(d) True strain, ε_x, location 2.

Figure 8.25: Stress σ_x and true strain ε_x in x-direction at location 1 and 2 plotted over time. The scale on the x-axis present the load fraction.

Compared to figure 8.18, figure 8.25 does not indicate a clear behaviour approaching the fixed boundary condition, as κ is increased. In figure 8.25b and 8.25d for the curve of κ equals 10^3, one can observe a sudden increase in strains at a load fraction of 0.5. The curves of κ equals 10^6 and 10^9 do not tend to increase in the same manner. Further, one can observe a reduction in capacity. This is indicated in figure 8.25a and 8.25c, as the load fraction that defines the capacity is reduced from 0.735 for the fixed boundary condition, to a load fraction between 0.4 and 0.6 for the boundaries modelled by springs.

The same assessment for the different locations are conducted for the stresses and strains in z-direction. The following figures present the results.

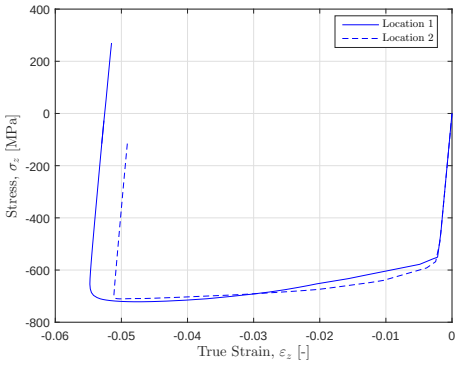

(a) Spring stiffness $\kappa = 1 \cdot 10^3$ [N/rad].

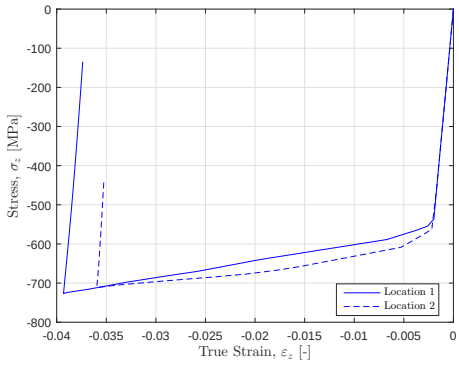

(b) Spring stiffness $\kappa = 1 \cdot 10^6$ [N/rad].

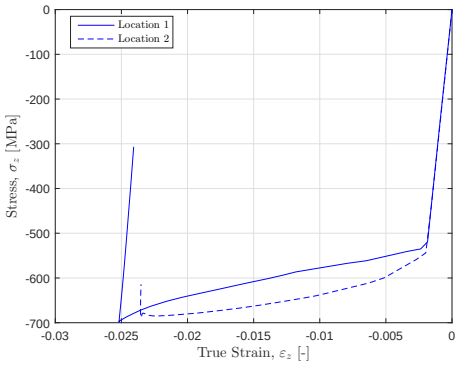

(c) Spring stiffness $\kappa = 1 \cdot 10^9$ [N/rad].

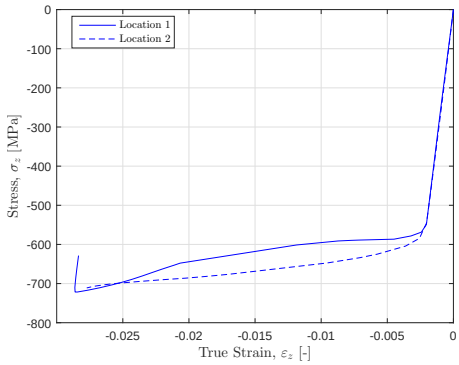

(d) Fixed boundary condition.

Figure 8.26: Stress σ_z versus true strain ε_z in z-direction at location 1 and 2 on the load side. Note the different scales between each figure.

For the stress versus true strain curves presented in figure 8.26 the increased stiffness approaches the behaviour of the fixed boundary condition. For all curves, first yield is located between a compressive stress with a magnitude of -500 and -600 [MPa]. Also, the strains at collapse are reduced as the spring stiffness is increased. After collapse, the final stress condition approaches the value of the fixed boundary condition assessment. This indicates better stiffener support of the plate, due to greater support at the stiffener ends as the spring stiffness κ is increased. The behaviour is better understood by the following figures, where the stresses and strains for location 1 and 2 are plotted over time.

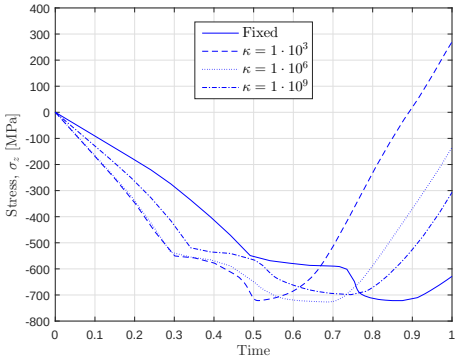

(a) Stress, σ_z, location 1.

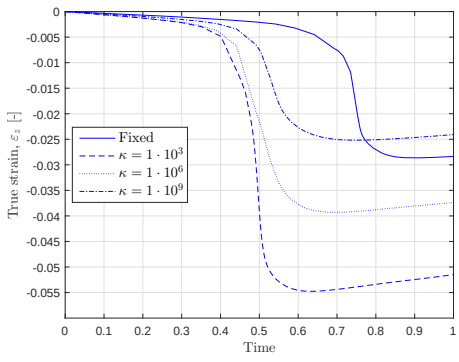

(b) True strain, ε_z, location 1.

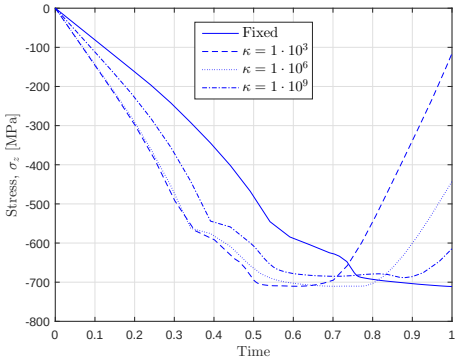

(c) Stress, σ_z, location 2.

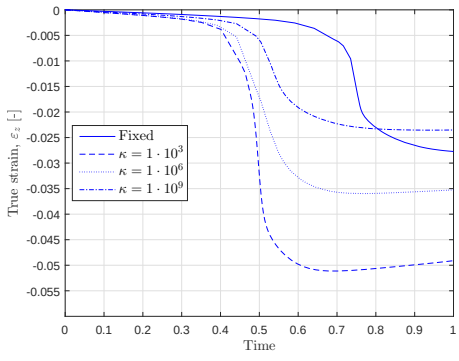

(d) True strain, ε_z, location 2.

Figure 8.27: Stress σ_z and true strain ε_z in z-direction at location 1 and 2 plotted over time. The scale on the x-axis present the load fraction.

Figure 8.26 indicates a behaviour approaching the fixed boundary condition as the spring stiffness κ is increased. Figure 8.27 substantiates this, as the curves in all cases approach the behaviour of the fixed boundary condition. Figure 8.27a and 8.27b present equal collapse load fractions (as from figure 8.18a and 8.18b), respectively 0.4, 0.45 and 0.5 for the three different magnitudes of spring stiffness. The same are observed for figure 8.27c and 8.27d. Comparing location 1 and 2, one can observe less compressive stress and true strain levels for location 2. This could indicate less support from the stiffener outlining the loaded area, as this stiffener is warping due to unsymmetrical loading. The assessment of the load side of the plate resulted in the following contour plots of stresses in x- and z-direction, as well as displacement in y-direction, in a fully loaded condition.

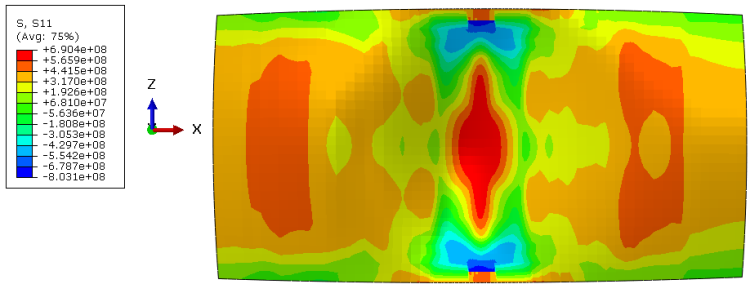

(a) Spring stiffness $\kappa = 1 \cdot 10^3$ [N/rad].

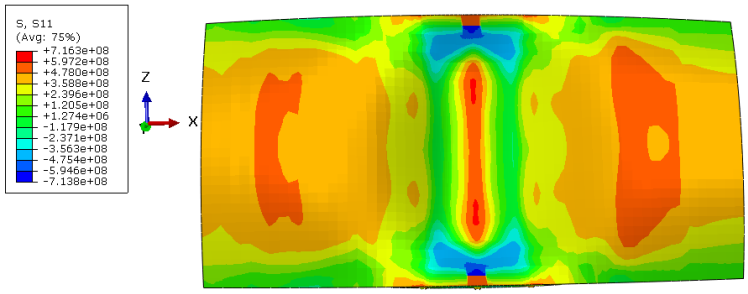

(b) Spring stiffness $\kappa = 1 \cdot 10^6$ [N/rad].

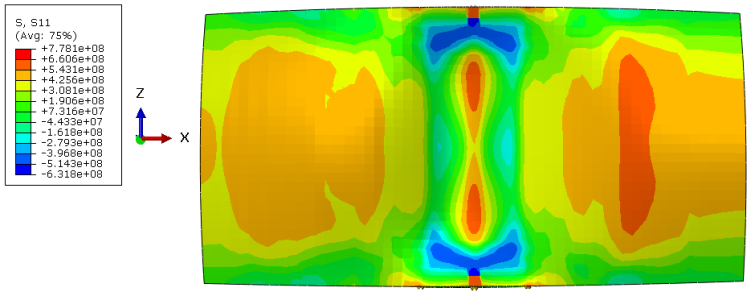

(c) Spring stiffness $\kappa = 1 \cdot 10^9$ [N/rad].

Figure 8.28: Contour plot of stresses in x-direction σ_x for fully loaded model for the different spring stiffness. The load fraction equals 1.

In figure 8.28a one can observe a maximum tensile stress of 690.4 [MPa] located at the centre of the plate, while the largest compressive stress is found equal -803.1 [MPa] located under the middle stiffener. As the spring stiffness was increased, the maximum tensile stress at the centre of the plate reduces to 597.2 [MPa], and the tensile stresses are increased to -713.8 [MPa] as shown in figure 8.28b. In figure 8.28c, the same stresses change to 425.6 [MPa] and -631.8 [MPa] respectively. The stiffeners do provide support for the plate in x-direction as the increased support reduces stresses in x-direction, hence Hooke's law applies.

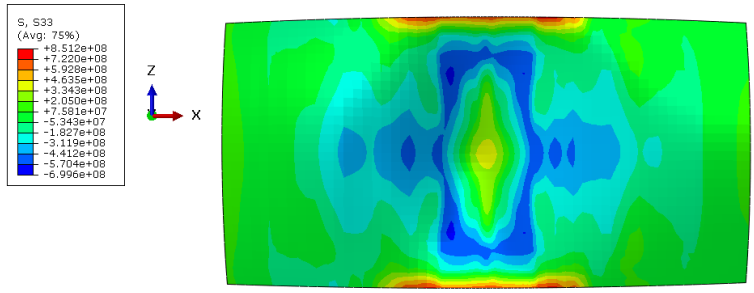

(a) Spring stiffness $\kappa = 1 \cdot 10^3$ [N/rad].

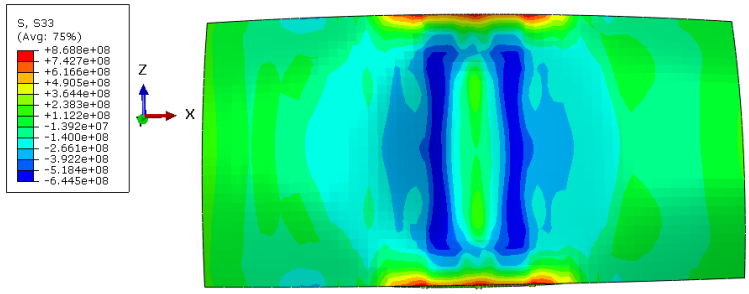

(b) Spring stiffness $\kappa = 1 \cdot 10^6$ [N/rad].

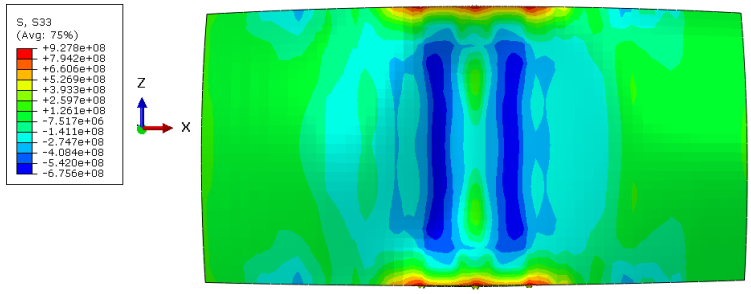

(c) Spring stiffness $\kappa = 1 \cdot 10^9$ [N/rad].

Figure 8.29: Contour plot of stresses in z-direction σ_z for fully loaded model for the different spring stiffness. The load fraction equals 1.

From figure 8.29a the tensile stress at the centre of the plate reaches a magnitude of 463.5 [MPa], while the largest compressive stress is located beside the middle stiffener, reaching a level of -570.4 [MPa]. The same locations in figure 8.29b reach a level of 364.4 and -644.5 [MPa] respectively. Further increase of the spring stiffness, presented in figure 8.29c, results in -141.1 [MPa] for the centre of the plate, and -675.6 [MPa] for the area besides the middle stiffener. As the stiffeners are assigned larger rotational restriction, due to increased spring stiffness, the collapse of the three middle stiffeners induce more compressive stresses in z-direction to the load side of the plate.

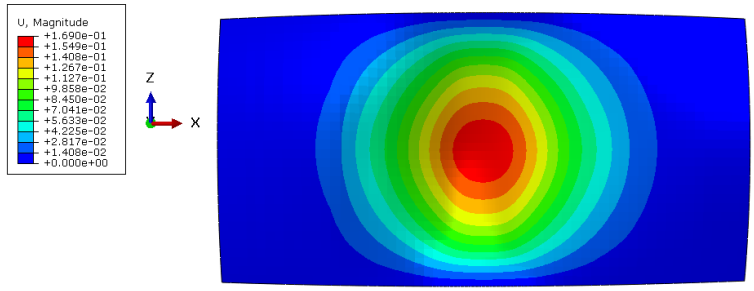

(a) Spring stiffness $\kappa = 1 \cdot 10^3$ [N/rad].

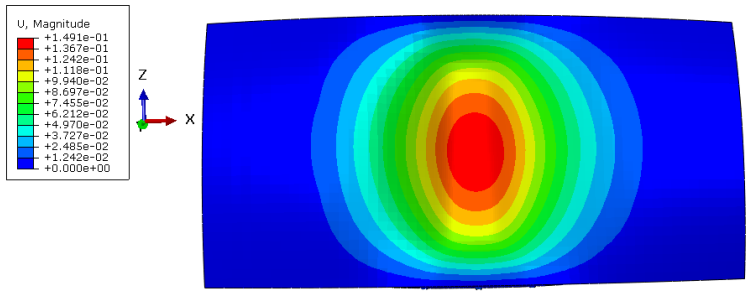

(b) Spring stiffness $\kappa = 1 \cdot 10^6$ [N/rad].

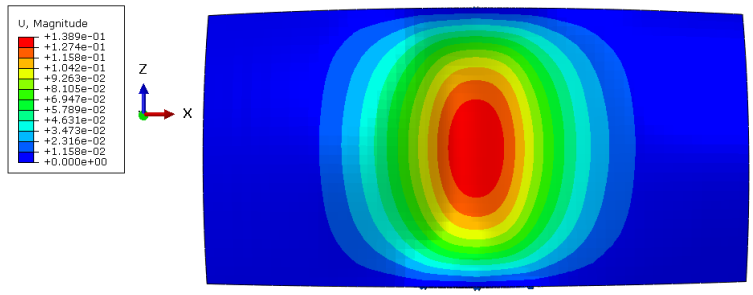

(c) Spring stiffness $\kappa = 1 \cdot 10^9$ [N/rad].

Figure 8.30: Contour plot of displacement in y-direction for fully loaded model for the different spring stiffness. The load fraction equals 1.

In figure 8.30 the maximum displacement in y-direction is 0.169, 0.1491 and 0.1389 [m] found from figure 8.30a, 8.30b and 8.30c, respectively. This indicates more support from the stiffeners, as the spring stiffness κ is increased.

For more plots of stress versus true strain from the boundary assessment, these could be found in appendix F.3.

8.4.4 Findings From the Bow Model Assessment

The four different boundary conditions, where three of them were modelled by application of rotational springs and one was fixed against both translation and rotation, gave four different load capacities. By applying the capacities (load fractions) in the contact pressure formula (equation 8.1), a critical ridge ice thickness $h_{i,crit}$ could be estimated. The empirical contact pressure $p_{c,emp}$ was estimated to 47 [MPa]. Simple calculations give the following equation:

$$h_{i,crit} = \sqrt{\frac{\delta \cdot p_{c,emp} \cdot A \cdot \big(\sin(\beta) - 0.1 \cdot \cos(\beta)\big)}{C_{geo} \cdot \sigma_f(\eta_b)}} \tag{8.4}$$

Applying the original values for the angle β, geometrical constant C_{geo}, contact area A and flexural strength $\sigma_f(\eta_b)$ (from table 8.5), and apply the load fraction δ to the empirical contact pressure $p_{c,emp}$, one obtain the following equation:

$$h_{i,crit} = 3.63 \cdot \sqrt{\delta} \tag{8.5}$$

Equation 8.5 could be applied to estimate the critical ice thickness $h_{i,crit}$ for each boundary condition, by use of the load fraction δ at collapse. Additionally, one could apply the load fraction to estimate both the critical contact pressure $p_{c,crit}$ and resultant force $F_{R,crit}$. Where the critical resultant force $F_{R,crit}$ is estimated by equation 8.6 and the critical contact pressure $p_{c,crit}$ is given by equation 8.7.

$$F_{R,crit} = \delta \cdot p_{c,emp} \cdot A \tag{8.6}$$

$$p_{c,crit} = \delta \cdot p_{c,emp} \tag{8.7}$$

From equation 8.6 A is the contact area. The following table presents the results and the maximum plate deflection u_{max} when δ equals 1.

Table 8.7: Critical values for the different boundary conditions.

Boundary	δ [-]	$h_{i,crit}$ [m]	$p_{c,crit}$ [MPa]	$F_{R,crit}$ [kN]	u_{max} [m]
Fixed	0.735	3.11	34.55	13820	0.1087
$\kappa = 10^3$	0.400	2.29	18.80	7520	0.1690
$\kappa = 10^6$	0.450	2.44	21.15	8460	0.1491
$\kappa = 10^9$	0.500	2.57	23.50	9400	0.1389

8.5 Discussion of the Bow Model Results

This section provides a discussion of the results from the bow model assessment for both fixed and varying boundary conditions. For this chapter, two main topics have been assessed. The first analysis applied fixed boundaries and and the empirical ice pressure found from measurements of ridged ice. The aim was to study the plate behaviour. The second analysis applied three different boundary conditions modelled by different supports applying rotational springs to the end of each stiffener, allowing the cross section to rotate about the plate edge. The aim of this assessment was to study the impact of various girder frame support and compare it to the fixed boundary model.

The Fixed Boundary Model

The fixed boundary problem was exposed to a pressure of 47 [MPa] obtained from the sea ice measurements applying the empirical ice pressure formula. At a load fraction δ equal 0.735, the middle stiffener started to develop plastic hinges close to the boundaries. While the stiffeners located next to the middle one initiated warping, and the plate centre collapsed. This indicated that the plate model could withstand a load of 34.55 [MPa], hence the critical ice height $h_{i,crit}$ became 3.11 [m], as given in table 8.7. The ridge had a total height of 3.63 [m] which turned out to be large enough to create collapse in the model. Thus, this is only valid if the ridge has an average flexural strength of 0.904 [MPa] and the geometrical coefficient equals 0.75. Also, the contact area must equal 0.4 [m^2] to create such a pressure. In figure F.15, F.16 and F.17 given in appendix F.1, one can observe the collapse and warping of the three middle stiffeners. It should be noted that the displacement is multiplied with a factor to be visible in these figures. The plastic hinges are located at each end of the middle stiffener. From figure F.16b one can observe a stress in y-direction, located at the webbing close to the ends, with a magnitude of -500 [MPa]. This indicates yielding across the webbing as the stress level is above the yield stress of the applied steel. The effect of this collapse is displayed in figure F.15 where the webbing of the three middle stiffeners suffers from compressive stresses with a magnitude of -609 [MPa] located close to the plate, prior to collapse. After collapse, the webbing suffers from tensile stresses with a magnitude of 686.4 [MPa] located close to the flange. In figure 8.7 and 8.8 one can observe how the stiffener support is activated and how the stress pattern changes due to collapse. Prior to collapse, the maximum displacement was found to equal 0.0022 [m], which is small compared to the displacement post buckling. After the collapse, the plate was displaced 0.1087 [m]. This indicates that the stiffeners are a critical support for the plate. In figure 8.8a one can observe compressive stresses in z-direction with a magnitude of -727.8 [MPa] located at the flange ends of the three middle stiffeners. Hence, large forces would be induced to the supportive frames prior to collapse. Post collapse, as shown in figure 8.8b, the magnitude of stresses at the flange ends have decreased to a value of -688.6 [MPa]. Thus, the five middle stiffeners now have stresses with large magnitude located at the flanges. These stress concentrations would induce larger transverse

stresses to the supportive frames, as two additional stiffeners now induce stresses to the support. This indicates that the boundaries of the plate should be assessed, as fixed boundary conditions would not describe actual conditions.

The Spring Modelled Boundary Model

The boundaries were assessed by applying three different springs with various stiffness. For the assessments, the stiffness κ were set to 10^3, 10^6 and 10^9 [N/rad]. The applied pressure was set to 47 [MPa]. In table 8.7 the load fractions δ and critical ice height $h_{i,crit}$ are given. For a spring stiffness κ of 10^3, the load fraction δ was found to equal 0.4 in general. This resulted in a critical ice height $h_{i,crit}$ of 2.29 [m]. Hence, an ice ridge height of 3.63 [m] would collapse the plate and surrounding supportive frames. Compared to the fixed model, the stiffeners did not suffer from the same development of a plastic hinge and warping. The maximum tensile plate stress found in figure 8.21 and 8.22 for a load fraction δ equals 1, were 690 and 722 [MPa] for x- and z-direction respectively. Compared to the fixed model, where the same stress components reached 690.1 and 686.4 [MPa]. This indicates better support from the stiffeners located at the plate when the boundaries are fixed, as the collapse load fraction is higher in the fixed boundary case. Also, more forces are transferred to the stiffeners as the plate stress is reduced in the fixed boundary model. The displacement found from the model with κ equals 10^3, was found equal 0.169 [m]. This is almost 0.07 [m] larger than for the fixed model. Relative to the stiffener height of 0.170 [m], the spring modelled boundary model suffer from large displacements.

As the spring stiffness along the boundaries was increased to κ equals 10^6, the load fraction δ increased to 0.45 and the critical ice height $h_{i,crit}$ became 2.44 [m]. A ridge height of 3.63 [m] would still result in plate collapse. Compared to what found from the assessment applying springs with κ equal 10^3, this boundary condition indicates slightly more warping of the two stiffeners surrounding the middle stiffener. Additionally, the middle stiffener indicates collapse. In figure 8.22 one can observe a change in stresses located at the stiffener flanges. The five middle stiffeners in figure 8.22a has a maximum tensile stress of 722 [MPa], while in figure 8.22b this is reduced to 616.6 [MPa]. This reduction is caused by a more even stress distribution for the flanges. Also, one can observe a reduction in stresses for the outermost located stiffeners. Similar behaviour for the plate stress could be observed for figure 8.21a and 8.21b, and figure 8.22a and 8.22b. The magnitude of the stress is increased, while the extent is reduced towards the centre of the plate. Additionally, the displacement reduces from 0.169 to 0.1491 [m] as κ is increased.

By applying a spring stiffness κ of 10^9 [N/rad] the critical ice thickness $h_{i,crit}$ increased to 2.57 [m] and the load fraction δ increased to 0.5. For a load fraction of 1, the maximum tensile plate stress in x- and z-direction were found to equal 778.1 and 660.6 [MPa] from figure 8.21c and 8.22c respectively. Compared to the model where κ equals 10^3, this model has an increased stress level in x-direction and a decreased stress level in z-direction. The change in stresses is reasonably

due to better support in z-direction, parallel to the stiffeners. For the stiffeners, the flange stress in z-direction was found to equal 660.6 [MPa] in tension. This is a decrease compared to the model with κ equal 10^3, while it is an increase compared to the model with κ equal 10^6. An important notice is the extent of the stresses. For this model, the five middle stiffeners are the most affected ones. While for the model applying κ equal 10^6, the seven middle stiffeners are impacted by the stress level of 616.6 [MPa]. The increased stress level for the last model, is reasonably due to higher stresses distributed to fewer stiffeners. The displacement in y-direction is reduced to a maximum value of 0.1389 [m] for the centre of the plate. Additionally, the area suffering from displacement is further reduced in extent (in x-direction) as the spring stiffness was increased. This implies that stiffer boundaries reduce the extent of the displacement for the plate field in x-direction, and increase it in z-direction.

Short Discussion of Results Presented in Appendix F.3

In general does the behaviour of the stress and true strain approach the fixed boundary behaviour as the spring stiffness is increased. By comparing the locations 1-10 for the plate, one observes a small increase in the load fraction δ, as the location of sampling is located further away from the plate centre. Additionally, it is observed that the true strain decrease rapidly. For location 9 and 10, the behaviour is different for the model with springs compared to the fixed boundary model. Reasonably due to slight differences in the modelling of the boundaries, and the locations were sufficiently close to the boundary. For the fixed boundary condition, all edges were fixed. While for the model with springs, the motion of the stiffener ends required ability to move in z-direction. To avoid errors in Abaqus, the plate edge between each stiffener could not be restricted with translation in z-direction, as the nodes defining the interaction between stiffener and plate would create an error.

For the stiffener assessment, the stress level was approximately identical in all cases. The main difference was the strain level. Between the weakest and stiffest spring, the strain level was reduced more than three times the initial value. For the fixed boundary problem, the strain reduction was approximately 10 times the strain value of the weakest spring boundary. The figures presenting stress and true strain plotted over time indicate an approach towards the fixed boundary condition as the spring stiffness was increased. For sampling location 5 and 6 (for the stiffeners, see figure F.10), located closest to the boundaries, the difference in behaviour was large. Reasonably affected by the same issue as for the sampling location 9 and 10 located at the plate. Also, the critical load fractions δ were increased compared to the ones found from the plate centre.

Chapter 9

Discussion of Results

This section will summarize all the discussions presented in chapter 3 - Measurements of Sea Ice Strength, chapter 5 - Review of Ship Classification, chapter 7 - Results of Analysis Based on Level Ice Measurements and Regulations and chapter 8 - Results of Analysis Based on Ridge Ice Measurements. Hence, only present the findings regarded most important. The reader should be familiar with the results previously presented, and also the results presented in the appendix.

Measurement of Sea Ice Strength

The measurements consisted of two types of ice, both level ice and ridged ice. For the level ice data, the findings coincide well with Timco and Weeks (2010). The low saline ice should have had higher compressive strength. Thus, from the data set it was found that the low saline ice also had high temperature in which made it ductile and porous (i.e. weak), hence only reached strengths up to 2.5 [MPa] in compression. The ice with higher salinity were cold and reached strengths up to 25 [MPa]. The flexural strength depends on the brine porosity, which in term depends on temperature, as low temperature give less porosity. This resulted in high flexural strength for the samples with high compressive strength (and low temperature). From the data set, there existed no data describing the volume of the samples. By applying a uniformly distributed random variable for description of the diameter, it was found that 10 [mm] variation of the diameter gave a deviation in the flexural strength of 6.356 [%]. The average flexural strength was found to equal 0.499 [MPa]. According to Ekeberg (2015), this level ice should be first-year ice.

For the ridged ice data, the salinities reached from 2 to 6 [%] and the compressive strength varied between 2 and 10 [MPa], while the temperatures were located between -17 to -20 [°C]. According to Ekeberg (2015) this is a second-year ridge, and was substantiated by low temperatures and porosities. As a result, the flexural strength became higher than for the level ice. The consolidation process is also a

factor affecting the porosity. Applying a variable diameter of 10 [mm] to account for the variation in volume that may occur, the flexural strength became 0.904 [MPa] with a deviation of 5.23 [%] compared to tests where the samples were assumed perfect without imperfections.

Review of Ship Classification

The two regulations applied in this thesis were provided by DNV GL and IACS. The main difference between the two regulations were the class criteria. DNV GL defined the class notations based on the ice thickness and ramming conditions that may occur during operation, and also the area of operation. While IACS defined their classes with respect to operational time and expected ice age without considering the operational area. From DNV GL, the load patch area was one of the input parameters, while for IACS one applied the calculated loads to provide both contact pressure and area. IACS also applied class coefficients decided by the vessel class, which in terms were applied in the calculation of the loads. DNV GL applied structural dimensions as a criterion for decision of the coefficients applying to the formulas. Also, location of the interaction area was a criterion stated by DNV GL. Holm (2012) found the plate thickness and design load to be generally higher for IACS class PC-1, compared to DNV GL class *Icebreaker* POLAR-10.

Results of Analysis Based on Level Ice Measurements and Regulations

The three different contact pressures were found to equal 1.475, 6.419 and 15.56 [MPa] from the empirical pressure model, DNV GL and IACS respectively. All pressures induced stresses above yield to the plate model and initiated non-linearities. As the pressure increased, the displacement, stresses and strain were increased. The behaviour is according to Moan (2003), as increased forces and pressures would induce larger body forces. The effect of the Poisson's ratio was also observed. All three assessments had occasions of increasing stress in z-direction with negative strains, until yielding occured in x-direction, and the strains ended up positive in z-direction. For the empirical pressure model, it was only observed yield stress between the middle stiffeners where the load was applied. While the other two models had a larger field of initial yield. The two middle stiffeners suffered from warping due to the empirical ice pressure, while the two outermost stiffeners suffered from warping as the ice pressure from the regulations were applied.

Results of Analysis Based on Ridge Ice Measurements

The analysis applied an ice ridge pressure estimated equal 47 [MPa] and four different boundary conditions. The first assessment applied fixed boundaries which indicated a collapse at a load fraction δ equal 0.735. This resulted in a critical contact pressure of 34.55 [MPa] and a critical ice height of 3.11 [m]. For loads higher than the critical load, the middle stiffener developed plastic hinges at the

ends and the two stiffeners located along the load boundary warped. The maximum deflection was found to 0.1087 [m] in y-direction. For the three boundary assessments applying springs to support the stiffener ends, the load fractions were reduced to 0.4, 0.45 and 0.5 for the springs with stiffness κ equals 10^3, 10^6 and 10^9 respectively. A collapse should occur faster as the support is reduced. The reduction in δ resulted in a reduced critical ice height $h_{i,crit}$, and also larger maximum displacement u_{max} of the plate centre. For these three models, the load fraction changed slightly as the sampling location was moved further from the plate centre. Further, it was found irregularities for the locations close to the boundaries when compared to the fixed model. As κ was increased, the stresses and true strains for each sampling location tended to approach the behaviour of the fixed model, as an infinitely stiff spring would act as a fixed boundary.

Chapter 10

Conclusions

Several topics have been investigated throughout this thesis. This chapter will present the conclusions of each topic. The main conclusions are listed in the end of this chapter, to give the reader the ability to get a good overview.

Measurements of Sea Ice Strength

The measurements of sea ice provide results of level ice and ridged ice, with 91 and 108 measurements respectively. The measurements behave according to Timco and Weeks (2010), as warm and porous ice behave ductile and cold ice, with less porosity, are stronger than the weak ductile ice. Further, it should be noted that the porosities are estimates based on temperature, density and salinity (based on Cox and Weeks (1983)). Deviation from actual conditions may therefore occur. The flexural strength is an empirical function based on the brine porosity of the measurements (based on Timco et al. (1994)). Due to the fact that both the flexural strength and brine porosity are based on empirical formulas, the obtained flexural strengths may not present the actual level ice and ridged ice which were physically measured. Additionally, the strength of ice is difficult to determine as it depends on grain size and direction, load rate, temperature, salinity and porosity. The temperature was found dominant compared to salinity, regarding ice strength. Further, it is believed that the measured levels of flexural strengths may occur during operations in ice infested waters. Also, the measurements are gathered with low spatial resolution. This will lead to a representation of the specific area where the measurements were conducted, as sea ice have large spatial and temporal variations. Additionally, it is difficult to say whether the modelling of defect variation is valid, as no data about the degree of defect for each sample existed.

Ice-Structure Interaction

The interaction model between ship and ice is a simplified model where both spalling and crushing are disregarded. Further, the contact area is simplified and given a fixed value, even tough the contact area will have temporal variations. The difficulty in such a model, is to define a length and height of the contact area. For a ship operating in ice, the number of interactions depend on the ice concentration, and typically be very large. Hence, the interaction model provides an estimate of one ice-structure interaction. Further, one could assume that the pressure condition may occur once during operations, while it is not necessarily a representation of the conditions presented by the sea ice data sets.

Review of Ship Classification

The two regulations presented by DNV GL and IACS are based on different sea ice observations and model tests. Their prediction of the contact pressure do differ. Additionally, do the safety factors and coefficients applied in their equations differ. After the scaling of the contact pressure, the two regulations provided contact pressures quite different in magnitude. Further, one could assume both regulations to account for uncertainty in the ice-structure interaction model by applying safety factors, and also apply ridged ice for load prediction as the pressure levels were significantly high compared to the empirical pressure obtained from level ice. Regarding the difference in pressure level between DNV GL and IACS, it is reason to believe that the design loads provided by IACS are generally higher than DNV GL, when considering the two classes PC-1 and *Icebreaker* POLAR-10.

Results of Analysis Based on Level Ice Measurements and Regulations

The plate model was exposed to three different contact pressures, one empirical and two obtained from regulations. For this assessment, the height of the contact area was set to 0.4 [m]. As lower contact area heights can occur, this could underestimate the force concentrations that may occur during ship-ice interaction. A high force concentration can cause severe damage to the plate. Hence, the plating is critical and the assessment with focus on the plate proved to be a good approach as the stiffener spacing was large. The results from the assessment indicate the dimensions to be a minimum requirement from the classification companies. Considering the magnitude of forces induced to the model, the stiffener dimensions should have been larger and the stiffener spacing should be reduced. To comply with the applied pressures, the model should have a thicker plate and a narrower stiffener spacing. By comparing the three different pressures, the empirical contact pressure model is low, reasonably due to absent of safety factors.

Results of Analysis Based on Ridge Ice Measurements

During the modelling of the bow model, the findings from the plate model were taken into account. This turned out to increase the capacity of the plate, regarding the pressure level from the ridged ice which was approximately 30 times the pressure from the level ice. The assessment of the bow model applied four different boundaries, one fixed and three modelled by rotational springs applied to the cross section of each stiffener end. Not unlikely was the fixed boundary more resistant to the applied pressure, compared to the three spring modelled boundaries. Further, the increased spring stiffness acted according to Moan (2003), as the behaviour indicated an approach towards the behaviour of the fixed model. Thus, there exist only an indication of such an approach. Hence, the spring stiffness should have been increased further. Also, the rotational springs were only able to account for warping of the supporting frames. In addition, only one type of failure was assessed in the model. From the model, it was found that the stiffeners also could develop plastic hinges, which in term also could occur for the supportive frames. The model did in all four cases enter the non-linear region, thus permanent deformations will not necessarily imply total failure. Compared to the boundaries with rotational springs, the fixed boundary condition is a non-conservative condition when assessing a local model.

Main Findings From the Conclusions

The main conclusions are listed by the bullet points below:

- The empirical contact model is able to give a simplified estimate of the contact pressure for one interaction with ice, as there are several simplified factors in the establishment of the empirical formula.
- The ice will have large temporal and spatial variation. Hence, the two data sets applied to estimate flexural strength will only be valid for the certain ice feature and location they present. Additionally, the ice feature will change property over time.
- The regulations provided by DNV GL and IACS provide different results regarding the contact pressure, and the method of obtaining the pressure differs.
- The DNV GL regulations provide an absolute minimum requirement for the dimensions of plate fields. This resulted in improvements for the bow model.
- The modelling of boundaries was able to represent warping of the supportive frames, and does not account for development of plastic hinges in the frames.
- The non-linear analysis proved to be a correct choice, regarding the fact that both models entered the non-linear behaviour region and suffered from permanent deformations. The permanent deformations were expected.

Chapter 11

Further Work and Recommendations

This section presents suggestions to further work which could be conducted to give a more detailed plate assessment. The assessments provided in this thesis do only consider static assessment of the models, with evenly distributed loads over a constant contact area. The applied ice pressures are found trough empirical formulas and regulations. Several measures could be further investigated to provide even more realistic and accurate results.

Both plate models had arbitrarily chosen main dimensions for the plates. Also, the curved bow model applied curvature, where span and radius were chosen trying to fit the hull angles of an ice going vessel. To give a better prediction of actual conditions, a FE-model of an actual ship bow could be applied in further assessments. This would provide more accurate dimensioning, hull angles and boundary conditions for the local plate models. The boundaries for the global bow model could be assumed fixed, as the distance between the loaded area and boundaries would be large. Hence, the local support for the local plate models would provide boundaries closer to actual conditions.

Regarding the fixed boundaries, they were found non-conservative in a perspective of actual conditions. Further, the boundaries were modelled by springs supporting the stiffener end cross section. The sampling points closest to the boundaries indicated a behaviour not approaching the behaviour of the fixed boundary, as the spring stiffness was increased. For further work, the modelling of the boundaries applying spring stiffness should be improved. The issue was found for the plate edge between the stiffeners. This issue could be fixed by applying translational springs with large stiffness in z-direction to prevent motion of the plate edge. Further studies could apply more spring stiffness tests to confirm that the spring modelled boundaries approach the fixed model, as the three tests conducted in this thesis only give indication of such an approach. Also, the supportive frames could collapse in the same manner as the middle stiffener of the bow model. To

simulate such a collapse, translational springs in y-direction could be applied along the plate edge in further studies.

The measurement of ice consisted of 91 and 108 different samples for level ice and ridged ice, respectively. By applying even more tests, one could develop an even better approximation of actual ice conditions for further studies. Additionally, one could perform flexural strength tests of sea ice to obtain a better estimate on flexural strength data. As ice not necessarily fail in bending, other failure modes could occur as well. In example, splitting and crushing may occur prior to bending failure. By conducting a contact problem between a bow model and a body with a material applying material properties of ice, one could perform an even more realistic assessment in further studies. This study could also include arbitrary shapes of the body, to investigate variety of the contact area.

Bibliography

Abaqus. Abaqus - solving nonlinear problems. ivt-abaqusdoc.ivt.ntnu.no:2080/v6.14/books/usb/pt03ch07s01aus49.html. Accessed: 2017-03-03.

Abaqus (2016). Abaqus - theory. http://ivt-abaqusdoc.ivt.ntnu.no:2080/v6.14/books/usb/default.htm. Accessed: 2017-04-01.

Cox, G. F. N. and Weeks, W. F. (1975). Brine drainage and initial salt entrapment in sodium chloride ice. Technical report, U.S. Cold regions research and engineering laboratory, report. No. 345.

Cox, G. F. N. and Weeks, W. F. (1983). Equations for determining the gas and brine volumes in sea-ice samples. *Journal of Glaciology*, 29(102).

Ekeberg, O.-C. (2015). Studies of ice ridge shape and geometry from upward looking sonar data.

Gans, H. and Woodmansee, P. (1992). An improved method of modeling porous materials using finite elements. *Computers & Structures*, 44(5):1055–1063.

Holm, H. (2012). Ice-induced loads on ship hulls. Master's thesis, Institutt for marin teknikk.

Høyland, K. V. (2015). Ice mechanics, a brief introduction.

Høyland, K. V. (n.d.). At-334 arctic marine measurements techniques, operations and transport - module i sea ice features and properties.

IACS (2016). Unified requirements for polar ships. *Retrived from http://www.iacs.org.uk/search-result?query=polar.*

Leira, B., Børsheim, L., Espeland, Ø., and Amdahl, J. (2009). Ice-load estimation for a ship hull based on continuous response monitoring. *Proceedings of the Institution of Mechanical Engineers, Part M: Journal of Engineering for the Maritime Environment*, 223(4):529–540.

Leira, B. J. (2011). Tmr4170 marine structure basic course. *Departmetn of Marine structure, NTNU, Norway.*

Leppäranta, M. and Manninen, T. (1988). The brine and gas content of sea ice with attention to low salinities and high temperatures.

Løset, S. (n.d.). Ice physics and mechanics.

Løset, S., Shkhinek, K. N., Gudmestad, O. T., and Høyland, K. V. (2006). *Actions from ice on arctic offshore and coastal structures*. LAN.

Moan, T. (2003). Finite element modelling and analysis of marine structures. *Department of Marine Technology, NTNU*.

Moslet, P. (2007). Field testing of uniaxial compression strength of columnar sea ice. *Cold Regions Science and Technology*, 48(1):1–14.

Pounder, E. R. (1965). *The physics of ice*. Oxford, etc. Pergamon Press.

Riska, K. (2011). Ship-ice interaction in ship design: Theory and practice. *Course Material NTNU*.

Riska, K. and Kämäräinen, J. (2011). A review of ice loading and the evolution of the finnish-swedish ice class rules. In *Proceedings of the SNAME Annual Meeting and Expo. November*, pages 16–18.

Sinha, N. (1989). Elasticity of natural types of polycrystalline ice. *Cold Regions Science and Technology*, 17:127–135.

Thorsen, I. B. (2012). Estimation and computation of ice-resistance for ship hulls. Master's thesis, Institutt for marin teknikk.

Timco, G. and Burden, R. (1997). An analysis of the shapes of sea ice ridges. *Cold regions science and technology*, 25(1):65–77.

Timco, G. et al. (1994). Flexural strength equation for sea ice. *Cold Regions Science and Technology*, 22(3):285–298.

Timco, G. and Frederking, R. (1990). Compressive strength of sea ice sheets. *Cold Regions Science and Technology*, 17(3):227–240.

Timco, G. and Weeks, W. (2010). A review of the engineering properties of sea ice. *Cold Regions Science and Technology*, 60(2):107–129.

Tuhkuri, J. (2014). Ice ridge formation.

Veritas, D. N. (2016). Rules for classification of ships: Part 5, chapter 1-ships for navigation in ice. *Retrieved from https://www.dnvgl.com/about/index.html*.

Weeks, W. and Assur, A. (1967). The mechanical properties of sea ice. *Cold Regions Science and Engineering*, 2(C):80.

WMO, W. M. O. (1970). *WMO Sea-ice Nomenclature*, volume 145. Secretariat of the World Meteorological Organization.

Appendix A

Sea Ice Measurement Data

This chapter contains data applied to obtain the plots presented in chapter 3. The data for level ice were measured at Frysjaodden between May 31^{st} and June 6^{th} 2004. The data for ridged ice were measured in the Barents Sea October 21^{st} 2004. The level ice data consist of vertical samples, while the ridged ice consist of a variety of orientations of the basal planes.

A.1 Level Ice Porosities and Flexural Strengths

Table A.1 presents the porosities calculated based on the measurements conducted by K. V. Høyland and the approximated flexural strength. The MATLAB scripts applied to obtain these values are given in appendix B. The porosities are obtained based on the assumptions that the diameter D had a constant value 70 [mm] and a length L 175 [mm].

Table A.1: Air porosities η_a, brine porosities η_b, total porosities η_T and flexural strength σ_f for a sample length L 175 [mm] and diameter D 70 [mm].

Sample #	η_a	η_b	η_T	σ_f
1	0.14189006	0.00710416	0.14899422	1.07219834
2	0.05143267	0.01215048	0.06358316	0.92050385
3	0.04621147	0.01091045	0.05712192	0.95230449
4	0.05068788	0.00971422	0.06040210	0.98587732
5	0.02177439	0.01016948	0.03194387	0.97273063
6	0.03999723	0.01170175	0.05169898	0.93169189
7	0.17836258	0.01025646	0.18861904	0.97027244
8	0.04680844	0.01286317	0.05967161	0.90341624
9	0.02556356	0.01200486	0.03756842	0.92409684
10	0.03536485	0.01238779	0.04775263	0.91472415
11	0.02576691	0.01267004	0.03843695	0.90796771

Sample #	η_a	η_b	η_T	σ_f
12	0.01387670	0.01073373	0.02461043	0.95707260
13	0.00632704	0.01243640	0.01876344	0.91355151
14	0.01143569	0.01330825	0.02474393	0.89314079
15	0.01725028	0.01120969	0.02845997	0.94437108
16	0.00411579	0.01048289	0.01459868	0.96395007
17	0.00973968	0.01304011	0.02277978	0.89929633
18	0.01155362	0.01369399	0.02524761	0.88446563
19	0.17059517	0.01124686	0.18184202	0.94339783
20	0.02733468	0.01267319	0.04000787	0.90789301
21	0.01780679	0.01303007	0.03083686	0.89952876
22	0.02438532	0.01296154	0.03734687	0.90111994
23	0.06429340	0.01213014	0.07642353	0.92100378
24	0.01399816	0.01090915	0.02490731	0.95233931
25	0.01757247	0.01226359	0.02983607	0.91773743
26	0.02132338	0.01438081	0.03570419	0.86951830
27	0.02661856	0.01199426	0.03861282	0.92435994
28	0.02163059	0.01173601	0.03336660	0.93082557
29	0.03231663	0.01556974	0.04788637	0.84502813
30	0.06028329	0.01251939	0.07280268	0.91155818
31	0.01666321	0.01106897	0.02773218	0.94808038
32	0.04307699	0.01462725	0.05770424	0.86430278
33	0.02895650	0.01475621	0.04371271	0.86160359
34	0.05754508	0.01293482	0.07047989	0.90174231
35	0.01671110	0.01188026	0.02859136	0.92719982
36	0.03022413	0.01337902	0.04360315	0.89153333
37	0.04551028	0.01590461	0.06141489	0.83842225
38	0.07372465	0.01329314	0.08701779	0.89348479
39	0.04561104	0.01089977	0.05651081	0.95259088
40	0.04022769	0.01572303	0.05595072	0.84198908
41	0.09997352	0.01690562	0.11687914	0.81937515
42	0.10424579	0.01313938	0.11738517	0.89700514
43	0.01497915	0.01163130	0.02661044	0.93348042
44	0.02103268	0.01554779	0.03658047	0.84546540
45	0.03725388	0.01617198	0.05342587	0.83323413
46	0.08654048	0.01419599	0.10073647	0.87347997
47	0.06960790	0.05748257	0.12709047	0.42979501
48	0.06536241	0.10027892	0.16564133	0.27343352
49	0.15751132	0.15349176	0.31100307	0.17580954
50	0.09408482	0.16389862	0.25798343	0.16281046
51	0.07828713	0.18585400	0.26414113	0.13951258
52	0.13818526	0.12234326	0.26052852	0.22506430
53	0.09082778	0.16108724	0.25191503	0.16618330
54	0.08879341	0.33849351	0.42728692	0.05751660
55	0.07747297	0.12761702	0.20508998	0.21540627
56	0.10513838	0.41049772	0.51563610	0.04068044
57	0.11116299	0.14952159	0.26068459	0.18116159

Sample #	η_a	η_b	η_T	σ_f
58	0.08782209	0.18393137	0.27175347	0.14135868
59	0.09672348	0.07707553	0.17379901	0.34399778
60	0.06625110	0.14450420	0.21075530	0.18826736
61	0.09662164	0.33558549	0.43220713	0.05836990
62	0.07000281	0.13483804	0.20484085	0.20314407
63	0.04017781	0.12883920	0.16901701	0.21325560
64	0.15788147	0.36782765	0.52570912	0.04974549
65	0.12925757	0.14986566	0.27912323	0.18068856
66	0.09007304	0.12451298	0.21458602	0.22101465
67	0.16864141	0.30883171	0.47747311	0.06704731
68	0.15324965	0.14946551	0.30271515	0.18123887
69	0.16548387	0.20339278	0.36887664	0.12411924
70	0.06488810	0.18862334	0.25351143	0.13691205
71	0.02124936	0.20776241	0.22901177	0.12065178
72	0.04719508	0.22719739	0.27439247	0.10673549
73	0.03870782	0.19814983	0.23685765	0.12846346
74	0.02435997	0.20654792	0.23090789	0.12160201
75	0.09311024	0.24059245	0.33370269	0.09838771
76	0.03493688	0.21142970	0.24636658	0.11784353
77	0.15953527	0.17165739	0.33119266	0.15399091
78	0.02378660	0.18564548	0.20943208	0.13971117
79	0.23232735	0.42018020	0.65250754	0.03892264
80	0.06925289	0.20902136	0.27827425	0.11967748
81	0.08603595	0.25940683	0.34544278	0.08808195
82	0.06494003	0.22657471	0.29151475	0.10714650
83	0.10572135	0.21190373	0.31762508	0.11748710
84	0.05724709	0.17768071	0.23492780	0.14760212
85	0.14996406	0.32877743	0.47874150	0.06043262
86	0.11040837	0.19977892	0.31018729	0.12709145
87	0.12018218	0.20458534	0.32476752	0.12315944
88	0.08711691	0.19363471	0.28075162	0.13237479
89	0.09164755	0.21122054	0.30286809	0.11800127
90	0.12457407	0.36253852	0.48711259	0.05104217
91	0.08036068	0.18477861	0.26513929	0.14054099

A.2 Ridged Ice Porosities and Flexural Strengths

Table A.2 presents the porosities calculated based on the measurements conducted by K. V. Høyland and the approximated flexural strength. The MATLAB scripts applied to obtain these values are given in appendix B. The porosities are obtained based on the assumptions that the diameter D had a constant value 70 [mm] and a length L 175 [mm].

Table A.2: Air porosities η_a, brine porosities η_b, total porosities η_T and flexural strength σ_f for a sample length L 175 [mm] and diameter D 70 [mm].

Sample #	η_a	η_b	η_T	σ_f
1	0.04588998	0.01364996	0.05953995	0.88544535
2	0.08215986	0.00863764	0.09079750	1.01901146
3	0.02718157	0.00800478	0.03518635	1.04001335
4	0.08767177	0.01147947	0.09915124	0.93736473
5	0.05192984	0.01071861	0.06264844	0.95748356
6	0.06733126	0.00816294	0.07549420	1.03464858
7	0.05776262	0.00865943	0.06642204	1.01830986
8	0.09297776	0.00728977	0.10026753	1.06532350
9	0.04085076	0.01166928	0.05252003	0.93251520
10	0.04685124	0.01043528	0.05728652	0.96527025
11	0.06736020	0.00826497	0.07562517	1.03122954
12	0.05072403	0.01342868	0.06415271	0.89040988
13	0.05649550	0.00973820	0.06623370	0.98517286
14	0.07972870	0.01044045	0.09016915	0.96512673
15	0.04179166	0.01338523	0.05517689	0.89139268
16	0.03506764	0.01264378	0.04771142	0.90859104
17	0.02308674	0.00575755	0.02884428	1.12653683
18	0.06573382	0.01374927	0.07948308	0.88323948
19	0.03051789	0.01339481	0.04391269	0.89117584
20	0.03061597	0.01380733	0.04442330	0.88195590
21	0.07729601	0.01926011	0.09655612	0.77824238
22	0.01978421	0.01046381	0.03024802	0.96447854
23	0.02367101	0.01247915	0.03615015	0.91252339
24	0.03838161	0.01309373	0.05147534	0.89805677
25	0.05687749	0.01069657	0.06757406	0.95808324
26	0.03603414	0.01120893	0.04724307	0.94439104
27	0.01512390	0.01140892	0.02653281	0.93918398
28	0.05571494	0.01171846	0.06743339	0.93126922
29	0.01701867	0.01165899	0.02867766	0.93277635
30	0.01748718	0.01358005	0.03106723	0.88700645
31	0.00000000	0.01129415	0.01129415	0.94216307
32	0.02386013	0.01271981	0.03657994	0.90678933
33	0.01778770	0.00857741	0.02636511	1.02095833
34	0.02282066	0.00943400	0.03225466	0.99421352

Sample #	η_a	η_b	η_T	σ_f
35	0.02879908	0.00746855	0.03626763	1.05882502
36	0.03356803	0.01263483	0.04620285	0.90880375
37	0.03596659	0.00999585	0.04596244	0.97768845
38	0.02788435	0.01033107	0.03821541	0.96817709
39	0.10552930	0.01084208	0.11637138	0.95414176
40	0.11930361	0.00781496	0.12711857	1.04655979
41	0.02286878	0.00967058	0.03253936	0.98716289
42	0.02170207	0.01081227	0.03251434	0.95494586
43	0.04556535	0.01036098	0.05592633	0.96734040
44	0.02969672	0.01687141	0.04656813	0.82000948
45	0.04824281	0.01368799	0.06193079	0.88459908
46	0.09461152	0.01292799	0.10753951	0.90190145
47	0.03623402	0.01272626	0.04896027	0.90663696
48	0.05022074	0.01134016	0.06156090	0.94096575
49	0.03132908	0.01421311	0.04554219	0.87311121
50	0.07581040	0.01502384	0.09083424	0.85606564
51	0.03700759	0.00920127	0.04620885	1.00128600
52	0.01474024	0.01007904	0.02481928	0.97530455
53	0.02236482	0.01429341	0.03665822	0.87138638
54	0.03239857	0.00979744	0.04219601	0.98343823
55	0.01877497	0.00699875	0.02577371	1.07616283
56	0.04888020	0.01080765	0.05968785	0.95507057
57	0.04364608	0.00982951	0.05347560	0.98250263
58	0.03212789	0.00900340	0.04113129	1.00741006
59	0.02293851	0.01066745	0.03360596	0.95887725
60	0.02386794	0.00872011	0.03258805	1.01636278
61	0.02652922	0.01160597	0.03813520	0.93412541
62	0.00344192	0.00941508	0.01285700	0.99478322
63	0.03236221	0.00894185	0.04130406	1.00933633
64	0.01956599	0.00912979	0.02869578	1.00348612
65	0.02445321	0.00935051	0.03380372	0.99673471
66	0.02698303	0.00679190	0.03377493	1.08407332
67	0.02218701	0.00701553	0.02920254	1.07552879
68	0.01177703	0.01000864	0.02178567	0.97732085
69	0.04947940	0.01148135	0.06096075	0.93731633
70	0.03098180	0.00909234	0.04007414	1.00464452
71	0.04005408	0.00731709	0.04737117	1.06432263
72	0.04529730	0.00872879	0.05402609	1.01608514
73	0.05068311	0.01048054	0.06116365	0.96401514
74	0.05253393	0.01097803	0.06351196	0.95049756
75	0.03594315	0.01510225	0.05104540	0.85445916
76	0.02643940	0.02222669	0.04866609	0.73248459
77	0.00631000	0.00729942	0.01360942	1.06496986
78	0.09555805	0.01480259	0.11036063	0.86063776
79	0.02979245	0.01102600	0.04081845	0.94922053
80	0.03877036	0.00815351	0.04692386	1.03496622

Sample #	η_a	η_b	η_T	σ_f
81	0.02974643	0.01064595	0.04039238	0.95946442
82	0.01869235	0.01131839	0.03001075	0.94153170
83	0.04232428	0.01735427	0.05967856	0.81115861
84	0.09942035	0.01312555	0.11254591	0.89732336
85	0.04338462	0.01422226	0.05760688	0.87291414
86	0.05574433	0.01269373	0.06843806	0.90740625
87	0.03189588	0.00833736	0.04023324	1.02882348
88	0.15780621	0.00845349	0.16625970	1.02499712
89	0.07760751	0.01124804	0.08885554	0.94336693
90	0.06579273	0.01404070	0.07983343	0.87684259
91	0.03242652	0.00937654	0.04180306	0.99594665
92	0.03655619	0.00783362	0.04438981	1.04591089
93	0.04586640	0.01219212	0.05805853	0.91948296
94	0.05904965	0.01872203	0.07777168	0.78722785
95	0.08505083	0.01920348	0.10425432	0.77917717
96	0.00000000	0.01203301	0.01203301	0.92339963
97	0.00000000	0.01302102	0.01302102	0.89973851
98	0.10911496	0.00693085	0.11604581	1.07873996
99	0.06304293	0.00997350	0.07301643	0.97833159
100	0.03163401	0.01226502	0.04389903	0.91770280
101	0.10134462	0.01340186	0.11474649	0.89101614
102	0.04583392	0.01068034	0.05651425	0.95852565
103	0.06609594	0.00843551	0.07453145	1.02558689
104	0.05583981	0.01214518	0.06798499	0.92063415
105	0.05702429	0.01636877	0.07339306	0.82946338
106	0.04184791	0.00826021	0.05010813	1.03138829
107	0.09825544	0.00792919	0.10618463	1.04260610
108	0.09200270	0.00842432	0.10042702	1.02595441

Appendix B

MATLAB Scripts

This section provides the MATLAB scripts applied to conduct estimates on porosities and flexural strengths. Additionally, the scripts that produce the plots for chapter 3 are given here. The MATLAB scripts are provided by K. V. Høyland and slightly modified to fit the input-files.

B.1 MATLAB - Porosityprogram.m

```
%This program reads Salinity (ppt), density (kg/l) and
%Temperature (C) calculates the porosity (air, brine and total) and return
clear all
save_file = 'yes';%'yes'; %Write 'yes' to save figure!

%Open data sheet:
%filename = 'levelice.xlsx';
filename = 'ridgedice.xlsx';
sheet = 1;
xlRange = 'G:J';
Phys_prop = xlsread(filename,sheet,xlRange);

%Transposes the Phys_prop vector to fit with this program
Phys_prop = transpose(Phys_prop);

%preallocate a diameter vector of zeros:
%D = zeros(length(Phys_prop(1,:)),1);

%create a vector consisting of values between 70 and 60 mm (norm dist)
%for k = 1:length(Phys_prop(1,:))
   %D(k) = rand + 69;
%end

%General dimensions for each specimen, can be set to other values
D               = 70; %diameter [mm]
l               = 175; %length  [mm]
area            = pi*(D/2)^2;
%area            = pi.*(D./2).^2;
vol             = area*l;
%vol             = area.*l;
Density         = 1000.*Phys_prop(1,:)./vol;
%Density         = 1000.*Phys_prop(1,:)./transpose(vol);  % [kg/l]
%Change the weight to density:
Phys_prop(1,:)  = Density;

    %After reading:
        %Phys_prop(1,i) = density [kg/l]
        %Phys_prop(2,i) = temperature
        %Phys_prop(3,i) = strength
        %Phys_prop(4,i) = salinity
strength       = Phys_prop(3,:); %Create a strength vector
temperature    = Phys_prop(2,:); %Create a temperature vector
Phys_prop(3,:) = Phys_prop(2,:); %exchange strength vector with temperature
Phys_prop(2,:) = Phys_prop(1,:); %exchange old temperature vector
```

```
45                                  %with weight
46      %After exchange:
47          %Phys_prop(1,i) = density [kg/l]
48          %Phys_prop(2,i) = density [kg/l]
49          %Phys_prop(3,i) = temperature
50          %Phys_prop(4,i) = salinity
51  n = size(Phys_prop,2);
52  Por = zeros(n,4);
53  density = [];
54      for i = 1 : n
55          if ~Phys_prop(1,i) || ~Phys_prop(2,i) || ~Phys_prop(3,i) || ...
56                  ~Phys_prop(4,i)
57              Por(i,1:4) = [i , zeros(1,3)];
58          else
59              density(i)  = (0.1*Phys_prop(1,i)+0.9*Phys_prop(2,i));...
60                  %/1000; % Unit [kg/l] or [Mg/m^3] to comply with
61                  %subfunction sb.m
62              Por(i,1:4)  = [i , porositykvh(Phys_prop(4,i), ...
63                  Phys_prop(3,i),density(i))];
64          end
65      end
66
67  %% - Plot
68  Por_var_vect = [];
69  for j = 1:n
70      if ~Por(j,4)
71          Por_for_plot(j,1:2) = [Por(j,1) , NaN];
72      else
73          Por_for_plot(j,1:2) = [Por(j,1) , Por(j,4)];
74          Por_var_vect = [Por_var_vect;Por(j,1) , Por(j,4)];
75      end
76  end
77  var_por = var(Por_var_vect(:,2));
78
79  % - Figure 4
80  fg4 = figure(4);clf;
81  scatter(strength, Por(:,4))
82  grid on
83  box on
84  ax = gca;
85  ax.XTick = 0:length(Phys_prop(1,:));
86  ax.YTick = 0:0.025:100;
87
88  tl1 = sprintf('\\textbf{Total porosity, }$\\mathbf{\\eta_T}$');
89  ll1 = sprintf('Hoyland - Matlab');
90  ll2 = sprintf('Cox and Weeks (1983)');
91  xl = xlabel('Compressive strength $$\sigma_{c,v}$$ [MPa]');
92  yl = ylabel('Porosity, $\eta_T$ [-]');
93  tl = title(strcat(tl1));
94  ll = legend(ll1,ll2,'location','best');
95  ll.Interpreter = 'latex';
96  tl.Interpreter = 'latex';
97  xl.Interpreter = 'latex';
98  yl.Interpreter = 'latex';
99  tl.FontSize = 16; xl.FontSize = 12 ; yl.FontSize = 12 ;
100 %ax.YLim = [0.9*min(Por_var_vect(:,2)),1.1*max(Por(:,4))];
101
102 %% - Print figure
103 filename    = 'RidgePorosityStrenghtCV';
104 %filename    = 'PorosityStrenghtCV';
105 postfix     = '.eps';
106 path        = 'plot/';
107 filetype    = '-depsc2';
108 fid         = strcat(path,filename,postfix);
109 m=1;
110 while exist(fid,'file')
111    m=m+1;
112    fid         = strcat(path,filename,'TestNumb',num2str(m),postfix);
113 end
114 fg4.Units = 'pixels';
115 fg4.PaperPositionMode = 'auto';
116 if (strcmp(save_file,'yes'))
117     fprintf('Saving figure: %s \n',fid);
118     print(fg4,filetype,fid);
119 else
120     disp('Not saving figure')
121 end
122
123
124 % - Figure 5 Air porosity versus sample nr
125 fg5 = figure(5);clf;
126 plot(Por(:,1), Por(:,2), 'ob')
127 grid on
128 ax = gca;
129 ax.XTick = [0:10:110];
130 ax.YTick = [0:0.05:100];
131
132 tl1 = sprintf('\\textbf{Air porosity, }$\\mathbf{\\eta_a}$');
133 ll1 = sprintf('Hoyland - Matlab');
134 ll2 = sprintf('Cox and Weeks (1983)');
135 xl = xlabel('Sample number');
136 %xl = xlabel('Sample');
137 yl = ylabel('Air fraction, $\eta_a$ [-]');
```

```
tl = title(strcat(tl1));
ll = legend(ll1,ll2,'location','best');
ll.Interpreter = 'latex';
tl.Interpreter = 'latex';
xl.Interpreter = 'latex';
yl.Interpreter = 'latex';
tl.FontSize = 16; xl.FontSize = 12 ; yl.FontSize = 12 ;
%ax.YLim = [0.9*min(Por_var_vect(:,2)),1.1*max(Por(:,4))];

%% - Print figure
filename    = 'RidgePorosityAirSample';
%filename    = 'PorosityAirSample';
postfix     = '.eps';
path        = 'plot/';
filetype    = '-depsc2';
fid1         = strcat(path,filename,postfix);
m=1;
while exist(fid1,'file')
   m=m+1;
   fid1         = strcat(path,filename,'TestNumb',num2str(m),postfix);
end
fg5.Units = 'pixels';
fg5.PaperPositionMode = 'auto';
if (strcmp(save_file,'yes'))
    fprintf('Saving figure: %s \n',fid1);
    print(fg5,filetype,fid1);
else
    disp('Not saving figure')
end

% - Figure 6 brine porosity versus sample nr
fg6 = figure(6);clf;
plot(Por(:,1), Por(:,3), 'ob')
grid on
ax = gca;
ax.XTick = [0:10:110];
ax.YTick = [0:0.005:0.025];

tl1 = sprintf('\\textbf{Brine porosity, }$\\mathbf{\\eta_b}$');
ll1 = sprintf('Hoyland - Matlab');
ll2 = sprintf('Cox and Weeks (1983)');
xl = xlabel('Sample number');
%xl = xlabel('Sample');
yl = ylabel('Brine porosity, $\eta_b$ [-]');
tl = title(strcat(tl1));
ll = legend(ll1,ll2,'location','best');
ll.Interpreter = 'latex';
tl.Interpreter = 'latex';
xl.Interpreter = 'latex';
yl.Interpreter = 'latex';
tl.FontSize = 16; xl.FontSize = 12 ; yl.FontSize = 12 ;
%ax.YLim = [0.9*min(Por_var_vect(:,2)),1.1*max(Por(:,4))];

%% - Print figure
filename    = 'RidgePorosityBrineSample';
%filename    = 'PorosityBrineSample';
postfix     = '.eps';
path        = 'plot/';
filetype    = '-depsc2';
fid2         = strcat(path,filename,postfix);
m=1;
while exist(fid2,'file')
   m=m+1;
   fid2         = strcat(path,filename,'TestNumb',num2str(m),postfix);
end
fg6.Units = 'pixels';
fg6.PaperPositionMode = 'auto';
if (strcmp(save_file,'yes'))
    fprintf('Saving figure: %s \n',fid2);
    print(fg6,filetype,fid2);
else
    disp('Not saving figure')
end

% - Figure 7 Total porosity versus sample nr
fg7 = figure(7);clf;
plot(Por(:,1), Por(:,4), 'ob')
grid on
ax = gca;
ax.XTick = [0:10:110];
ax.YTick = [0:0.05:100];

tl1 = sprintf('\\textbf{Total porosity, }$\\mathbf{\\eta_T}$');
ll1 = sprintf('Hoyland - Matlab');
ll2 = sprintf('Cox and Weeks (1983)');
xl = xlabel('Sample number');
%xl = xlabel('Sample');
yl = ylabel('Total porosity, $\eta_T$ [-]');
tl = title(strcat(tl1));
ll = legend(ll1,ll2,'location','best');
ll.Interpreter = 'latex';
tl.Interpreter = 'latex';
xl.Interpreter = 'latex';
```

```
yl.Interpreter = 'latex';
tl.FontSize = 16; xl.FontSize = 12 ; yl.FontSize = 12 ;
%ax.YLim = [0.9*min(Por_var_vect(:,2)),1.1*max(Por(:,4))];

%% - Print figure
filename    = 'RidgePorosityTotalSample';
%filename    = 'PorosityTotalSample';
postfix     = '.eps';
path        = 'plot/';
filetype    = '-depsc2';
fid3         = strcat(path,filename,postfix);
m=1;
while exist(fid3,'file')
   m=m+1;
   fid3         = strcat(path,filename,'TestNumb',num2str(m),postfix);
end
fg7.Units = 'pixels';
fg7.PaperPositionMode = 'auto';
if (strcmp(save_file,'yes'))
    fprintf('Saving figure: %s \n',fid3);
    print(fg7,filetype,fid3);
else
    disp('Not saving figure')
end
```

B.2 MATLAB - Porositykvh.m

```
function P = porositykvh(S,T,rho)

%The salinity is given in [ppt], the density in [kg/l]=[Mg/m3] and
%the temperature is given in [C].
% The following indexes are used:
%_i is used for sea ice
%_pi for pure ice
%_a for air
%_b for birne

S_i = S;
rho_i = rho;
rho_pi = 0.917 - 1.403e-4*T;


 if T >= -1.9
     S_b = sb(T);
     rho_b = 1 + 0.0008*S_b;
     brine_frac = (rho_i*S_i)/(rho_b*S_b);
     air_frac = 1 - rho_i./rho_pi + brine_frac*((rho_b./rho_pi)-1);
 else
     brine_frac = rho_i.*S_i./F_1(T);
     air_frac = 1 - rho_i./rho_pi + rho_i.*S_i.*F_2(T)/F_1(T);
 end
  if air_frac < 0
      air_frac = 0;
  end
P = [air_frac brine_frac brine_frac+air_frac];
end
```

B.3 MATLAB - sb.m

```
function salbrine = sb(T)
    %Calculates the salinity of seawater given the freezing point.
    %The inverse of the UNESCO formula given by Lepparanta (1983) is used.
    %The salinity goes in [ppt] and the temp in [C]
%     T = -0;
    sw = 34;
    Tf = -0.0575*sw+0.001710523*sw^1.5-0.0002154996*sw^2;
    if T - Tf < 0;
        while abs(T - Tf) > 0.001;
            sw = sw + 0.01;
            Tf = -0.0575*sw+0.001710523*sw^1.5-0.0002154996*sw^2;
        end
    else
        while abs(T - Tf) > 0.001;
            sw = sw - 0.01;
            Tf = -0.0575*sw+0.001710523*sw^1.5-0.0002154996*sw^2;
        end
    end

```

```
20      salbrine = sw;
21  end
```

B.4 MATLAB - F_1.m

```
1   function f = F_1(T)
2
3   if(T>-22.9)
4       alpha_0 = -4.732;
5       alpha_1 = -22.45;
6       alpha_2 = -0.6397;
7       alpha_3 = -0.01074;
8
9       f  = alpha_0 + alpha_1*T + alpha_2*T.^2 + alpha_3*T.^3;
10  else
11      alpha_0 = 9899;
12      alpha_1 = 1309;
13      alpha_2 = 55.27;
14      alpha_3 = 0.716;
15
16      f  = alpha_0 + alpha_1*T + alpha_2*T.^2 + alpha_3*T.^3;
17  end
```

B.5 MATLAB - F_2.m

```
1   function f = F_2(T)
2
3   if(T>-22.9)
4       alpha_0 = 0.08903;
5       alpha_1 = -0.01763;
6       alpha_2 = -0.000533;
7       alpha_3 = -0.000008801;
8
9       f  = alpha_0 + alpha_1*T + alpha_2*T.^2 + alpha_3*T.^3;
10  else
11      alpha_0 = 8.547;
12      alpha_1 = 1.089;
13      alpha_2 = 0.04518;
14      alpha_3 = 0.0005819;
15
16      f  = alpha_0 + alpha_1*T + alpha_2*T.^2 + alpha_3*T.^3;
17  end
```

B.6 MATLAB - PlotData.m

This script is programmed to plot the flexural strength and write result files, hence not provided by K. V. Høyland.

```
1   function PlotData(Por)
2   %This function reads the Por-Vector from KVH-programs and saves it to a txt
3   %file for further use. It also calculates the mean of data to se whether
4   %the values change for different diameters.
5
6
7   %Create a new txt-file:
8   filename    = 'RidgePorosityData';
9   %filename    = 'PorosityData';
10  postfix     = '.txt';
11  fid         = strcat(filename,postfix);
12  m=1;
13  while exist(fid,'file')
14      m=m+1;
15      fid         = strcat(filename,'TestNumb',num2str(m),postfix);
16  end
17  outdat = fopen(fid,'wt+');
18
19  %Calculate mean values:
20  MeanAir = mean(Por(:,2));
```

```
MeanBrine = mean(Por(:,3));
MeanTot = mean(Por(:,4));

%Pre allocating the flexural strength vector:
Flexural = zeros(length(Por(:,1)),1);

%Calculates the flexural strength of ice by brine porosity:
for j = 1:length(Por(:,1))
    Flexural(j) = 1.76*exp(-5.88*sqrt(Por(j,3)));
end

MeanFlexural = mean(Flexural);

%Write data from Por-vector to txt-file:
fprintf(outdat, '%12.8f & %12.8f & %12.8f & %12.8f \\\\ \n',...
    MeanAir, MeanBrine, MeanTot, MeanFlexural);
fprintf(outdat, 'Mean Air porosity %12.8f \n', MeanAir);
fprintf(outdat, 'Mean Brine porosity %12.8f \n', MeanBrine);
fprintf(outdat, 'Mean Total porosity %12.8f \n', MeanTot);
fprintf(outdat, 'Mean Flexural strength %12.8f \n', MeanFlexural);
fprintf(outdat,'Sample \t Air \t Brine \t Total \t Flexural Strength \n');
for i = 1:length(Por(:,1))
    fprintf(outdat,...
    '\t %d & \t%12.8f & \t%12.8f & \t%12.8f & \t%12.8f \\\\ \n',...
    Por(i,1), Por(i,2), Por(i,3), Por(i,4), Flexural(i));
end
fclose('all');

Flex = zeros(20,2);
for k = 1:500
    Flex(k,1) = 1.76*exp(-5.88*sqrt(k*0.001));
    Flex(k,2) = k*0.001;
end

% - Figure 1
save_file = 'yes'; %Saves figure, 'no' does not save figure
fg1 = figure(1);clf;
%Scatter plot of the flexural strength versus brine porosity
hold on
plot(Por(:,3),Flexural, 'ob')
plot(Flex(:,2),Flex(:,1), 'b')
grid on
box on
ax = gca;
ax.XTick = 0:0.05:1;
ax.YTick = 0:0.2:1.5;

tl1 = sprintf('\\textbf{Flexural Strength, }$\\mathbf{\\sigma_f}$');
yl = ylabel('Flexural strength $\sigma_{f}(\eta_b)$ [MPa]');
xl = xlabel('Brine Porosity, $\eta_b$ [-]');
%ll1 = sprintf('Approx. $\sigma_{f}(\eta_b)$');
%ll2 = sprintf('Empirical Formula $\sigma_f(\eta_b)$');
tl = title(strcat(tl1));
ll = legend({'Measured $\sigma_{f}(\eta_b)$','Timco et al. (1994)'},'location','best','interpreter','latex');
ll.Interpreter = 'latex';
tl.Interpreter = 'latex';
xl.Interpreter = 'latex';
yl.Interpreter = 'latex';
tl.FontSize = 16; xl.FontSize = 12 ; yl.FontSize = 12 ; ll.FontSize = 14;
%ax.YLim = [0.9*min(Por_var_vect(:,2)),1.1*max(Por(:,4))];

%% - Print figure
filename    = 'RidgePorosityFlexural';
%filename    = 'PorosityFlexural';
postfix     = '.eps';
path        = 'plot/';
filetype    = '-depsc2';
fid         = strcat(path,filename,postfix);
m=1;
while exist(fid,'file')
   m=m+1;
   fid         = strcat(path,filename,'TestNumb',num2str(m),postfix);
end
fg1.Units = 'pixels';
fg1.Position = [7.575714285714286e+02 3.541428571428571e+02 ...
    8.754285714285714e+02 5.154285714285714e+02];
fg1.PaperPositionMode = 'auto';
if (strcmp(save_file,'yes'))
    fprintf('Saving figure: %s \n',fid);
    print(fg1,filetype,fid);
else
    disp('Not saving figure')
end



end
```

B.7 MATLAB - Plot.m

This script is programmed to plot the temperature and salinity versus the porosity, hence not provided by K. V. Høyland.

```
clc
save_file = 'yes'; %Write 'yes' to save figure!
fg2 = figure(21);clf;
fg3 = figure(22);clf;
filename = 'ridgedice.xlsx';
%filename = 'levelice.xlsx';
sheet = 1;
xlRange = 'G:J';
LevelIce = xlsread(filename,sheet,xlRange)


weight          = LevelIce(:,1); %grams
temperature     = LevelIce(:,2); %C
strength        = LevelIce(:,3); %MPa [N/mm2];
salinity        = LevelIce(:,4); % [%]
D               = 70; %diameter [mm]
l               = 175; %length  [mm]
area            = pi*(D/2)^2;
vol             = area*l;
density         = weight./vol;  % [g/mm3]

max_strength = max(strength);

%% plotting set up
filename    = 'RidgedIce';
%filename    = 'LevelIce';
postfix     = '.eps';
path        = 'plot/';
filetype    = '-depsc2';
fid         = strcat(path,filename,postfix);
fid1        = strcat(path,filename,'temp',postfix);


%% Plotting
%xmin = 0;
%xmax = 0.03;
%ymin = 0;

figure(21); %Plotting strength versus salinity
scatter(strength, salinity);
grid on
box on
%ll1 = sprintf('Maximum stress: %6.2fMPa',max_strength);

xl = xlabel('Compressive strength $$\sigma_{c,v}$$ [MPa]');
xl.Interpreter = 'latex';
xl.FontSize = 12 ;


yl = ylabel('Salinity $$S$$ [\%]');
%ll = legend(ll1,'location','northwest','location','best');
%ll.Interpreter = 'latex';
yl.Interpreter = 'latex';
yl.FontSize = 12 ;

figure(22); %Plotting temperature versus strength
scatter(strength, temperature);
grid on
box on
%ll1 = sprintf('Maximum stress: %6.2fMPa',max_strength);

xl = xlabel('Compressive strength $$\sigma_{c,v}$$ [MPa]');
xl.Interpreter = 'latex';
xl.FontSize = 12 ;

yl = ylabel('Temperature $$T_i$$ [$$^\circ$$C]');
%ll = legend(ll1,'location','northwest','location','best');
%ll.Interpreter = 'latex';
yl.Interpreter = 'latex';
yl.FontSize = 12 ;



% -- Print
plot_size = [2,2,16,10];
fg2.Units = 'centimeters';
fg2.Position = plot_size;
fg2.PaperPositionMode = 'auto';
fg3.Units = 'centimeters';
fg3.Position = plot_size;
fg3.PaperPositionMode = 'auto';

if (strcmp(save_file,'yes'))
    fprintf('Saving figure: %s \n',fid);
    fprintf('Saving figure: %s \n',fid1);
```

```
86      print(fg2,filetype,fid);
87      print(fg3,filetype,fid1);
88  else
89      disp('Not saving figure')
90  end
```

Appendix C

Element Choice for Plate Model

This chapter will provide information about the element choice applied to the assessment of the plate model where the loads were found from level ice measurements and the dimensions provided by regulations.

C.1 Plate Elements - Abaqus

One of the steps in a finite element analysis is choosing the correct element type for the analysis. There exist several element types that are preferred for certain analysis, as they do not eliminate important factors that contribute to the final result. Hence, there are several issues that should be considered regarding element selection. This section focuses on the most applicable element types found in Abaqus.

The reader should be familiar with the finite element theory presented by Moan (2003). The theory in this section refer to Abaqus (2016).

C.1.1 Requirements for the Element

The element must apply to a static model where large displacements could occur. Hence, non-linear geometry may be induced. Considering the ratio between the thickness and the main dimensions of the plate field, one must differentiate between thin and thick shells. Also, one wants to avoid locking and hourglass modes in the model. Finally, the results should be as close to the exact solution as possible. Further, one should study the different elements and their certain properties.

C.1.2 Element Comparison

Abaqus provides several different element types. Both triangular and rectangular elements, with different number of nodes. This section will only consider the most relevant elements in which apply to the structure. As there are no rounded shapes which require refinement of the mesh, only rectangular elements are further assessed. Abaqus presents a wide range of different elements regarding different properties and node numbers, hence a combination of these provides even more elements.

Figure C.1 presents the different rectangular elements of different node numbers.

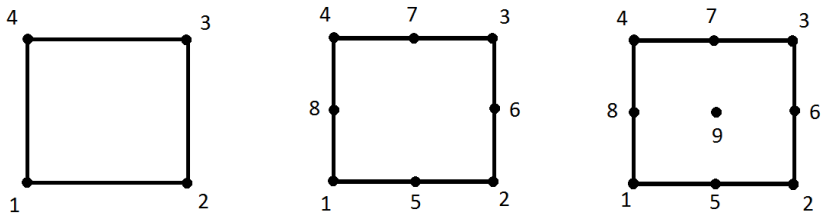

Figure C.1: Element types regarding node number, presented by Abaqus. *Left:* 4-node element. *Middle:* 8-node element. *Right:* 9-node element

Further, Abaqus defines a set of indexes to name their elements. Due to this, the name of the element defines the element properties. The table below defines these properties for three-dimensional shell elements only.

- **Position 1** Defines the type.
  - **S** Conventional stress/displacement shell
  - **SC** Continuum stress/displacement shell
  - **STRI** Triangular stress/displacement thin shell
  - **DS** Heat transfer shell
- **Position 2** Defines the number of nodes.
- **Position 3** Optional position.
  - **R** Reduced integration
- **Position 4** Optional position.
  - **5** Defines the number of d.o.f.
  - **T** Coupled temperature-displacement
  - **S** Smal-strain formulation in Abaqus/explicit only
- **Position 5** Optional position.

– **W** Warping considered in small-strain formulation in Abaqus/explict only

For this analysis, the following elements are relevant: S4, S4R, S4R5, S8R, S8R5 and S9R5. The properties of these elements are presented in table C.1

Table C.1: Element properties as presented by Abaqus.

Property/element	S4	S4R	S4R5	S8R	S8R5	S9R5
General thin/thick shells	✓	✓				
Thick shells only				✓		
Thin shells only			✓		✓	✓
Small strain			✓	✓	✓	✓
6 D.O.F.	✓	✓		✓		
5 D.O.F.			✓		✓	✓
Reduced integration		✓	✓	✓	✓	✓
Shear flexible element	✓	✓		✓		
Hourglass control		✓	✓			

The S4 element is a general-purpose element suitable for most applications. For problems dominated by in-plane bending, this is recommended. Reasonably due to the assumed strain formulation applied in the membrane response. As full integration is applied in both membrane and bending terms, the element does not suffer from hourglass modes in the respective terms. Thus, the transverse shear response is constant over the element. The element is suitable for non-linear geometry problems.

The S4R element applies reduced integration in order to avoid shear and membrane locking. As the element has hourglass modes that may propagate over a mesh, the element applies hourglass control. Equal the S4 element, S4R is a general-purpose element suitable for most applications. The element is suitable for thin shell applications, where the plate thickness is low compared to the span. As the element is shear flexible, transverse shear is integrated accurate over the entire element. Also, the element has reduced integration. The element is suitable for non-linear geometry problems.

The S4R5 element applies small strain formulation and uses reduced degrees of freedom. This element is suitable for large models with small strains and linear geometric behaviour. The hourglass control is applied to this element as well. The membrane and bending terms are integrated using reduced integration.

The S8R element does not need hourglass control as it has a non-propagating single hourglass mode. The element applies to small strain formulation. Shear and membrane locking is avoided by applying uniformly reduced integration. The S8R

element does converge towards shear flexible theory for thick plate, thus it does not neccessarily converge towards classic theory for thin shells. Where the classic theory refers to Kirchhoff-Love theory.

The S8R5 and S9R5 elements are applicable to fracture mechanics problems and apply to thin shells only. Also, they require small strains. The elements are also preferred if the model is subjected to contact with other structures during deformation. Hourglass modes does propagate over the mesh, thus hourglass control is applied to handle this.

C.1.3 Choice of Element

Abaqus differentiates between thick and thin shells, where the limit for thin shells is a thickness-to-main-structural-dimension less than 1/10. Hence, the shear flexible formulation applies to thin shells. The shear flexible formulation states that the normals to the shell surface do not necessarily remain perpendicular to the surface post deformation. This adds transverse shear flexibility to the structural property. The classical formulation neglects these shear strains, so that the normal to the shell surface remains orthogonal to the surface after deformation. The hourglass modes are deformation modes that may result in zero strain at the integration points. This is due to reduced integration of the elements, hence for some elements(4- and 9-node) this is controlled to avoid the hourglass modes. As for the S4 element, which applies full integration for bending and membrane stiffness terms, hourglass modes are not a concern. Thus, for the transverse shear behaviour, reduced integration is applied and the control of hourglass is necessary. The thin shell elements, are subjected to two types of locking. Transverse shear locking, and membrane locking do develop, and could be avoided by choosing a element that does not suffer from locking, such as the S4 and S4R elements.

Regarding the dimensions of the model, the model is found to be classified as a thin model. Also, as the deformations are assumed to be of a certain magnitude, the geometry could be found non-linear. The two elements that do not suffer from locking is S4 and S4R, and hourglass modes are either controlled or non-existing for the respective elements. In addition, the elements are capable of including the transverse shear strains in the computations. So that the choice of element is either S4 or S4R. Due to the mesh refinement, the computational time increases as the number of elements increases. Regarding this, the element with reduced integration would be preferred, so that the choice of element is the S4R.

Appendix D

Additional Results - Plate Assessment

This chapter contains results from the plate assessment that provide additional information about the plate response. The analysis providing the results are conducted in the same manner as presented in the main part of the thesis. The reader should be familiar with the method and applied pressure from previous discussed material, as no further information about assessment is given here.

D.1 Additional Results From Empirical Ice Pressure Model

This section provides results from the assessment of the ice pressure model, with the pressure from the empirical ice pressure model.

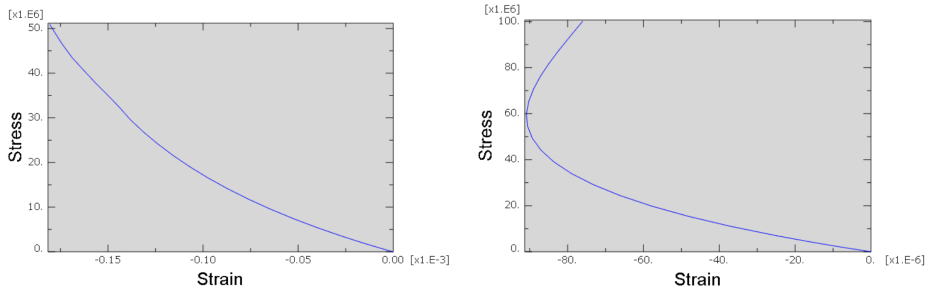

(a) Mesh size: 120 [mm] (b) Mesh size: 15 [mm]

Figure D.1: Stress-strain curve from location 2.2, in z-direction

Figure D.1a shows the same tendency as figure D.1b does, initially. Note that

the two figures have a different scale at the strain axis. Due the mesh refinement, figure D.1b shows a more accurate result. Additionally, the sampling location might have changed slightly due to the refinement.

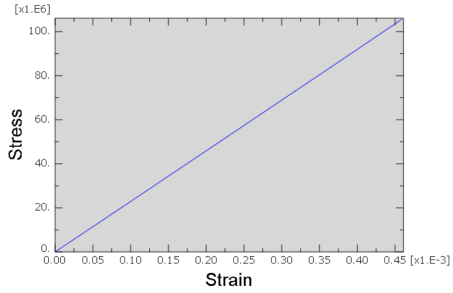

(a) Mesh size: 120 [mm]

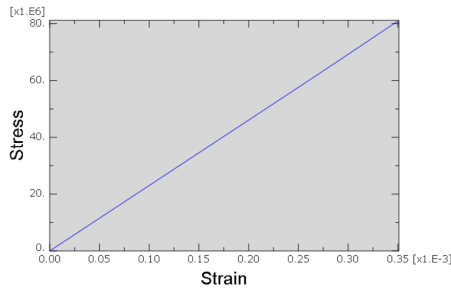

(b) Mesh size: 15 [mm]

Figure D.2: Stress-strain curve from location 2.3, in z-direction

Figure D.2 shows a perfectly linear behaviour. This could be expected as the sampling location is sufficiently distanced from the area where the load is applied. Considering the development in figure 7.6, D.1 and D.2 one see the convergence towards linear behaviour even clearer.

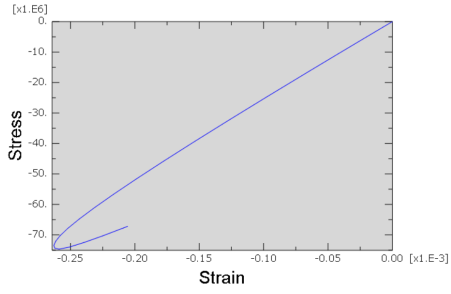

(a) Mesh size: 120 [mm]

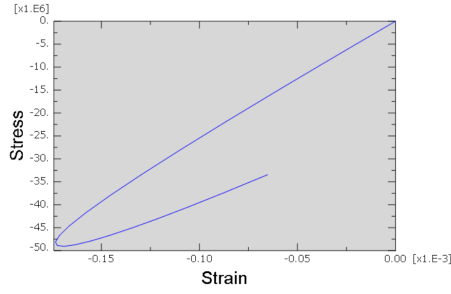

(b) Mesh size: 15 [mm]

Figure D.3: Stress-strain curve from location 1.2, in x-direction

Figure D.3 presents the effect of stiffener yielding and hence loss of support. Initially, the stiffeners do support the plate out of plane, so that compression occurs at location (1.2). The curves turn when the stiffeners closest to the applied pressure warps, so that support is no longer present. This effect is reduced as one move over to location (1.3), as indicated by figure D.4. Equally location (2.3), the behaviour is closer to linear as one has a greater distance to the applied load.

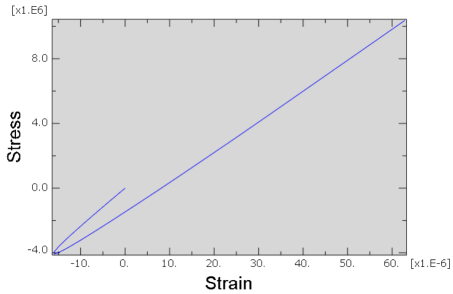

(a) Mesh size: 120 [mm]

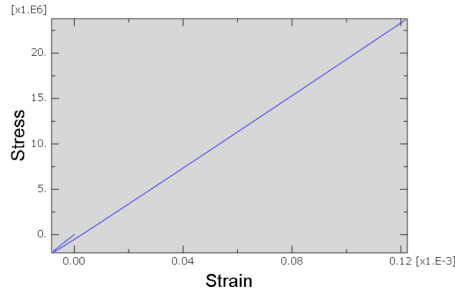

(b) Mesh size: 15 [mm]

Figure D.4: Stress-strain curve from location 1.3, in x-direction

D.2 Additional Results From DNV GL Ice Pressure Model

This section provides results from the assessment of the ice pressure model with applied pressure obtained from the DNV GL regulations.

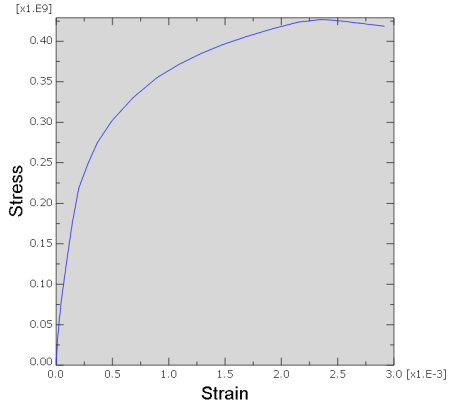

(a) Mesh size: 120 [mm]

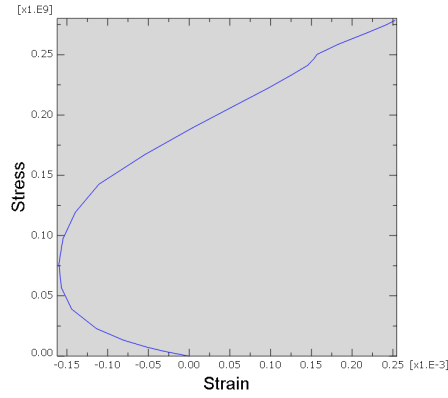

(b) Mesh size: 15 [mm]

Figure D.5: Stress-strain curve from location 2.2, in z-direction

From figure D.5 one could observe that the stress strain curves do not correlate. This is due to large element size in figure D.5a and hence the location of the sampling point. The response are obviously non linear, considering the plots.

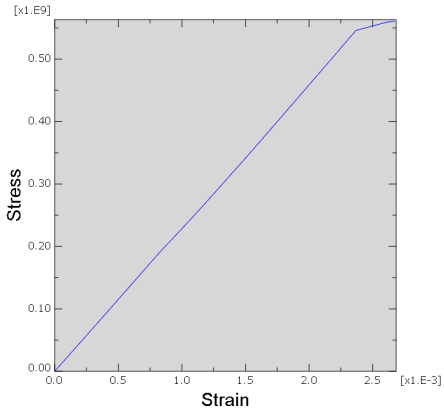

(a) Mesh size: 120 [mm]

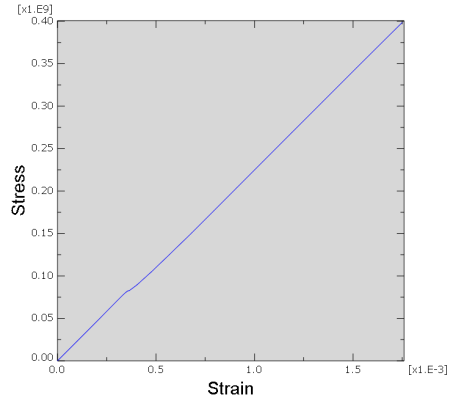

(b) Mesh size: 15 [mm]

Figure D.6: Stress-strain curve from location 2.3, in z-direction

Figure D.6 shows almost perfect linear behaviour, which is reasonable due to the

distance from the loaded area. As for the plate model with the empirical ice pressure, this model shows the same behaviour regarding the increase in linearity, due to distance from the loaded area.

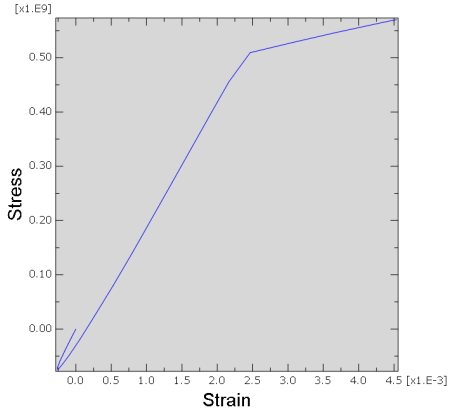

(a) Mesh size: 120 [mm]

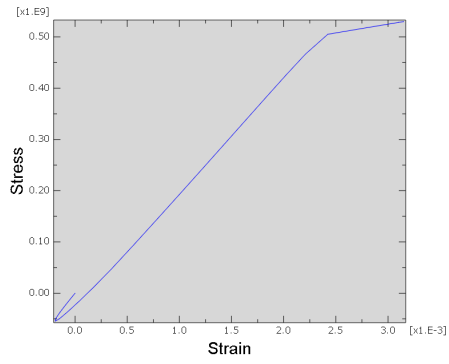

(b) Mesh size: 15 [mm]

Figure D.7: Stress-strain curve from location 1.2, in x-direction

Figure D.7 shows how the increased load, compared to figure D.3, impacts the stress strain relation. One could observe how the plate behaviour has changed from the curve presented in figure D.3 to a more non linear stress strain behaviour in figure D.7, with only the same behaviour as figure D.3 initially, before the effect of linearity until yielding occur. Figure D.8 presents the same effect as in z-direction, with linearity due to increased distance from the loaded area.

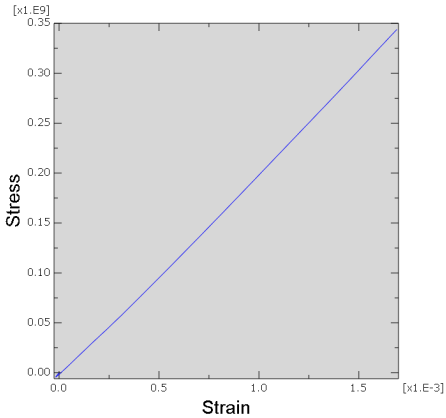

(a) Mesh size: 120 [mm]

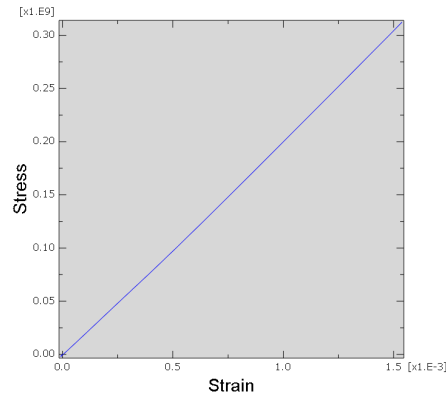

(b) Mesh size: 15 [mm]

Figure D.8: Stress-strain curve from location 1.3, in x-direction

D.3 Additional Results From IACS Ice Pressure Model

By applying a pressure of 15.56 [MPa], as calculated from regulations provided by IACS, the following plots were obtained for location (1.1) (see figure 7.4).

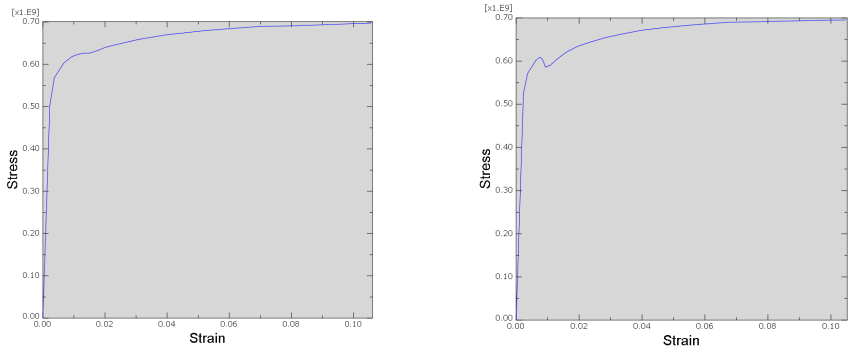

(a) Mesh size: 120 [mm]

(b) Mesh size: 15 [mm]

Figure D.9: Stress-strain curve from location 1.1, in x-direction

From figure D.9 one could observe that the results for both 120 and 15 [mm] mesh has larger strains and stresses compared to the ones presented in figure 7.11. Thus the initial yield stress tends to be higher in magnitude. The initial yield stress in figure D.9a is approximate 500 [MPa] while figure D.9b yields at approximate 525 [MPa]. For the mesh of 15 [mm], the strain value at initial yield is approximate 0.0025 [-].

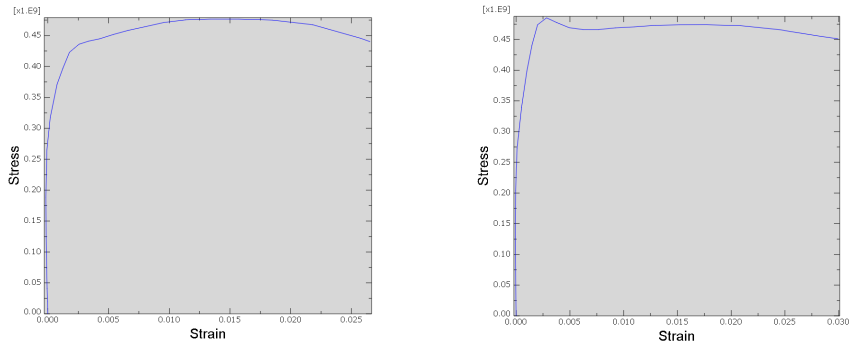

(a) Mesh size: 120 [mm]

(b) Mesh size: 15 [mm]

Figure D.10: Stress-strain curve from location 1.1, in z-direction

In figure D.10 one could observe a small effect of the Poisson's ratio for the initial part of the curve. Further, when the strain in z-direction reaches its minimum

value, and the plate reaches its initial yield in x-direction, the stresses in z-direction became dominant and the curve turns. The relation between stresses and strains in both directions are given in figure D.11.

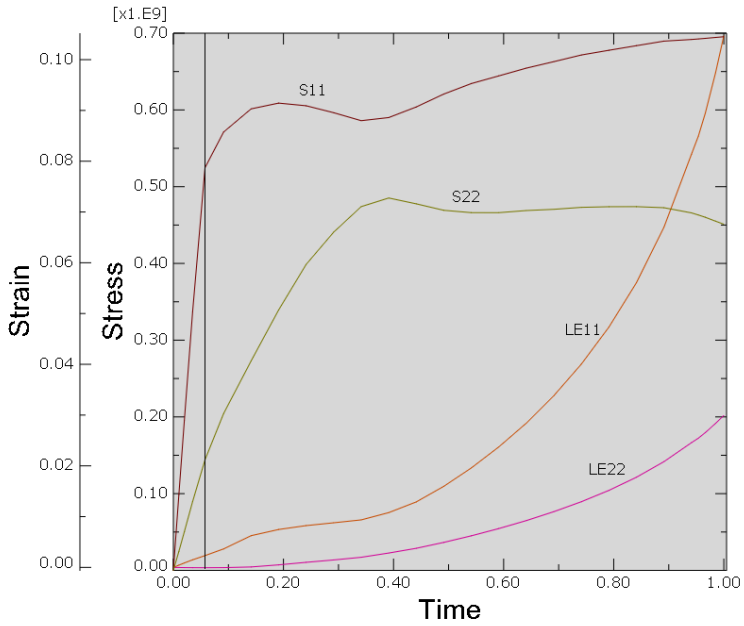

Figure D.11: Stress and strain in both x- and z-direction plotted over time. The labels are corresponding to the stresses in the following manner: S11 and LE11 define the stress and strains in x-direction respectively, S22 and LE22 define the stress and strains in z-direction respectively.

The black line in figure D.11 defines the location where initial yield in x-direction (S11) occurs, and also the minimum value of the strain in z-direction (LE22). As for the two previous pressure models, this substantiates the assumption of how the strains and stresses are related in the linear region of the stress analysis.

The previously presented plots of stress strain curves result in the following plots of displacements and stresses in x- and z-direction, respectively given in figure D.12, D.13 and D.14.

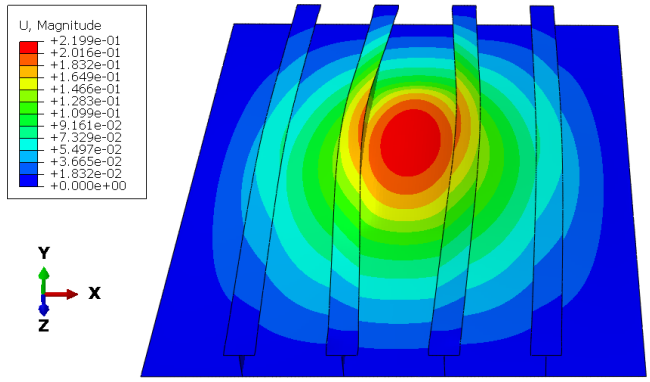

Figure D.12: Displacement of the plate field, with a 15 [mm] mesh size.

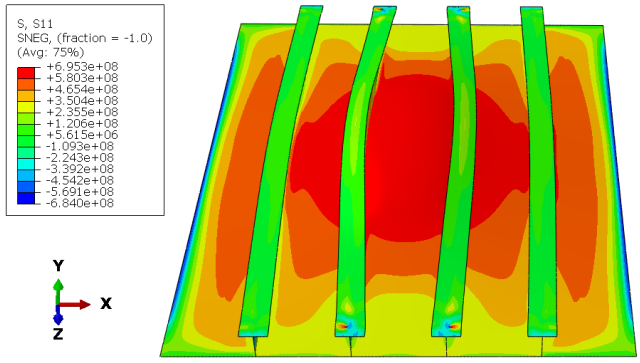

Figure D.13: Stress in x-direction in the plate field, with a 15 [mm] mesh size.

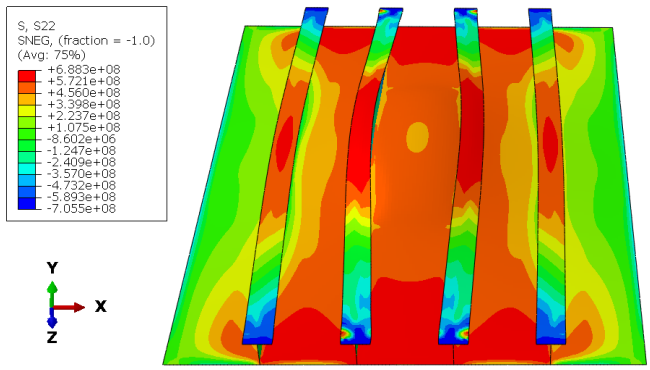

Figure D.14: Stress in z-direction in the plate field, with a 15 [mm] mesh size.

The largest displacement was found to be 219.9 [mm] in figure D.12. In x-direction, the largest tensile stress had a magnitude of 695.3 [MPa], as given by figure D.13. In z-direction, the stiffeners suffered from the most critical tensile and compressive stress, with magnitudes of respectively 688.3 and -705.5 [MPa]. Figure D.14 presents the stresses in z-direction.

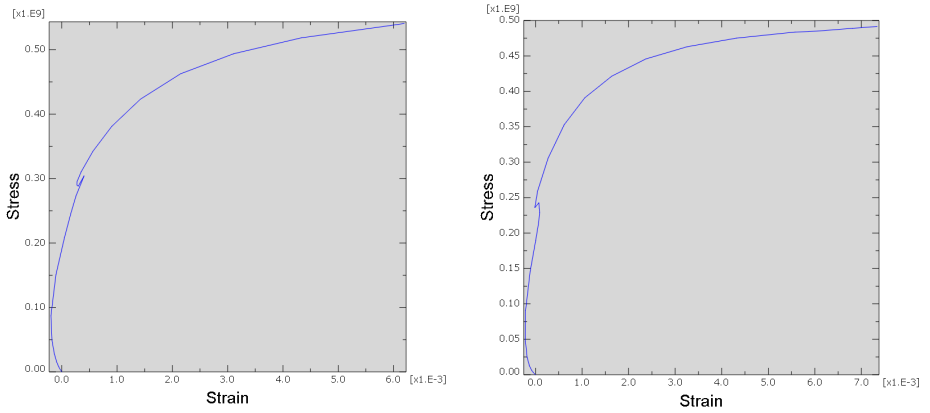

(a) Mesh size: 120 [mm]

(b) Mesh size: 15 [mm]

Figure D.15: Stress-strain curve from location 2.2, in z-direction

Compared to the two previously presented pressure models, this pressure induce sufficiently stresses such that both 120 and 15 [mm] stress strain curves in figure D.15 show almost same behaviour. The strains do start to develop in the negative direction, while the pressure level is sufficient to override this development.

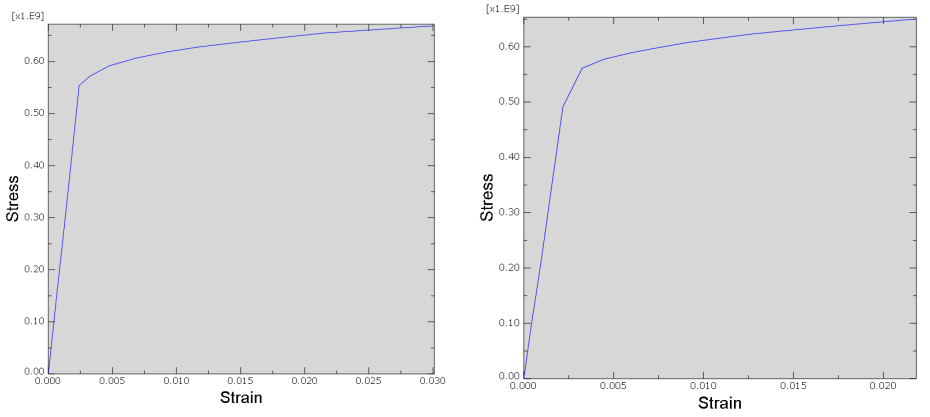

(a) Mesh size: 120 [mm]

(b) Mesh size: 15 [mm]

Figure D.16: Stress-strain curve from location 2.3, in z-direction

As the mesh is refined, figure D.16 shows that due to refinement, the stress-strain

relation tends to behave even more non-linear.

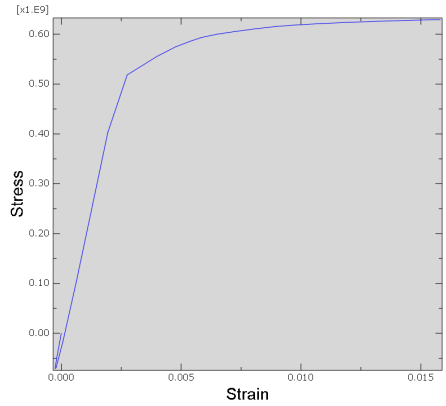

(a) Mesh size: 120 [mm]

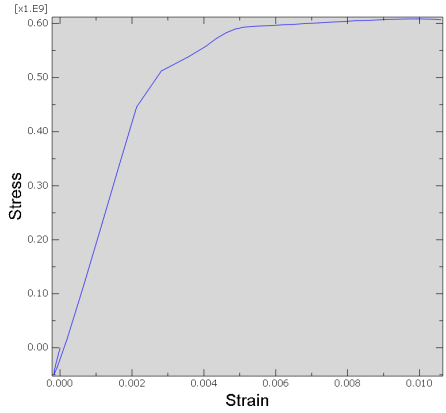

(b) Mesh size: 15 [mm]

Figure D.17: Stress-strain curve from location 1.2, in x-direction

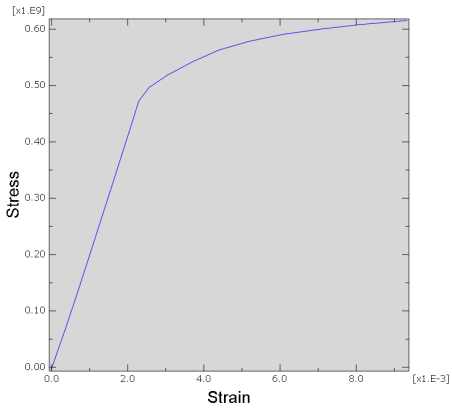

(a) Mesh size: 120 [mm]

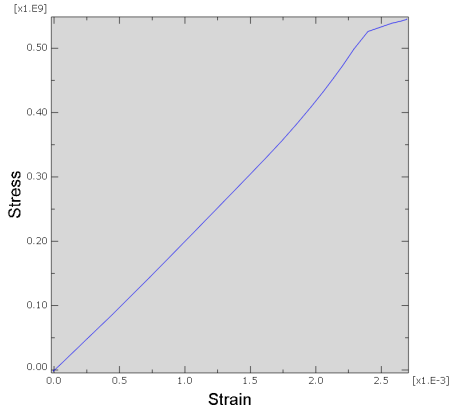

(b) Mesh size: 15 [mm]

Figure D.18: Stress-strain curve from location 1.3, in x-direction

Figure D.17 and D.18 show how the non-linearity decreases due to increased distance between the sampling and loading location.

Appendix E

Additional Results - Stiffener Assessment

This chapter provides results that are of interest, thus not of such importance they are provided in the main part of this thesis, as they provide results of stiffener assessment. The reader should in this chapter be familiar with the results in the main part and how they were conducted.

The assessment of the stiffeners are regarded additional results, since the extend of the main part are somewhat limited. The stiffeners were assessed applying several sampling points as presented in figure E.1.

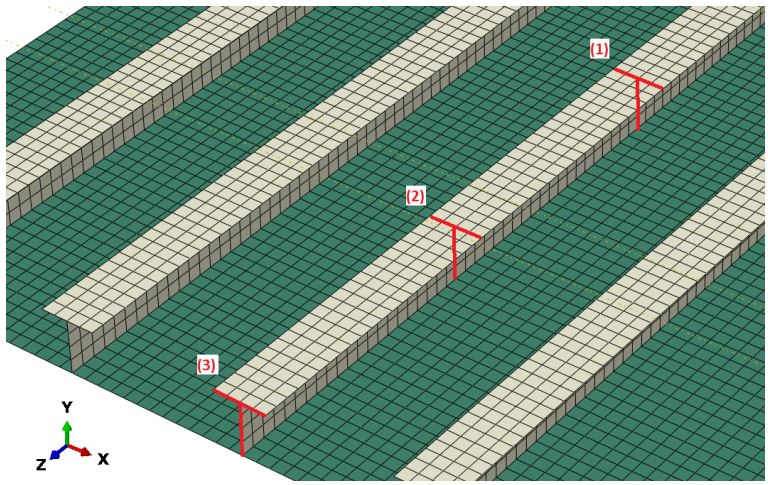

Figure E.1: The sampling locations for the stiffeners. Three points along each red line are applied for the flange.

As previously presented, in figure E.1, stresses in the longitudinal direction were

measured at three locations. These locations had three points for sampling of stresses along the flanges, as presented in figure E.2.

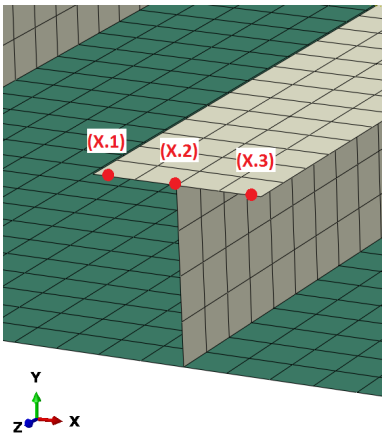

Figure E.2: Sampling points for the three locations along the stiffener closest to the applied stress. (X.Y) define the location, where X refers to the numbering obtained from figure E.1 and Y defines the position of the sampling point corresponding to the numbering in this figure (1 to 3).

E.1 Additional Results From Empirical Ice Pressure Model

The stiffeners in figure 7.10 had the largest compressive stress at the ends, with a magnitude of -557.1 [MPa] and the largest tension of 484.7 [MPa] occurring at the middle of the stiffeners. This gave rise to the assessment of the stresses induced in the stiffener flanges, as they were important for the response of the plate.

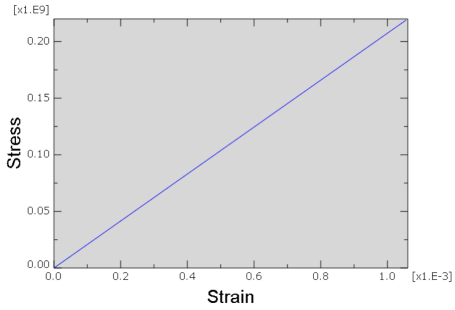

(a) Position (1.1)

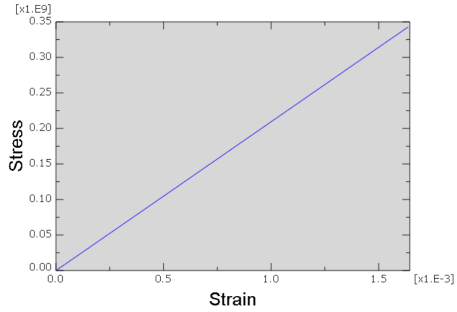

(b) Position (1.2)

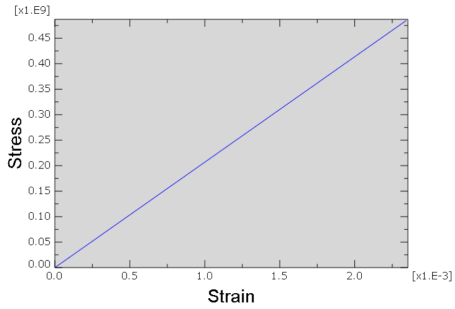

(c) Position (1.3)

Figure E.3: Stress-strain curve from location 1, in z-direction

Due to the applied pressure, the stiffeners will deform sideways (x-direction) as well as out of plane (y-direction). Due to this deformation, the stiffener warps as rotation around the z-axis requires less work. As a result, position (1.1) will have less stress due to compression and bending. While position (1.2) will suffer from bending stresses that override the compressive stresses due to the close position to the neutral axis. In position (1.3) the tension and bending stresses both cooperate to induce stresses. The results are presented in figure E.3.

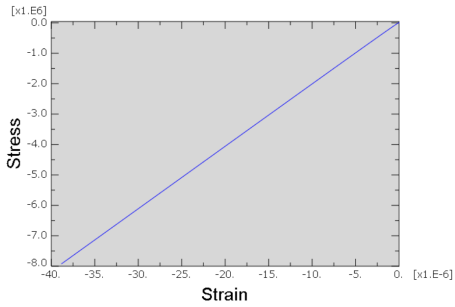

(a) Position (2.1)

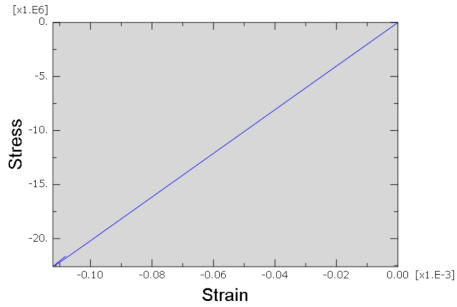

(b) Position (2.2)

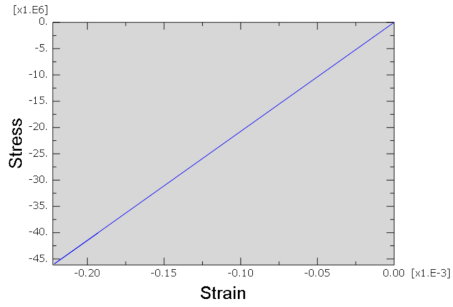

(c) Position (2.3)

Figure E.4: Stress-strain curve from location 2, in z-direction

Figure E.4 presents results corresponding to figure E.1, the stress strain curves were found linear for all three positions. Considering figure 7.10, this is the location with least stress.

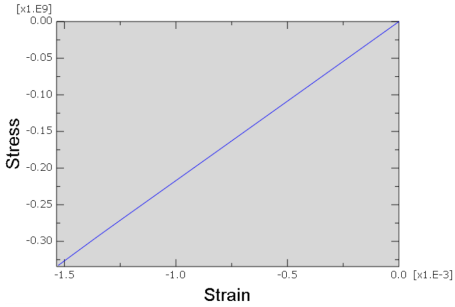

(a) Position (3.1)

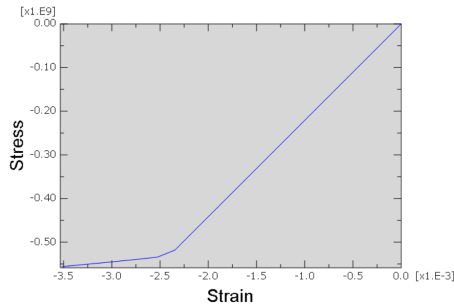

(b) Position (3.2)

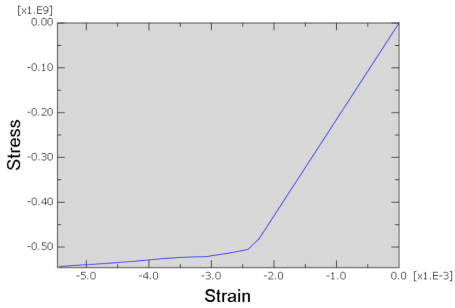

(c) Position (3.3)

Figure E.5: Stress-strain curve from location 3, in z-direction

In figure E.5 the warping of the beam does affect the results regarding the position, compared to the results for location 1. The boundaries constrain the beam, and the bending of the beam induces dominant compressive stresses with yield magnitude. Comparing figure E.5a with figure E.5c, the non-linear behaviour is visible due to more compressive stresses. This effect exists due to an impact of warping.

E.2 Additional Results From DNV GL Ice Pressure Model

Figure 7.16 presents that compressive forces of 619.6 [MPa] and tension forces of 608.7 [MPa] occur in the stiffeners due to the applied ice pressure. This is further assessed in this section by measurements at three different points at three different locations along the flanges, as presented in the beginning of this chapter. As the pressure was increased, also the second pair of stiffeners were subjected to stresses. Thus, the second pair of stiffeners were not further assessed.

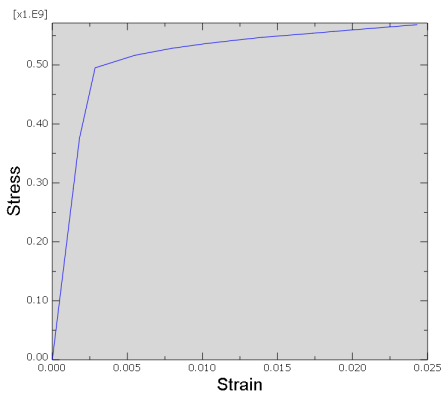

(a) Position (1.1)

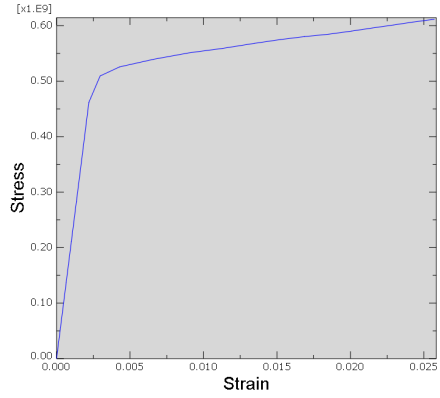

(b) Position (1.2)

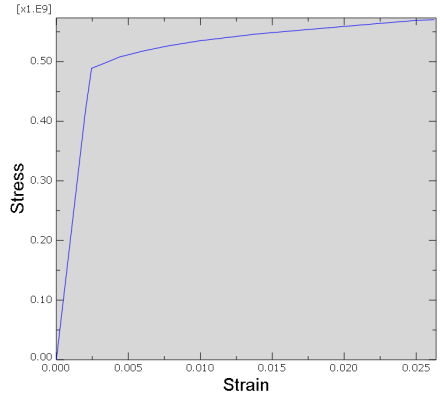

(c) Position (1.3)

Figure E.6: Stress-strain curve from location 1, in z-direction

Due to increased pressure, figure E.6 presents almost equal curves for all positions along the flanges. Due to the increased pressure, the warping effect was surpassed by equal yielding across the flange as the stiffeners reach plasticity and the plate had different behaviour.

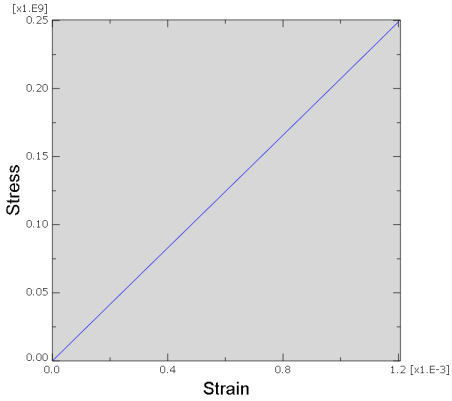

(a) Position (2.1)

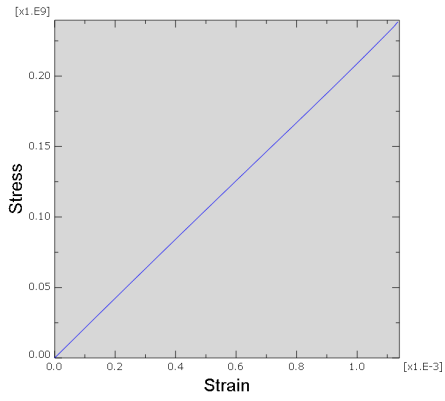

(b) Position (2.2)

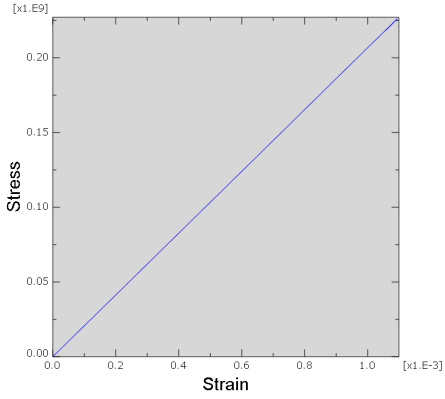

(c) Position (2.3)

Figure E.7: Stress-strain curve from location 2, in z-direction

Sampling location 2, provides linear behaviour at all three points across the flange, as shown by figure E.7. According to figure 7.16, location 2 is the location along the stiffeners with least stress, as it is located at the turning point from tensile to compressive stresses.

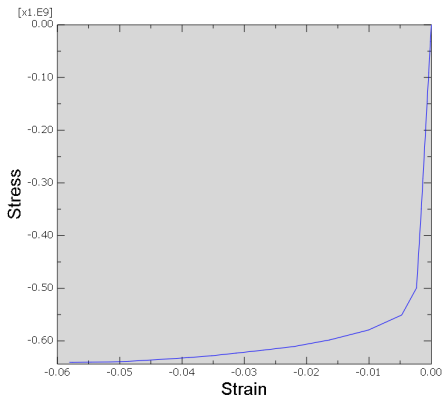

(a) Position (3.1)

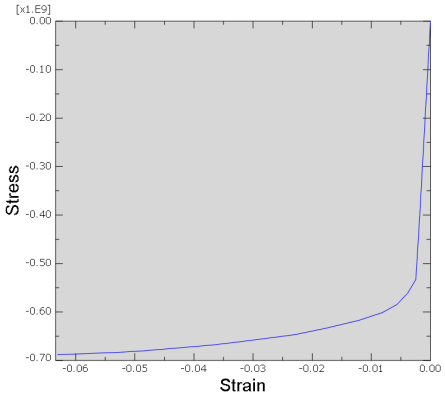

(b) Position (3.2)

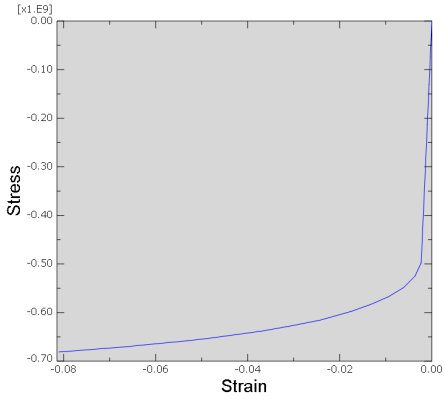

(c) Position (3.3)

Figure E.8: Stress-strain curve from location 3, in z-direction

Figure E.8 presents stress-strain curves for the end of the stiffeners. One observes small differences in the stress and strain levels regarding the sampling points across the flange. This does most likely occur due to small warping of the stiffeners. As for location 1, one observes non-linear material behaviour here.

E.3 Additional Results From IACS Ice Pressure Model

This section provides assessment of the stiffeners. Figure D.14 shows that the large stresses occur in the stiffener flanges. The largest compressive stress occurred at the flange ends, and had a magnitude of -705.5 [MPa] while the tensile stress had a magnitude of 688.3 [MPa], located at the middle of the stiffener span.

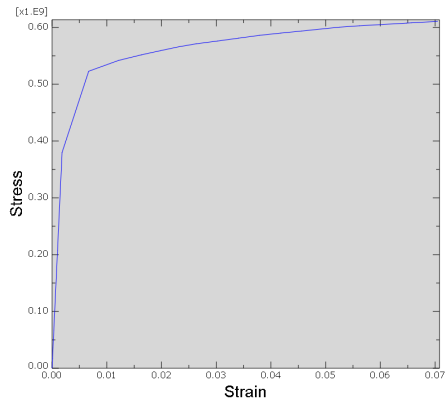

(a) Position (1.1)

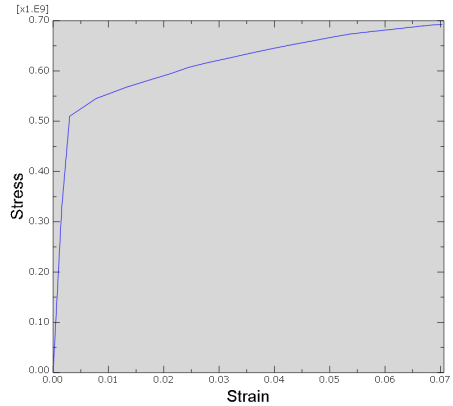

(b) Position (1.2)

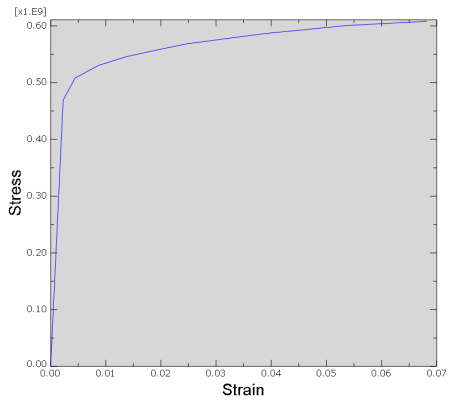

(c) Position (1.3)

Figure E.9: Stress-strain curve from location 1, in z-direction

Figure E.9 shows that the warping effect is almost eliminated due to the increased pressure and that the cross section of the flange has almost the same behaviour. It is reason to believe that the increased pressure includes more of the plate and let the stiffener closest to the loaded area behave more as a loaded beam.

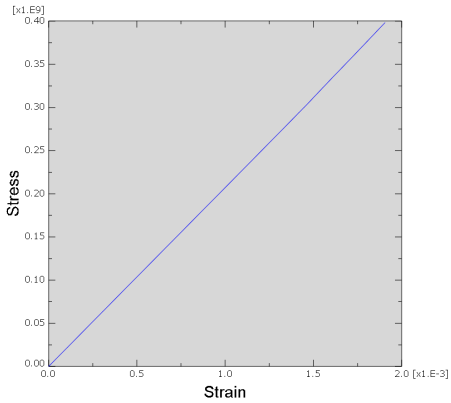

(a) Position (2.1)

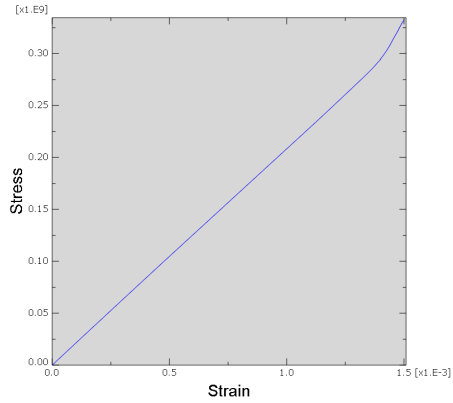

(b) Position (2.2)

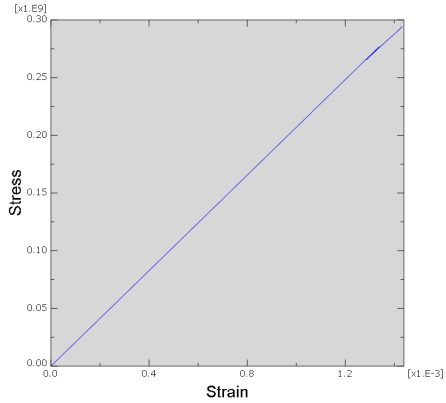

(c) Position (2.3)

Figure E.10: Stress-strain curve from location 2, in z-direction

Figure E.10 presents the same behaviour as for the model subjected to the loads obtained from the DNV GL regulations. Here, one also observes truly linear behaviour.

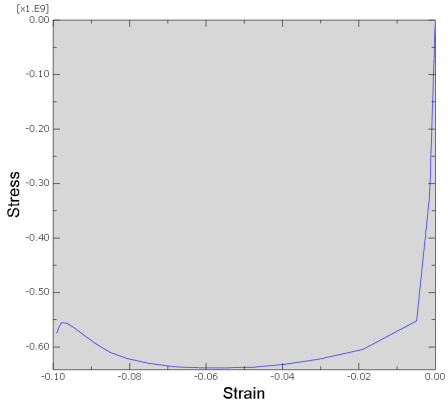

(a) Position (3.1)

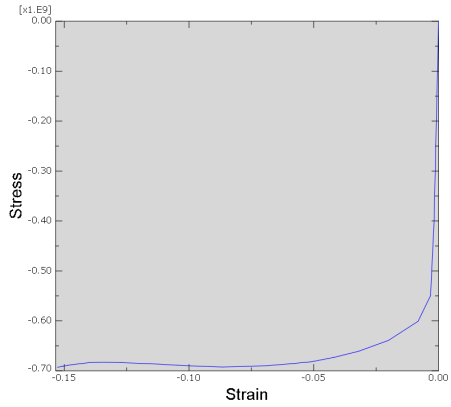

(b) Position (3.2)

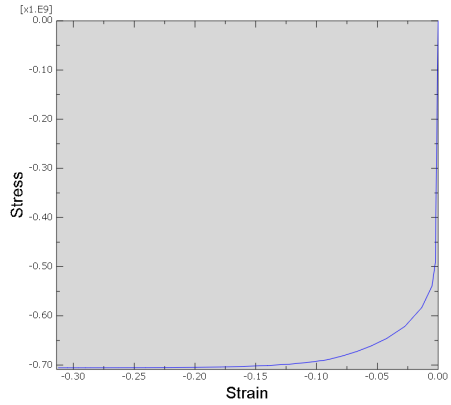

(c) Position (3.3)

Figure E.11: Stress-strain curve from location 3, in z-direction

The stress strain curves for the stiffener ends measured at the flange, are given in figure E.11. There exist small differences for the three sampling points, hence this is believed to occur due to small warping of the stiffeners.

Appendix F

Additional Results - Bow Model

This chapter extends results from the analysis of the plate and stiffeners for the local bow model. The reader should be familiar with the set-up of the analysis, as no further details are given here.

F.1 Plate Assessment - Bow Model

The following subsections provide plots of stress versus true strain for the plate sampling locations excluded from the main part of the thesis.

F.1.1 Location 3 and 4 - Stiffener Side

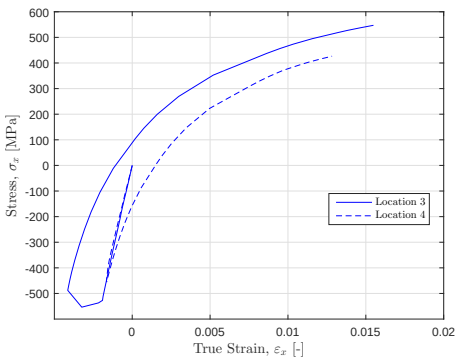

(a) Stress σ_x versus true strain ε_x

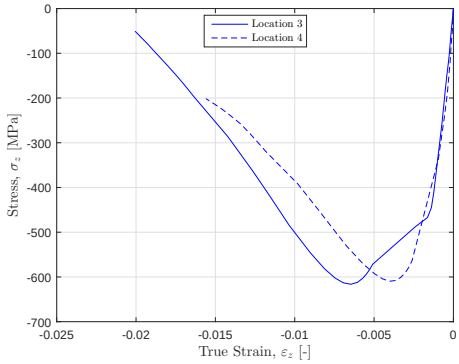

(b) Stress σ_z versus true strain ε_z

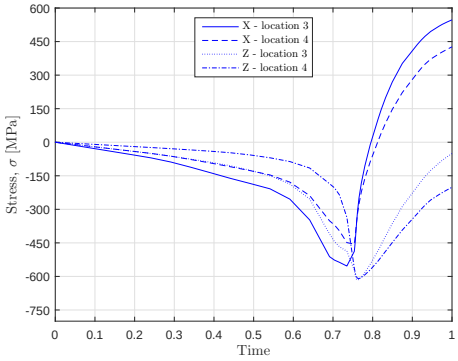

(c) Stress σ plotted versus time.

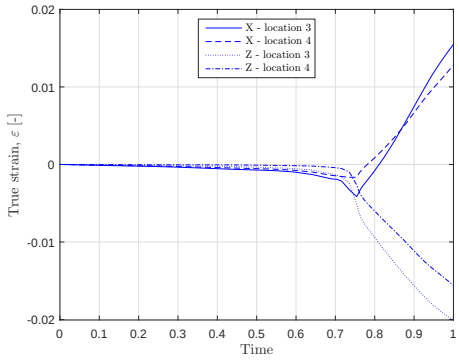

(d) True strain ε plotted versus time.

Figure F.1: Stresses and true strains for location 3 and 4. The time axis describes the load increments, where 0 equals unloaded condition and 1 equals fully loaded.

F.1.2 Location 5 and 6 - Stiffener Side

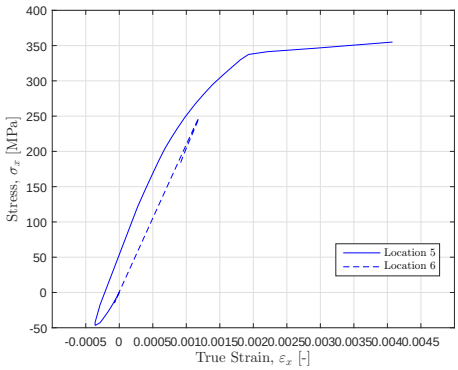

(a) Stress σ_x versus true strain ε_x

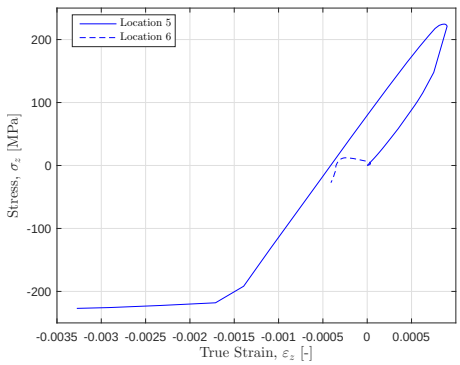

(b) Stress σ_z versus true strain ε_z

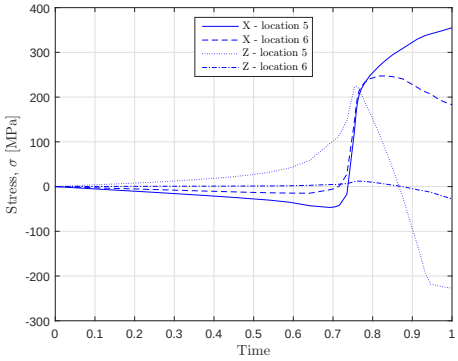

(c) Stress σ plotted versus time.

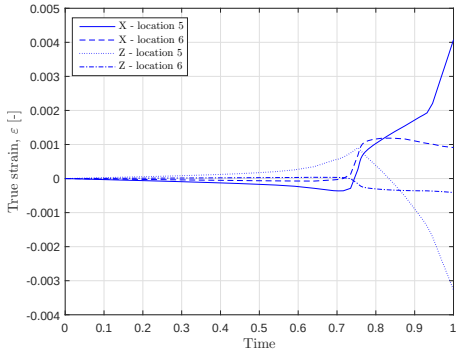

(d) True strain ε plotted versus time.

Figure F.2: Stresses and true strains for location 5 and 6. The time axis describes the load increments, where 0 equals unloaded condition and 1 equals fully loaded.

F.1.3 Location 7 and 8 - Stiffener Side

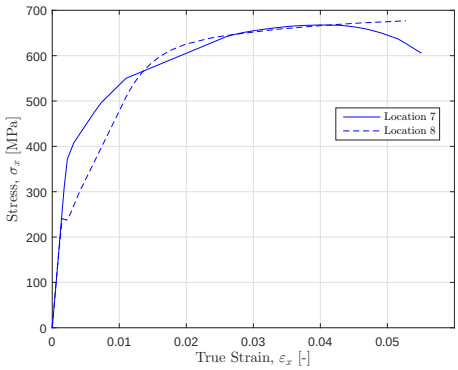

(a) Stress σ_x versus true strain ε_x

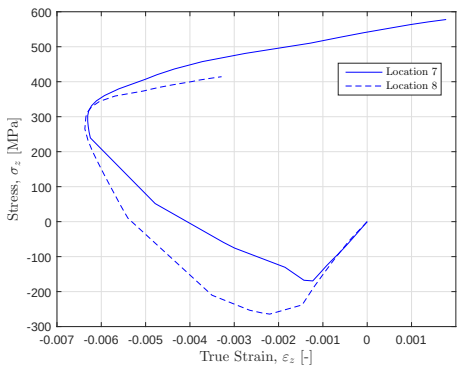

(b) Stress σ_z versus true strain ε_z

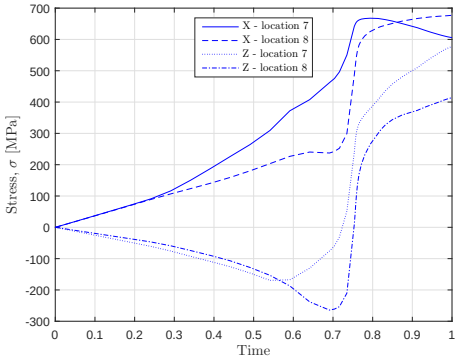

(c) Stress σ plotted versus time.

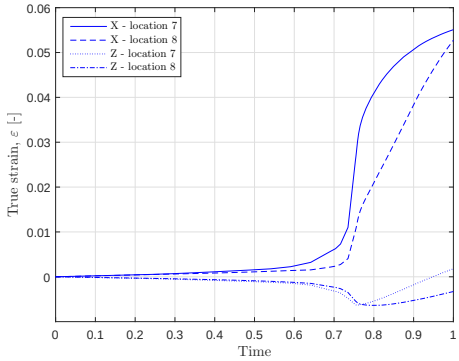

(d) True strain ε plotted versus time.

Figure F.3: Stresses and true strains for location 7 and 8. The time axis describes the load increments, where 0 equals unloaded condition and 1 equals fully loaded.

F.1.4 Location 9 and 10 - Stiffener Side

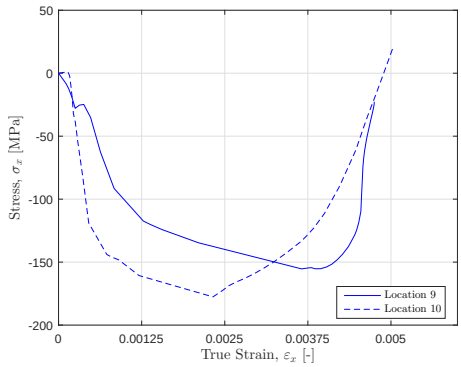

(a) Stress σ_x versus true strain ε_x

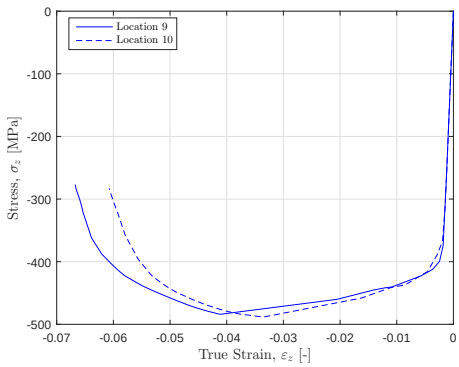

(b) Stress σ_z versus true strain ε_z

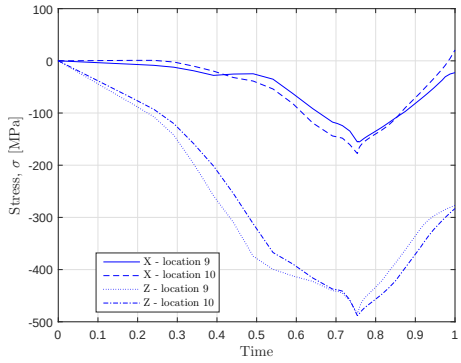

(c) Stress σ plotted versus time.

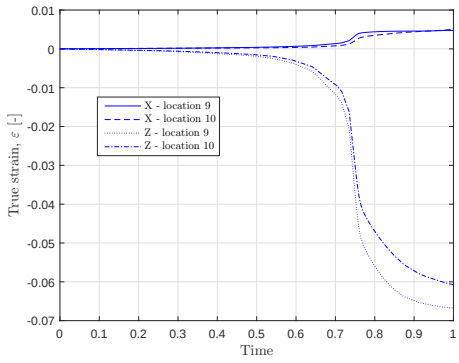

(d) True strain ε plotted versus time.

Figure F.4: Stresses and true strains for location 9 and 10. The time axis describes the load increments, where 0 equals unloaded condition and 1 equals fully loaded.

F.1.5 Comments to the Figures - Stiffener Side

From the figures presenting stress and true strain plotted over time, one can observe the same tendency for all figures. When the load fraction is between 0.7 and 0.8, the three middle stiffeners collapse, hence the plate looses it's support. Further, it is observed that the stresses and strains are reduced as the sampling location is moved further from the loaded area. Looking at location 1-6, one should notice that the stresses in x-direction are reduced from approximately 680 to 250 [MPa]. The true strain in x-direction is reduced from 0.05 to 0.001 [-]. In z-direction, the stresses are reduced from 450 to almost 0 [MPa]. The strains are reduced from -0.02 to -0.0004 [-].

F.1.6 Location 3 and 4 - Load Side

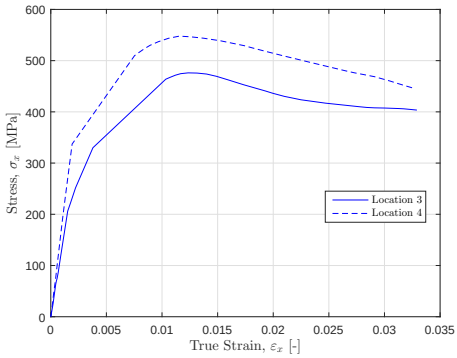

(a) Stress σ_x versus true strain ε_x

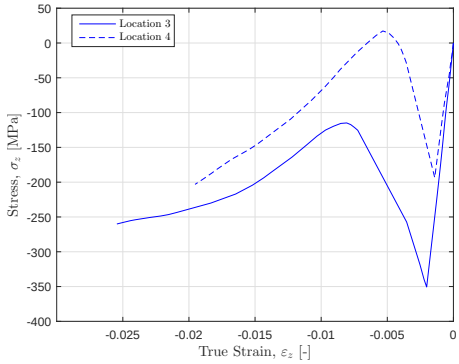

(b) Stress σ_z versus true strain ε_z

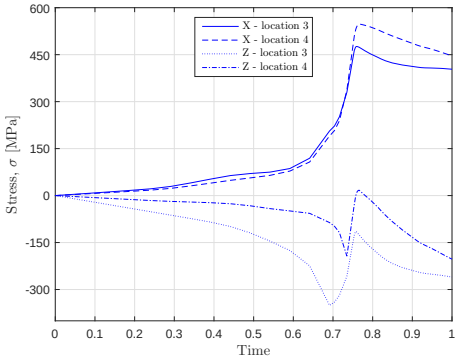

(c) Stress σ plotted versus time.

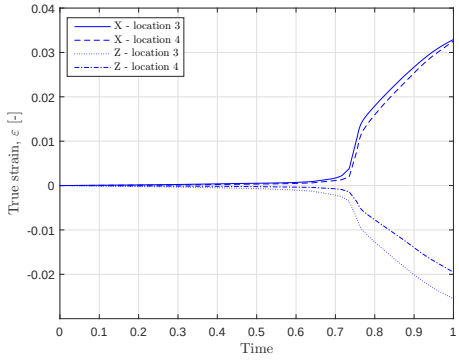

(d) True strain ε plotted versus time.

Figure F.5: Stresses and true strains for location 3 and 4. The time axis describes the load increments, where 0 equals unloaded condition and 1 equals fully loaded.

F.1.7 Location 5 and 6 - Load Side

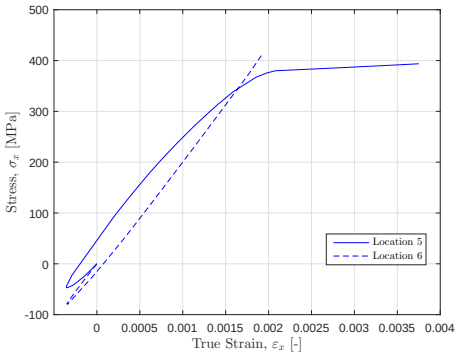

(a) Stress σ_x versus true strain ε_x

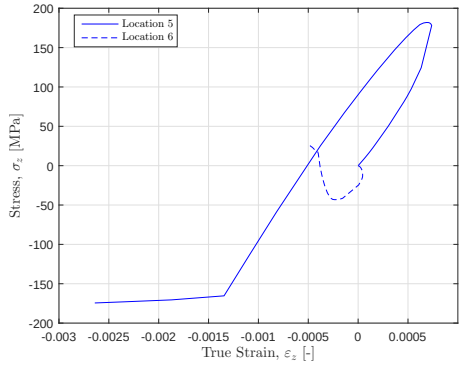

(b) Stress σ_z versus true strain ε_z

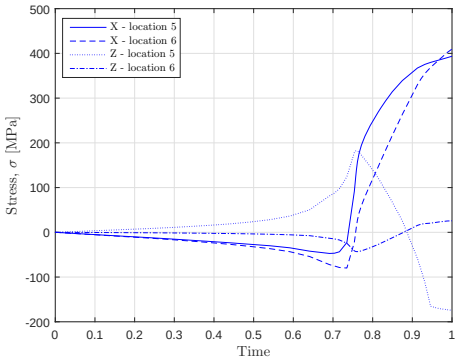

(c) Stress σ plotted versus time.

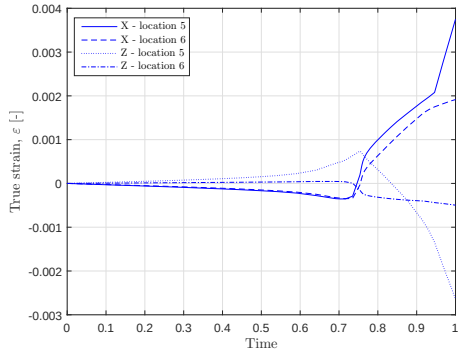

(d) True strain ε plotted versus time.

Figure F.6: Stresses and true strains for location 5 and 6. The time axis describes the load increments, where 0 equals unloaded condition and 1 equals fully loaded.

F.1.8 Location 7 and 8 - Load Side

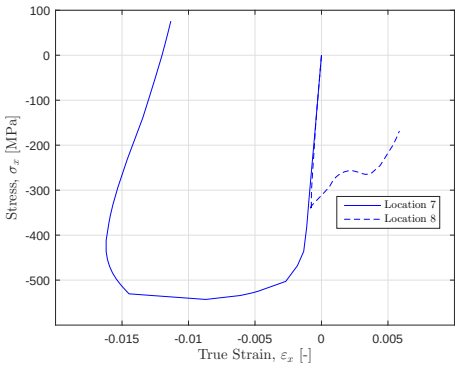

(a) Stress σ_x versus true strain ε_x

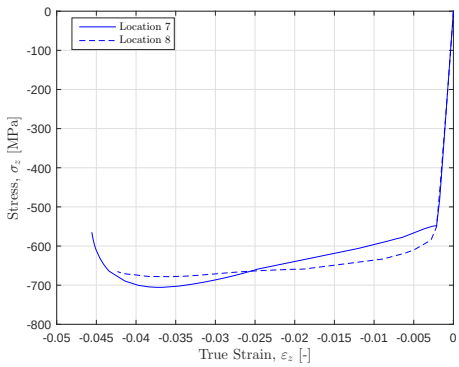

(b) Stress σ_z versus true strain ε_z

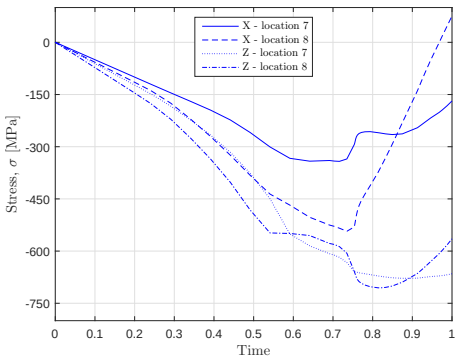

(c) Stress σ plotted versus time.

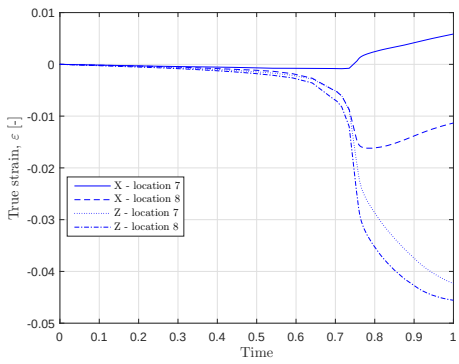

(d) True strain ε plotted versus time.

Figure F.7: Stresses and true strains for location 7 and 8. The time axis describes the load increments, where 0 equals unloaded condition and 1 equals fully loaded.

F.1.9 Location 9 and 10 - Load Side

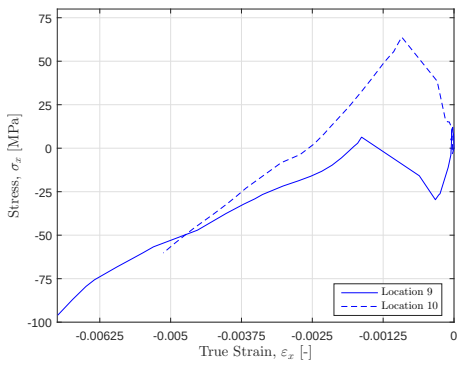

(a) Stress σ_x versus true strain ε_x

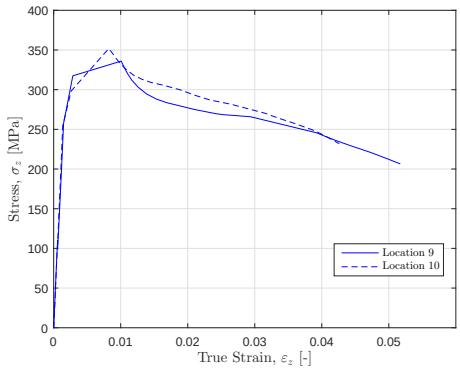

(b) Stress σ_z versus true strain ε_z

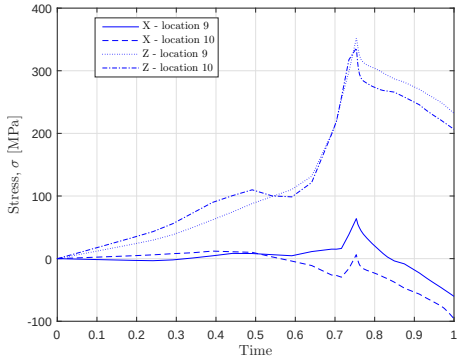

(c) Stress σ plotted versus time.

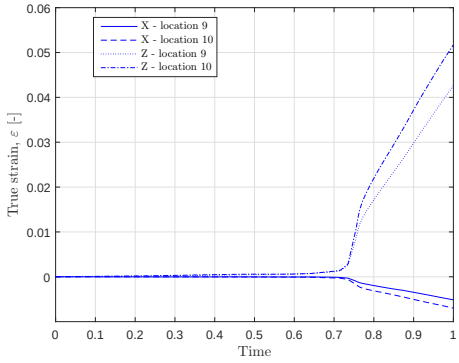

(d) True strain ε plotted versus time.

Figure F.8: Stresses and true strains for location 9 and 10. The time axis describes the load increments, where 0 equals unloaded condition and 1 equals fully loaded.

F.1.10 Comments to the Figures - Load Side

The same tendency is observed for the plots presenting the stress and true strain over time, when the load fraction reaches a value between 0.7 and 0.8. Reasonably due to a collapse of the three middle stiffeners. The load side stresses and strains change as the sampling location increases the distance from the load. Between location 1 and 6, the stress in x-direction changes from approximately -200 to 400 [MPa]. While the true strain changes from approximately -0.015 to 0.002 [-]. The change from compression to tension is reasonably because the stiffeners far from the loaded area still support the plate in z-direction only, and the dented area suffers from compression resulting in tension for the surrounding areas. In z-direction, the stress varies from approximately -620 [MPa] at location 1, to 20 [MPa] at location 6. The true strain is reduced from approximately -0.028 to -0.0005 [-].

F.2 Stiffener Assessment - Bow Model

This section presents the analysis and results of the stiffener assessment. As the plate analysis indicated stiffener buckling for a load fraction larger than 0.735, an assessment of the stiffeners closest to the applied load was found necessary. As the extend of the main part was somewhat limited, this assessment was put in the appendix. The same procedure as for the plate was conducted at the stiffeners. Figure F.9 presents the two stiffeners assessed, with numbering of each stiffener.

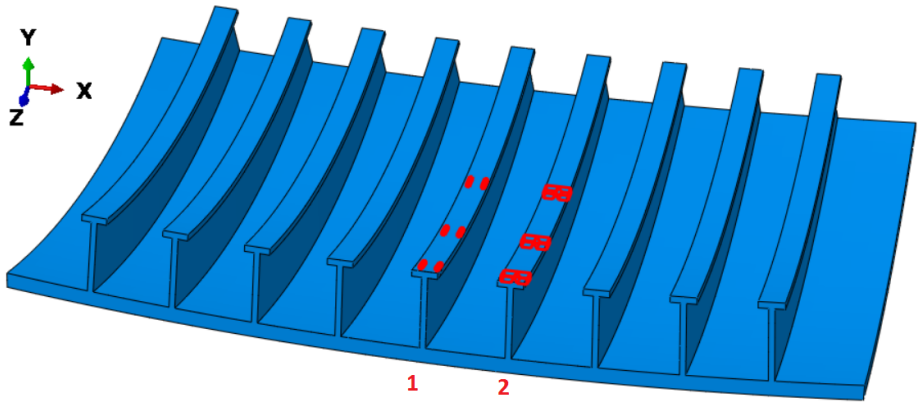

Figure F.9: Numbering of the stiffeners. Stiffener 1 is located at the middle of the plate. Stiffener 2 is located at the edge of the load patch.

Each flange of stiffener 1 and 2 had six sampling locations as shown in figure F.10.

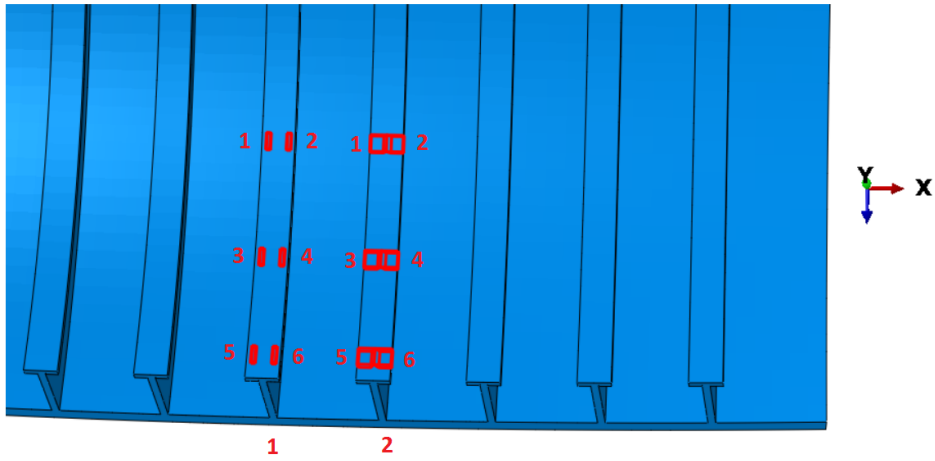

Figure F.10: Numbering of the flanges for stiffener 1 and 2.

The stiffeners indirectly impacted by the contact pressure, were considered less critical, hence neglected in the analysis. Additionally, they were left out of the assessment to give priority to other assessments. For the sampling locations presented in figure F.10, stresses in z-direction were measured for all locations. This resulted in the following plots for stiffener 1.

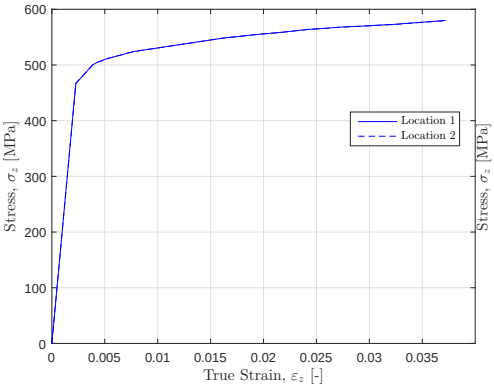

(a) location 1 and 2 for stiffener 1.

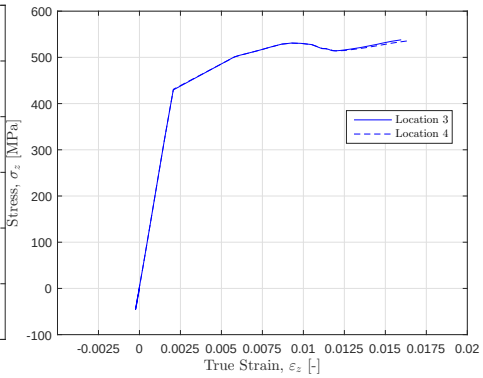

(b) location 3 and 4 for stiffener 1.

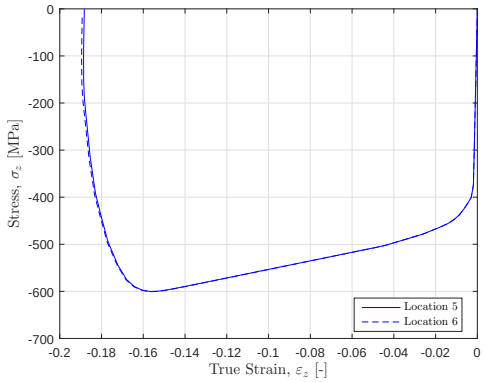

(c) location 5 and 6 for stiffener 1.

Figure F.11: Stress σ_z versus true strain ε_z in z-direction.

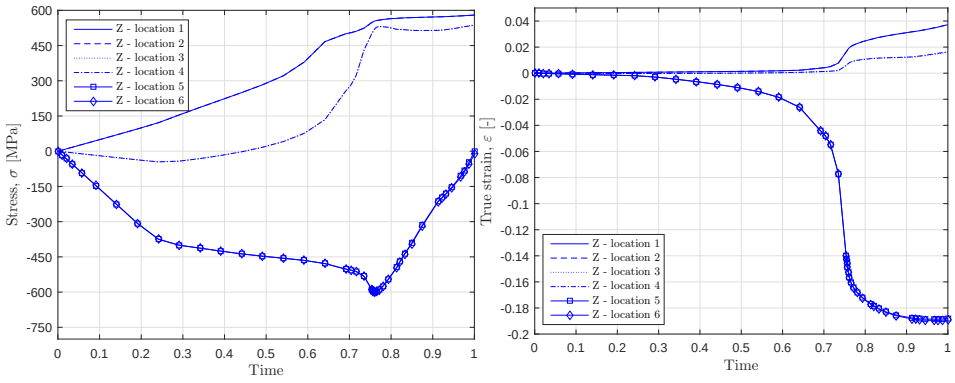

(a) Stress σ_z plotted versus time.

(b) True strain ε_z plotted versus time.

Figure F.12: The time axis describes the load increments, where 0 equals unloaded condition and 1 equals fully loaded.

From figure F.11a, F.11b and F.11c one can observe almost identical behaviour for each pair of locations. This indicates of no warping of the stiffener. For location 1, 2, 3 and 4 one could observe a typical stress-strain curve with a defined yield point. In figure F.11a the yield stress is approximately 480 [MPa], while in figure F.11b it is approximately 450 [MPa]. In figure F.11c two locations of the curves are of interest. The first location indicates the yield stress at an approximate value of -400 [MPa] in compression. The second location at a true strain of 0.16 and a stress level of -600 [MPa] indicates the point of collapse for stiffener 1. This is confirmed by figure F.12a and F.12b, between a load fraction from 0.7 to 0.8 [-]. From previous assessment of the plate the same behaviour between a load fraction of 0.7 to 0.8 was observed. The stress-strain curve presented in figure F.11c indicates that stiffener 1 suffers from a development of a plastic hinge, hence collapses.

For stiffener 2, the following plots were obtained from the analysis. Similar stiffener 1, stiffener 2 had 6 sampling locations, as indicated by figure F.10.

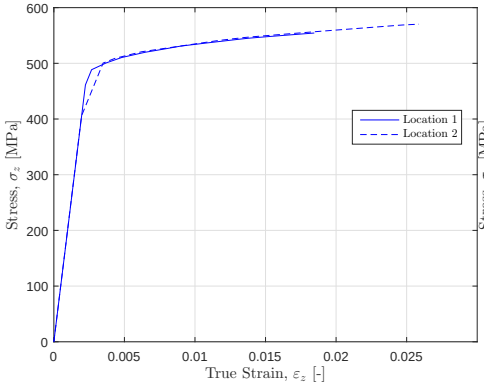

(a) location 1 and 2 for stiffener 2.

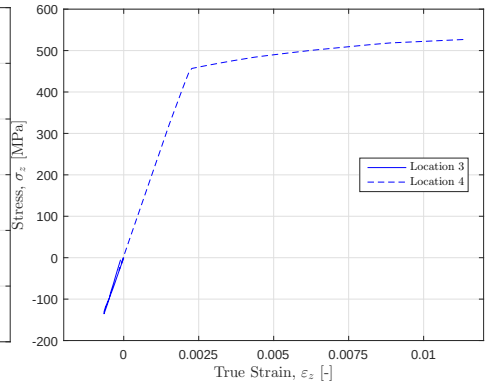

(b) location 3 and 4 for stiffener 2.

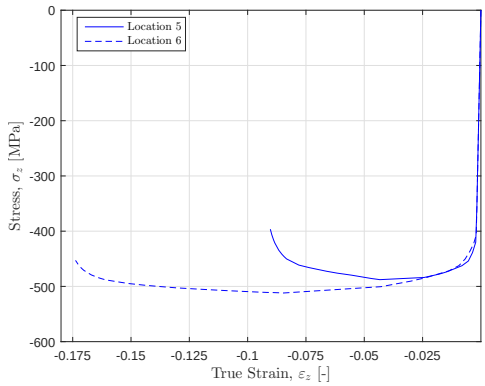

(c) location 5 and 6 for stiffener 2.

Figure F.13: Stress σ_z versus true strain ε_z in z-direction.

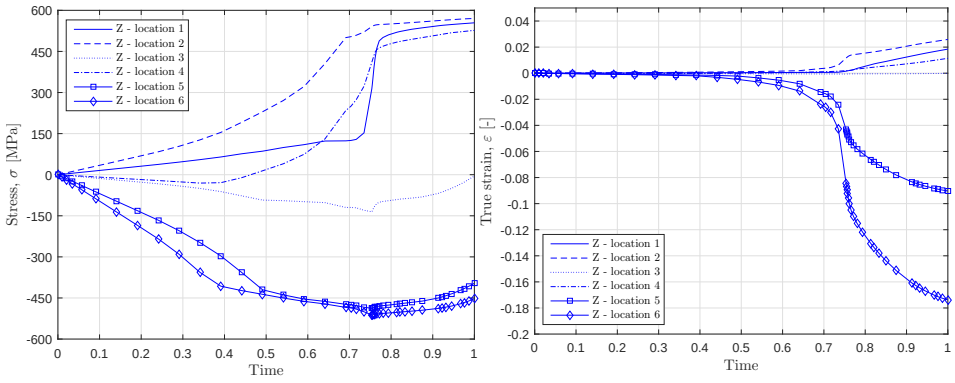

(a) Stress σ_z plotted versus time.

(b) True strain ε_z plotted versus time.

Figure F.14: The time axis describes the load increments, where 0 equals unloaded condition and 1 equals fully loaded.

In figure F.13a one can observe a small difference between the two locations. The strains at location 2 reach a higher level than at location 1, while the stress level is almost equal. Thus, the curves tend to behave equal until a true strain level of 0.018 [-]. The yield stress for both curves is approximately 480 [MPa] in tension. From figure F.13b one observes a different behaviour comparing location 3 and 4. Comparing location 3 and 4, location 3 has almost no stresses or strains. This is well substantiated by figure F.14a and F.14b. The yield stress at location 4 is approximately 450 [MPa]. In figure F.13c one observes the effect of the boundary condition and the fact that the stiffener obviously warps. Until yield at a compressive stress of 480 [MPa], the behaviour is similar, while the difference starts at a true strain level of -0.025 [-]. From figure F.14b this strain level is also located between a load fraction of 0.7 to 0.8. This indicates that the warping of stiffener 2 occur at the same time as the collapse happens for stiffener 1.

The following figures present contour plots for both stiffeners in z- and y-direction. The stresses in y-direction for both flange and web, and the stresses in z-direction for the web will only be presented graphically.

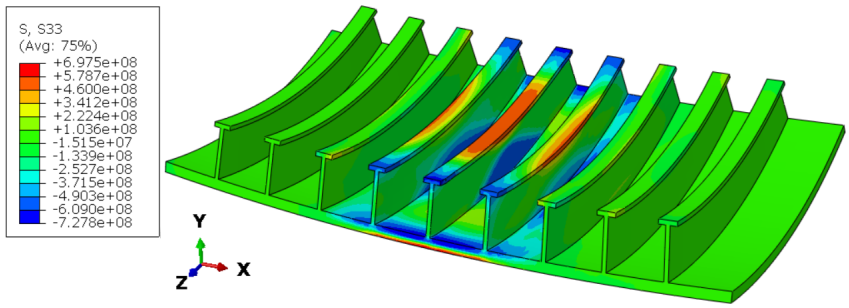

(a) Load fraction equal 0.735

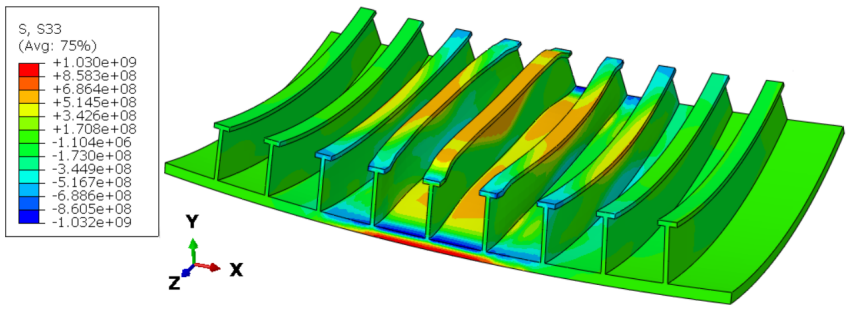

(b) Load fraction equal 1

Figure F.15: Contour plot of the stress in z-direction of the bow model for two different load fractions.

Figure F.15a indicates a maximum tensile stress of 578.7 [MPa], and a maximum compressive stress of -727.8 [MPa] (stiffener 1) and -609 [MPa] (stiffener 2) at the flanges. In figure F.15b these values have changed to 686.4, -688.6 and -860.5 [MPa] respectively. The web of both stiffeners is mostly impacted by the stresses at the midpoint, close to the flanges.

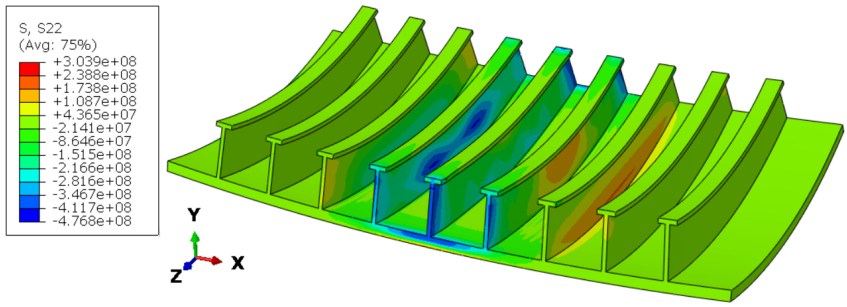

(a) Load fraction equal 0.735

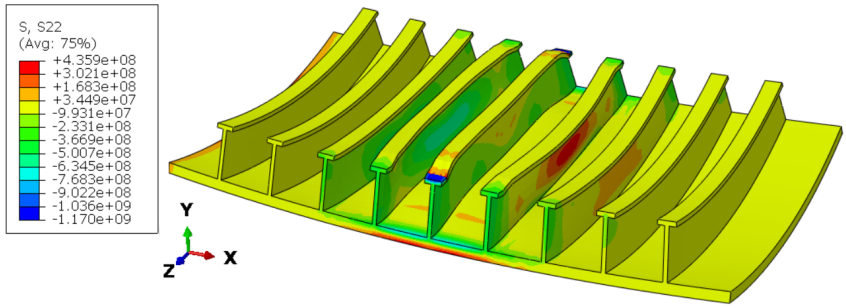

(b) Load fraction equal 1

Figure F.16: Contour plot of the stress in y-direction of the bow model for two different load fractions.

Figure F.16 indicates small stresses in the flanges for both stiffeners. The exception is location 5 and 6 for stiffener 1, where the magnitude reaches a compressive stress of -1170 [MPa].

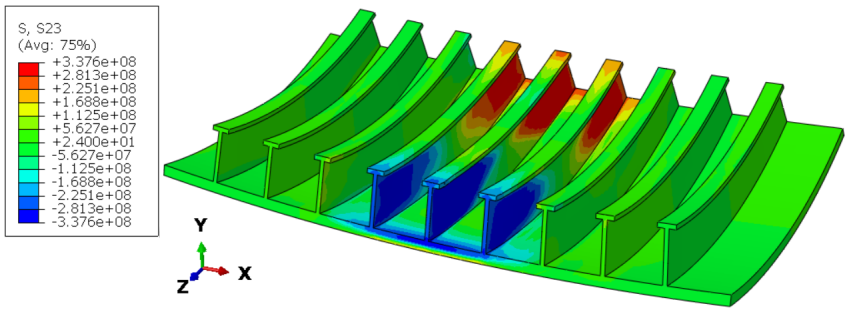

(a) Load fraction equal 0.735

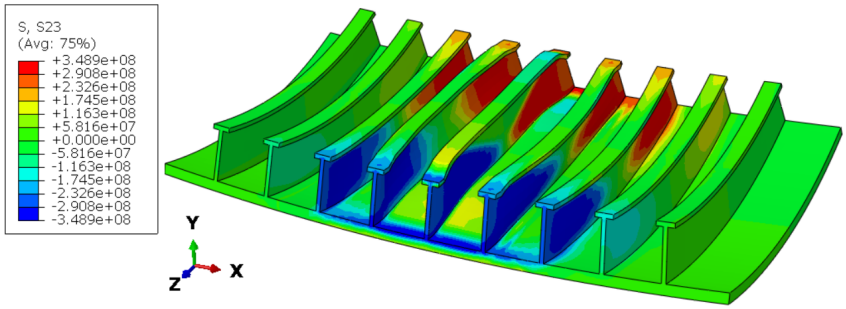

(b) Load fraction equal 1

Figure F.17: Contour plot of the shear stress in yz-direction of the bow model for two different load fractions.

Figure F.17 presents large shear stresses in the yz-direction. Prior to the collapse (figure F.17a) only the three stiffeners located above the loaded area suffer from shear stresses with an absolute value of 337.6 [MPa]. After the collapse, these shear stresses have increased to an absolute value of 348.9 [MPa] and additionally impacted the two stiffeners next to the ones located over the loaded area.

F.3 Boundary Condition Assessment - Bow Model

This section provides additional results from the assessment of the boundary conditions. Information about set-up and sampling points are given in the main part, unless other specified.

F.3.1 Plate Assessment - Various Boundaries

The figures presented here provide results for the plate assessment, where the sampling locations are presented previously. Discussion and comments on the plots are given in the main part.

F.3.2 Stiffener Side - Location 3 and 4

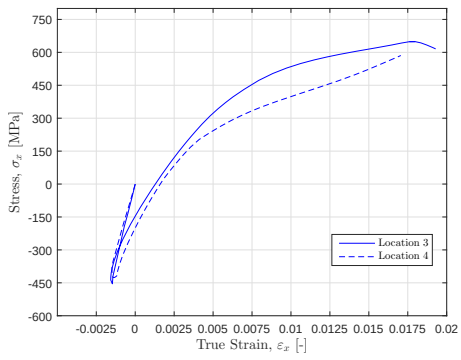

(a) Spring stiffness $\kappa = 1 \cdot 10^3$ [N/rad]

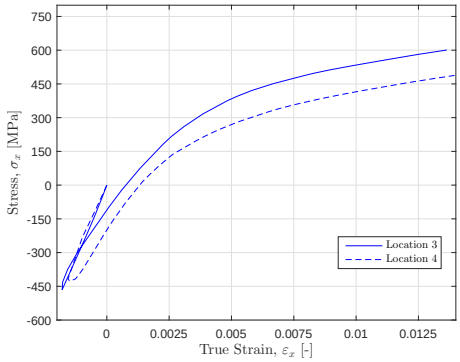

(b) Spring stiffness $\kappa = 1 \cdot 10^6$ [N/rad]

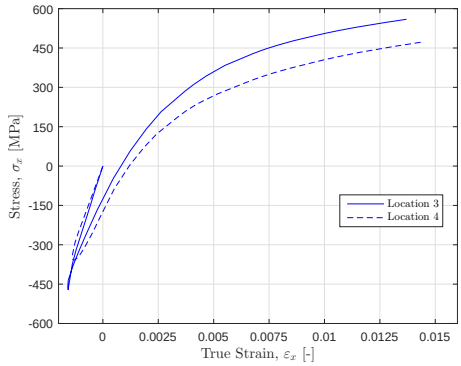

(c) Spring stiffness $\kappa = 1 \cdot 10^9$ [N/rad]

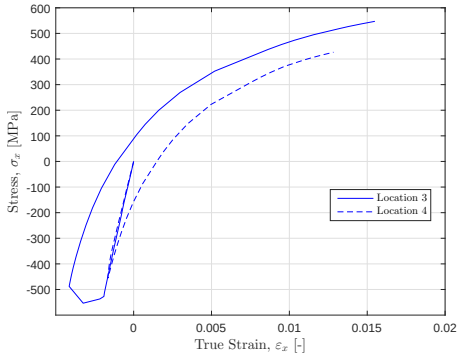

(d) Fixed boundary condition.

Figure F.18: Stress σ_x versus true strain ε_x in x-direction at location 3 and 4 on the stiffener side.

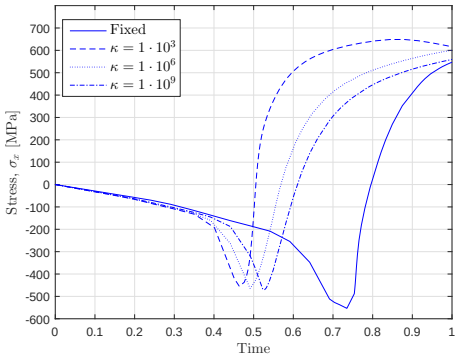

(a) Stress, σ_x, location 3

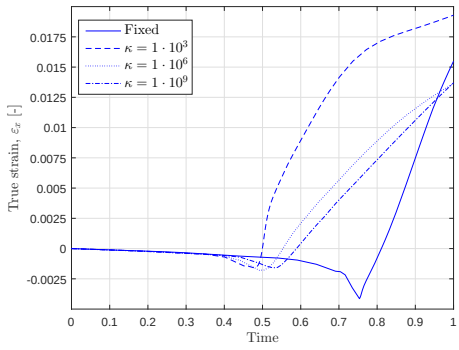

(b) True strain, ε_x, location 3

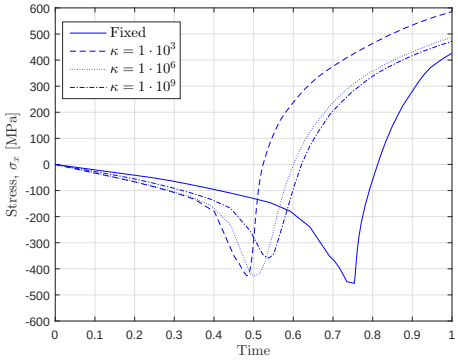

(c) Stress, σ_x, location 4

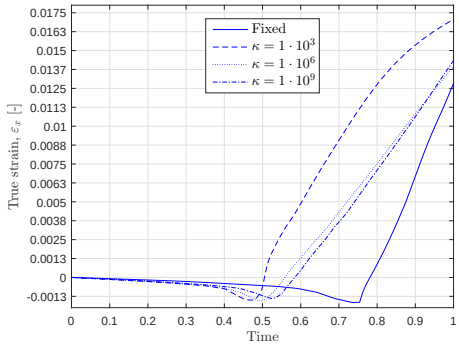

(d) True strain, ε_x, location 4

Figure F.19: Stress σ_x and true strain ε_x in x-direction at location 3 and 4 plotted over time. The scale on the x-axis presents the load fraction.

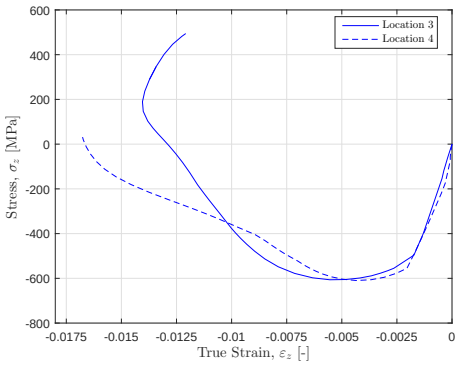

(a) Spring stiffness $\kappa = 1 \cdot 10^3$ [N/rad]

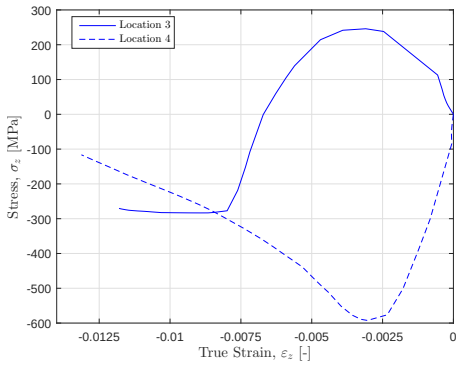

(b) Spring stiffness $\kappa = 1 \cdot 10^6$ [N/rad]

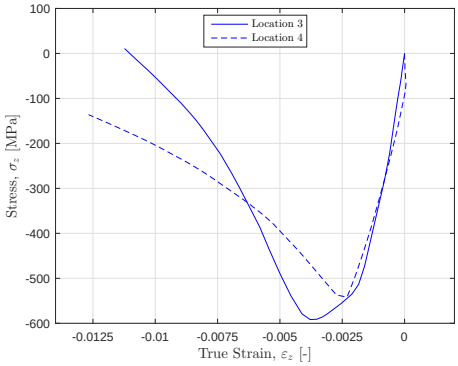

(c) Spring stiffness $\kappa = 1 \cdot 10^9$ [N/rad]

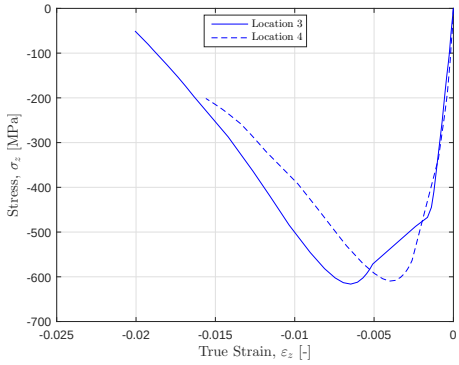

(d) Fixed boundary condition.

Figure F.20: Stress σ_z versus true strain ε_z in z-direction at location 3 and 4 on the stiffener side. Note the different scales between each figure.

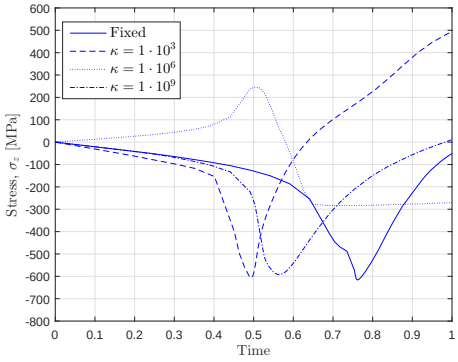

(a) Stress, σ_z, location 3

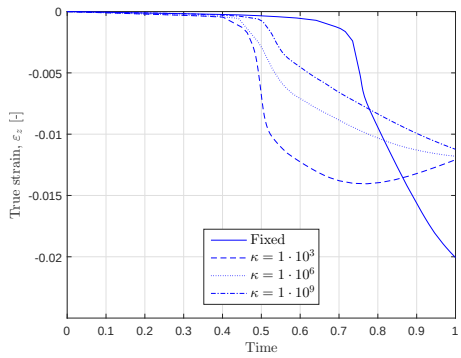

(b) True strain, ε_z, location 3

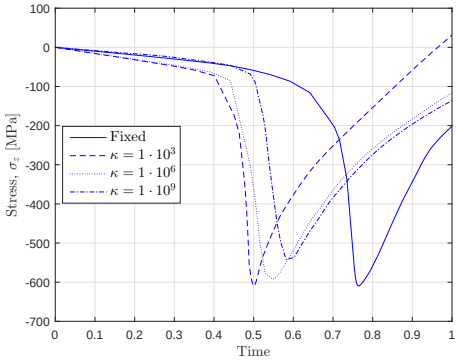

(c) Stress, σ_z, location 4

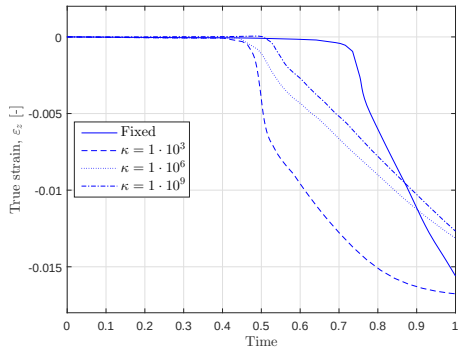

(d) True strain, ε_z, location 4

Figure F.21: Stress σ_z and true strain ε_z in z-direction at location 3 and 4 plotted over time. The scale on the x-axis presents the load fraction.

F.3.3 Stiffener Side - Location 5 and 6

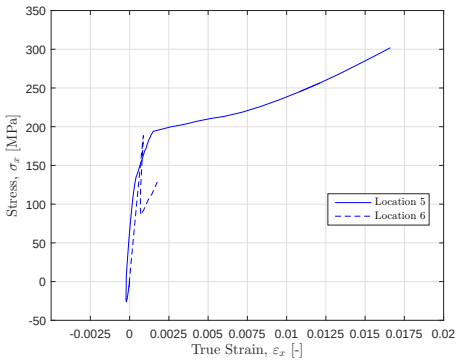

(a) Spring stiffness $\kappa = 1 \cdot 10^3$ [N/rad]

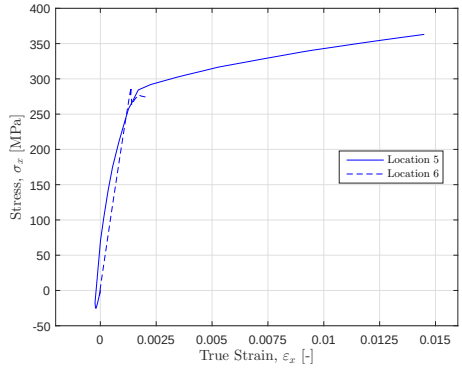

(b) Spring stiffness $\kappa = 1 \cdot 10^6$ [N/rad]

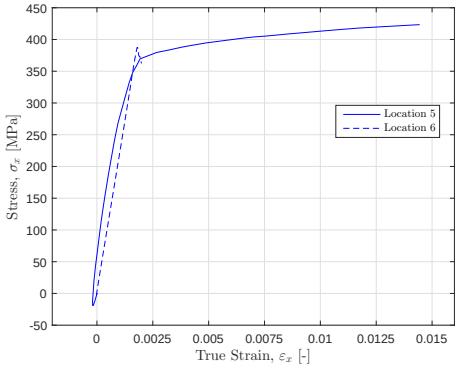

(c) Spring stiffness $\kappa = 1 \cdot 10^9$ [N/rad]

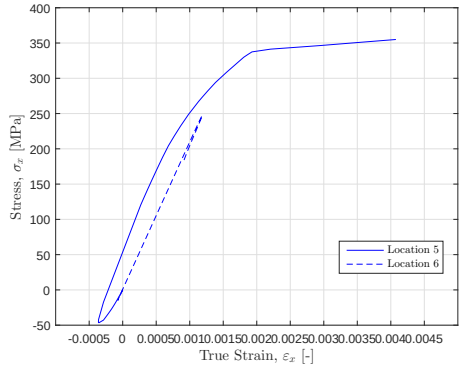

(d) Fixed boundary condition.

Figure F.22: Stress σ_x versus true strain ε_x in x-direction at location 5 and 6 on the stiffener side.

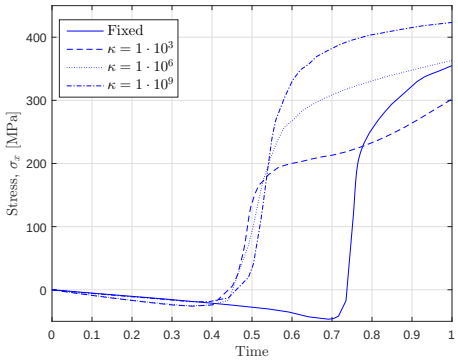

(a) Stress, σ_x, location 5

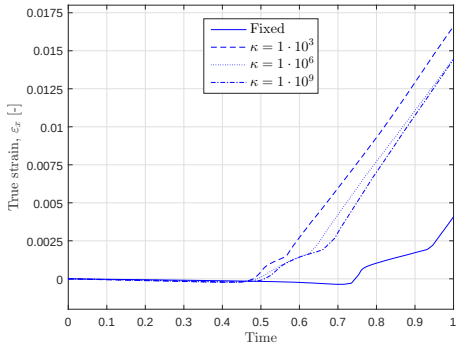

(b) True strain, ε_x, location 5

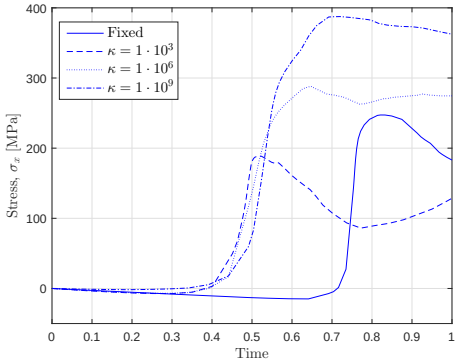

(c) Stress, σ_x, location 6

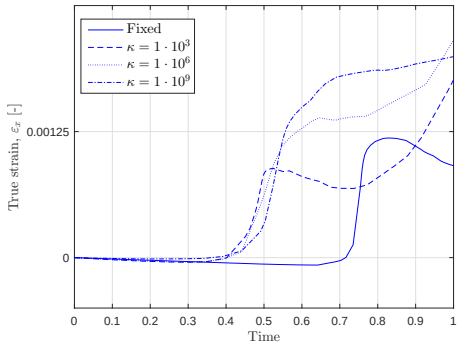

(d) True strain, ε_x, location 6

Figure F.23: Stress σ_x and true strain ε_x in x-direction at location 5 and 6 plotted over time. The scale on the x-axis presents the load fraction.

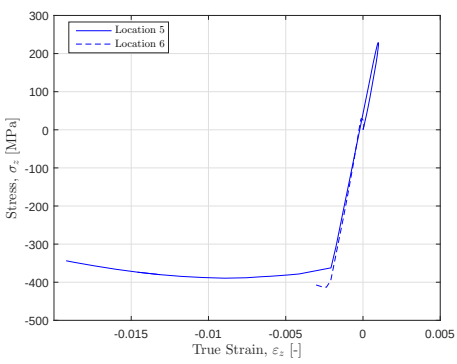

(a) Spring stiffness $\kappa = 1 \cdot 10^3$ [N/rad]

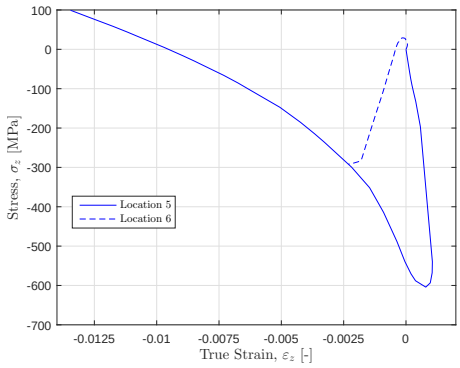

(b) Spring stiffness $\kappa = 1 \cdot 10^6$ [N/rad]

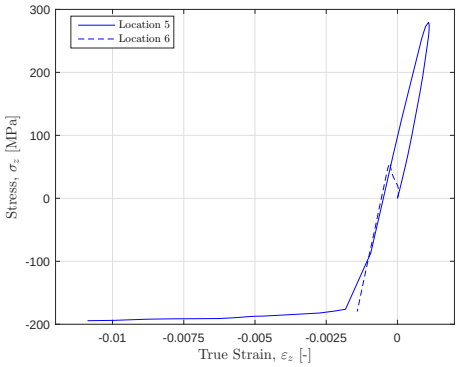

(c) Spring stiffness $\kappa = 1 \cdot 10^9$ [N/rad]

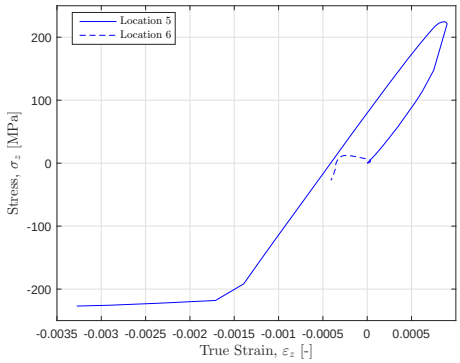

(d) Fixed boundary condition.

Figure F.24: Stress σ_z versus true strain ε_z in z-direction at location 5 and 6 on the stiffener side. Note the different scales between each figure.

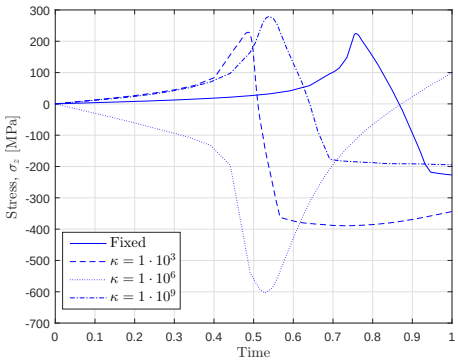

(a) Stress, σ_z, location 5

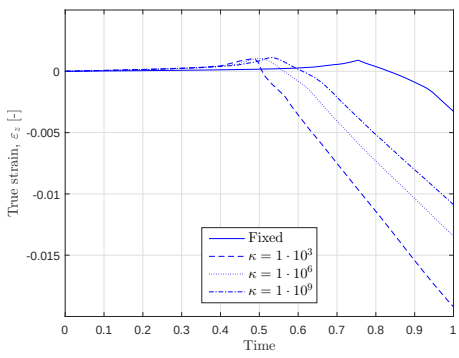

(b) True strain, ε_z, location 5

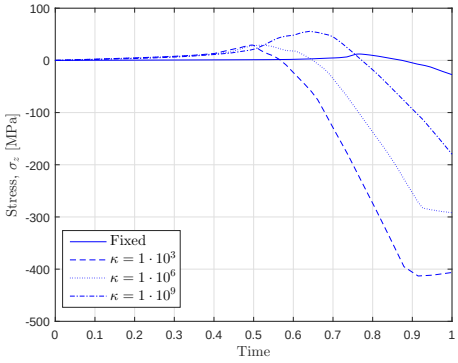

(c) Stress, σ_z, location 6

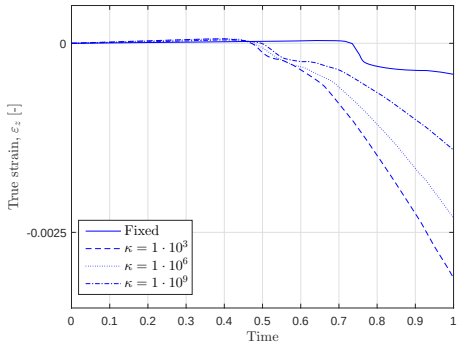

(d) True strain, ε_z, location 6

Figure F.25: Stress σ_z and true strain ε_z in z-direction at location 5 and 6 plotted over time. The scale on the x-axis presents the load fraction.

F.3.4 Stiffener Side - Location 7 and 8

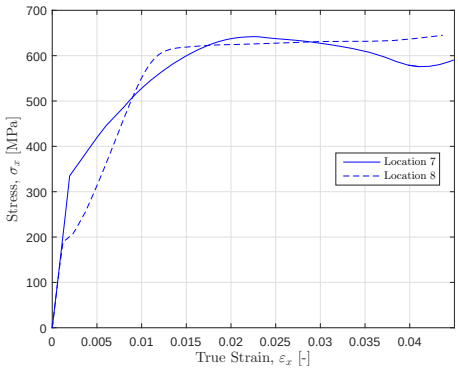

(a) Spring stiffness $\kappa = 1 \cdot 10^3$ [N/rad]

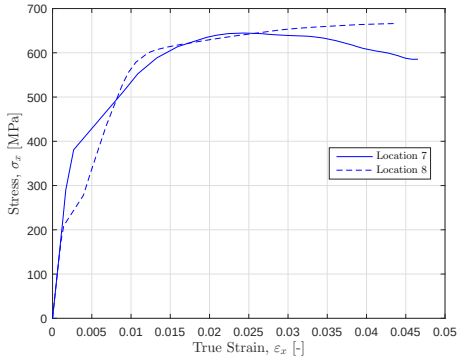

(b) Spring stiffness $\kappa = 1 \cdot 10^6$ [N/rad]

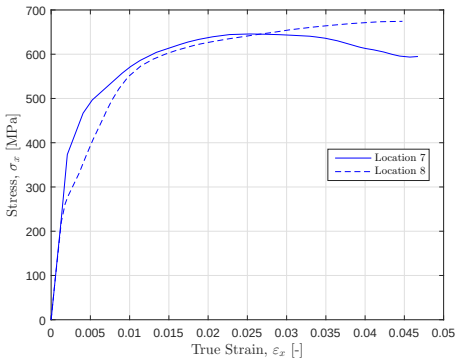

(c) Spring stiffness $\kappa = 1 \cdot 10^9$ [N/rad]

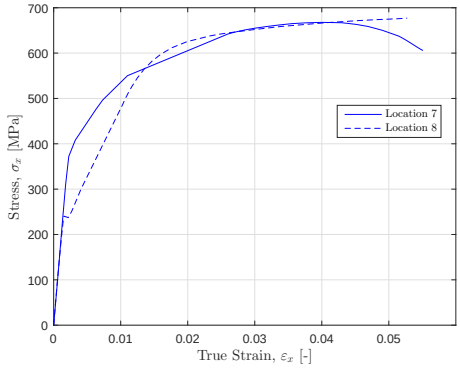

(d) Fixed boundary condition.

Figure F.26: Stress σ_x versus true strain ε_x in x-direction at location 7 and 8 on the stiffener side.

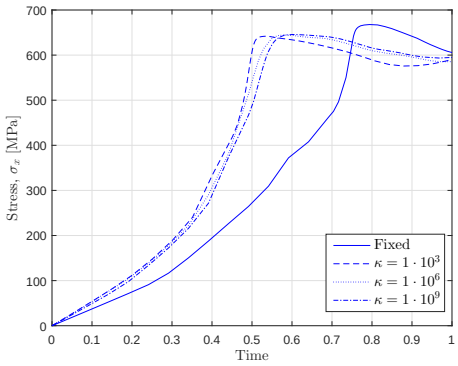

(a) Stress, σ_x, location 7

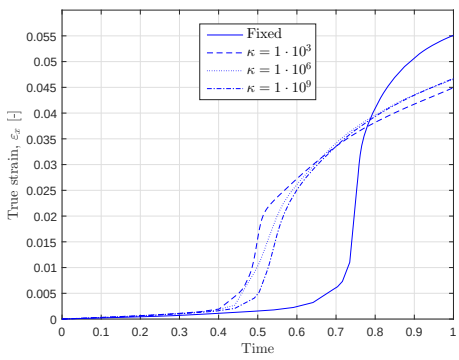

(b) True strain, ε_x, location 7

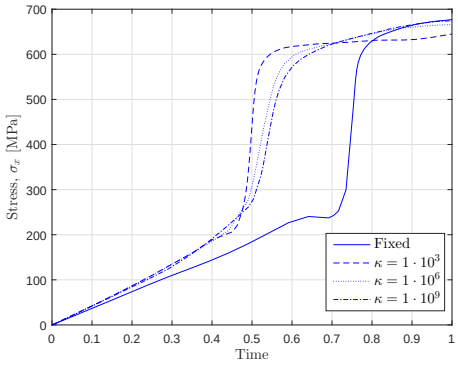

(c) Stress, σ_x, location 8

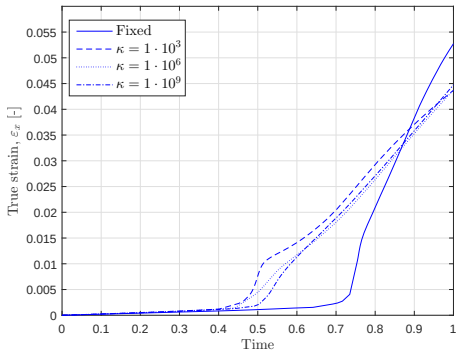

(d) True strain, ε_x, location 8

Figure F.27: Stress σ_x and true strain ε_x in x-direction at location 7 and 8 plotted over time. The scale on the x-axis presents the load fraction.

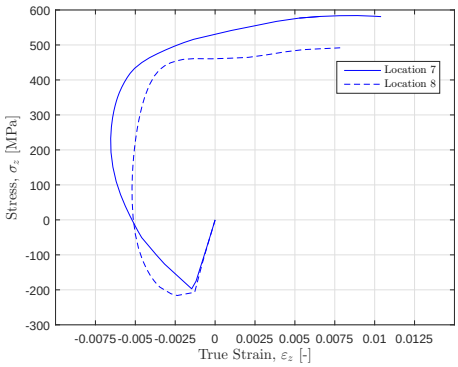

(a) Spring stiffness $\kappa = 1 \cdot 10^3$ [N/rad]

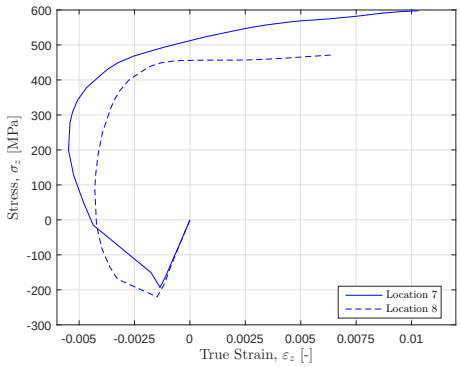

(b) Spring stiffness $\kappa = 1 \cdot 10^6$ [N/rad]

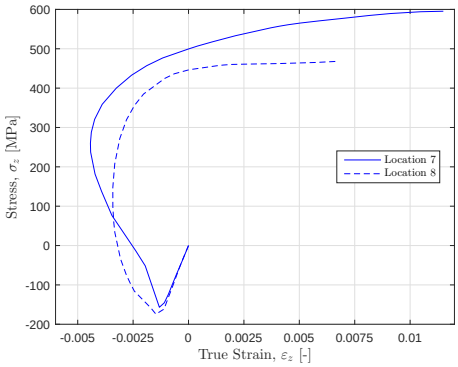

(c) Spring stiffness $\kappa = 1 \cdot 10^9$ [N/rad]

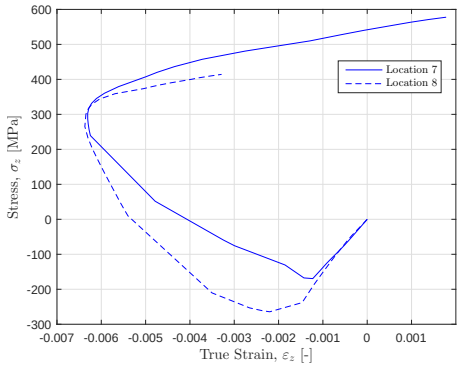

(d) Fixed boundary condition.

Figure F.28: Stress σ_z versus true strain ε_z in z-direction at location 7 and 8 on the stiffener side. Note the different scales between each figure.

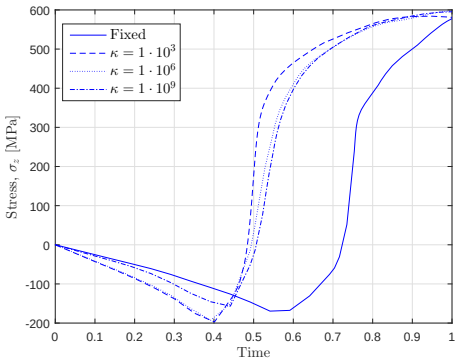

(a) Stress, σ_z, location 7

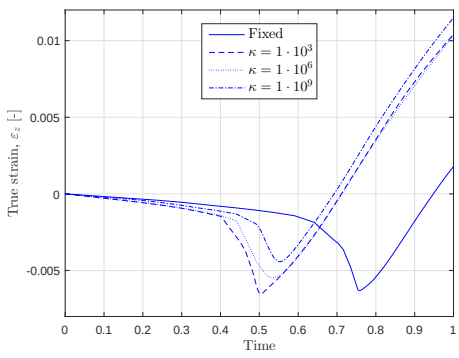

(b) True strain, ε_z, location 7

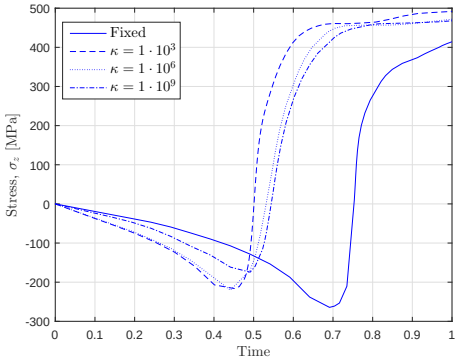

(c) Stress, σ_z, location 8

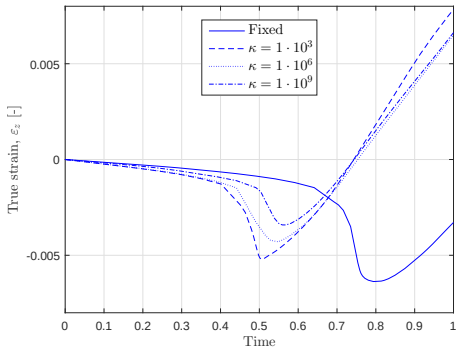

(d) True strain, ε_z, location 8

Figure F.29: Stress σ_z and true strain ε_z in z-direction at location 7 and 8 plotted over time. The scale on the x-axis presents the load fraction.

F.3.5 Stiffener Side - Location 9 and 10

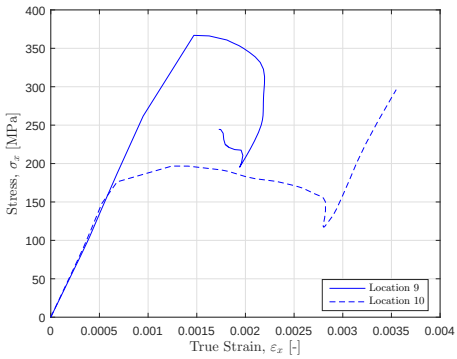

(a) Spring stiffness $\kappa = 1 \cdot 10^3$ [N/rad]

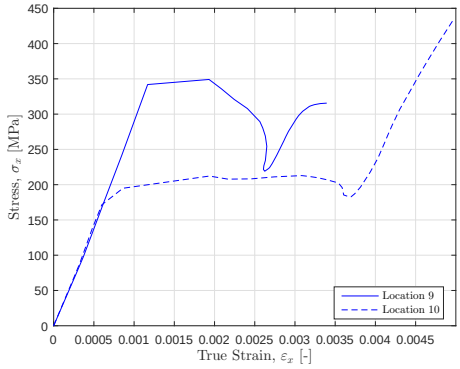

(b) Spring stiffness $\kappa = 1 \cdot 10^6$ [N/rad]

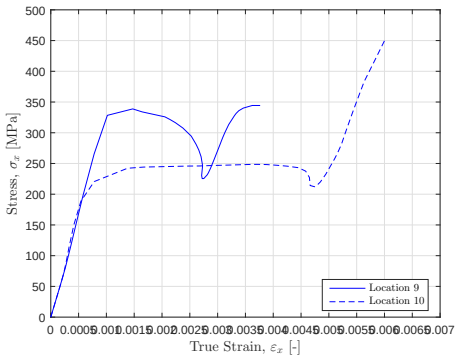

(c) Spring stiffness $\kappa = 1 \cdot 10^9$ [N/rad]

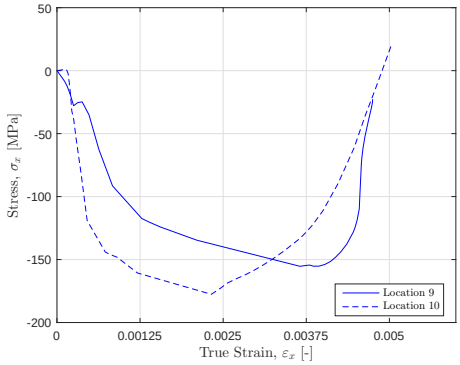

(d) Fixed boundary condition.

Figure F.30: Stress σ_x versus true strain ε_x in x-direction at location 9 and 10 on the stiffener side.

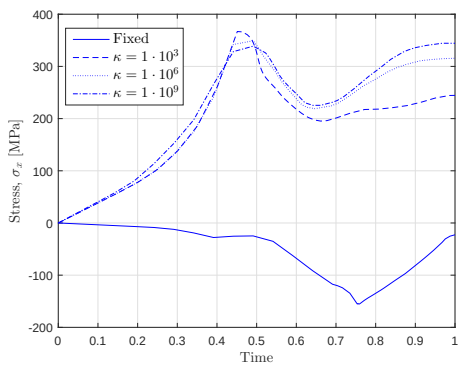

(a) Stress, σ_x, location 9

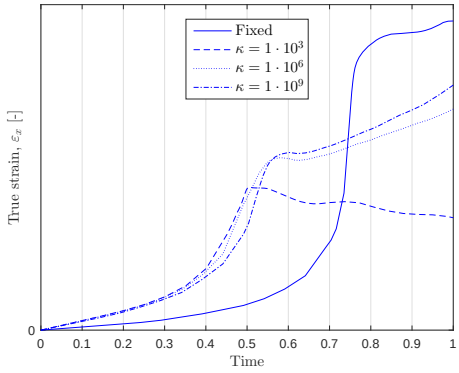

(b) True strain, ε_x, location 9

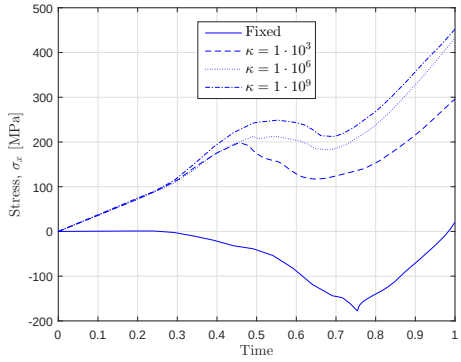

(c) Stress, σ_x, location 10

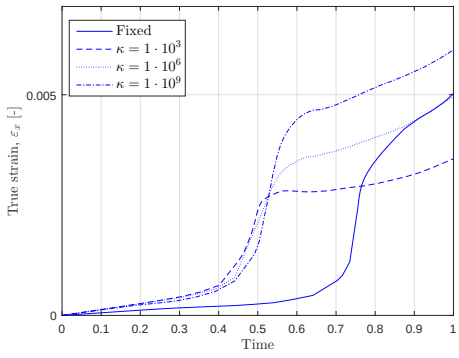

(d) True strain, ε_x, location 10

Figure F.31: Stress σ_x and true strain ε_x in x-direction at location 9 and 10 plotted over time. The scale on the x-axis presents the load fraction.

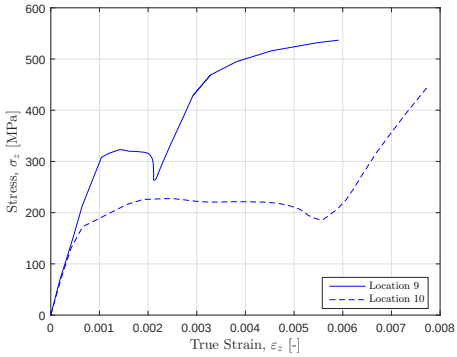

(a) Spring stiffness $\kappa = 1 \cdot 10^3$ [N/rad]

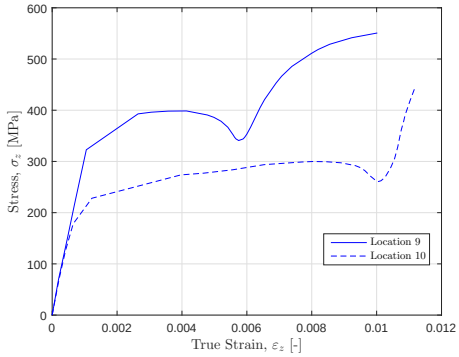

(b) Spring stiffness $\kappa = 1 \cdot 10^6$ [N/rad]

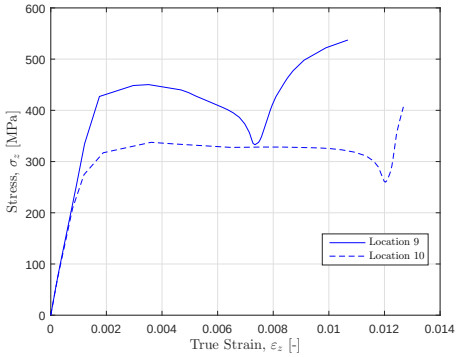

(c) Spring stiffness $\kappa = 1 \cdot 10^9$ [N/rad]

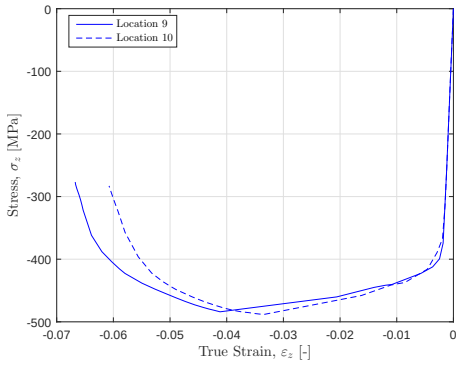

(d) Fixed boundary condition.

Figure F.32: Stress σ_z versus true strain ε_z in z-direction at location 9 and 10 on the stiffener side. Note the different scales between each figure.

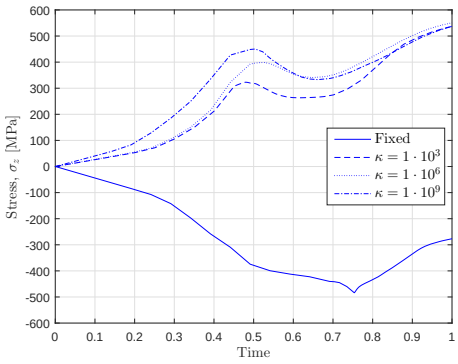

(a) Stress, σ_z, location 9

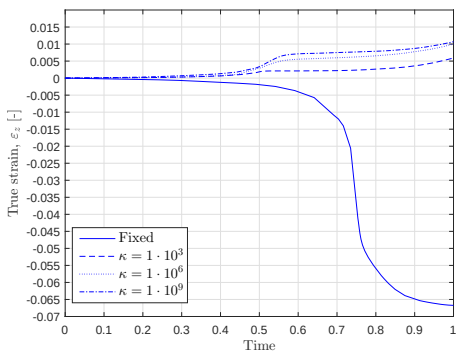

(b) True strain, ε_z, location 9

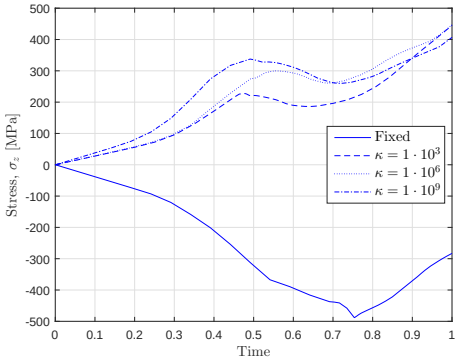

(c) Stress, σ_z, location 10

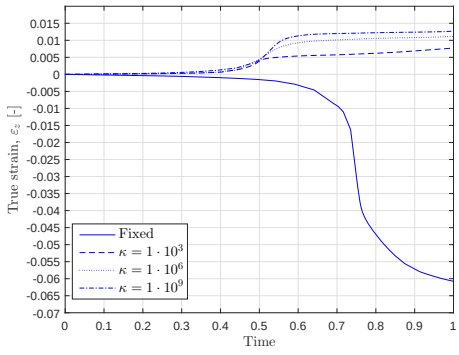

(d) True strain, ε_z, location 10

Figure F.33: Stress σ_z and true strain ε_z in z-direction at location 9 and 10 plotted over time. The scale on the x-axis presents the load fraction.

F.3.6 Load Side - Location 3 and 4

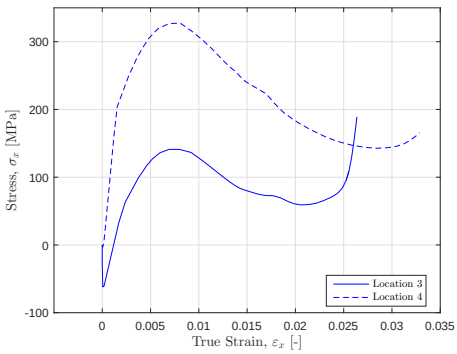

(a) Spring stiffness $\kappa = 1 \cdot 10^3$ [N/rad]

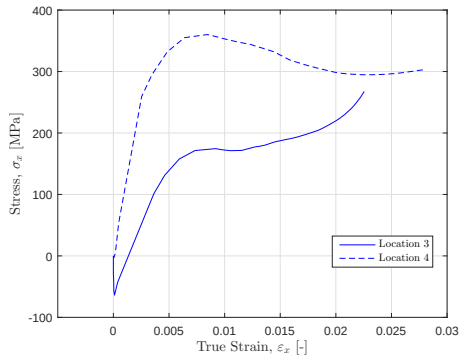

(b) Spring stiffness $\kappa = 1 \cdot 10^6$ [N/rad]

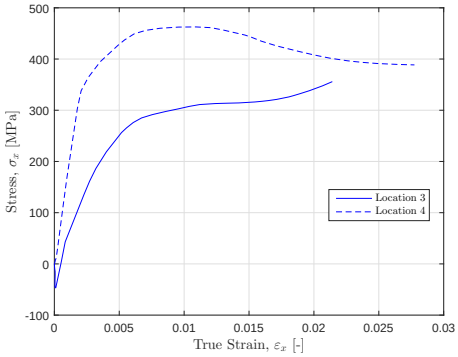

(c) Spring stiffness $\kappa = 1 \cdot 10^9$ [N/rad]

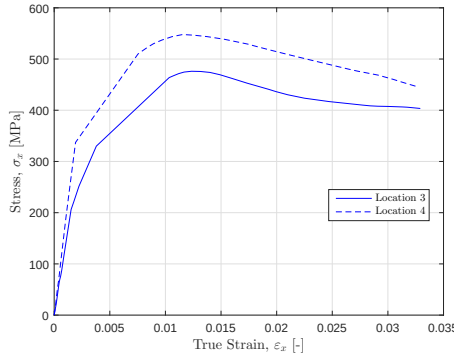

(d) Fixed boundary condition.

Figure F.34: Stress σ_x versus true strain ε_x in x-direction at location 3 and 4 on the load side.

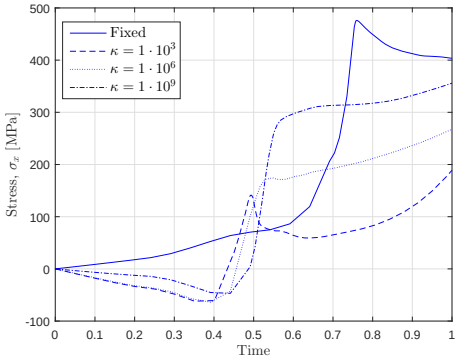

(a) Stress, σ_x, location 3

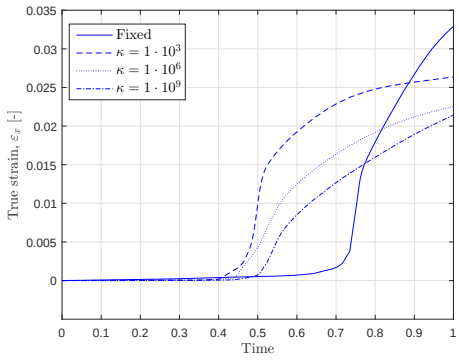

(b) True strain, ε_x, location 3

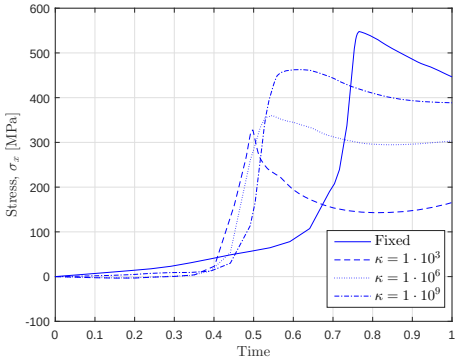

(c) Stress, σ_x, location 4

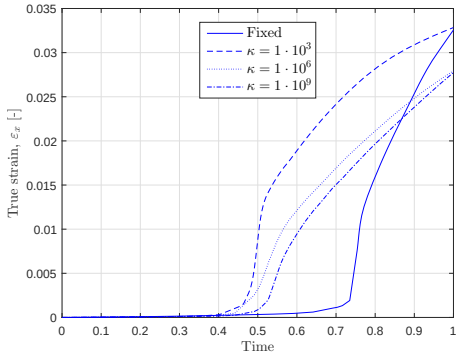

(d) True strain, ε_x, location 4

Figure F.35: Stress σ_x and true strain ε_x in x-direction at location 3 and 4 plotted over time. The scale on the x-axis presents the load fraction.

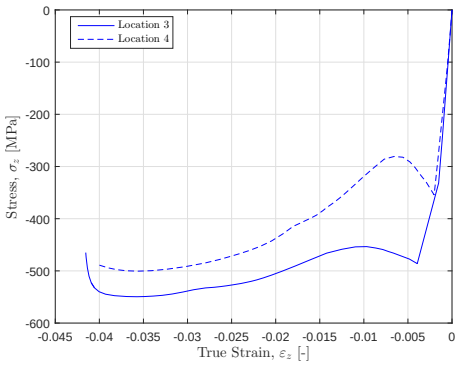

(a) Spring stiffness $\kappa = 1 \cdot 10^3$ [N/rad]

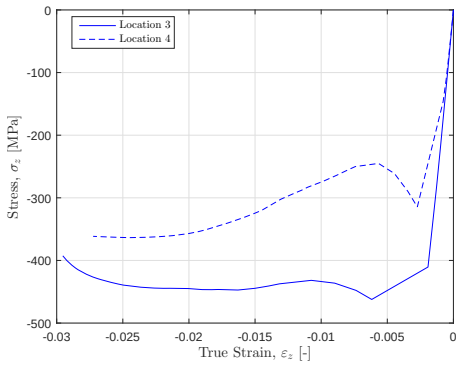

(b) Spring stiffness $\kappa = 1 \cdot 10^6$ [N/rad]

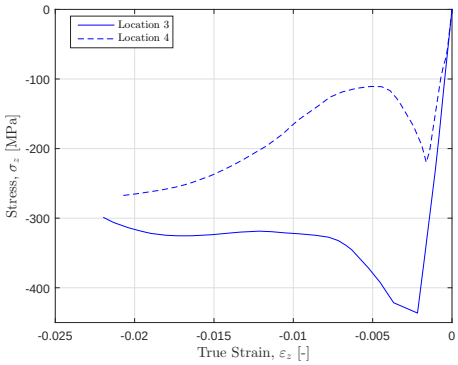

(c) Spring stiffness $\kappa = 1 \cdot 10^9$ [N/rad]

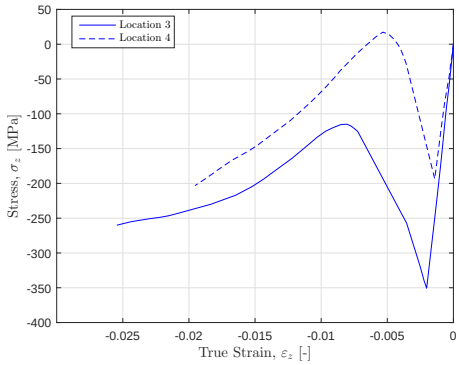

(d) Fixed boundary condition.

Figure F.36: Stress σ_z versus true strain ε_z in z-direction at location 3 and 4 on the load side. Note the different scales between each figure.

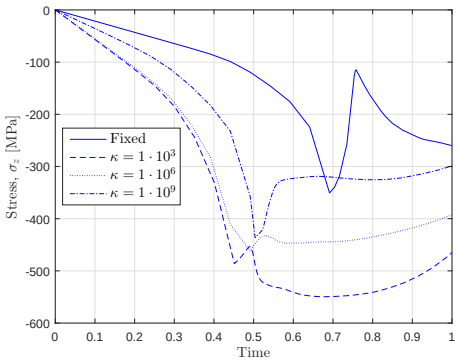

(a) Stress, σ_z, location 3

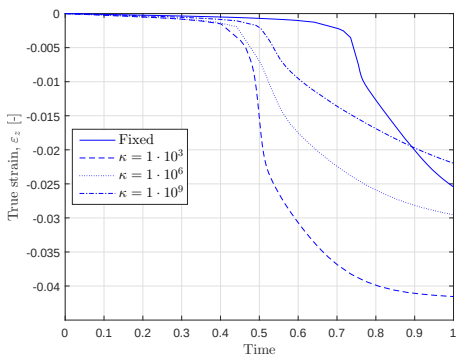

(b) True strain, ε_z, location 3

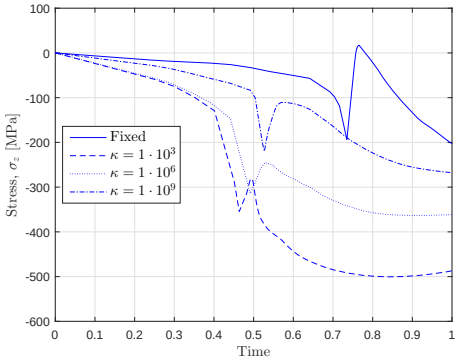

(c) Stress, σ_z, location 4

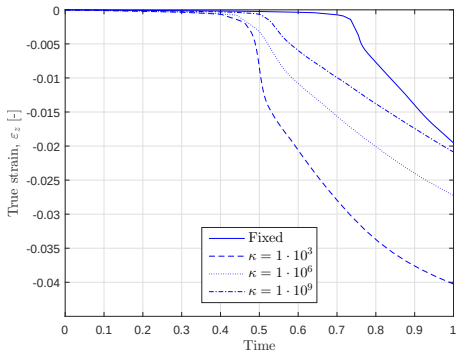

(d) True strain, ε_z, location 4

Figure F.37: Stress σ_z and true strain ε_z in z-direction at location 3 and 4 plotted over time. The scale on the x-axis presents the load fraction.

F.3.7 Load Side - Location 5 and 6

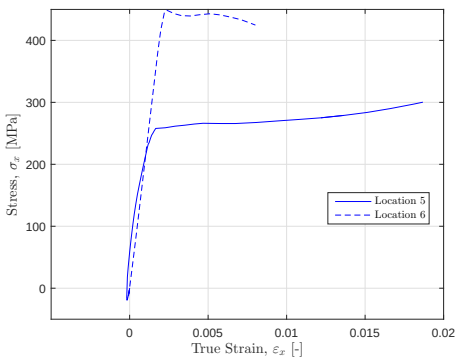

(a) Spring stiffness $\kappa = 1 \cdot 10^3$ [N/rad]

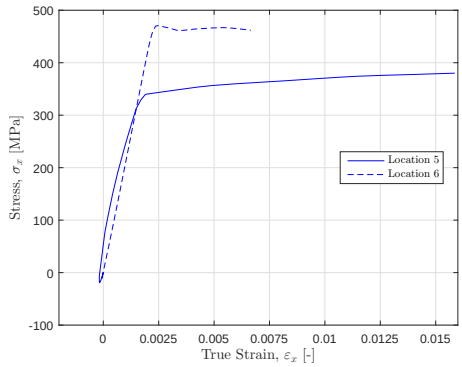

(b) Spring stiffness $\kappa = 1 \cdot 10^6$ [N/rad]

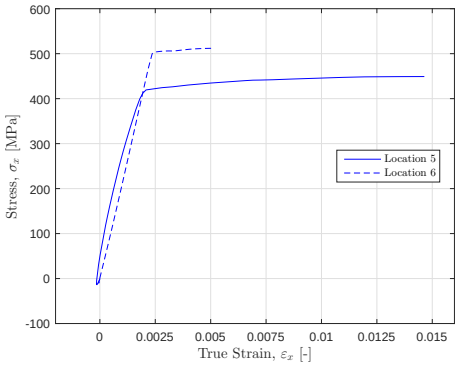

(c) Spring stiffness $\kappa = 1 \cdot 10^9$ [N/rad]

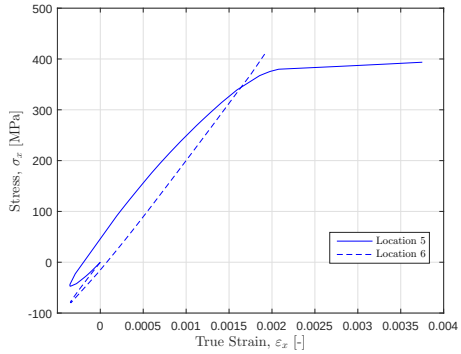

(d) Fixed boundary condition.

Figure F.38: Stress σ_x versus true strain ε_x in x-direction at location 5 and 6 on the load side.

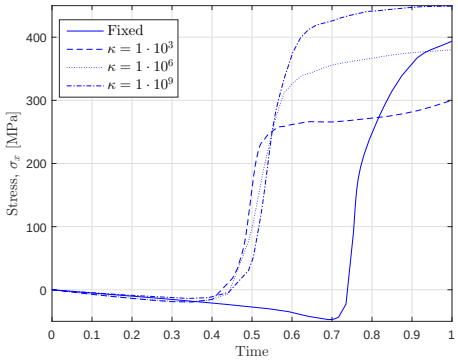

(a) Stress, σ_x, location 5

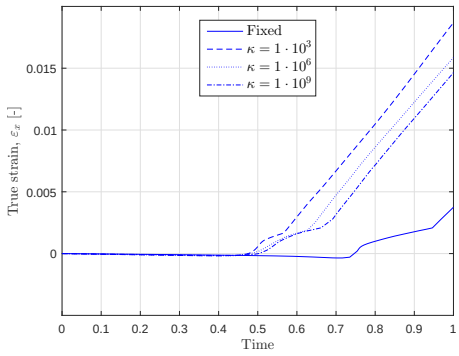

(b) True strain, ε_x, location 5

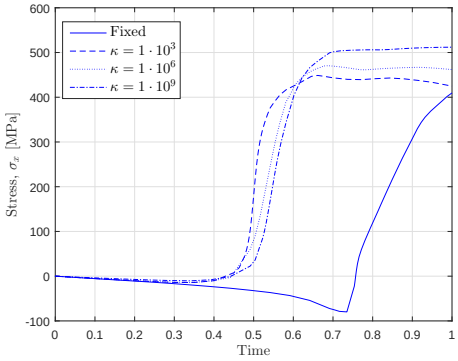

(c) Stress, σ_x, location 6

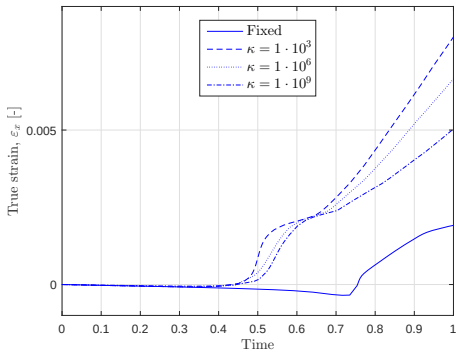

(d) True strain, ε_x, location 6

Figure F.39: Stress σ_x and true strain ε_x in x-direction at location 5 and 6 plotted over time. The scale on the x-axis presents the load fraction.

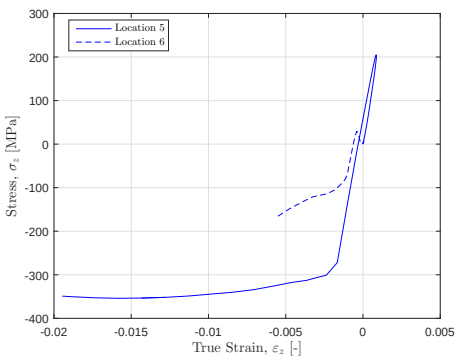

(a) Spring stiffness $\kappa = 1 \cdot 10^3$ [N/rad]

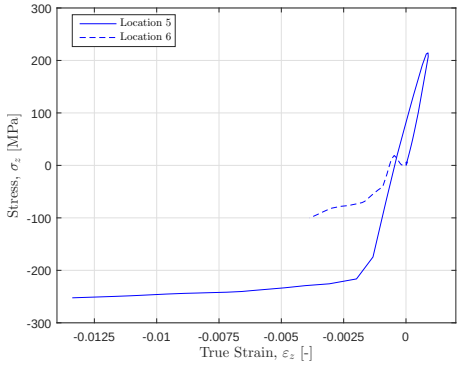

(b) Spring stiffness $\kappa = 1 \cdot 10^6$ [N/rad]

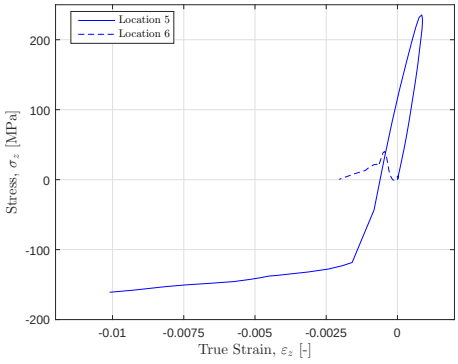

(c) Spring stiffness $\kappa = 1 \cdot 10^9$ [N/rad]

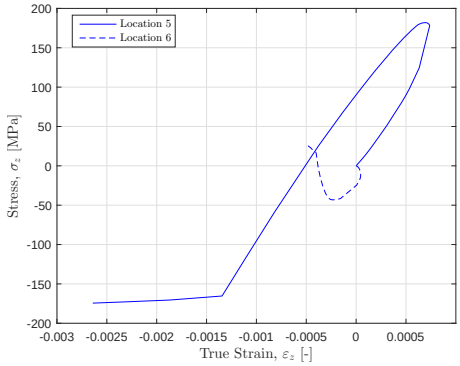

(d) Fixed boundary condition.

Figure F.40: Stress σ_z versus true strain ε_z in z-direction at location 5 and 6 on the load side. Note the different scales between each figure.

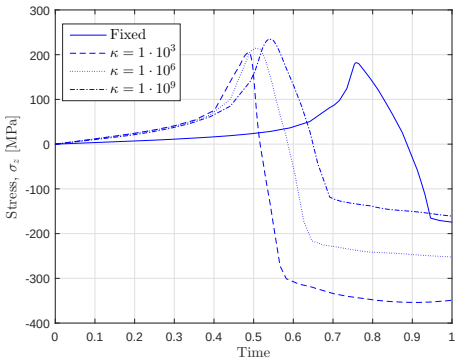

(a) Stress, σ_z, location 5

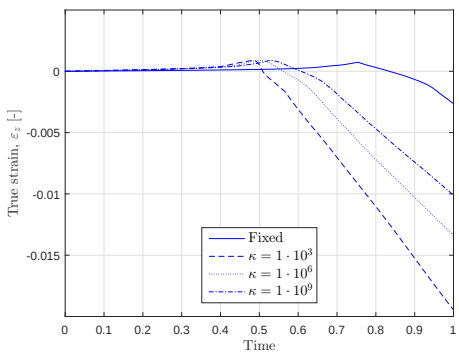

(b) True strain, ε_z, location 5

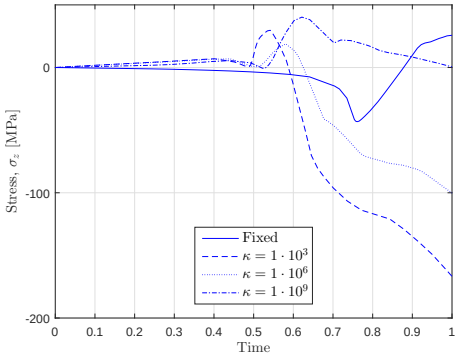

(c) Stress, σ_z, location 6

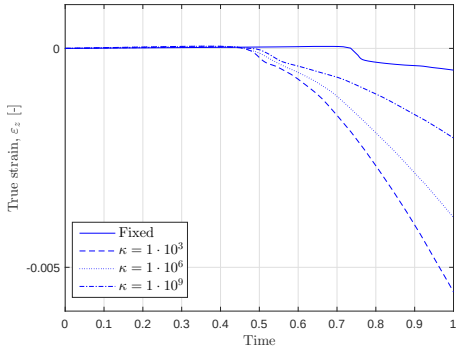

(d) True strain, ε_z, location 6

Figure F.41: Stress σ_z and true strain ε_z in z-direction at location 5 and 6 plotted over time. The scale on the x-axis presents the load fraction.

F.3.8 Load Side - Location 7 and 8

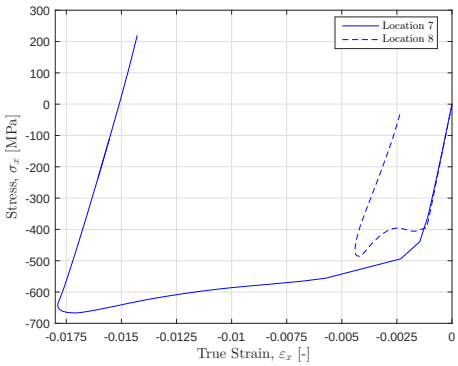

(a) Spring stiffness $\kappa = 1 \cdot 10^3$ [N/rad]

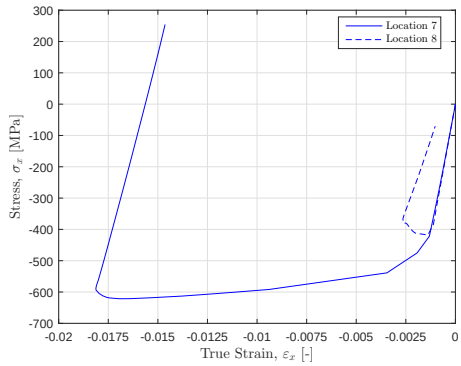

(b) Spring stiffness $\kappa = 1 \cdot 10^6$ [N/rad]

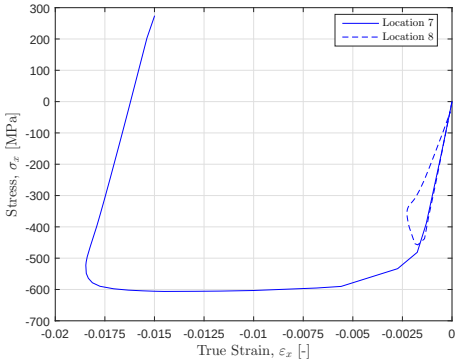

(c) Spring stiffness $\kappa = 1 \cdot 10^9$ [N/rad]

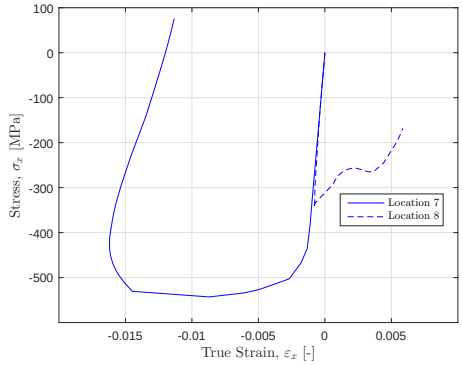

(d) Fixed boundary condition.

Figure F.42: Stress σ_x versus true strain ε_x in x-direction at location 7 and 8 on the load side.

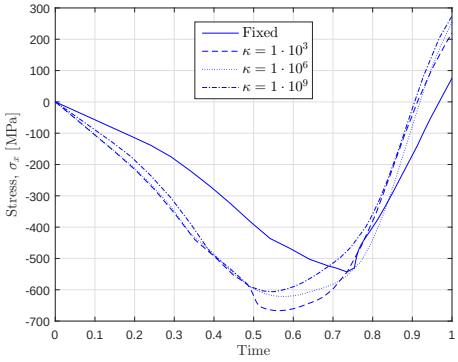

(a) Stress, σ_x, location 7

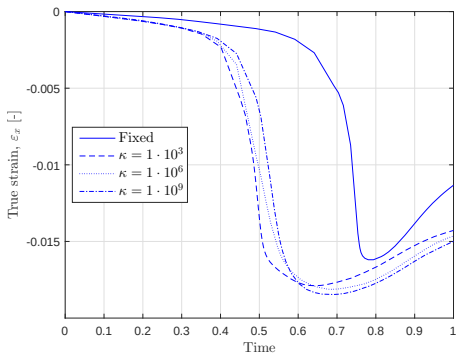

(b) True strain, ε_x, location 7

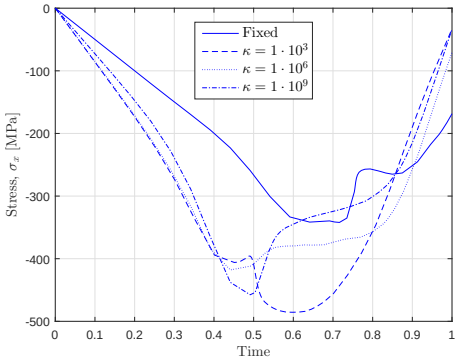

(c) Stress, σ_x, location 8

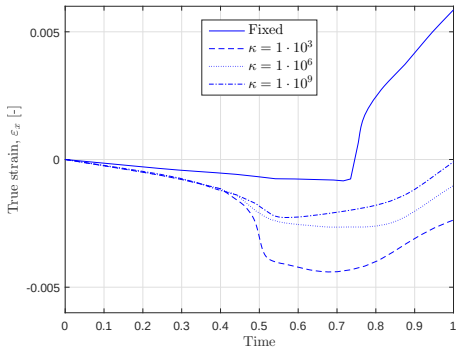

(d) True strain, ε_x, location 8

Figure F.43: Stress σ_x and true strain ε_x in x-direction at location 7 and 8 plotted over time. The scale on the x-axis presents the load fraction.

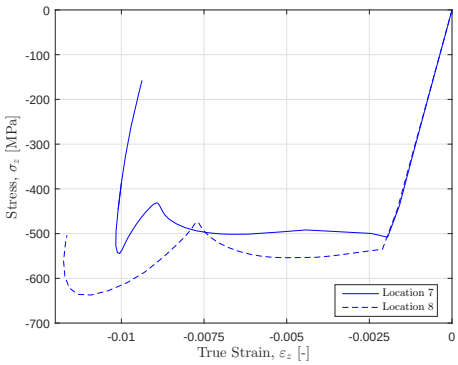

(a) Spring stiffness $\kappa = 1 \cdot 10^3$ [N/rad]

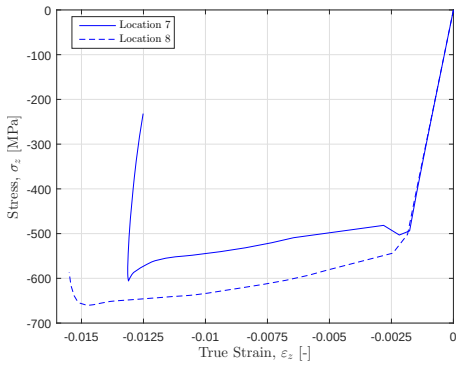

(b) Spring stiffness $\kappa = 1 \cdot 10^6$ [N/rad]

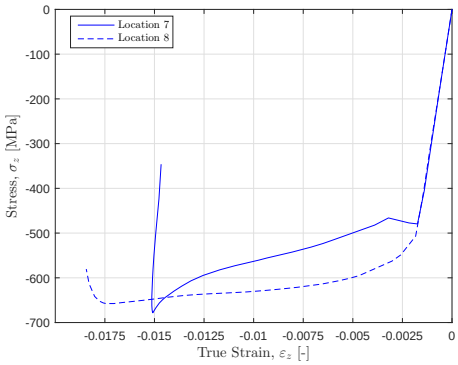

(c) Spring stiffness $\kappa = 1 \cdot 10^9$ [N/rad]

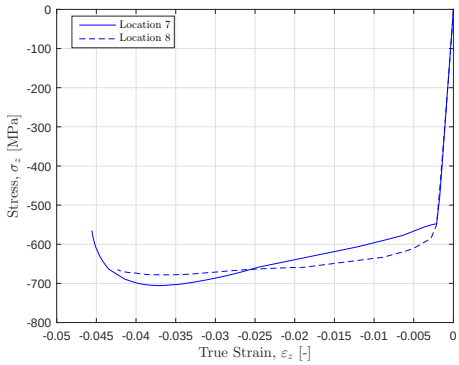

(d) Fixed boundary condition.

Figure F.44: Stress σ_z versus true strain ε_z in z-direction at location 7 and 8 on the load side. Note the different scales between each figure.

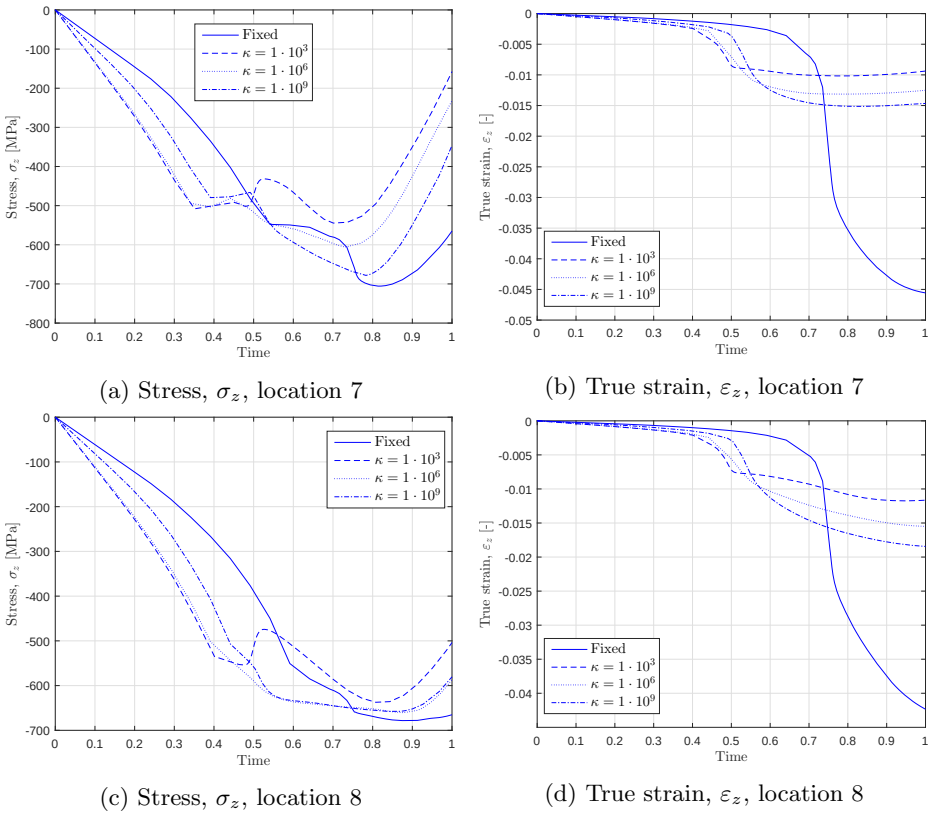

(a) Stress, σ_z, location 7

(b) True strain, ε_z, location 7

(c) Stress, σ_z, location 8

(d) True strain, ε_z, location 8

Figure F.45: Stress σ_z and true strain ε_z in z-direction at location 7 and 8 plotted over time. The scale on the x-axis presents the load fraction.

F.3.9 Load Side - Location 9 and 10

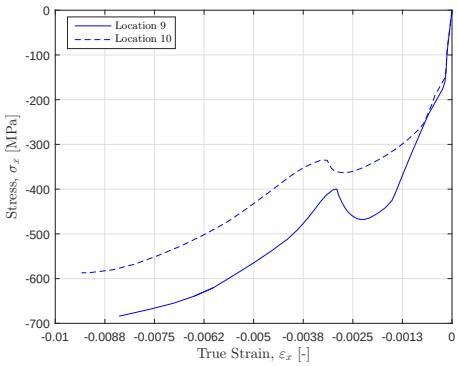

(a) Spring stiffness $\kappa = 1 \cdot 10^3$ [N/rad]

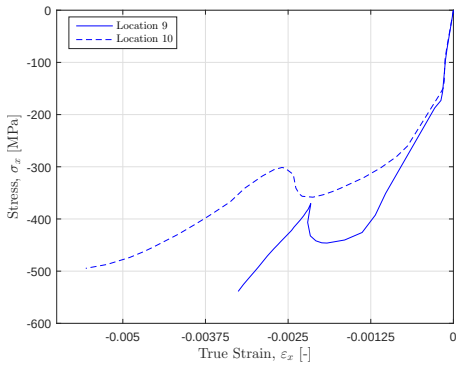

(b) Spring stiffness $\kappa = 1 \cdot 10^6$ [N/rad]

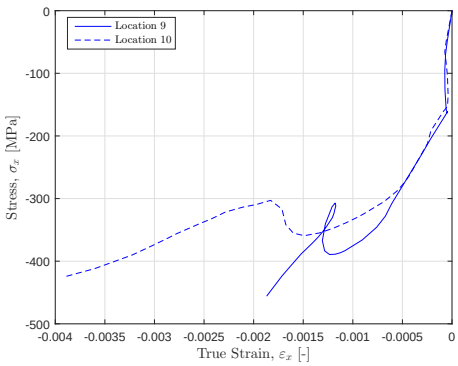

(c) Spring stiffness $\kappa = 1 \cdot 10^9$ [N/rad]

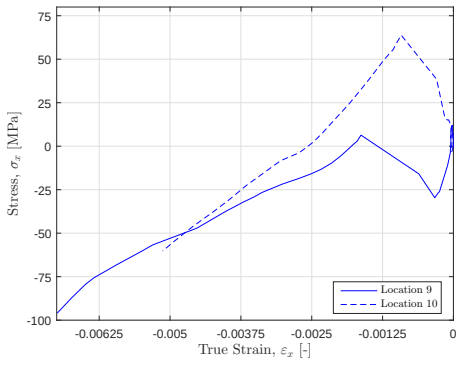

(d) Fixed boundary condition.

Figure F.46: Stress σ_x versus true strain ε_x in x-direction at location 9 and 10 on the load side.

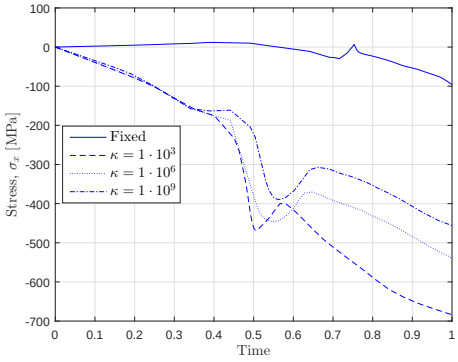

(a) Stress, σ_x, location 9

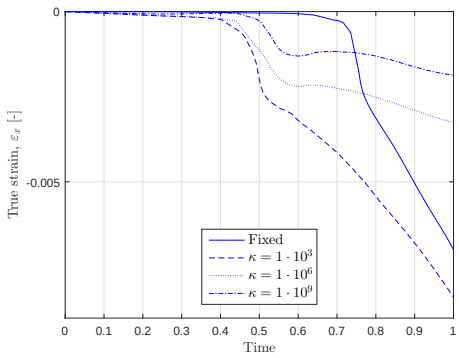

(b) True strain, ε_x, location 9

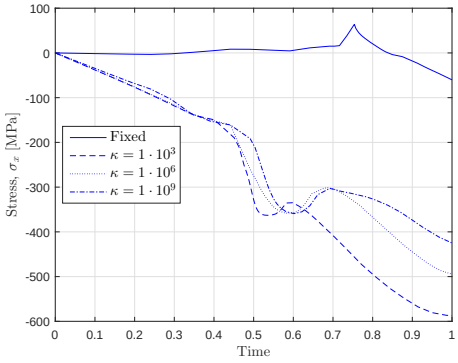

(c) Stress, σ_x, location 10

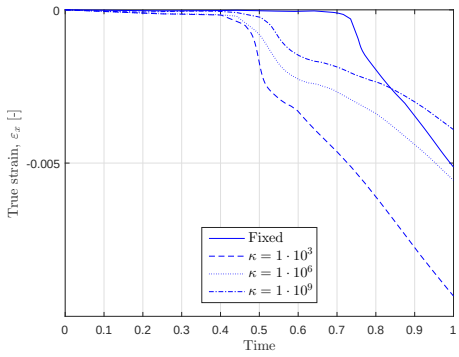

(d) True strain, ε_x, location 10

Figure F.47: Stress σ_x and true strain ε_x in x-direction at location 9 and 10 plotted over time. The scale on the x-axis presents the load fraction.

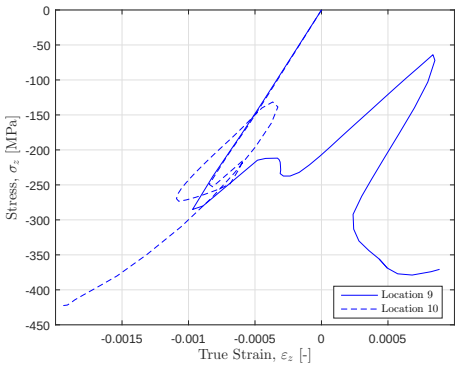

(a) Spring stiffness $\kappa = 1 \cdot 10^3$ [N/rad]

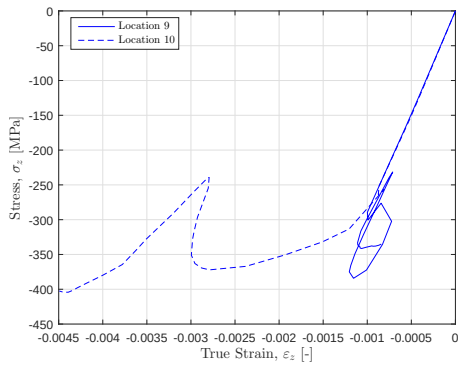

(b) Spring stiffness $\kappa = 1 \cdot 10^6$ [N/rad]

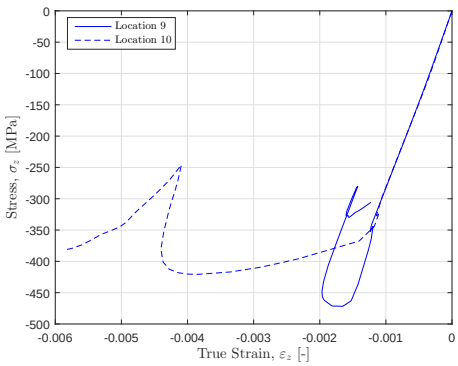

(c) Spring stiffness $\kappa = 1 \cdot 10^9$ [N/rad]

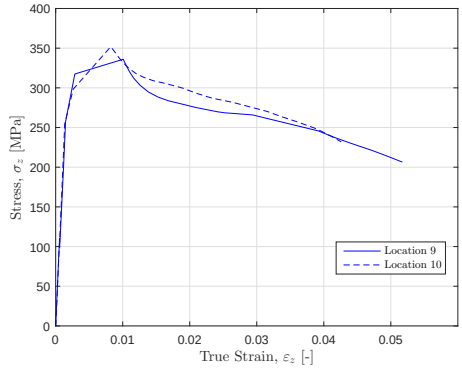

(d) Fixed boundary condition.

Figure F.48: Stress σ_z versus true strain ε_z in z-direction at location 9 and 10 on the load side. Note the different scales between each figure.

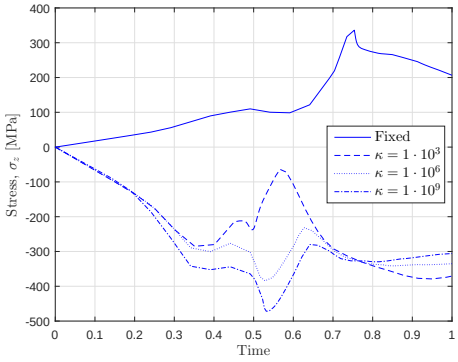

(a) Stress, σ_z, location 9

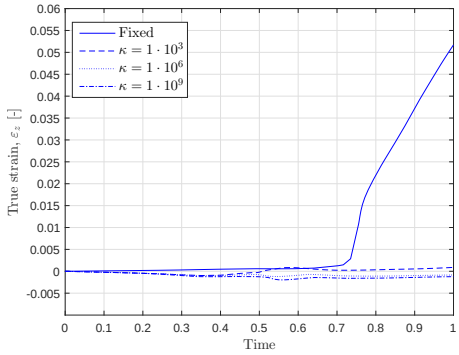

(b) True strain, ε_z, location 9

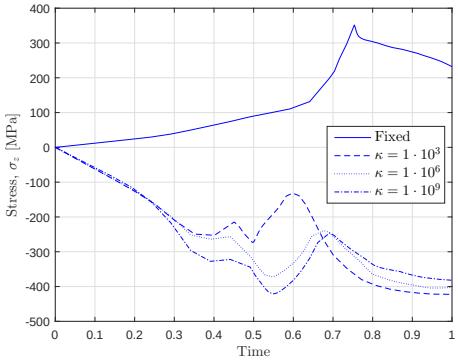

(c) Stress, σ_z, location 10

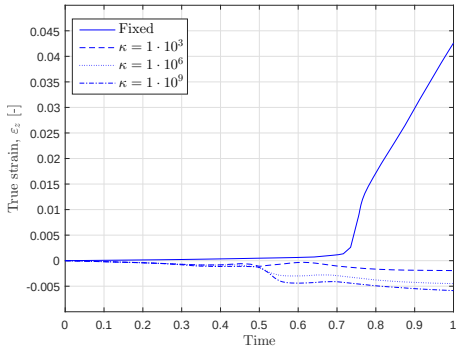

(d) True strain, ε_z, location 10

Figure F.49: Stress σ_z and true strain ε_z in z-direction at location 9 and 10 plotted over time. The scale on the x-axis presents the load fraction.

F.3.10 Stiffener Assessment - Various Boundaries

The stiffeners have been assessed as previously described in appendix F.2. No further details about the set-up will be given here. Comments to the plots are given in the main part.

F.3.11 Stiffener 1 - Location 1 and 2

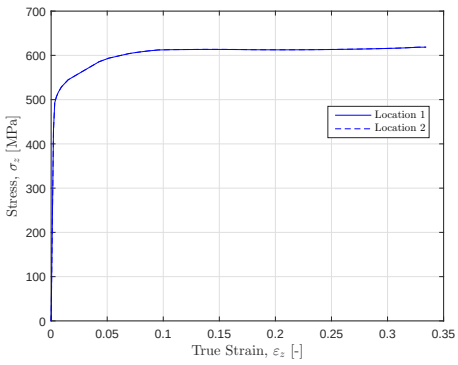

(a) Spring stiffness $\kappa = 1 \cdot 10^3$ [N/rad]

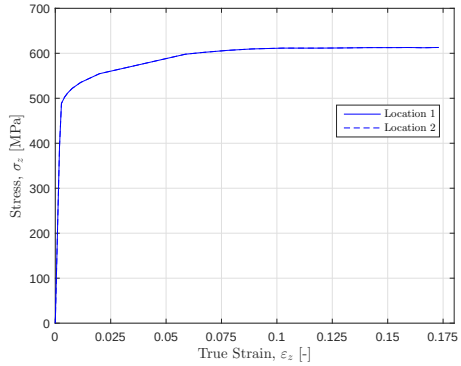

(b) Spring stiffness $\kappa = 1 \cdot 10^6$ [N/rad]

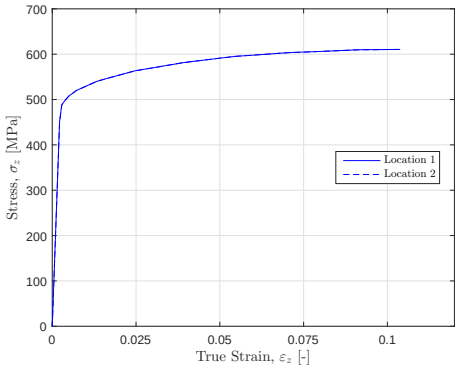

(c) Spring stiffness $\kappa = 1 \cdot 10^9$ [N/rad]

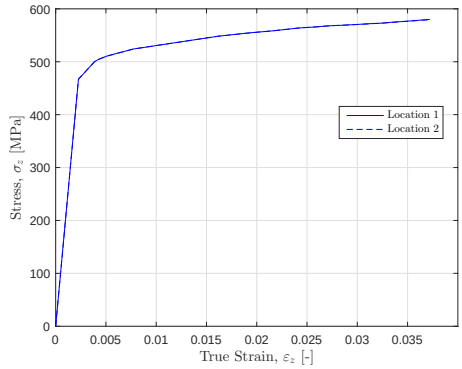

(d) Fixed boundary condition.

Figure F.50: Stress σ_z versus true strain ε_z in z-direction at location 1 and 2 on the stiffener flange. Note the different scales between each figure.

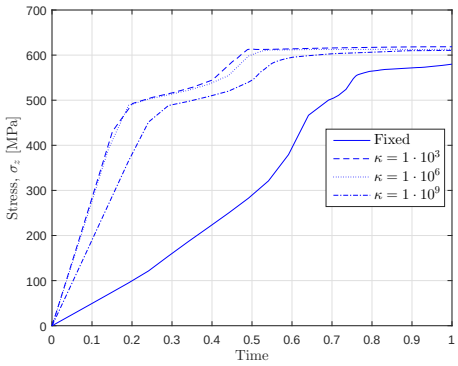

(a) Stress, σ_z, location 1

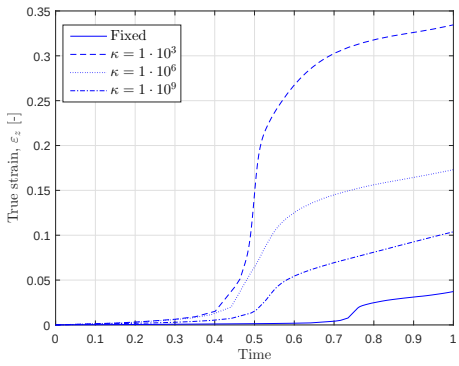

(b) True strain, ε_z, location 1

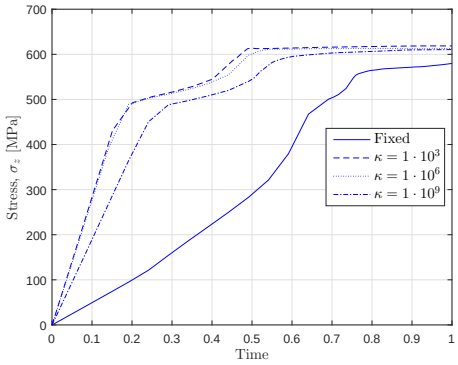

(c) Stress, σ_z, location 2

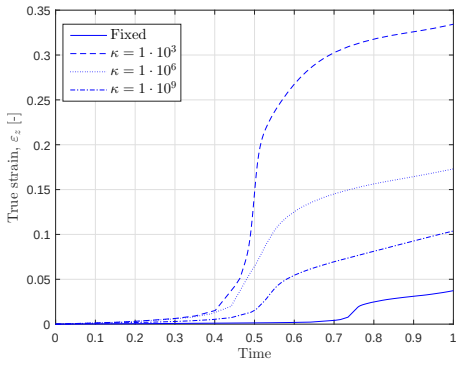

(d) True strain, ε_z, location 2

Figure F.51: Stress σ_z and true strain ε_z in z-direction at the stiffener flange for location 1 and 2 plotted over time. The scale on the x-axis presents the load fraction.

F.3.12 Stiffener 1 - Location 3 and 4

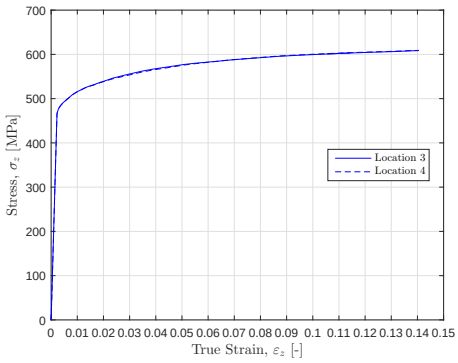

(a) Spring stiffness $\kappa = 1 \cdot 10^3$ [N/rad]

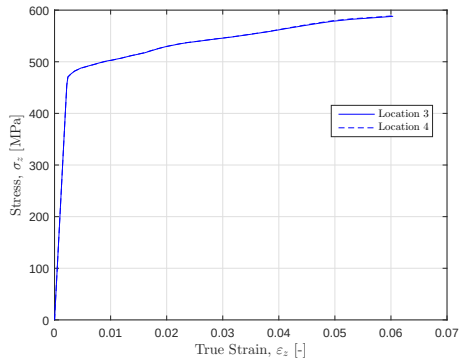

(b) Spring stiffness $\kappa = 1 \cdot 10^6$ [N/rad]

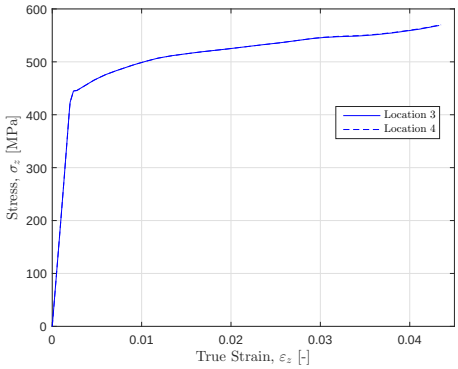

(c) Spring stiffness $\kappa = 1 \cdot 10^9$ [N/rad]

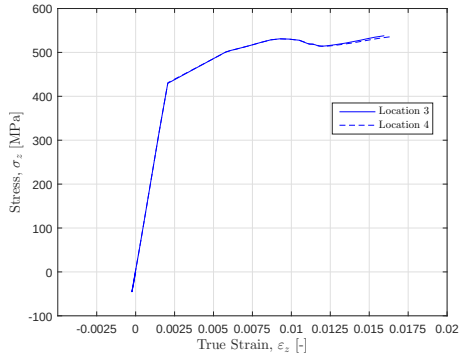

(d) Fixed boundary condition.

Figure F.52: Stress σ_z versus true strain ε_z in z-direction at location 3 and 4 on the stiffener flange. Note the different scales between each figure.

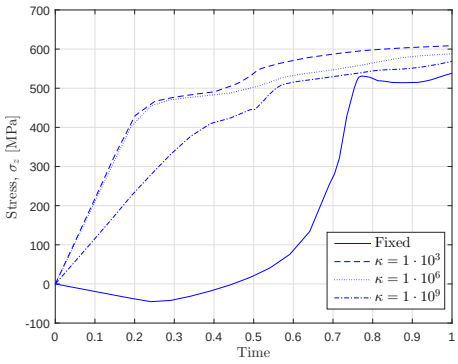

(a) Stress, σ_z, location 3

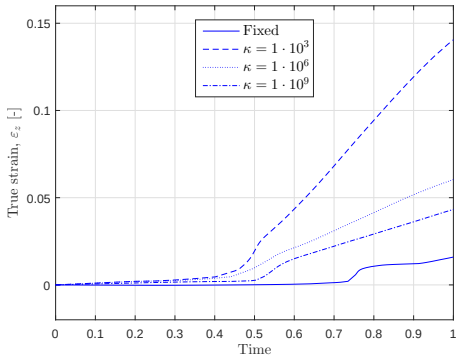

(b) True strain, ε_z, location 3

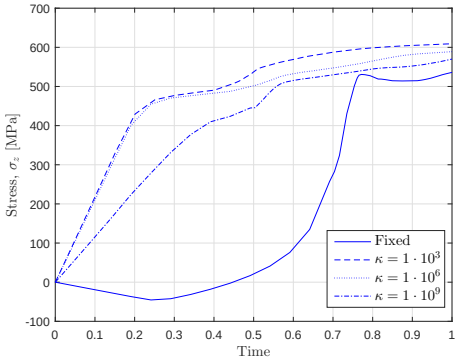

(c) Stress, σ_z, location 4

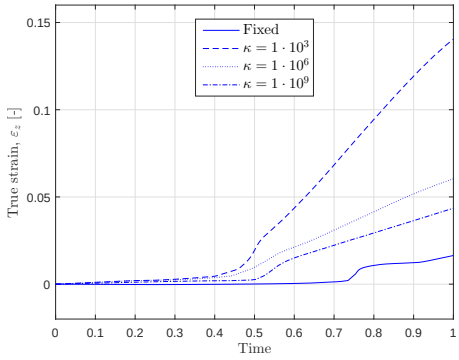

(d) True strain, ε_z, location 4

Figure F.53: Stress σ_z and true strain ε_z in z-direction at the stiffener flange for location 3 and 4 plotted over time. The scale on the x-axis presents the load fraction.

F.3.13 Stiffener 1 - Location 5 and 6

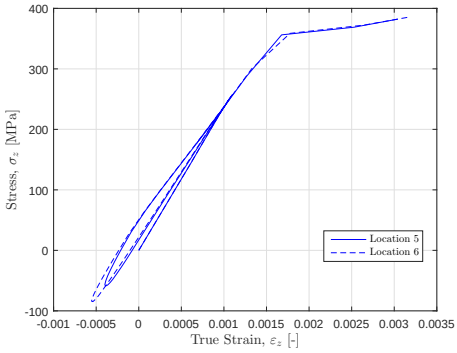

(a) Spring stiffness $\kappa = 1 \cdot 10^3$ [N/rad]

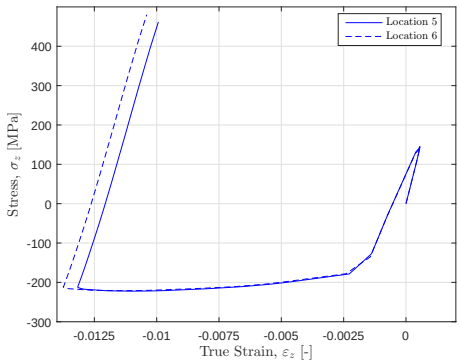

(b) Spring stiffness $\kappa = 1 \cdot 10^6$ [N/rad]

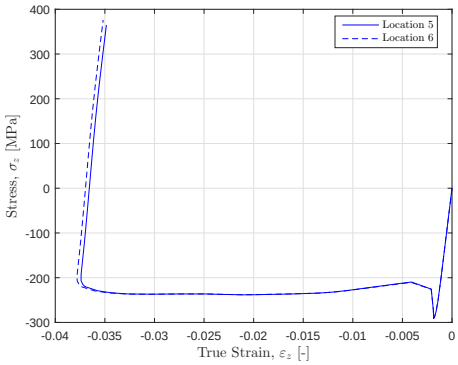

(c) Spring stiffness $\kappa = 1 \cdot 10^9$ [N/rad]

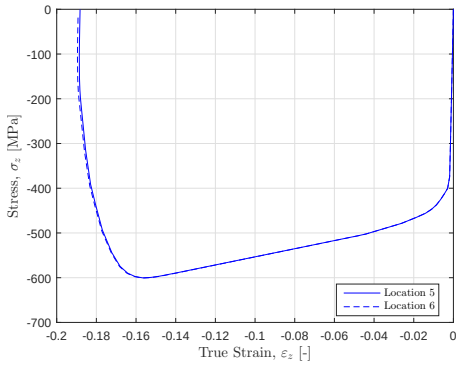

(d) Fixed boundary condition.

Figure F.54: Stress σ_z versus true strain ε_z in z-direction at location 5 and 6 on the stiffener flange. Note the different scales between each figure.

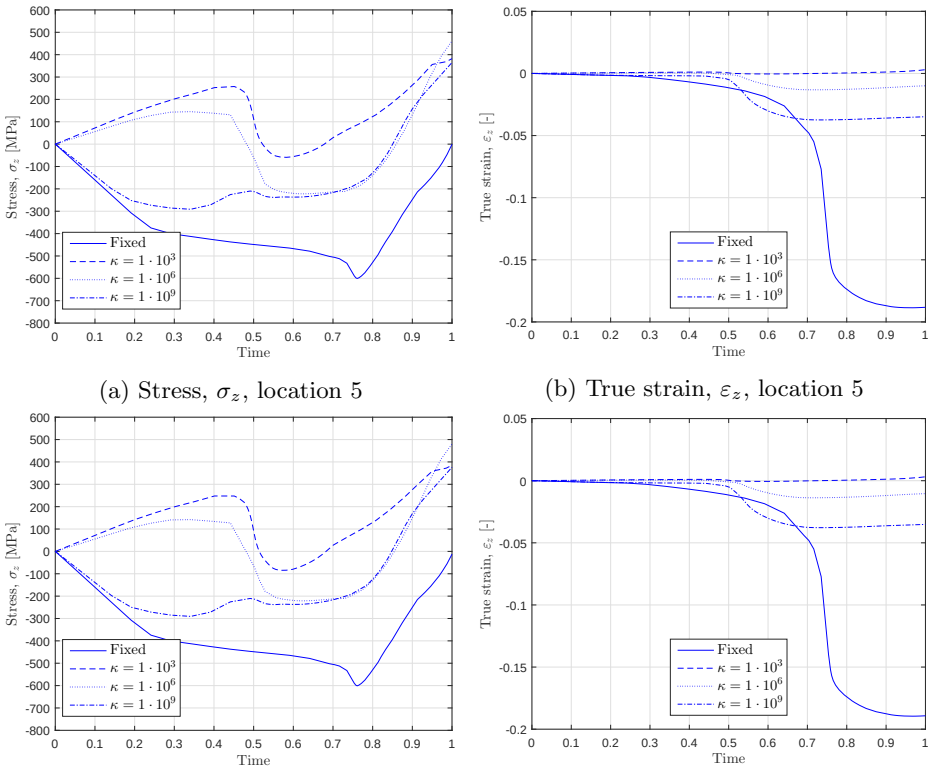

(a) Stress, σ_z, location 5

(b) True strain, ε_z, location 5

(c) Stress, σ_z, location 6

(d) True strain, ε_z, location 6

Figure F.55: Stress σ_z and true strain ε_z in z-direction at the stiffener flange for location 5 and 6 plotted over time. The scale on the x-axis presents the load fraction.

F.3.14 Stiffener 2 - Location 1 and 2

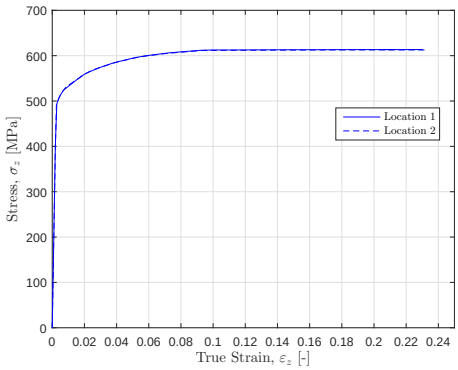

(a) Spring stiffness $\kappa = 1 \cdot 10^3$ [N/rad]

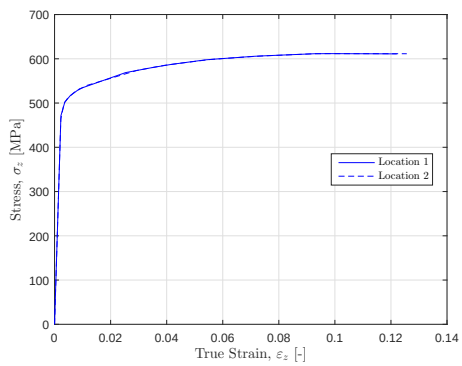

(b) Spring stiffness $\kappa = 1 \cdot 10^6$ [N/rad]

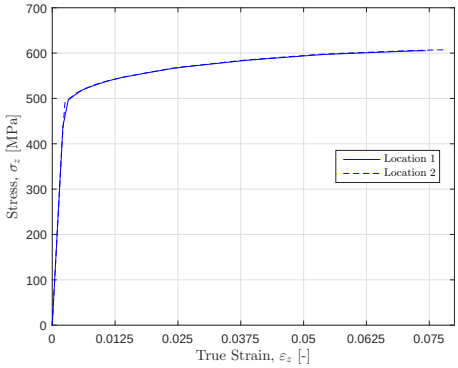

(c) Spring stiffness $\kappa = 1 \cdot 10^9$ [N/rad]

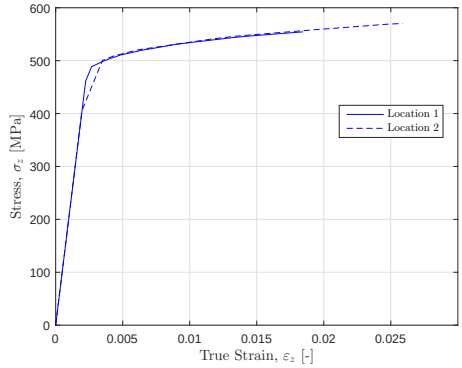

(d) Fixed boundary condition.

Figure F.56: Stress σ_z versus true strain ε_z in z-direction at location 1 and 2 on the stiffener flange. Note the different scales between each figure.

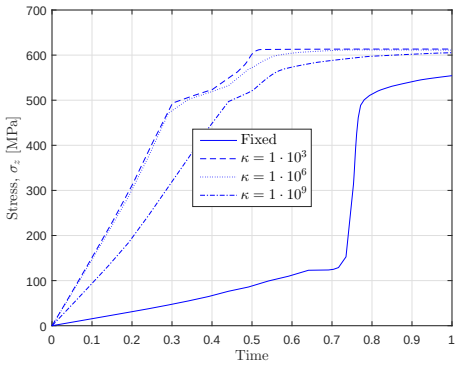

(a) Stress, σ_z, location 1

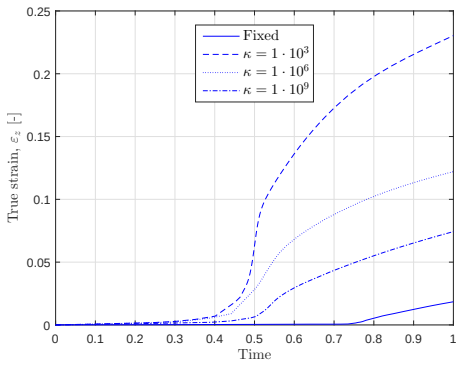

(b) True strain, ε_z, location 1

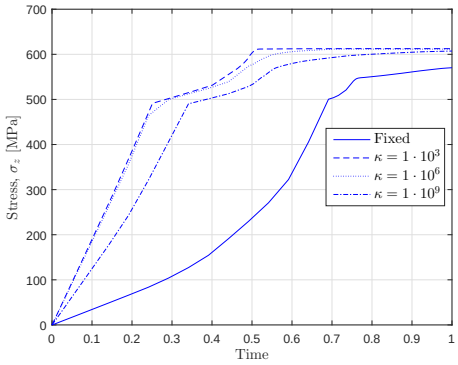

(c) Stress, σ_z, location 2

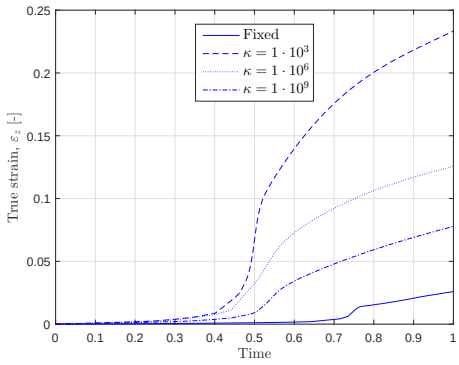

(d) True strain, ε_z, location 2

Figure F.57: Stress σ_z and true strain ε_z in z-direction at the stiffener flange for location 1 and 2 plotted over time. The scale on the x-axis presents the load fraction.

F.3.15 Stiffener 2 - Location 3 and 4

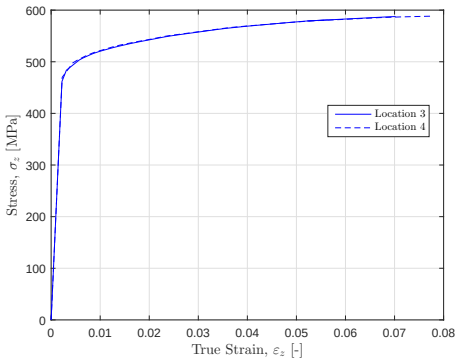

(a) Spring stiffness $\kappa = 1 \cdot 10^3$ [N/rad]

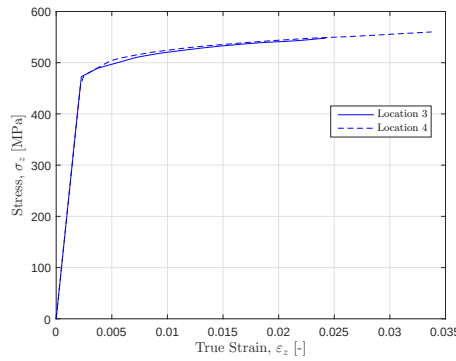

(b) Spring stiffness $\kappa = 1 \cdot 10^6$ [N/rad]

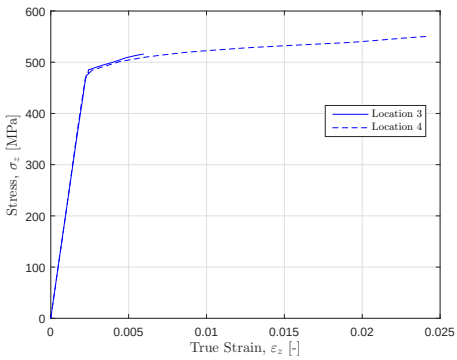

(c) Spring stiffness $\kappa = 1 \cdot 10^9$ [N/rad]

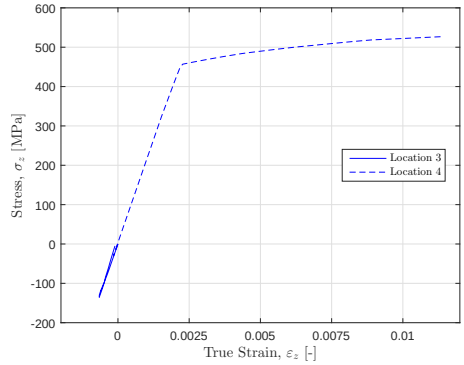

(d) Fixed boundary condition.

Figure F.58: Stress σ_z versus true strain ε_z in z-direction at location 3 and 4 on the stiffener flange. Note the different scales between each figure.

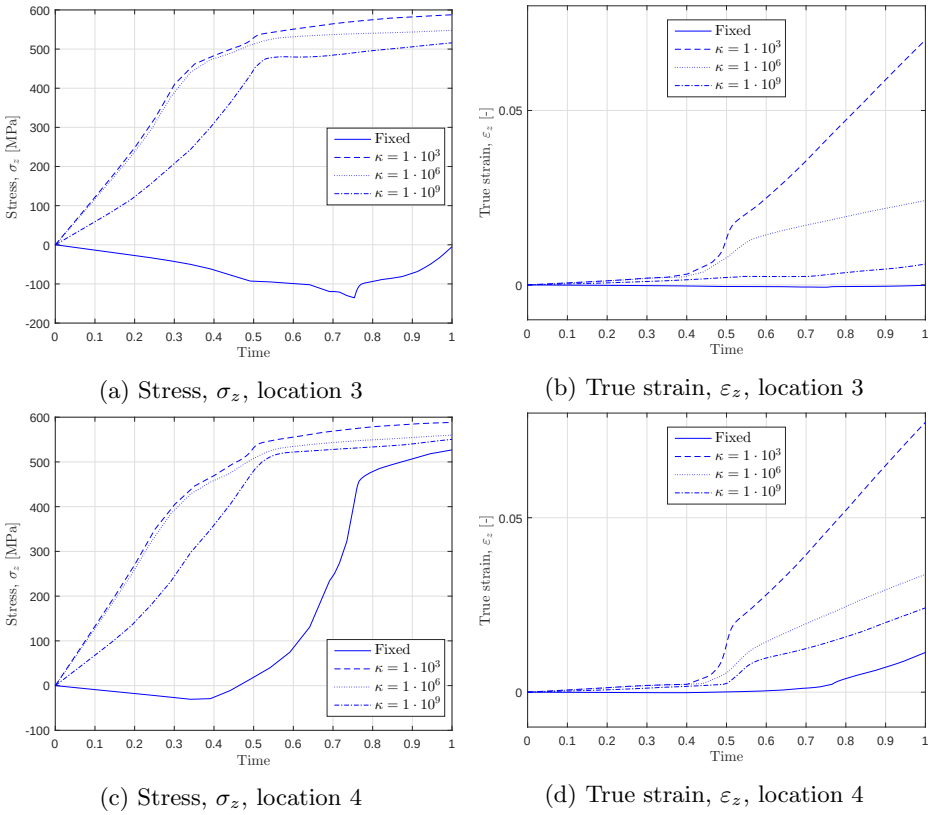

(a) Stress, σ_z, location 3

(b) True strain, ε_z, location 3

(c) Stress, σ_z, location 4

(d) True strain, ε_z, location 4

Figure F.59: Stress σ_z and true strain ε_z in z-direction at the stiffener flange for location 3 and 4 plotted over time. The scale on the x-axis presents the load fraction.

F.3.16 Stiffener 2 - Location 5 and 6

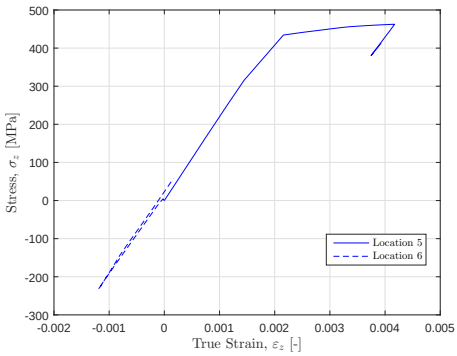

(a) Spring stiffness $\kappa = 1 \cdot 10^3$ [N/rad]

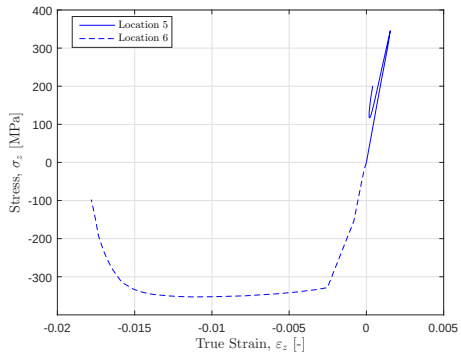

(b) Spring stiffness $\kappa = 1 \cdot 10^6$ [N/rad]

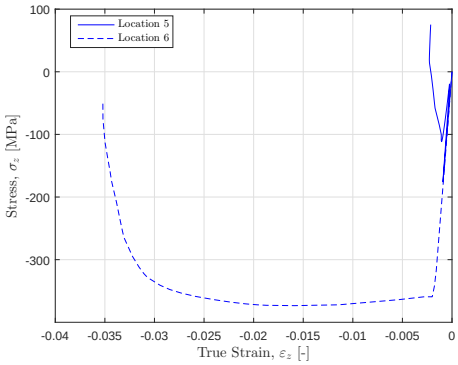

(c) Spring stiffness $\kappa = 1 \cdot 10^9$ [N/rad]

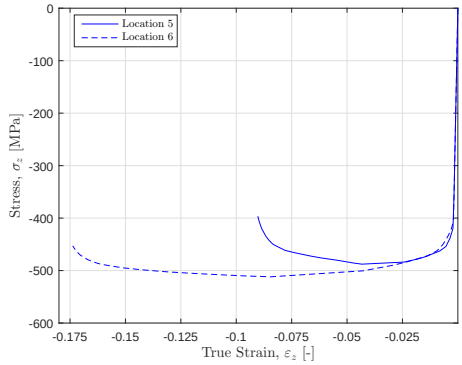

(d) Fixed boundary condition.

Figure F.60: Stress σ_z versus true strain ε_z in z-direction at location 5 and 6 on the stiffener flange. Note the different scales between each figure.

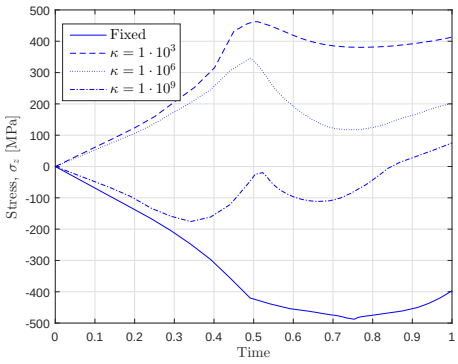

(a) Stress, σ_z, location 5

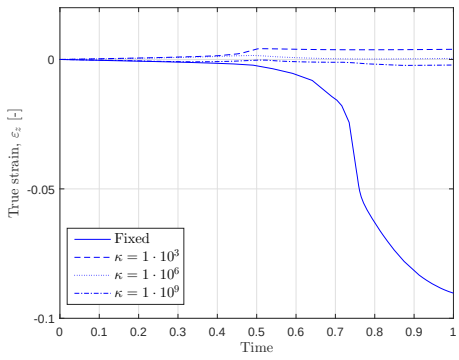

(b) True strain, ε_z, location 5

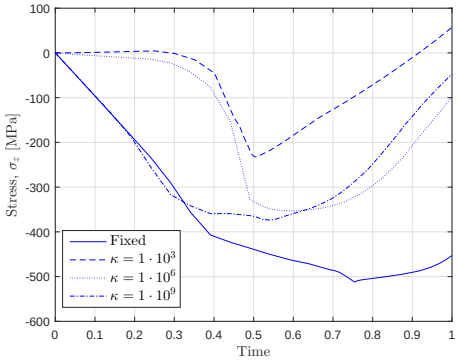

(c) Stress, σ_z, location 6

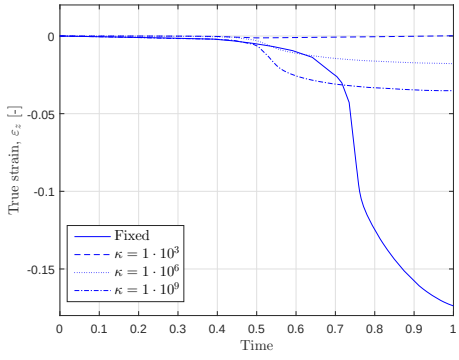

(d) True strain, ε_z, location 6

Figure F.61: Stress σ_z and true strain ε_z in z-direction at the stiffener flange for location 5 and 6 plotted over time. The scale on the x-axis presents the load fraction.

F.3.17 Contour Plot of Stiffeners

The following section provides contour plots for the stiffeners with stresses in y- and z-direction. The stresses for the webbing will only be plotted graphically giving priority to the assessment of the plate and flanges. Additionally, no further comments are given here.

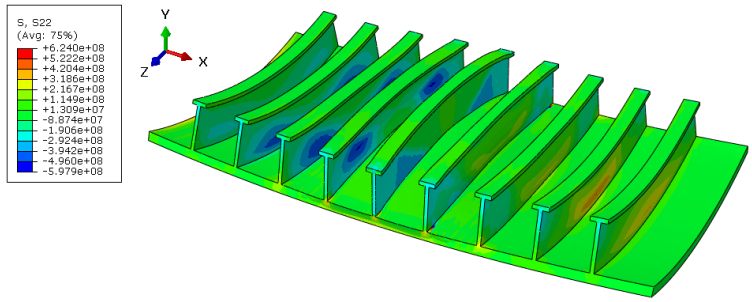

(a) Spring stiffness $\kappa = 1 \cdot 10^3$ [N/rad]

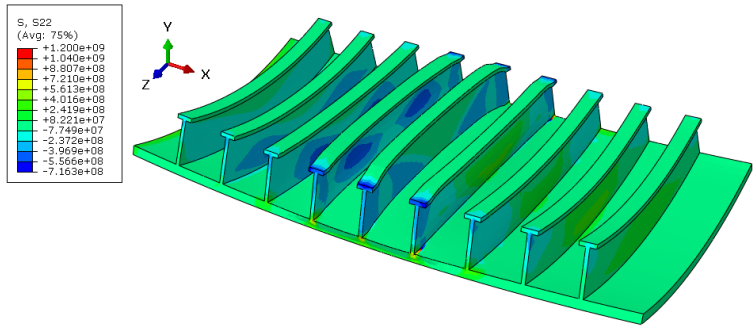

(b) Spring stiffness $\kappa = 1 \cdot 10^6$ [N/rad]

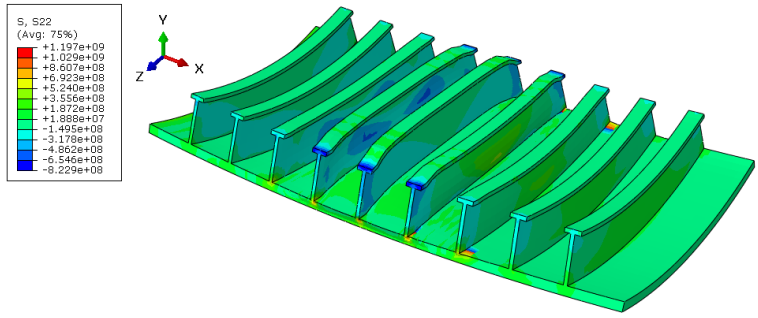

(c) Spring stiffness $\kappa = 1 \cdot 10^9$ [N/rad]

Figure F.62: Contour plot of stresses in y-direction σ_y for fully loaded model for the different spring stiffness. The load fraction equals 1.

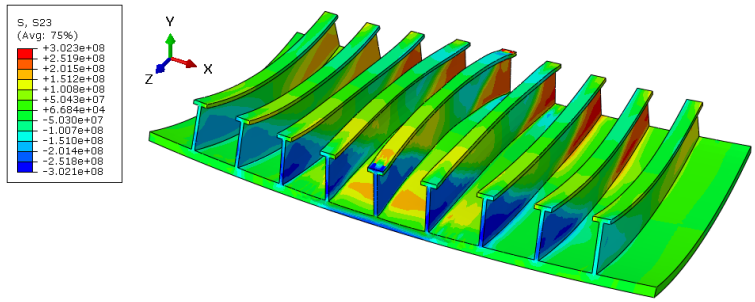

(a) Spring stiffness $\kappa = 1 \cdot 10^3$ [N/rad]

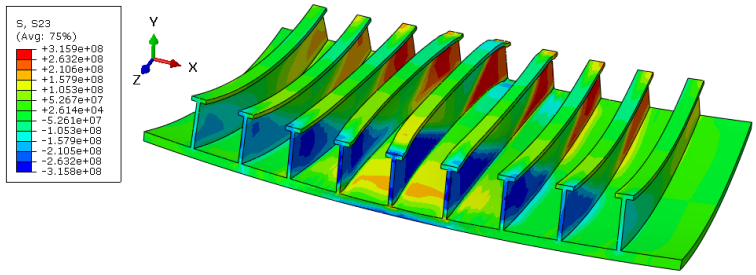

(b) Spring stiffness $\kappa = 1 \cdot 10^6$ [N/rad]

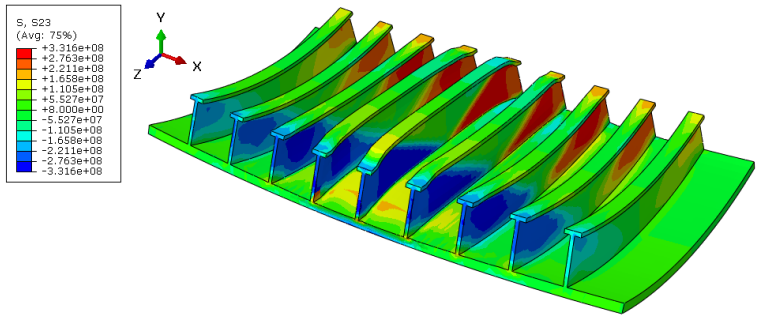

(c) Spring stiffness $\kappa = 1 \cdot 10^9$ [N/rad]

Figure F.63: Contour plot of stresses in yz-direction τ_{yz} for fully loaded model for the different spring stiffness. The load fraction equals 1.

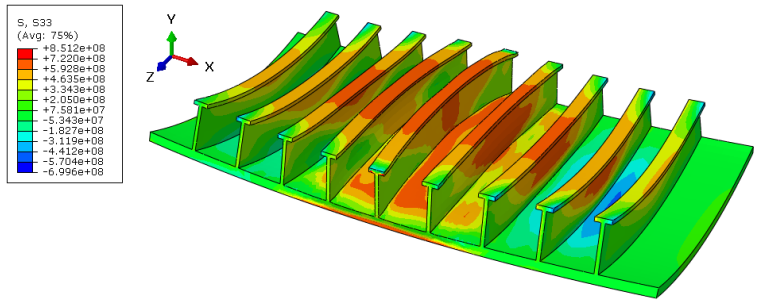

(a) Spring stiffness $\kappa = 1 \cdot 10^3$ [N/rad]

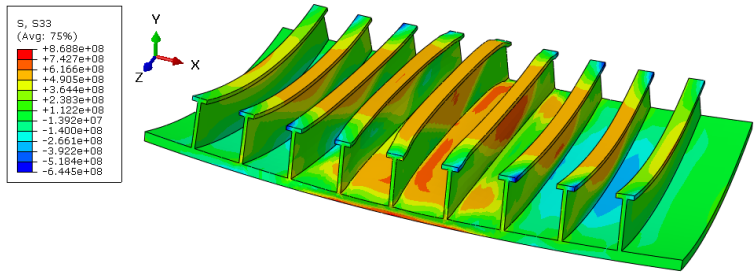

(b) Spring stiffness $\kappa = 1 \cdot 10^6$ [N/rad]

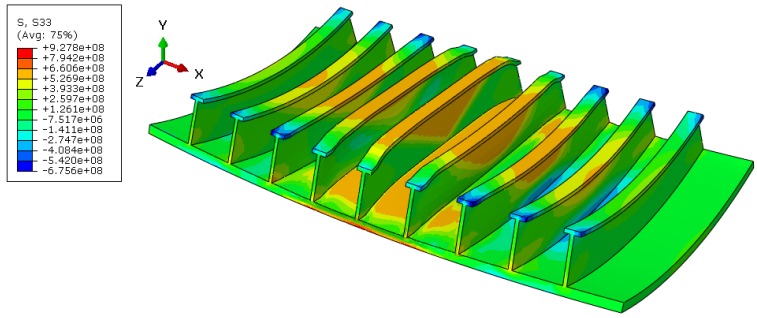

(c) Spring stiffness $\kappa = 1 \cdot 10^9$ [N/rad]

Figure F.64: Contour plot of stresses in z-direction σ_z for fully loaded model for the different spring stiffness. The load fraction equals 1.

Appendix G

MATLAB Scripts for Plotting

This section provides the MATLAB scripts applied to plot figures for the bow model assessment. The scripts presented here will not be able to provide all the results as they were modified to produce results for each part individually.

G.1 MATLAB - plateover.m

```
clc
save_file = 'yes'; %Write 'yes' to save figure!

%Filenames to choose:
%Files with 24 data sets:
filename = 'PlateOver';
%filename = 'PlateUnder';
%filename = 'WebStiff1';
%filename = 'FlangeStiff1';
%filename = 'WebStiff2';
%filename = 'FlangeStiff2';

%Files with only 16 datasets:
%filename = 'PlateOver2';
%filename = 'PlateUnder2';

%File type and fid
postfix = '.rpt';
fid     = strcat(filename,postfix);

%Initial start and end:
startRow    = 2;
endRow      = 45;


%For files with 24 datasets:
for i = 1:24
    [x, vect] = importfile(fid, startRow, endRow);

    %labeling and struct creation:
    if i > 0 && i <= 6
        Data(i).LE11 = vect;
    elseif i >6 && i <= 12
        Data(i-6).LE33 = vect;
    elseif i >12 && i <= 18
        Data(i-12).S11 = vect;
    elseif i >18 && i <= 24
        Data(i-18).S33 = vect;
    end

 %Update of data reading:
```

```
 startRow = startRow + 45;
 endRow = endRow + 45;

end

%Plotting of stress strain figures:
fg1 = figure(1);clf;

hold on
plot(Data(4).LE11, Data(4).S11/1000000, 'b')
plot(Data(6).LE11, Data(6).S11/1000000,'--b')
grid on
box on
ax = gca;
ax.XTick = -0.05:0.01:0.07;
ax.YTick = -500:100:900;
ax.YAxis.Exponent = 0;
ax.XAxis.Exponent = 0;

xl = xlabel('True Strain, $\varepsilon_x$ [-]');
yl = ylabel('Stress, $\sigma_x$ [MPa]');
ll1 = sprintf('Location 1');
ll2 = sprintf('Location 2');
ll = legend(ll1,ll2,'location','best');
ll.Interpreter = 'latex';
xl.Interpreter = 'latex';
yl.Interpreter = 'latex';
xl.FontSize = 12 ; yl.FontSize = 12 ;


%% - Print figure
filename    = 'PlateS11Loc12';
postfix     = '.eps';
path        = 'plot/';
filetype    = '-depsc2';
fid         = strcat(path,filename,postfix);

fg1.Units = 'pixels';
fg1.PaperPositionMode = 'auto';
if (strcmp(save_file,'yes'))
    fprintf('Saving figure: %s \n',fid);
    print(fg1,filetype,fid);
else
    disp('Not saving figure')
end

%Position 3 and 4
fg2 = figure(2);clf;

hold on
plot(Data(1).LE11, Data(1).S11/1000000,'b')
plot(Data(5).LE11, Data(5).S11/1000000,'--b')
grid on
box on
ax = gca;
ax.XTick = -0.05:0.005:0.02;
ax.YTick = -500:100:900;
ax.YAxis.Exponent = 0;
ax.XAxis.Exponent = 0;

xl = xlabel('True Strain, $\varepsilon_x$ [-]');
yl = ylabel('Stress, $\sigma_x$ [MPa]');
ll1 = sprintf('Location 3');
ll2 = sprintf('Location 4');
ll = legend(ll1,ll2,'location','best');
ll.Interpreter = 'latex';
xl.Interpreter = 'latex';
yl.Interpreter = 'latex';
xl.FontSize = 12 ; yl.FontSize = 12 ;


%% - Print figure
filename    = 'PlateS11Loc34';
postfix     = '.eps';
path        = 'plot/';
filetype    = '-depsc2';
fid         = strcat(path,filename,postfix);

fg2.Units = 'pixels';
fg2.PaperPositionMode = 'auto';
if (strcmp(save_file,'yes'))
    fprintf('Saving figure: %s \n',fid);
    print(fg2,filetype,fid);
else
    disp('Not saving figure')
end

%Position 5 and 6
fg3 = figure(3);clf;

hold on
plot(Data(2).LE11, Data(2).S11/1000000,'b')
plot(Data(3).LE11, Data(3).S11/1000000,'--b')
```

```
grid on
box on
ax = gca;
ax.XTick = -0.05:0.0005:0.02;
ax.YTick = -500:50:900;
ax.YAxis.Exponent = 0;
ax.XAxis.Exponent = 0;

xl = xlabel('True Strain, $\varepsilon_x$ [-]');
yl = ylabel('Stress, $\sigma_x$ [MPa]');
ll1 = sprintf('Location 5');
ll2 = sprintf('Location 6');
ll = legend(ll1,ll2,'location','best');
ll.Interpreter = 'latex';
xl.Interpreter = 'latex';
yl.Interpreter = 'latex';
xl.FontSize = 12 ; yl.FontSize = 12 ;


%% - Print figure
filename    = 'PlateS11Loc56';
postfix     = '.eps';
path        = 'plot/';
filetype    = '-depsc2';
fid         = strcat(path,filename,postfix);

fg3.Units = 'pixels';
fg3.PaperPositionMode = 'auto';
if (strcmp(save_file,'yes'))
    fprintf('Saving figure: %s \n',fid);
    print(fg3,filetype,fid);
else
    disp('Not saving figure')
end

%-------------------------------------------------------------------------
%Plotting of stress strain figures S33:
%-------------------------------------------------------------------------
fg4 = figure(4);clf;

hold on
plot(Data(4).LE33, Data(4).S33/1000000, 'b')
plot(Data(6).LE33, Data(6).S33/1000000,'--b')
grid on
box on
ax = gca;
ax.XTick = -0.05:0.005:0.07;
ax.YTick = -500:100:900;
ax.YAxis.Exponent = 0;
ax.XAxis.Exponent = 0;

xl = xlabel('True Strain, $\varepsilon_z$ [-]');
yl = ylabel('Stress, $\sigma_z$ [MPa]');
ll1 = sprintf('Location 1');
ll2 = sprintf('Location 2');
ll = legend(ll1,ll2,'location','best');
ll.Interpreter = 'latex';
xl.Interpreter = 'latex';
yl.Interpreter = 'latex';
xl.FontSize = 12 ; yl.FontSize = 12 ;


%% - Print figure
filename    = 'PlateS33Loc12';
postfix     = '.eps';
path        = 'plot/';
filetype    = '-depsc2';
fid         = strcat(path,filename,postfix);

fg4.Units = 'pixels';
fg4.PaperPositionMode = 'auto';
if (strcmp(save_file,'yes'))
    fprintf('Saving figure: %s \n',fid);
    print(fg4,filetype,fid);
else
    disp('Not saving figure')
end

%Position 3 and 4
fg5 = figure(5);clf;

hold on
plot(Data(1).LE33, Data(1).S33/1000000,'b')
plot(Data(5).LE33, Data(5).S33/1000000,'--b')
grid on
box on
ax = gca;
ax.XTick = -0.05:0.005:0.02;
ax.YTick = -700:100:900;
ax.YAxis.Exponent = 0;
ax.XAxis.Exponent = 0;

xl = xlabel('True Strain, $\varepsilon_z$ [-]');
```

```
yl = ylabel('Stress, $\sigma_z$ [MPa]');
ll1 = sprintf('Location 3');
ll2 = sprintf('Location 4');
ll = legend(ll1,ll2,'location','best');
ll.Interpreter = 'latex';
xl.Interpreter = 'latex';
yl.Interpreter = 'latex';
xl.FontSize = 12 ; yl.FontSize = 12 ;


%% - Print figure
filename    = 'PlateS33Loc34';
postfix     = '.eps';
path        = 'plot/';
filetype    = '-depsc2';
fid         = strcat(path,filename,postfix);

fg5.Units = 'pixels';
fg5.PaperPositionMode = 'auto';
if (strcmp(save_file,'yes'))
    fprintf('Saving figure: %s \n',fid);
    print(fg5,filetype,fid);
else
    disp('Not saving figure')
end

%Position 5 and 6
fg6 = figure(6);clf;

hold on
plot(Data(2).LE33, Data(2).S33/1000000,'b')
plot(Data(3).LE33, Data(3).S33/1000000,'--b')
grid on
box on
ax = gca;
ax.XTick = -0.05:0.0005:0.02;
ax.YTick = -700:100:900;
ax.YAxis.Exponent = 0;
ax.XAxis.Exponent = 0;

xl = xlabel('True Strain, $\varepsilon_z$ [-]');
yl = ylabel('Stress, $\sigma_z$ [MPa]');
ll1 = sprintf('Location 5');
ll2 = sprintf('Location 6');
ll = legend(ll1,ll2,'location','best');
ll.Interpreter = 'latex';
xl.Interpreter = 'latex';
yl.Interpreter = 'latex';
xl.FontSize = 12 ; yl.FontSize = 12 ;


%% - Print figure
filename    = 'PlateS33Loc56';
postfix     = '.eps';
path        = 'plot/';
filetype    = '-depsc2';
fid         = strcat(path,filename,postfix);

fg6.Units = 'pixels';
fg6.PaperPositionMode = 'auto';
if (strcmp(save_file,'yes'))
    fprintf('Saving figure: %s \n',fid);
    print(fg6,filetype,fid);
else
    disp('Not saving figure')
end


%Timeplot
fg45 = figure(45);clf;

hold on
plot(x,Data(4).S11/1000000,'b')
plot(x,Data(6).S11/1000000,'--b')
plot(x,Data(4).S33/1000000,':b','MarkerSize',3)
plot(x,Data(6).S33/1000000,'-.b','MarkerSize',3)
grid on
box on
ax = gca;
ax.XTick = 0:0.1:1;
ax.YTick = -900:150:900;
ax.YAxis.Exponent = 0;
ax.XAxis.Exponent = 0;

xl = xlabel('Time');
yl = ylabel('Stress, $\sigma$ [MPa]');
ll1 = sprintf('X - location 1');
ll2 = sprintf('X - location 2');
ll3 = sprintf('Z - location 1');
ll4 = sprintf('Z - location 2');
ll = legend(ll1,ll2,ll3,ll4,'location','best');
ll.Interpreter = 'latex';
xl.Interpreter = 'latex';
```

```
yl.Interpreter = 'latex';
xl.FontSize = 12 ; yl.FontSize = 12 ;


%% - Print figure
filename    = 'PlateTimeS';
postfix     = '.eps';
path        = 'plot/';
filetype    = '-depsc2';
fid         = strcat(path,filename,postfix);

fg45.Units = 'pixels';
fg45.PaperPositionMode = 'auto';
if (strcmp(save_file,'yes'))
    fprintf('Saving figure: %s \n',fid);
    print(fg45,filetype,fid);
else
    disp('Not saving figure')
end

%TimePlot for strains
fg46 = figure(46);clf;

hold on
plot(x,Data(4).LE11,'b')
plot(x,Data(6).LE11,'--b')
plot(x,Data(4).LE33,':b')
plot(x,Data(6).LE33,'-.b')
grid on
box on
ax = gca;
ax.XTick = 0:0.1:1;
ax.YTick = -0.05:0.01:0.09;
ax.YAxis.Exponent = 0;
ax.XAxis.Exponent = 0;

xl = xlabel('Time');
yl = ylabel('True strain, $\varepsilon$ [-]');
ll1 = sprintf('X - location 1');
ll2 = sprintf('X - location 2');
ll3 = sprintf('Z - location 1');
ll4 = sprintf('Z - location 2');
ll = legend(ll1,ll2,ll3,ll4,'location','best');
ll.Interpreter = 'latex';
xl.Interpreter = 'latex';
yl.Interpreter = 'latex';
xl.FontSize = 12 ; yl.FontSize = 12 ;


%% - Print figure
filename    = 'PlateTimeLE';
postfix     = '.eps';
path        = 'plot/';
filetype    = '-depsc2';
fid         = strcat(path,filename,postfix);

fg46.Units = 'pixels';
fg46.PaperPositionMode = 'auto';
if (strcmp(save_file,'yes'))
    fprintf('Saving figure: %s \n',fid);
    print(fg46,filetype,fid);
else
    disp('Not saving figure')
end

%Timeplot
fg49 = figure(49);clf;

hold on
plot(x,Data(1).S11/1000000,'b')
plot(x,Data(5).S11/1000000,'--b')
plot(x,Data(1).S33/1000000,':b','MarkerSize',3)
plot(x,Data(5).S33/1000000,'-.b','MarkerSize',3)
grid on
box on
ax = gca;
ax.XTick = 0:0.1:1;
ax.YTick = -900:150:900;
ax.YAxis.Exponent = 0;
ax.XAxis.Exponent = 0;

xl = xlabel('Time');
yl = ylabel('Stress, $\sigma$ [MPa]');
ll1 = sprintf('X - location 3');
ll2 = sprintf('X - location 4');
ll3 = sprintf('Z - location 3');
ll4 = sprintf('Z - location 4');
ll = legend(ll1,ll2,ll3,ll4,'location','best');
ll.Interpreter = 'latex';
xl.Interpreter = 'latex';
yl.Interpreter = 'latex';
xl.FontSize = 12 ; yl.FontSize = 12 ;

```

```
414
415 %% - Print figure
416 filename    = 'PlateTimeS34';
417 postfix     = '.eps';
418 path        = 'plot/';
419 filetype    = '-depsc2';
420 fid         = strcat(path,filename,postfix);
421
422 fg49.Units = 'pixels';
423 fg49.PaperPositionMode = 'auto';
424 if (strcmp(save_file,'yes'))
425     fprintf('Saving figure: %s \n',fid);
426     print(fg49,filetype,fid);
427 else
428     disp('Not saving figure')
429 end
430
431 %TimePlot for strains
432 fg50 = figure(50);clf;
433
434 hold on
435 plot(x,Data(1).LE11,'b')
436 plot(x,Data(5).LE11,'--b')
437 plot(x,Data(1).LE33,':b')
438 plot(x,Data(5).LE33,'-.b')
439 grid on
440 box on
441 ax = gca;
442 ax.XTick = 0:0.1:1;
443 ax.YTick = -0.05:0.01:0.09;
444 ax.YAxis.Exponent = 0;
445 ax.XAxis.Exponent = 0;
446
447 xl = xlabel('Time');
448 yl = ylabel('True strain, $\varepsilon$ [-]');
449 ll1 = sprintf('X - location 3');
450 ll2 = sprintf('X - location 4');
451 ll3 = sprintf('Z - location 3');
452 ll4 = sprintf('Z - location 4');
453 ll = legend(ll1,ll2,ll3,ll4,'location','best');
454 ll.Interpreter = 'latex';
455 xl.Interpreter = 'latex';
456 yl.Interpreter = 'latex';
457 xl.FontSize = 12 ; yl.FontSize = 12 ;
458
459
460 %% - Print figure
461 filename    = 'PlateTimeLE34';
462 postfix     = '.eps';
463 path        = 'plot/';
464 filetype    = '-depsc2';
465 fid         = strcat(path,filename,postfix);
466
467 fg50.Units = 'pixels';
468 fg50.PaperPositionMode = 'auto';
469 if (strcmp(save_file,'yes'))
470     fprintf('Saving figure: %s \n',fid);
471     print(fg50,filetype,fid);
472 else
473     disp('Not saving figure')
474 end
475
476 %Timeplot
477 fg51 = figure(51);clf;
478
479 hold on
480 plot(x,Data(2).S11/1000000,'b')
481 plot(x,Data(3).S11/1000000,'--b')
482 plot(x,Data(2).S33/1000000,':b','MarkerSize',3)
483 plot(x,Data(3).S33/1000000,'-.b','MarkerSize',3)
484 grid on
485 box on
486 ax = gca;
487 ax.XTick = 0:0.1:1;
488 ax.YTick = -900:100:900;
489 ax.YAxis.Exponent = 0;
490 ax.XAxis.Exponent = 0;
491
492 xl = xlabel('Time');
493 yl = ylabel('Stress, $\sigma$ [MPa]');
494 ll1 = sprintf('X - location 5');
495 ll2 = sprintf('X - location 6');
496 ll3 = sprintf('Z - location 5');
497 ll4 = sprintf('Z - location 6');
498 ll = legend(ll1,ll2,ll3,ll4,'location','best');
499 ll.Interpreter = 'latex';
500 xl.Interpreter = 'latex';
501 yl.Interpreter = 'latex';
502 xl.FontSize = 12 ; yl.FontSize = 12 ;
503
504
505 %% - Print figure
506 filename    = 'PlateTimeS56';
```

```
507 postfix     = '.eps';
508 path        = 'plot/';
509 filetype    = '-depsc2';
510 fid         = strcat(path,filename,postfix);
511
512 fg51.Units = 'pixels';
513 fg51.PaperPositionMode = 'auto';
514 if (strcmp(save_file,'yes'))
515     fprintf('Saving figure: %s \n',fid);
516     print(fg51,filetype,fid);
517 else
518     disp('Not saving figure')
519 end
520
521 %TimePlot for strains
522 fg52 = figure(52);clf;
523
524 hold on
525 plot(x,Data(2).LE11,'b')
526 plot(x,Data(3).LE11,'--b')
527 plot(x,Data(2).LE33,':b')
528 plot(x,Data(3).LE33,'-.b')
529 grid on
530 box on
531 ax = gca;
532 ax.XTick = 0:0.1:1;
533 ax.YTick = -0.005:0.001:0.009;
534 ax.YAxis.Exponent = 0;
535 ax.XAxis.Exponent = 0;
536
537 xl = xlabel('Time');
538 yl = ylabel('True strain, $\varepsilon$ [-]');
539 ll1 = sprintf('X - location 5');
540 ll2 = sprintf('X - location 6');
541 ll3 = sprintf('Z - location 5');
542 ll4 = sprintf('Z - location 6');
543 ll = legend(ll1,ll2,ll3,ll4,'location','best');
544 ll.Interpreter = 'latex';
545 xl.Interpreter = 'latex';
546 yl.Interpreter = 'latex';
547 xl.FontSize = 12 ; yl.FontSize = 12 ;
548
549
550 %% - Print figure
551 filename    = 'PlateTimeLE56';
552 postfix     = '.eps';
553 path        = 'plot/';
554 filetype    = '-depsc2';
555 fid         = strcat(path,filename,postfix);
556
557 fg52.Units = 'pixels';
558 fg52.PaperPositionMode = 'auto';
559 if (strcmp(save_file,'yes'))
560     fprintf('Saving figure: %s \n',fid);
561     print(fg52,filetype,fid);
562 else
563     disp('Not saving figure')
564 end
```

G.2 MATLAB - importfile.m

```
 1 function [X,PlateOver1] = importfile(filename, startRow, endRow)
 2 %IMPORTFILE Import numeric data from a text file as column vectors.
 3 %   [X,PLATEOVER1] = IMPORTFILE(FILENAME) Reads data from text file
 4 %   FILENAME for the default selection.
 5 %
 6 %   [X,PLATEOVER1] = IMPORTFILE(FILENAME, STARTROW, ENDROW) Reads data from
 7 %   rows STARTROW through ENDROW of text file FILENAME.
 8 %
 9 % Example:
10 %   [X,PlateOver1] = importfile('PlateOver.rpt',2, 45);
11 %
12 %    See also TEXTSCAN.
13
14 % Auto-generated by MATLAB on 2017/04/25 18:38:34
15
16 %% Initialize variables.
17 delimiter = ' ';
18 %if nargin<=2
19  %   startRow = 2;
20  %   endRow = 45;
21 %end
22
23 %% Format string for each line of text:
24 %   column1: double (%f)
25 % column2: double (%f)
```

```
% For more information, see the TEXTSCAN documentation.
formatSpec = '%f%f%[^\n\r]';

%% Open the text file.
fileID = fopen(filename,'r');

%% Read columns of data according to format string.
% This call is based on the structure of the file used to generate this
% code. If an error occurs for a different file, try regenerating the code
% from the Import Tool.
textscan(fileID, '%[^\n\r]', startRow(1)-1, 'WhiteSpace', '', 'ReturnOnError', false);
dataArray = textscan(fileID, formatSpec, endRow(1)-startRow(1)+1, 'Delimiter', delimiter, 'MultipleDelimsAsOne',
       true, 'ReturnOnError', false);
for block=2:length(startRow)
    frewind(fileID);
    textscan(fileID, '%[^\n\r]', startRow(block)-1, 'WhiteSpace', '', 'ReturnOnError', false);
    dataArrayBlock = textscan(fileID, formatSpec, endRow(block)-startRow(block)+1, 'Delimiter', delimiter, '
           MultipleDelimsAsOne', true, 'ReturnOnError', false);
    for col=1:length(dataArray)
        dataArray{col} = [dataArray{col};dataArrayBlock{col}];
    end
end

%% Close the text file.
fclose(fileID);

%% Post processing for unimportable data.
% No unimportable data rules were applied during the import, so no post
% processing code is included. To generate code which works for
% unimportable data, select unimportable cells in a file and regenerate the
% script.

%% Allocate imported array to column variable names
X = dataArray{:, 1};
PlateOver1 = dataArray{:, 2};
```